THE HEAT TRANSFER COEFFICIENT ON FILM COOLED SURFACES

by

H. D. AMMARI, B.Sc.

Thesis submitted to the University of Nottingham
for the degree of Doctor of Philosophy

August 1989

To the memory of

My Parents

CONTENTS

	Page
ABSTRACT	i
ACKNOWLEDGEMENTS	iii
LIST OF FIGURES	iv
LIST OF PLATES	ix
LIST OF TABLES	x
NOMENCLATURE	xi
CHAPTER 1 : INTRODUCTION	1
1.1 The Gas Turbine	1
1.2 Cooling of Gas Turbine Blades	2
1.3 Parameters of Film Cooling	8
1.4 Theory of Heat Transfer from Film Cooled Surfaces	10
1.5 Turbine Blade Cooling Design Considerations	12
1.6 Outline of Thesis	13
CHAPTER 2 : LITERATURE SURVEY	15
2.1 Introduction	15
2.2 The Heat Transfer Coefficient	17
2.2.1 General	17
2.2.2 Coolant to Mainstream Density Ratio	18
2.2.3 Mainstream Pressure Gradient	23
2.3 The Adiabatic Wall Effectiveness	25
2.4 Theoretical Models and Correlations	27
2.5 Numerical Work	30
2.6 Concluding Remarks	32
CHAPTER 3 : OBJECTIVES AND EXPERIMENTAL METHODS	33
3.1 Objectives of Present Work	33
3.2 Experimental Methods of acquiring the Heat Transfer Coefficient	35
3.2.1 Heat Transfer Techniques	35
3.2.2 Mass Transfer Techniques	36
3.3 Choice of Experimental Technique	37
3.4 Mass Transfer Analogy	38
CHAPTER 4 : THE SWOLLEN POLYMER TECHNIQUE	41
4.1 The Swollen Polymer Technique	41
4.1.1 The Constant Rate Period	42
4.1.2 Determination of Mass Transfer Coefficients	44
4.2 Laser Holographic Interferometry	45
4.2.1 Fringe Order Identification	46
4.2.2 Relationship Between Recession and Fringe Order	48
4.3 Applications	49
4.4 Selection of Suitable Polymer-Swelling Agent System for the Current Work	50

CHAPTER 5 : THE EXPERIMENTAL APPARATUS 52
5.1 The Wind Tunnel 52
5.1.1 The Entrance Section 55
5.1.2 The Test Section 56
5.1.3 The Test Plate 59
5.1.4 The Discharge Section 63
5.2 The Injection System 65
5.3 Instrumentation 67
5.4 The Holographic Table 68
5.5 The Air-Gauge System 71

CHAPTER 6 : EXPERIMENTAL PROGRAMME, OPERATING CONDITIONS AND PROCEDURES 76
6.1 Experimental Programme 76
6.2 Operating Conditions 80
6.3 Experimental Procedure 85
6.3.1 Setting of the Pressure Gradients 85
6.3.2 Boundary Layer Measurements 85
6.3.3 Test Preliminaries 86
6.3.4 Test Procedure 87
6.4 Reduction of the Experimental Data 88
6.5 Consistency and Repeatability of Results 92

CHAPTER 7 : VALIDATION OF THE EXPERIMENTAL TECHNIQUE 96
7.1 Experimental Qualification at Zero Injection 96
7.2 Experimental Validation at Non-Unity Density Ratios 101
7.2.1 Simulation of Density Ratio 101
7.2.2 Preliminary Considerations 102
7.2.3 Estimation of Schmidt Numbers 103
7.2.4 Experimental Methodology 104
7.2.5 Presentation and Discussion of Results 104
7.3 Conclusions 110

CHAPTER 8 : DISCUSSION OF EXPERIMENTAL RESULTS 112
8.1 Presentation of Results 112
8.2 Effect of Density ratio 113
8.2.1 Single Normal hole 113
8.2.2 Single Row of 90° Holes 115
8.2.3 Single Row of 35° Holes 120
8.2.4 Comparison of Data of 90° and 35° Holes 127
8.3 Effect of Mainstream Acceleration 130
8.4 Combined Effects of Acceleration and Density Ratio 144
8.5 Correlating Parameters 150
8.6 Applicability of Current Work 162
8.7 Final Discussion 170

CHAPTER 9 : NUMERICAL STUDIES 172
9.1 Introduction 172
9.2 Description of the Computer Scheme 173
9.2.1 General 173
9.2.2 Components of PHOENICS 174
9.3 Application of PHOENICS in the Present Work 176
9.3.1 The Problems Simulated 176
9.3.2 Mathematical and Physical Models 177
9.3.3 PHOENICS Near-Wall Treatment 178
9.3.4 Computational Details 182
9.4 Presentation and Discussion of Results 190
9.5 Concluding Remarks 205

CHAPTER 10 : CONCLUSIONS 209
10.1 Injection Hydrodynamic Effects 210
10.2 Density Ratio 211
10.3 Mainstream Acceleration 213
10.4 Numerical Studies Using PHOENICS 214
10.5 Recommendations for Future Work 215

REFERENCES 217

APPENDIX A : Choice of Suitable Swelling Agent 225

APPENDIX B : Calibration of the Air Gauge 233

APPENDIX C : Experimental Difficulties Encountered 237

APPENDIX D : Uncertainty Analysis 235

APPENDIX E : Calculation of Diffusion Coefficients and Schmidt Numbers 240

ABSTRACT

A systematic investigation of the effects of coolant-to-mainstream density ratio and mainstream acceleration on the heat transfer following injection through a row of holes in a flat plate into a turbulent boundary layer is described. A mass transfer technique was employed which uses a swollen polymer surface and laser holographic interferometry. The constant concentration of the test surface simulated isothermal conditions. Density ratios in excess of unity, representative of gas turbine operating conditions, were obtained using foreign gas injection into mainstream air. The experimental technique was validated for such measurements.

The cooling film heat transfer coefficient was measured for a range of blowing configurations and flow conditions; the holes were spaced at three-diameter intervals and inclined at 35° or 90° to the mainstream, and the ranges of the other pertinent test parameters covered were,

$0.5 \leq$ blowing rate ≤ 2.0,

$1.0 \leq$ density ratio ≤ 1.52, and

$0.0 \leq$ acceleration parameter $\leq 5 \times 10^{-6}$.

However, the tests with mainstream acceleration were performed with 35° injection only.

The heat transfer coefficient was found to be increased by injection, and with the blowing rate for both 35° and 90° injection. Close to the injection site, normal blowing produced higher heat transfer coefficients than angled blowing, but gave lower coefficients far downstream.

There were large differences in behaviour between the two injection angles with varying density ratio. For normal injection, the heat transfer coefficient at a fixed blowing rate was insensitive to the variation of density ratio, whereas for 35° injection strong dependence was observed, an increase in the density ratio leading to a decrease in the coefficient. Similar behaviour for the inclined injection case was also found in the presence of strong favourable pressure gradient.

As mainstream acceleration acts to suppress injection induced turbulence, the heat transfer coefficient under the film with and without density ratio was found to decrease in the presence of mainstream acceleration

relative to that in absence of acceleration. The heat transfer coefficient was observed to relate to the acceleration parameter in an approximately linear manner, an increase in the acceleration resulting in a decrease in the coefficient.

For normal injection, good scaling of the heat transfer coefficient including density ratios was achieved with the blowing parameter. For 35° injection, the coolant to mainstream velocity ratio was seen to scale the data best. Correlations for the heat transfer data using these scaling parameters and incorporating the distance downstream are formulated as $(x/D)M^{-0.5}$ for normal injection and $(x/D)(u_c/u_\infty)^{-4/3}$ for 35° injection. With these correlations data obtained at density ratios not representative of gas turbine practice can be adapted for design calculations.

The predictions of a computational fluid dynamics general purpose program called PHOENICS were tested against the present measurements and those of others. In general, the computed results of film cooling effectiveness agreed reasonably well with available experimental data. The ability to predict the heat transfer coefficient associated with film cooling was satisfactory for normal injection, but not as satisfactory for injection through 35° holes.

ACKNOWLEDGEMENTS

The author is indebted to several people who have assisted in the experimental and numerical programmes of this research.

Thanks are due to his supervisors Dr. N. Hay and Mr. D. Lampard for their guidance and encouragement throughout the entire project.

Many thanks are also extended to the following: Prof. G. B. Warburton for the use of the laboratories; CHAM Ltd. for providing the computer programs; Mr. S. Robertshaw and his staff of the Faculty workshop for their help with the construction of components of the experimental apparatus, and Mr. V. Hawley and his team of the L4 laboratory for maintaining the apparatus.

Finally, the author gratefully acknowledges Mu'tah University in Jordan for their financial sponsorship.

LIST OF FIGURES

	Page
Fig. 1.1 Progress in aero-engine turbine entry temperature.	3
Fig. 1.2 Cooling concept of a modern turbine blade.	4
Fig. 1.3 Effectiveness of air cooling techniques [4].	7
Fig. 1.4 Parameters of film cooling.	9
Fig. 2.1 Schematic representation of injection through a hole.	16
Fig. 2.2 Variation of h/h_o with the blowing rate (Forth [31]).	21
Fig. 2.3 Two-dimensional film cooling model.	29
Fig. 5.1 Layout of the wind tunnel.	54
Fig. 5.2 Details of the test section (excluding the roof).	58
Fig. 5.3 Profiles of contours in the test section.	60
Fig. 5.4 Details of the test plate.	62
Fig. 5.5 Injection geometry.	64
Fig. 5.6 Foreign gas injection System.	66
Fig. 5.7 Layout of the optical setup.	70
Fig. 5.8 Saturation arrangement of air-gauge air supply.	74
Fig. 6.1 Variation of mainstream velocity and acceleration parameter in absence of injection.	83
Fig. 6.2 Velocity profiles in absence of injection.	84
Fig. 6.3 Sequence in a swollen polymer technique experiment.	89
Fig. 6.4 Interferograms depicting contours of constant mass transfer coefficients of normal air injection at M=2.	93
Fig. 6.5 h/h_o contours downstream of injection through a row of holes.	94
Fig. 7.1 Variation of Stanton number without injection in the streamwise direction.	97
Fig. 7.2 Variation of mass transfer coefficients and corresponding Stanton numbers in absence of injection.	99
Fig. 7.3 Turbulence intensity profiles without injection.	100

Fig. 7.4 Prediction of Schmidt number of n-tetradecane diffusing in various gas mixtures at 27°C. 105

Fig. 7.5 Distribution of normalized mass transfer coefficient for foreign gas injection of equal density but different transport property. 108

Fig. 7.6 Distribution of normalized mass transfer coefficient for foreign gas injection of equal density but different transport property. 109

Fig. 8.1 h/h_o contours following normal injection through a single hole. 114

Fig. 8.2 h/h_o contours following normal injection through a row of holes. 116

Fig. 8.3 h/h_o contours following normal injection through a single hole and a row of holes. 118

Fig. 8.4 Effect of density ratio on h/h_o for normal injection through a row of holes. 119

Fig. 8.5 h/h_o contours following injection at 35° through a row of holes. 121

Fig. 8.6 Effect of density ratio on h/h_o for 35° injection through a row of holes. 123

Fig. 8.7 Variation of h/h_o with the blowing rate. 125

Fig. 8.8 Comparison of h/h_o results with those of others for 35° injection. 126

Fig. 8.9 Comparison of h/h_o results with those of others for 35° injection. 128

Fig. 8.10 Comparison of contours of constant mass (heat) transfer coefficients for 90° and 35° injection through a row of holes at M=1. 129

Fig. 8.11 Lateral distribution of h/h_o at two downstream locations for 90° and 35° injection via a row of holes. 131

Fig. 8.12 Interference fringes depicting contours of constant mass (heat) transfer coefficients for air injection through a row of 35° holes at M=1. 132

Fig. 8.13 Mean velocity and turbulence intensity profiles in the presence of both injection and acceleration, M=1.5. 134

Fig. 8.14 Variation of the laterally averaged heat transfer coefficient downstream of injection at 35° through a row of holes. 136

Fig. 8.15 Effect of moderate mainstream acceleration on the laterally averaged heat transfer coefficient, row of holes, α=35°. 137

Fig. 8.16 Effect of moderate mainstream acceleration on the centreline heat transfer coefficient, row of holes, α=35°. 139

Fig. 8.17 Effect of strong mainstream acceleration on the laterally averaged heat transfer coefficient, row of holes, α=35°. 140

Fig. 8.18 Effect of acceleration parameter on the laterally averaged heat transfer coefficient, row of holes, α=35°. 142

Fig. 8.19 Mean velocity and turbulence intensity profiles at x/D=5 following injection at 35° through row of holes. 143

Fig. 8.20 Variation of the laterally averaged heat transfer coefficient downstream of injection at 35° through a row of holes. 145

Fig. 8.21 Effect of strong mainstream acceleration on the laterally averaged heat transfer coefficient, row of holes, α=35°. 147

Fig. 8.22 Effect of density ratio on the heat transfer coefficient in the presence of strong mainstream acceleration, $K=5x10^{-6}$, row of holes, α=35°. 149

Fig. 8.23 Effect of both the density ratio and strong acceleration on the laterally averaged heat transfer coefficient, row of holes, α=35°. 151

Fig. 8.24 Effect of injection parameters on h/h_o for normal injection through a row of holes. 152

Fig. 8.25 Correlation of h/h_o for normal injection through a row of holes. 153

Fig. 8.26 Correlated h/h_o data for $x/D \leq 25$ and $0.5 \leq M \leq 1.5$ for normal injection. 154

Fig. 8.27 Comparison of predicted and experimental data of h/h_o for normal injection. 156

Fig. 8.28 Effect of injection parameters on h/h_o for injection at 35° through a row of holes. 157

Fig. 8.29 Correlation of h/h_o for injection at 35° through a row of holes. 159

Fig. 8.30 Comparison of predicted and experimental data of h/h_o for inclined injection. 160

Fig. 8.31 Correlation of the laterally averaged heat transfer coefficient in the presence of mainstream acceleration for injection at 35° through a row of holes. 161

Fig. 8.32 Correlation of h/h_o data for $0.0 \leq K \leq 5x10^{-6}$ and $0.5 \leq u_j/u_\infty \leq 1.5$, row of holes, $\alpha=35°$. 163

Fig. 8.33 Axial film cooling effectiveness distributions for injection through a row of holes at an angle of 35° with the main flow. 165

Fig. 8.34 Heat load distribution downstream of injection at 35° through a row of holes. 166

Fig. 8.35 Centreline heat load distribution downstream of injection at 35° through a row of holes. 168

Fig. 8.36 Centreline heat load distribution downstream of injection at 90° and 35° through a row of holes. 169

Fig. 9.1 Geometry used. 183

Fig. 9.2 Grid used. 185

Fig. 9.3 Comparison between predicted and measured Stanton number in the streamwise direction in absence of injection. 192

Fig. 9.4 Comparison between predicted and measured velocity profiles in absence of injection. 192

Fig. 9.5 Comparison between predicted and measured h/h_o following injection through a row of holes. 193

Fig. 9.6 Lateral distribution of predicted and measured h/h_o following normal injection through a row of holes. 194

Fig. 9.7 Comparison between predicted and measured h/h_o following injection through a row of holes. 196

Fig. 9.8 Lateral distribution of predicted and measured h/h_o following injection through a row of holes. 197

Fig. 9.9 Comparison between predicted and measured h/h_o following injection through a row of holes. 198

Fig. 9.10 Comparison between predicted and measured velocity profiles downstream of the centreline of a hole. 200

Fig. 9.11 Lateral distribution of predicted and measured h/h_o following injection through a row of holes. 201

Fig. 9.12 Comparison between predicted and measured laterally averaged effectiveness following injection through a row of holes. 203

Fig. 9.13 Comparison between predicted and measured effectiveness following injection through a row of holes. 204

Fig. 9.14 Comparison between predicted and measured laterally averaged effectiveness following injection through a row of holes. 206

Fig. 9.15 Comparison between predicted and measured effectiveness following injection through a row of holes. 207

Fig. A.1 Volume swelling of silicone rubber RTV615 by swelling agents with time. 226

Fig. A.2 Effect of tolerated vapour pressure on predicted constant rate period. 228

Fig. A.3 Effect of temperature on predicted constant rate period. 228

Fig. A.4 Comparison of predicted constant rate period for three different systems. 229

Fig. A.5 Variation of manometer pressure due to evaporation of swelling agent from the swollen polymer by the air-gauge supply with time. 231

Fig. A.6 Predicted fringe order for experiments of 15 minutes duration. 232

Fig. B.1 Calibration of the air-gauge. 234

LIST OF PLATES

		Page
Plate 5.1	General view of the wind tunnel.	53
Plate 5.2	View of the test section.	57
Plate 5.3	Test plate.	61
Plate 5.4	View of the holographic setup.	69
Plate 5.5	Air-gauge assembly.	73

LIST OF TABLES

	Page
Table 2.1 Summary of the parameters covered by other workers.	19
Table 6.1 Range of film cooling parameters covered in the experimental work.	78
Table 6.2 Sequence of tests conducted, a row of holes.	81
Table 7.1 Schmidt number of n-tetradecane in air, gases and gas mixtures at 300K and 1 atm.	106

NOMENCLATURE

a	mass fraction of swelling agent in the swollen polymer coating
b	height of injection layer, eq. (2.1)
C	concentration of swelling agent vapour
C_1, C_2, σ_k, σ_ε	empirical constants in turbulence model
C_f	skin-friction factor
c	mass fraction
c_p	specific heat
D	injection hole diameter
E	constant for the law of the wall
H	shape factor of boundary layer
h	heat transfer coefficient, or specific enthalpy
$\bar{h}$	lateral average heat transfer coefficient
$\hat{h}$	centreline heat transfer coefficient
I	momentum flux ratio ($=\rho_c u_c^2/\rho_\infty u_\infty^2$)
i_1	illuminating angle of the object in the optical setup
i_2	viewing angle of the object in the optical setup
K	acceleration parameter ($=\nu(du_\infty/dx)/u_\infty^2$)
k	kinetic energy of turbulence
k_v	Von Karman constant, eq. (9.4)
L	distance between virtual start of aerodynamic boundary layer and start of concentration boundary layer
M	blowing rate (mass flux ratio=$\rho_c u_c/\rho_\infty u_\infty$)
m"	mass flux
N	refractive index
Nu	Nusselt number
n	fringe order number
P	pressure
P1, P2	air-gauge manometer pressure readings
P_∞	smooth-wall sublayer resistance function
Pr	Prandtl number
q	heat flux
R	blade surface curvature, or the gas constant
Re	Reynolds number
S	change in optical path-length
Sc	Schmidt number
Sh	Sherwood number

St	Stanton number
s	distance between centres of injection holes, or slot width
T	temperature
Tu	turbulence intensity
t	time
u	velocity component in x-direction
u′	time-averaged rms fluctuating velocity in x-direction
u_τ	friction velocity
v	velocity component in y-direction, or volume fraction
w	velocity component in z-direction
X	distance from virtual origin of aerodynamic boundary layer
x	downstream distance from injection hole origin
y	vertical distance from the test surface
z	lateral distance from injection hole origin

Greek

α	injection inclination to the streamwise direction
δ	recession of polymer coating, or thickness of boundary layer
δ^*	boundary layer displacement thickness
ε	dissipation rate of turbulence
η	effectiveness
$\bar{\eta}$	lateral average effectiveness
$\hat{\eta}$	centreline effectiveness
θ	temperature difference parameter, eq. (1.6)
λ	wavelength of laser light
μ	viscosity
ν	kinematic viscosity
ρ	density
τ	shear stress

Subscript

aw	adiabatic wall
c	coolant, or polymer coating
D	injection hole diameter
eff	effective
f	injection
iw	impermeable wall
l	laminar
MF	moderate favourable pressure gradient
m	mass transfer
mo	mass transfer in absence of injection
o	zero injection

oMF	zero injection, moderate favourable pressure gradient
oSF	zero injection, strong favourable pressure gradient
p	grid cell node
SF	strong favourable pressure gradient
s	swelling agent
sc	swollen polymer coating
t	turbulent
w	wall
θ	temperature difference parameter, eq. (1.6)
∞	mainstream
∞o	mainstream conditions at the hole origin outside of the boundary layer
∞x	local mainstream conditions outside of the boundary layer

CHAPTER 1

INTRODUCTION

This Chapter introduces the subject of film cooling of surfaces and explains its application to gas turbines. It also highlights the need for film cooling research and touches on the problems associated with such research.

1.1 THE GAS TURBINE

Gas turbine engines, which are highly efficient and sophisticated machines, have established a wide scope of applications especially in the field of aircraft propulsion. The design of advanced aircraft gas turbine engines is directed by a number of factors. These include, in addition to the key objectives of reduced fuel consumption and high performance, the factors of high reliability and durability, low initial and maintenance cost, and low weight. The most important of all is the engine fuel consumption that accounts for over 30 percent of direct operating cost [1].

The performance of gas turbines has improved considerably over the past three decades. The advancement in providing higher engine thermal efficiency, and hence greater engine specific power and reduced fuel consumption, is achieved by increasing the turbine inlet temperature and the cycle pressure ratio. Modern aircraft turbofan engines are operating at 1600K turbine inlet temperatures and approximately 25:1 pressure ratios [2]. These improved cycle conditions impose an extremely hostile environment on the critical hot components in the engine. Thus, careful design considerations are needed to maintain acceptable reliability and long service life.

One of the principal limitations to progress in enhancing the thermal efficiency is the requirement of turbine inlet gas temperatures far above the melting point of stator vane and rotor blade materials. Initially, this problem

was dealt with by developing new materials with significantly improved high temperature properties, such as creep strength and resistance to thermal fatigue. The high temperature alloys have resulted in increased usable metal temperatures of about 10°C per year [3]. However, the competitive nature of the gas turbine industry has demanded ever higher engine performance, requiring turbine inlet temperatures to increase at a rate exceeding that achievable by development of improved materials.

1.2 COOLING OF GAS TURBINE BLADES

To ensure the structural integrity of the blades when exposed to a high temperature environment for prolonged periods of time, cooling schemes are introduced. The schemes generally utilize the relatively cold pressurised air bled from the compressor discharge. Internal cooling is not sufficient and the exposed blade surfaces can be kept below critical temperatures only by means of additional external surface cooling. The introduction of cooling produced an upward step of roughly 100°C in turbine entry temperature and a subsequent rate of increase of about 20°C per year [4]. Fig. 1.1 portrays the substantial contribution of cooling in raising turbine operating temperatures.

Gas turbine blades may be cooled by liquids or gases. Liquid coolants provide potential thermodynamic advantages over air coolants, however, the practical engineering difficulties associated with the liquid systems, particularly for aeropropulsion applications, and the relative simplicity of the latter has resulted in the wide spread use of the gas cooling systems. In the present study, work is limited to situations in which the coolant and the mainstream fluids are gases.

There are various cooling techniques used in advanced gas turbines, that have progressed from simple convection systems to more sophisticated arrangements as illustrated in Fig. 1.2.

The techniques used are briefly,

i) Convection cooling: Internal radial serpentine passages of basically rectangular cross section are used to cool the midchord regions of the

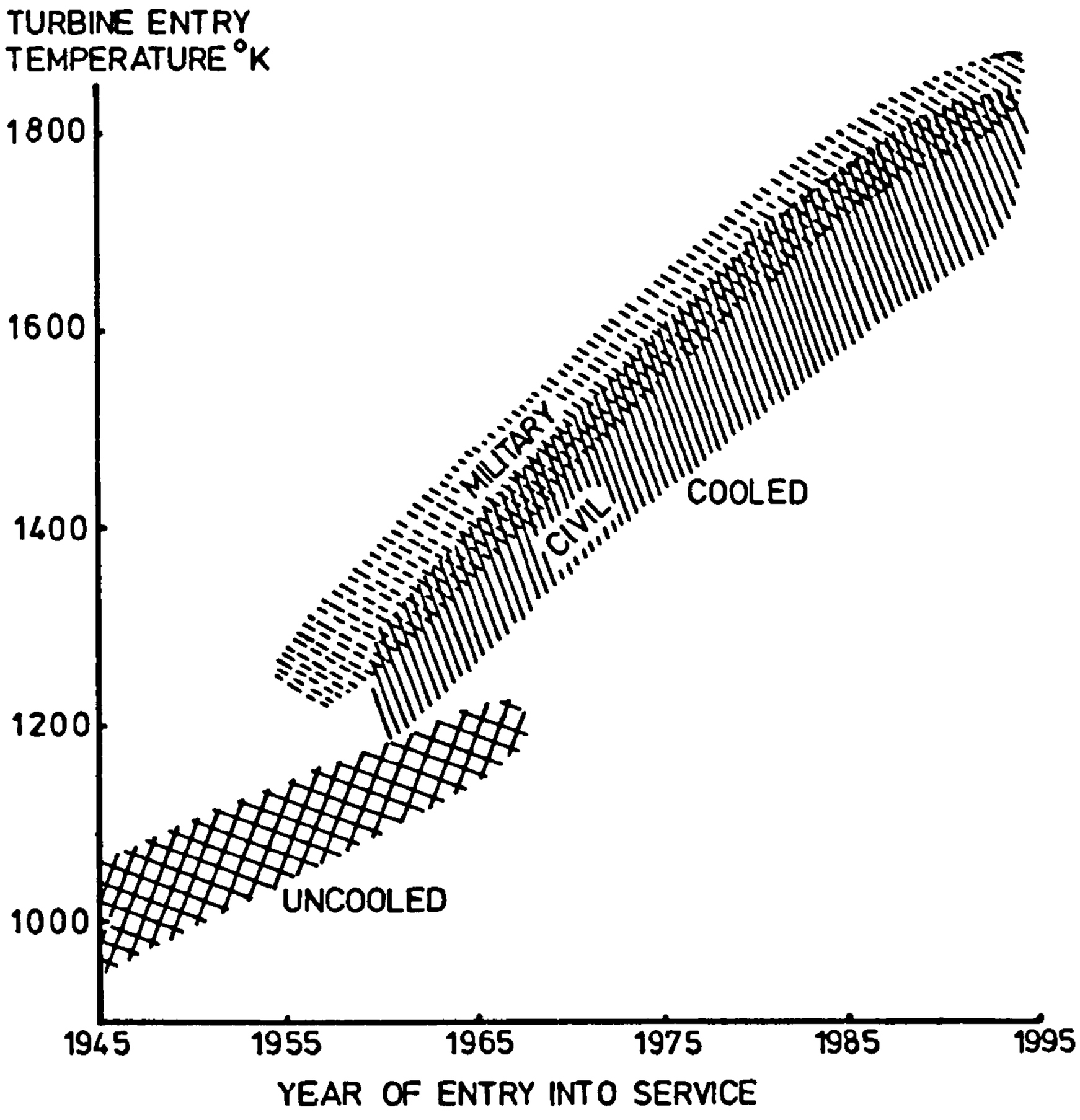

Fig. 1.1 Progress in aero-engine turbine entry temperature.

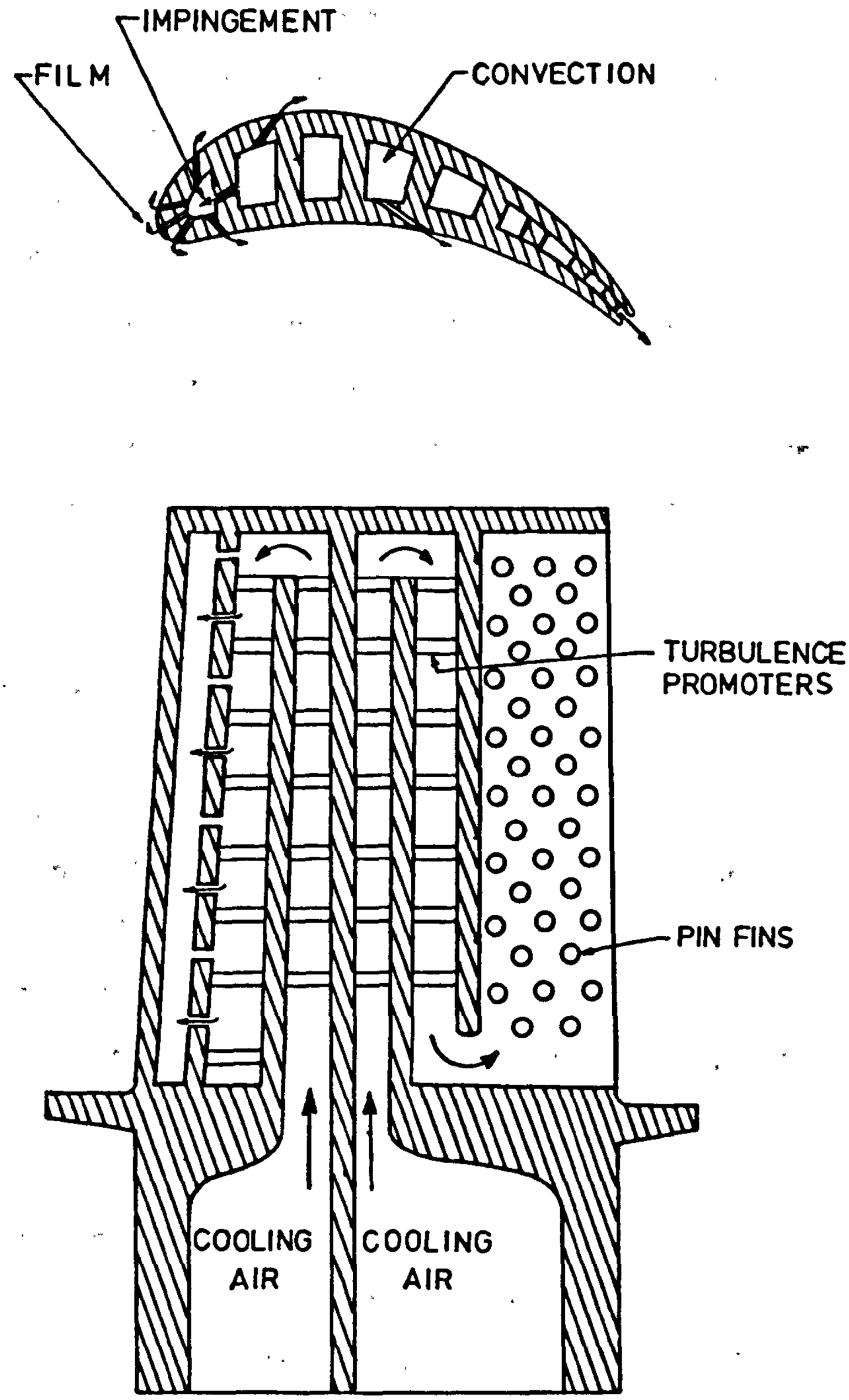

Fig. 1.2 Cooling concept of a modern turbine blade.

blades. The coolant circulates within the passages, takes energy directly from the surface by forced convection.

ii) Impingement cooling: Perforated inserts are incorporated inside the passages. The coolant passes through the small holes impinges on the inside blade wall, enhancing the heat transfer rate. Impingement cooling is a very high performance scheme that offers a great cooling potential and, therefore, is mainly used at the leading edge of the blade.

iii) Pin fin arrays cooling: Pin fins are generally incorporated in the trailing edge of the blade, typically of equal height and diameter, and located in staggered patterns. They serve as heat transfer augmentation devices by turbulating the coolant as it passes around them.

iv) Transpiration cooling: Parts of the outer skin of the blade are made of porous material. The coolant is effused out through the skin pores into the hot mainstream gases offering high potential cooling effectiveness. Additionally, the heat transfer coefficient is reduced [5]. However, the problems involved with this method, such as manufacture of the skin of the blade, lack of material strength, and clogging of the fine pores, restrict its usage, especially in aircraft applications.

v) Film cooling: The coolant is permitted to eject to the surface through a variety of configurations, two-dimensionally such as normal and angled flush slots, and tangential slots, or three-dimensionally such as a single row of discrete holes, multiple staggered rows of holes, and slots with discontinuities. The coolant is injected over parts of the blade surface in such a way that it remains close to the surface forming a protective insulating layer from the hot mainstream gas. Film cooling is a principal method of cooling turbine blades, and is required at many vulnerable regions of the blade surface from the leading edge to the trailing edge.

Further it is worth noting that injection through continuous slots provides more efficient cooling performance than through discrete holes, due to the fact that slot injection mixing with the hot mainstream is less intensive. But, the high turbine blade stress levels, and the aerodynamic

penalties makes the use of slot cooling undesirable. Injection through a single row of holes, however, produces an extremely nonuniform conditions due to the resulting three-dimensional effects of jet-mainstream mixing especially over the downstream regions close to the holes. Numerical treatment of such flows is therefore difficult, and most of the work on film cooling has been experimentally based.

A broad indication of the potential cooling effectiveness from some of the cooling techniques is shown in Fig. 1.3.

For any turbine blade cooling arrangement, the turbine inlet temperature and the resulting thermal efficiency can only be increased to a certain level. Beyond that, penalties associated with cooling air injection exceed the benefits. The penalties involve losses in aerodynamic efficiency produced by mixing of low momentum coolant and high velocity mainstream gas, and power needed for compression and pumping of the cooling air that bypasses the combustion chamber. Moffat [6] cited that the turbine efficiency is dropped possibly by as much as 1% for each 1% coolant discharged through the blades. In addition, there is a thermodynamic penalty associated with the cooling air removing heat from the hot mainstream gas over the blades. The direct impact on the operating expenses of the engine is indicated by Elovic and Koffel [7], who reported that each one percent of compressor discharge air used for cooling results in about 0.75% increase in specific fuel consumption in a typical high bypass, high pressure ratio turbofan engine.

The main requirements, therefore, that are demanded from the designer of turbine hot components are,

i) Minimizing cooling air consumption with an arrangement of minimum interference with the hot mainstream aerodynamics, so as to reduce the engine fuel consumption and give maximum engine efficiency.

ii) Accomplishing minimum blade and vane overall temperature levels and local temperature gradients to avoid thermal stresses.

The challenge of these requirements can be alleviated if predictions of local gas-side heat transfer coefficients of the component are more accurate.

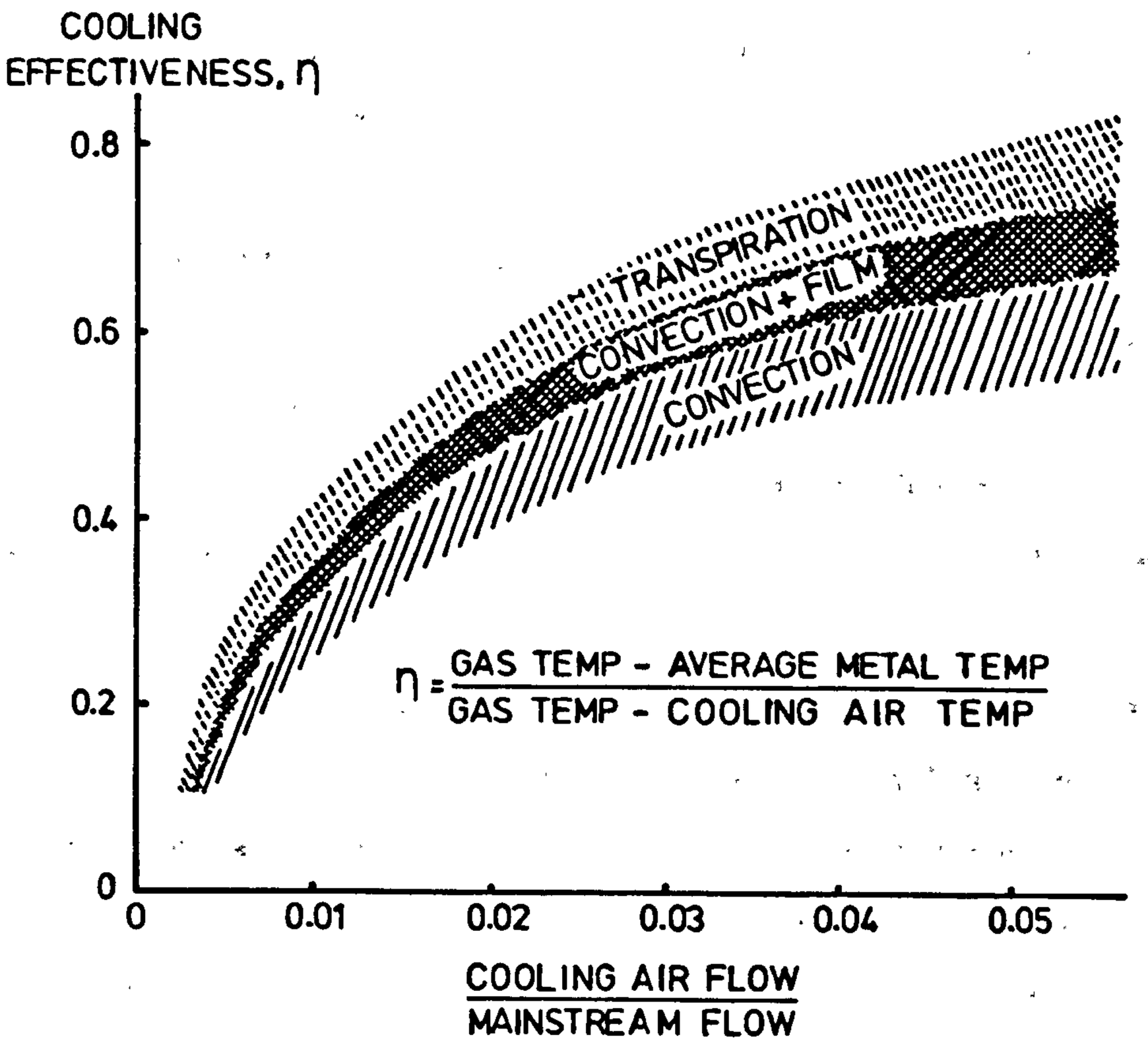

Fig. 1.3 Effectiveness of air cooling techniques [4].

Stepka [8] estimated the uncertainties in calculated heat transfer coefficients to be 35% which, for realistic engine conditions, would result uncertainties of 98K in metal surface temperature. This order of uncertainty has forced turbine hot components designers to require over-cooling to insure acceptable reliability and life. Thus, adversely affecting the cycle efficiency.

Despite recent advances in the development of ceramic coatings that have permitted higher turbine entry temperatures, turbine blade cooling remains a necessary major cooling mechanism.

This research is concerned only with film cooling, although an optimized blade cooling system utilizes film cooling and a combination of the cooling schemes outlined above.

1.3 PARAMETERS OF FILM COOLING

A major factor contributing to the complexity of the film cooling situation is the large number of parameters involved.

The various parameters governing the film cooling process include the geometrical configuration of the holes and the aerodynamic characteristics of the flows as presented in Fig. 1.4.

Systematic studies of film cooling parameters have given some insight into some of their influence. But further work is still required to produce general quantitative information of their individual and combined influence and to cover the whole field of conditions involved, especially those typical of gas turbine practice. However, in any one film cooling investigation the number of parameters varied is usually very restricted, due to time and cost limitations.

A review of the available literature describing the influence of these parameters on film cooling performance is given in the following chapter.

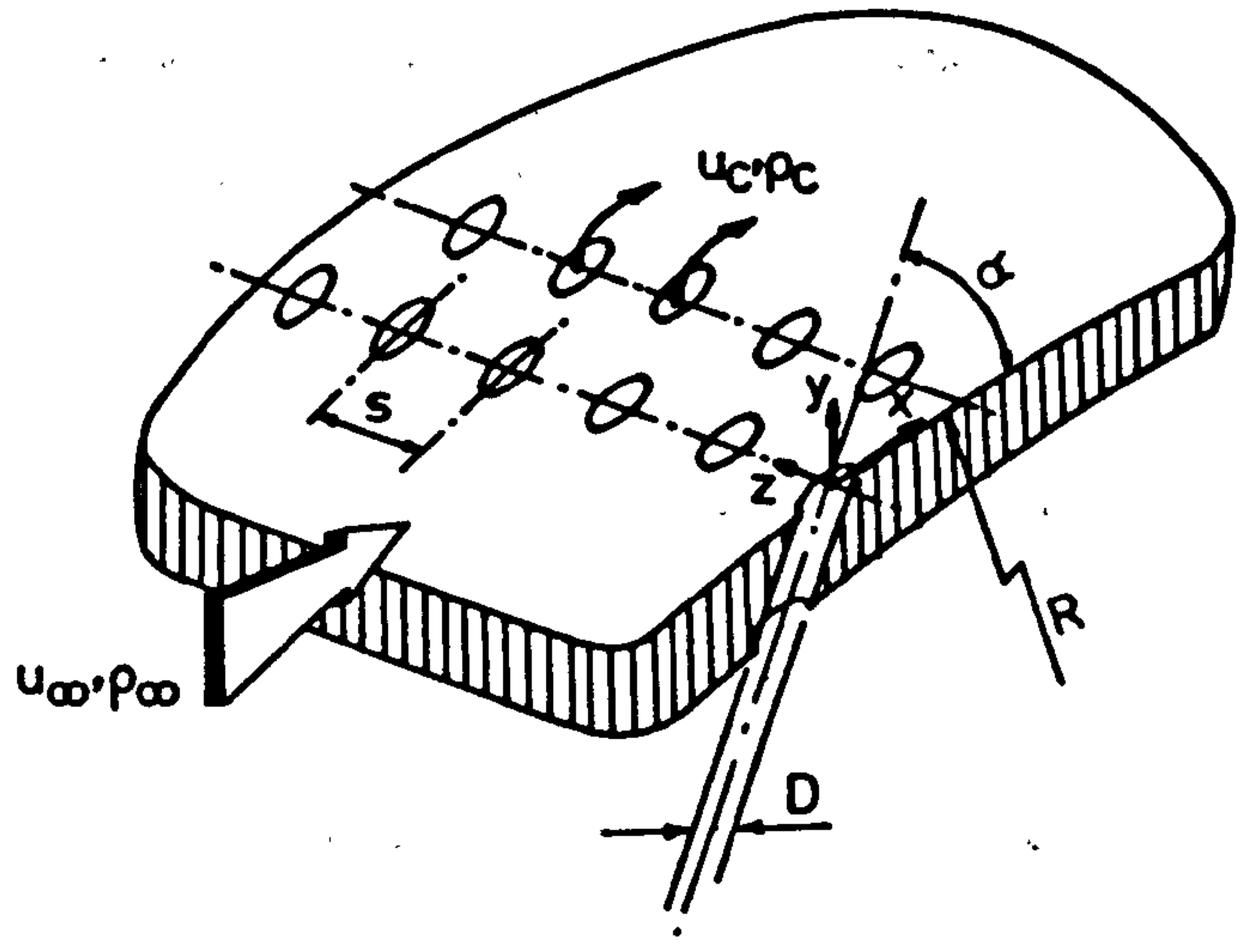

Flow,

Velocity ratio, u_c/u_∞

Density ratio, ρ_c/ρ_∞

{ Blowing rate, $M=\rho_c u_c/\rho_\infty u_\infty$ }

{ Momentum flux ratio, $I=\rho_c u_c^2/\rho_\infty u_\infty^2$ }

Pressure gradient, dP/dx

Mainstream Reynolds number, Re_D

Boundary layer, δ, δ^*/D

Mainstream turbulence intensity, Tu

Coolant Reynolds number, Re_c

Surface roughness

Compressibility

Geometric,

Hole inclination, α

Hole spacing to diameter ratio, s/D

Hole shape

Surface curvature, R

Number and spacing of rows, and hole arrangement (staggered, in-line)

Fig 1.4 Parameters of Film Cooling

1.4 THEORY OF HEAT TRANSFER FROM FILM COOLED SURFACES

For constant property flows, the connection between heat flux, q_o, and temperature at a particular position on an impervious turbine blade surface is conventionally described by a heat transfer coefficient defined through the equation,

$$q_o = h_o (T_\infty - T_w) \qquad \text{- - - (1.1)}$$

where T_∞ is the mainstream gas temperature which is equivalent to the adiabatic wall temperature for low Mach number flows, or the recovery mainstream temperature in the case of high Mach number flows. T_w is the wall temperature and h_o the associated heat transfer coefficient.

On film cooled blade surfaces, the heat flux, q_f, is customarily represented by adopting an equivalent equation given by [9],

$$q_f = h_f (T_{aw} - T_w) \qquad \text{- - - (1.2)}$$

here, h_f is the heat transfer coefficient in the presence of the film and T_{aw} is the adiabatic wall temperature, i.e., the temperature which the wall assumes when there is no heat flux from the wall surface into its interior. T_{aw} is representative of the local temperature of the film.

For constant property flows, h_f is independent of the temperature field, but is a property of the flow field.

In most experimental work the adiabatic wall temperature is expressed in a dimensionless form called the adiabatic wall film cooling effectiveness, η_{aw}, given by,

$$\eta_{aw} = (T_\infty - T_{aw})/(T_\infty - T_c) \qquad \text{- - - (1.3)}$$

where T_c is the temperature of the coolant, the recovery coolant temperature for high speed flows.

In the vicinity of the injection site, η_{aw} is close to unity ($T_{aw} \approx T_c$), i.e. the film is very efficient. Far downstream, η_{aw} is close to zero ($T_{aw} \approx T_\infty$), where the boundary layer recovers to its undisturbed condition.

In experiments following the adiabatic wall approach, the heat transfer coefficient h_f must be obtained from other experiments employing a constant

wall temperature along the surface or constant heat flux.

An alternative approach called "Superposition", first developed by Metzger et al [10], expresses the heat flux, q_f, to a film cooled surface by a different relation given by,

$$q_f = h\,(T_\infty - T_w) \qquad \text{- - - (1.4)}$$

here T_w is the temperature of the isothermal wall and h is the heat transfer coefficient with injection. In this relation the parameter that accounts for the effects of injection is the newly defined parameter h. Its effect can be seen by combining equations (1.1) to (1.4), i.e.,

$$q_f/q_o = h/h_o = h_f/h_o\,(1 - \eta_{aw}\,\theta) \qquad \text{- - - (1.5)}$$

where θ is a dimensionless temperature difference parameter defined by,

$$\theta = (T_\infty - T_c)/(T_\infty - T_w) \qquad \text{- - - (1.6)}$$

The linearity of the expression (1.5) has been demonstrated experimentally for incompressible flows [10, 11] and for compressible variable property flows [12].

Equation (1.5) yields $h_f = h$, when $\theta = 0$ (i.e. when $T_\infty = T_c$). This case has been used by Metzger et al [13] and by Ville and Richards [14] to determine h_f by extrapolation from measurements of h made over a range of θ.

When h = 0, i.e. the average surface heat transfer rate is zero [15], $\eta_{aw} = 1/\theta$, hence θ becomes like the conventional effectiveness a measure of the mixing between the main and the coolant flows.

It is worth noting that Choe et al [16] have presented the film cooling data by supplying h at $\theta = 0$ and $\theta = 1$ (obtained by changing T_c from T_∞ to T_w), so that h can be acquired at any value of θ as follows,

$$h = h_{\theta=0} - \theta\,(h_{\theta=0} - h_{\theta=1})$$

They have also shown that the adiabatic effectiveness can be obtained from the same data,

$$\eta_{aw} = 1 - h_{\theta=1}/h_{\theta=0}$$

The two approaches are equally well founded in theory and data from one method can be transformed to the other [16]. However, adiabatic wall

conditions experiments provide an advantage in that the problem which have a three temperature potentials T_∞, T_g and T_w is reduced to a two temperature one, T_{aw} and T_w.

In conclusion, there are two parameters of major concern to designers of film cooled surfaces. Using the adiabatic wall approach, equation (1.2) reveals that detailed information on the adiabatic wall temperature T_{aw} represented by the effectiveness η_{aw} and on the distribution of the heat transfer coefficient h, are required in order to predict the blade local surface temperature. Or, if using the superposition approach (equation 1.4), information on h obtained at two values of θ=0 and 1, are required.

1.5 TURBINE BLADE COOLING DESIGN CONSIDERATIONS

The implementation of internal and external cooling increases the life of vanes and blades substantially. The design of such cooling arrangements that provide an acceptable blade life is dependent on the accurate determination of the surface temperature distribution of the blade. The blade surface temperature is in turn dependent on the external heat flux to the surface from the hot mainstream, the heat conduction within the blade material and the heat convection to the cooling air.

The distribution of the heat flux around the surface of a turbine blade, under typical engine operating conditions, is generally highest at the stagnation region of the leading edge, and the trailing edge region on both the suction and the pressure sides. Other regions of high heat flux are the thin boundary layer pressure side, and the laminar-to-turbulent transition region on the suction side.

It is thus clear that most of the blade surface requires cooling to reduce the surface temperature levels and gradients. Rows of normal injection holes are therefore required at the blade leading edge and inclined injection configurations are required at the remaining high heat flux regions.

However, with film cooling the boundary layer theory used for calculation of the heat transfer distribution is no longer applicable, the

momentum of the coolants injected through a number of angled discrete holes is significant, at least over a certain distance downstream of injection. The coolant to mainstream density variations, the wide variety of injection configurations and other parameters all add to the complexity of the situation.

It follows that, the thermal design of film cooled blades, at present, is based on experimental information acquired at modelled or real engine conditions. The designer is, therefore, forced to rely on expensive and time-consuming experimentation.

A vast amount of systematic research has taken place on film cooling in an effort to quantify the process. However, the available data are still inadequate to produce general correlations or numerical models for design purposes. Consequently, there remains a strong need for further acquisition of experimental data especially at simulated engine operating conditions. The present research provides information on the heat transfer coefficient at density ratios and pressure gradients representative of the engine environment. An attempt is also made to correlate this information to provide better predictability for future designs.

1.6 OUTLINE OF THESIS

Chapter 2 reviews the most relevant studies that have been done previously on the film cooling process, particularly on the heat transfer coefficient following injection through discrete holes. The objectives of the current work followed by a brief description of the experimental methods for acquiring the heat transfer coefficient are outlined in Chapter 3. Chapter 4 provides an explanation of the experimental method used, whereas a description of the apparatus is given in Chapter 5. The experimental programme, operating conditions and procedures are presented in Chapter 6.

Validation of the present experimental mass transfer method for the measurement of the cooling film heat transfer coefficient with density ratios is provided in Chapter 7. Chapter 8 presents and discusses the experimental results.

In addition to the experimental part of this study, Chapter 9 is concerned with the theoretical part describing the appropriateness of a numerical procedure for the solution of the film cooling problem. The final conclusions drawn from the present research and recommendations for the future work are given in Chapter 10.

CHAPTER 2

LITERATURE SURVEY

This Chapter reviews the present state of the art of film cooling with a view to summarise the effects of the various parameters on film cooling performance.

2.1 INTRODUCTION

Extensive work has been done into film cooling during the last 30 years. Early work was concentrated on two-dimensional injection through continuous slots. This work has been surveyed by Goldstein [9] and further updated by Hartnett [17]. As it refers to slots it will not be referred to here unless it helps to explain a certain point. An effort was also made on transpiration cooling, a comprehensive survey of which is found in [17]. But for the past 20 years film cooling research has been mainly directed at three-dimensional injection through discrete holes, due to its practical usefulness in applications to gas turbine airfoils.

Considerable experimental data exist on film cooling with injection through discrete holes. It is important, however, to understand the physical mechanism of the interaction between the mainstream and the injectant, since the mixing process is highly three-dimensional, and of a greater extent and influence than that of slots. An insight into the manner in which a jet mixes with a mainstream is gained through flow visualization studies [18, 19 & 20]. These studies have shown that as a jet emerges from the surface it is deflected in the streamwise direction and takes on a "kidney" shape caused by a pressure difference created between upstream and downstream lips of the jet at exit (Fig. 2.1). Counter-rotating .vortex patterns are also formed just downstream of an injection hole. These vortices dominate the flow in the nearfield and persist to the farfield, augmenting the entrainment of mainstream

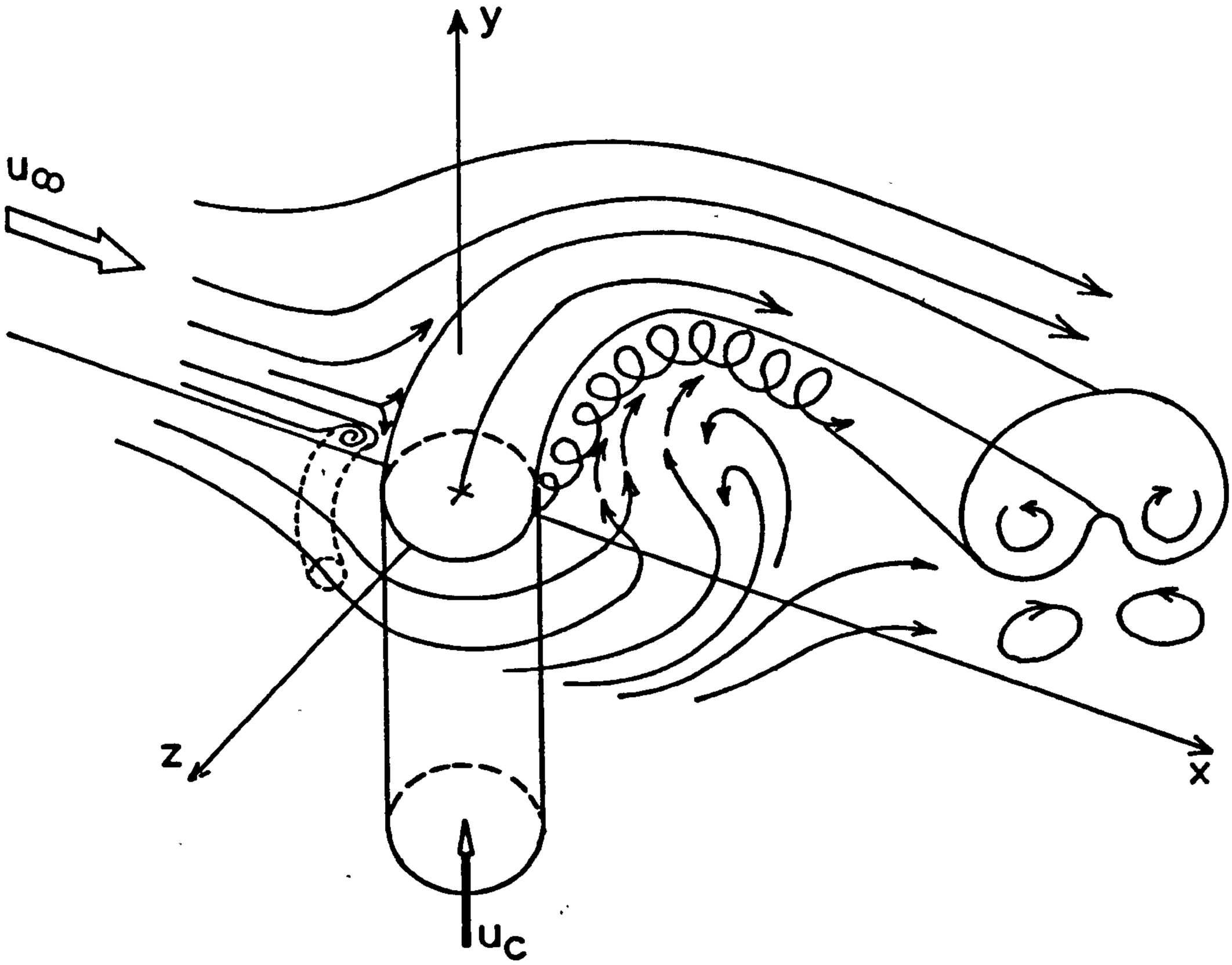

Fig. 2.1 Schematic representation of injection through a hole.

fluid, and introducing high intensity turbulence, thereby enhancing the heat transfer. Moreover, as the blowing rate is raised, a region of recirculating flow is generated immediately after a hole. The complex behaviour becomes even stronger when the blowing rate and/or the blowing angle are increased.

The extensive intermixing process has a great influence on the film cooling effectiveness and the heat transfer coefficient. Many of the film cooling data relate only to the effect of injection on the adiabatic effectiveness. The effect on the heat transfer coefficient, however, is necessary to fully assess the film cooling process, in particular at the region near the injection site which is the region of interest. Most of the recent experimental research on film cooling is, therefore, concerned with the heat transfer coefficient as is the case in the current work.

Following is a brief discussion of the investigations that are pertinent to the present experimental work, with an emphasis on the influence of coolant to mainstream density ratio and mainstream pressure gradients on the heat transfer coefficient.

2.2 THE HEAT TRANSFER COEFFICIENT

2.2.1 General

A number of studies on local and lateral average heat transfer coefficients have been reported. These studies involved different geometry of holes with different injection angles under various mainstream and coolant conditions. These studies have revealed that the heat transfer coefficient (local and lateral average) is appreciably influenced by injection, with the influence being more substantial near the holes, and varies with the various parameters of film cooling.

Blowing, in general, enhances the heat transfer coefficient close to a hole with a monotonic decrease toward the unblown value far downstream. This effect is significantly intensified as the blowing rate or the injection angle is increased [21, 22]. However, injection from a shallow angle results in higher coefficients than in normal injection far downstream, since the effects

of normal jets fall off more quickly with distance from the holes [21].

The effect of mainstream Reynolds or Mach number on the heat transfer coefficient was found to be small [23], [24] respectively. The injectant whether it is turbulent or laminar appears to have a similar influence on the heat transfer coefficient [25]. The boundary layer thickness was shown by Liess [24] to have a negligible effect on the lateral average heat transfer coefficient. The approach boundary layer (turbulent or transitional [26], turbulent or laminar [25]) made only a little or no difference to the heat transfer coefficient.

Kruse [27] noted that, with small hole spacing the lateral average heat transfer coefficients immediately downstream of the injection location were higher than with large hole spacing. The Stanton number, St, was also increased when the spacing of "holes" and "rows" was decreased [28]. Similar behaviour was also reported by Crawford et al [29] who also examined the effect on St due to changing the number of rows of holes. The St trends were seen to be similar for two cases of different number of rows, indicating a dominance of the flow near the surface by injection. However, for low blowing ($M \leq 0.4$) through rows of holes on a convex surface, and with the coolant being of similar temperature to that of the surface, the structure of the curved boundary layer was found to be dominated by the curvature effects [30].

The work primarily dealing with the influence of coolant to mainstream density ratio and mainstream pressure gradients on the heat transfer coefficient is listed in Table 2.1. The table also includes the range of parameters under which the heat transfer coefficient was measured.

2.2.2 Coolant to Mainstream Density Ratio

Published work on the effect of coolant to mainstream density ratio on the heat transfer coefficient is very limited. Most has been reported by Jones and his co-workers [12, 31 & 32]. They have used a test facility, the isentropic light piston tunnel, in which the heat transfer coefficient was

Reference	Slot	Sin-gle hole	rows of holes	s/D	Incli-nation angle	ρc/ρoo	M	δ*/D	D (mm)	dP/dx	K ($x10^6$)	u_{oo} or Ma. No	Re_D or Re	x/D	Technique mass (M) heat (H)	h	$\bar{h}$	η	Experimental technique
[12]			1	2.5	30	0.81/1.22 1.66/2	0.12-1.2			0.0		Ma= 0.55	2.7x 10^7/m	2-98	H		✓	✓	I.L.P.T.
[31]	✓		1, 2	2.5	30	0.81/1.22 1.66/2	0.12-1.2			0.0		Ma= 0.55	2.7x 10^7/m	2-98	H		✓	✓	I.L.P.T.
[32]	✓		1, 2	2.5	30	0.81/1.22 1.66/2	0.12-1.2			0.0		Ma= 0.55	2.7x 10^7/m	2-98	H		✓	✓	I.L.P.T.
[33]			1	2.5	30	0.81/1.22 1.66/2	0.3-1.45			0.0		Ma= 0.55	2.7x 10^7/m		H		✓		I.L.P.T.
[22]		✓	1	3	35	1.0/0.85	0.1-1.95	0.14D-.21Dcm		0.0		30.5-61	0.22-.44x10		H	✓	✓	✓	Wall heat flux
[34]			2	3	35	1.0-1.62	0.48-1.6		0.5	0.0					H		✓	✓	I.L.P.T.
[36]			1	2.5	30	1.25/1.67	0.15 0.4/1			0.0		Ma= 0.55	2.7x 10^7/m	2-56	H		✓	✓	I.L.P.T.
[39]		✓	2	3	35	0.84	0.35-1.5		23.5 10.92	✓	0.45 1.05	15		0-50	H	✓	✓	✓	Wall heat flux
[24]			1	3	35		0.1-2	0.04-0.62		✓	(4-2) -0.55	Ma= 0.3-0.9			H		✓	✓	Blowdown wind tunnel
[27]			1	1.5-3	10/45/ 90	1.24	0.5-2		2	✓		60		0-60	H		✓	✓	Wall heat flux
[26]			1	3	35/90	1.0	0.5-2	.63/.21 .1/.19	2.3	✓	0.5/1 -0.85	25			M	✓	✓		Swollen polymer tech.
[38]	✓				20	1.0	0.2-1		0.25"	✓	.65/1.2 2.5/5.5	80/40 20ft/s		7"/D	H		✓	✓	Transient cooling block
[37]	✓				30	1.0				✓		135 ft/s			H		✓	✓	Wall heat flux

I. L. P. T. Isentropic Light Piston Tunnel.

Table 2.1 Summary of the parameters covered by other workers.

measured with density ratios representative of real engine conditions. The change in the density ratio was obtained directly by varying the coolant to mainstream temperature ratio. However, their results suffer from being averaged in the spanwise direction.

In all of their studies, Forth [31], Forth and Jones [32] and Forth et al [12], the investigations of the influence of density ratio on film cooling performance were carried out on a flat plate with a turbulent boundary layer. Injection was at 30° to the flow direction through a single row of holes, two staggered rows of holes and a slot. The lateral spacing between the holes was 2.5 dia and row spacing for the two rows of holes was 2 dia. They have shown a significant effect of density ratio for all of the geometries investigated. Their results were, however, generally involved in scaling the film-cooling performance taking into account the variations in the density ratio, a matter discussed later in this chapter. They have also shown that the substantial effect of the density ratio is dependent upon the injection geometry and may alter according to whether jet lift off occurs, but their results regarding the specific influence of density ratio on the heat transfer coefficient were somewhat inconclusive. In addition, they have investigated the influence of the wall to mainstream temperature ratio. This accounts for the variation of properties through the film layer. They have stated that the film cooled heat transfer coefficient obtained in constant properties experiments can underpredict the heat transfer coefficient in the engine (with $T_w/T_\infty \approx 0.6$) by about 12%. At locations far downstream from injection this can be the dominant effect.

The work of Forth [31] with injection through a row of holes, seems to be, at present, the only available data in which the heat transfer coefficient with variable density ratio is documented. A close examination of this data is therefore worthwhile. The data reproduced in Fig. 2.2 indicate the following noteworthy features,

i) The spanwise average heat transfer coefficient ratios with and without injection, $\bar{h}/h_\infty$, are seen to be always above one. Injection through a row

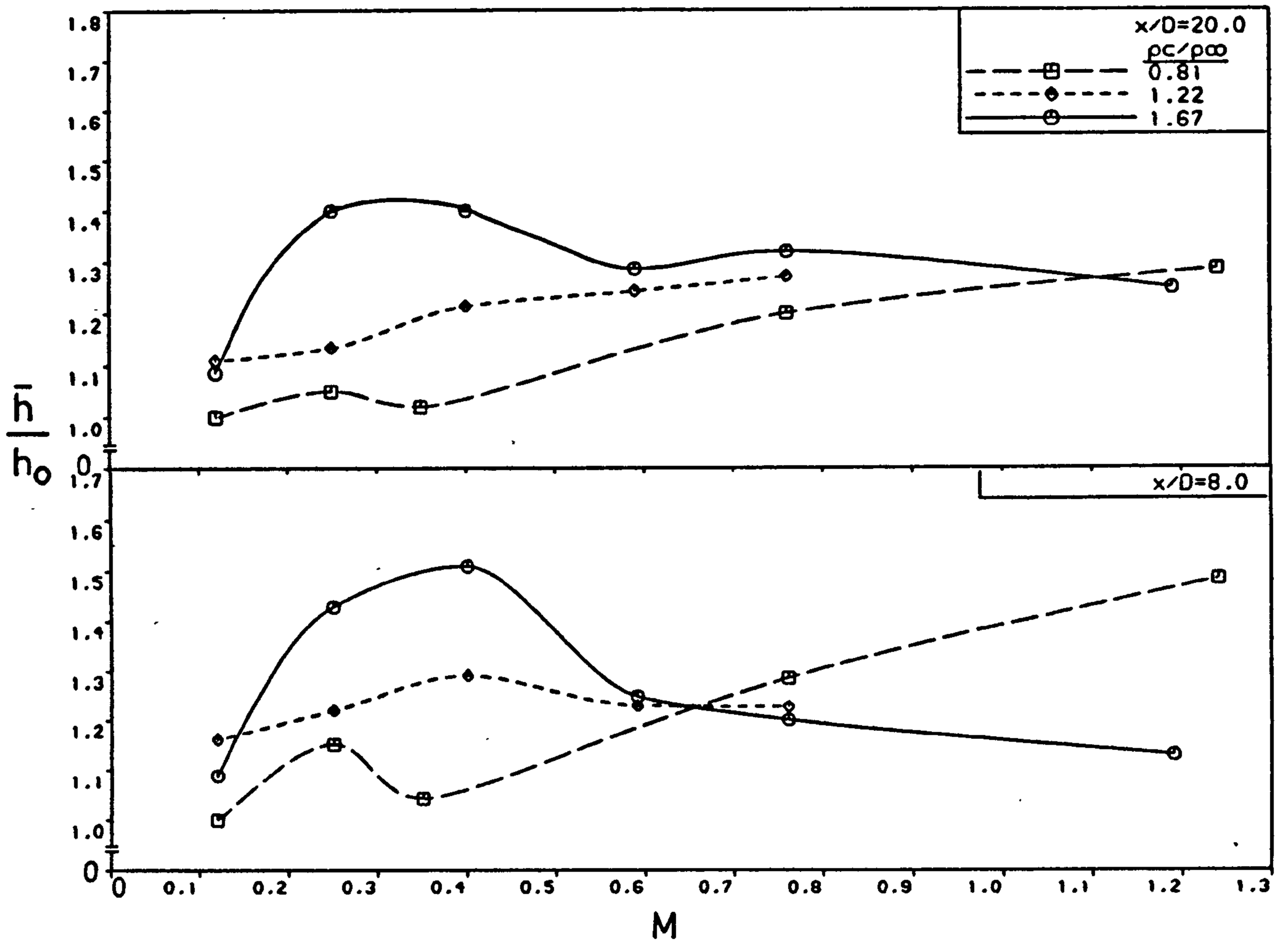

Fig. 2.2 Variation of $\bar{h}/h_o$ with the blowing rate (Forth [31]).

of holes, therefore, according to [31], enhances the heat transfer coefficient over the whole cooled surface at all density ratios and for all blowing rates. This is consistent with the data of Liess [24] at unity density ratio, however, the steady state experiments of Eriksen and Goldstein [22] at ρ_j/ρ_∞=0.85 produced $\bar{h}/h_o$ ratios about 5% below unity downstream of injection at M=0.5.

ii) At ρ_j/ρ_∞=0.81, the trends of $\bar{h}/h_o$ are similar in manner to those of Liess [24] and Hay et al [21] obtained at ρ_j/ρ_∞=1.0. That is, close to the holes, the ratio $\bar{h}/h_o$ increases as M is increased, and decays monotonically with distance downstream.

iii) As ρ_j/ρ_∞ was increased to 1.67, the ratio $\bar{h}/h_o$ appeared to increase as M was raised to about 0.4. As M was raised further to 1.2, $\bar{h}/h_o$ tended to decrease gradually with increased M near the holes and reached values lower than those at ρ_j/ρ_∞=0.81, but continued to rise slowly further downstream. This is in contrast to that at density ratio close to unity (point ii)).

iv) The observed behaviour in the ratio $\bar{h}/h_o$ highlighted in point iii) seems to be gradual with increased density ratio. At ρ_j/ρ_∞=1.22 the decrease in $\bar{h}/h_o$ close to the holes at M>0.4 is very much less distinct.

It is worth noting that the ratios of $\bar{h}/h_o$ in Fig. 2.2 include the effects of wall to mainstream temperature ratio.

A decrease in the heat transfer coefficient with film cooling for increasing the density ratio was observed earlier by Eriksen and Goldstein [22]. They measured about 2% decrease in the heat transfer coefficient downstream of injection at 35° through a row of holes for unheated air injection (ρ_j/ρ_∞=1.0) than that for a heated injection (ρ_j/ρ_∞=0.85) at M=1.0. They have attributed this effect to the difference in the momentum flux ratio, I, between the unheated and heated injection. However, for injection through a single normal hole, Eriksen and Goldstein [23] found insignificant difference in the heat transfer coefficient for this variation in density ratio.

Loftus and Jones [33] injected a relatively colder air into a mainstream air through a row of holes, but their report was concentrated more on establishing the linearity of the relation of the superposition model for variable property flows than the actual effect of coolant to mainstream density ratio.

An empirical variable property correction for a film cooled turbulent boundary layer was formulated by Ligrani and Camci [34]. The correction relation provides a means to determine changes of the heat transfer coefficient due to variable property, including density ratios, from the constant property heat transfer coefficient and adiabatic film cooling effectiveness values available in the literature. However, this was based over a range of conditions on a particular injection geometry of two staggered rows of holes with an arrangement similar to that of Jabbari and Goldstein [35], and therefore can not be generalised.

In all of the work reviewed above, the density ratio was achieved by varying either the temperature of the coolant or that of the mainstream. Recently Teekaram et al [36] have shown that using foreign gas injection in a heat transfer test facility is viable without resorting to a mass transfer analogy. This is a major finding since future experimental work with density ratios can readily be represented with foreign gas injection.

2.2.3 Mainstream Pressure Gradient

The influence of mainstream pressure gradient on the heat transfer coefficient under a cooling film has received little attention (see Table 2.1). Work on two-dimensional film cooling in the presence of mainstream acceleration has been reported by Hartnett et al [37] and Warren and Metzger [38] for blowing via an angled flush slot. In both of these studies, acceleration on a flat plate was produced by contours placed in the roof of the test section of the wind tunnel. They found that the effect of low acceleration was weak. However, in the latter study [38] at low M, an appreciable decrease in the heat transfer coefficient with injection was

observed at high acceleration. For that case, the favourable pressure gradient without injection was sufficiently strong for re-transition of the turbulent boundary layer to laminar. But at injection rates approaching unity, the depressed heat transfer coefficients increased toward their fully turbulent values.

The influence of mainstream acceleration on the heat transfer coefficient for injection via two staggered rows of holes inclined at 35° to the flow direction was investigated by Jabbari and Goldstein [39]. In this study, the highest acceleration parameter, K ($=\nu(du_\infty/dx)/u_\infty^2$), examined was about 1.05×10^{-6}. They found that the centreline heat transfer coefficient normalized by that without injection was insignificantly affected by acceleration when the blowing rate was less than one. But when M was of the order of unity or above, the heat transfer ratio was reduced by about 10% close to the injection point. Far downstream, the reduction in the coefficients ratio showed dependence on M, being very small for M=1.0 and about 10% for M=1.5. They also found that the spanwise average heat transfer coefficient ratio $\bar{h}/h_o$ was reduced by acceleration when M was one, and the reduction extended further downstream at larger M. They have suggested that this was possibly caused by suppression of injection induced turbulence by mainstream acceleration.

Liess [24] and Kruse [27] using thermal techniques considered injection through a single row of holes in the presence of mainstream acceleration. Liess [24], with the pressure gradient extending only to about 20 hole diameters downstream, and injection at 35°, noted that suppression of the development of streamwise vortices by the mainstream acceleration produced a fall in the spanwise average heat transfer coefficients compared to the constant mainstream velocity values. Kruse [27], on the other hand, with acceleration parameter changing from about 4×10^{-6} to 2×10^{-6} in the first 20 hole diameters downstream, and injection at 10°,45° and 90°, found the effect of pressure gradient on the film-cooled heat transfer coefficient to be generally weak. Kruse also examined the effect of adverse pressure gradient ($K\approx-0.55\times10^{-6}$) on

the heat transfer coefficient. There again the effect was weak. This is in agreement with the results of Hay et al [26] for injection through a row of holes inclined at 35° or 90° and for similar range of blowing rates where K=-0.85x10^{-6}. However, the results of Hay et al at favourable pressure gradients were at variance with those of Kruse. In a series of experiments using a mass transfer technique conducted at mild and strong favourable pressure gradients of K=1.0x10^{-6} and 5.0x10^{-6} respectively, Hay et al [26] measured a substantial reduction in the ratio of the heat transfer coefficient with and without injection h/h_o. They have reported a decrease in $\bar{h}/h_o$ values of about 20%-30% of those at zero acceleration by the mild acceleration at low blowing rate (M=0.5), but as M was raised the $\bar{h}/h_o$ values approached the zero acceleration values. Hay et al also noted that the effect of strong acceleration, in which relaminarization of the boundary layer has taken place, in lowering the heat transfer coefficient was even more significant, particularly at low blowing rates. However, when M was raised to about 2.0, the depressed heat transfer coefficient was increased and a tendency to overcome the relaminarization effect was observed, although full recovery to zero acceleration levels did not occur.

2.3 THE ADIABATIC WALL EFFECTIVENESS

The determination of the adiabatic wall effectiveness is outside the scope of the current work, however, due to its important connection with the heat transfer coefficient in defining the film cooling process, and a lot of the effectiveness experiments give also an insight into the flowfield and mixing associated with film cooling, a short look is worthwhile.

The literature is rich in reports of experiments with injection through holes that take into account the influence of the various important film cooling parameters on the effectiveness. Highlights of the principal findings of these studies are as follows,

- The effectiveness increases with the blowing rate up to an optimum value of M in the range 0.4 - 0.5 for density ratios of unity. Further increase in M

results in lower effectiveness [40].

- The effectiveness increases, in general, with increase in density ratio, particularly at large blowing rates. Further, the optimum value of M increases with increasing density ratio [41].
- The effectiveness decreases modestly with favourable pressure gradients, but increases substantially with adverse pressure gradients [42].
- The effectiveness is relatively independent of the mainstream Reynolds number [43].
- The effectiveness is maximum at smaller values of M when the jet is laminar than when turbulent [25].
- The effectiveness, in general, decreases moderately with increase in turbulence intensity or in turbulence scale [44].
- The effectiveness decreases with the presence of surface roughness at low M, whereas it increases at high M [45].
- The spanwise average effectiveness is little influenced by the boundary layer displacement thickness δ^*, but it decreases as δ^* increases beyond 0.2 hole diameters [24].
- The effectiveness increases with decreasing streamwise injection angle, however lateral uniformity of effectiveness is better at large angles [27].
- The effectiveness increases with decreasing hole spacing to diameter ratio [27].
- The effectiveness is higher for two staggered rows of holes than for a single row of holes [35].
- The effectiveness for two rows of holes is higher for the staggered than for the in-line configuration [46].
- The effectiveness is improved as the exit area of the injection hole is increased for the same coolant mass flow rate [47].
- The average effectiveness is higher over a convex surface than over a flat plate, while the concave surface results in lowest effectiveness comparatively [48].

- The average effectiveness downstream of two staggered rows of holes correlates well with two-dimensional film cooling parameters [35].

2.4 THEORETICAL MODELS AND CORRELATIONS

Most of the available theoretical models in the literature have been developed primarily to estimate the film cooling effectiveness. These models were usually based on one of two approaches; the line or point heat sink [49], and the energy balance in the film layer approach [50]. The models were first proposed for injection through slots and were later modified for injection through holes. A detailed review of the two-dimensional injection models can be found in [9].

It is worth noting that, in both approaches the blowing rate was suggested to be the key parameter governing the fluid mechanics of the film cooling process.

Generally, the models were inadequate to predict the effectiveness at high blowing rates, while reasonable agreement with some experimental data were attained at low M. Further, the energy balance models do not address themselves to large density differences between coolant and mainstream. The weakness in these relations is attributed to the aerodynamic effects of injection that have not been comprehended, especially at high blowing rates when jet lift-off takes place.

There have also been numerous attempts at formulating correlations based on experimental results. Most of these correlations were centred on the effectiveness for injection through slots. The effectiveness data were often presented in terms of the mass flux ratio M for constant-property flows, even for injection through a hole [51], whilst the momentum flux ratio I or the velocity ratio u_j/u_∞ have been used to correlate results in the presence of density gradients [47, 52] for single rows of holes.

Similarly, the cooling film heat transfer coefficients for injection through slots have been shown by Metzger et al [10, 53] and Foster and Haji-Sheik [54] to correlate reasonably well with the mass flux ratio at constant

density. The greatest deviation of the data in their empirical correlations occurred at distances immediately downstream of the slot. Unfortunately, these data cannot be used at turbine operating density ratios unless proper scaling can be established and applied.

Recently, Fitt et al [55] have reported considerable progress in predicting the precise manner in which injection occurs. A two-dimensional, irrotational, inviscid, incompressible (but with $\rho_c \neq \rho_\infty$) model, with no separated regions was proposed, (see Fig. 2.3). The flowfield was then solved analytically by expressing the flows in the slot, mainstream and film regions as dimensionless, asymptotic expansions and matching pressures across the dividing streamline. One of the main results obtained was that, the height of the injection layer, b/s, was related to the momentum flux ratio I by,

$$\frac{b}{s} = o\left[\left[\frac{\rho_c u_c^2}{\rho_\infty u_\infty^2}\right]^{1/3}\right] \qquad \text{- - - (2.1)}$$

This result implies that the height of the injection layer scales with I for slot flows without separation.

Forth and Jones [32] extended this result in the injection region to the viscous jet-mainstream mixing region downstream. For correct scaling of the mixing process, Forth and Jones invoked an empirical relation [56] in which a dimensionless jet velocity maximum scaled well with the parameter,

$$\frac{x}{b}\,\frac{u_\infty^2}{u_f^2}$$

where b is the height of a tangential slot for $\rho_c = \rho_\infty$, and u_f is the velocity in the film layer. Therefore for $\rho_c \neq \rho_\infty$ scaling would occur with,

$$\frac{x}{b}\,\frac{\rho_\infty u_\infty^2}{\rho_c u_f^2}$$

Using equation (2.1), the velocity field would depend on,

$$\frac{x}{s}\left[\frac{\rho_c u_c^2}{\rho_\infty u_\infty^2}\right]^{-2/3} \qquad \text{- - - (2.2)}$$

Thus the velocity field in the viscous region would be a function of downstream distance, x/s, and I. In addition, the Reynolds analogy suggests that the temperature field and therefore the heat transfer parameters would

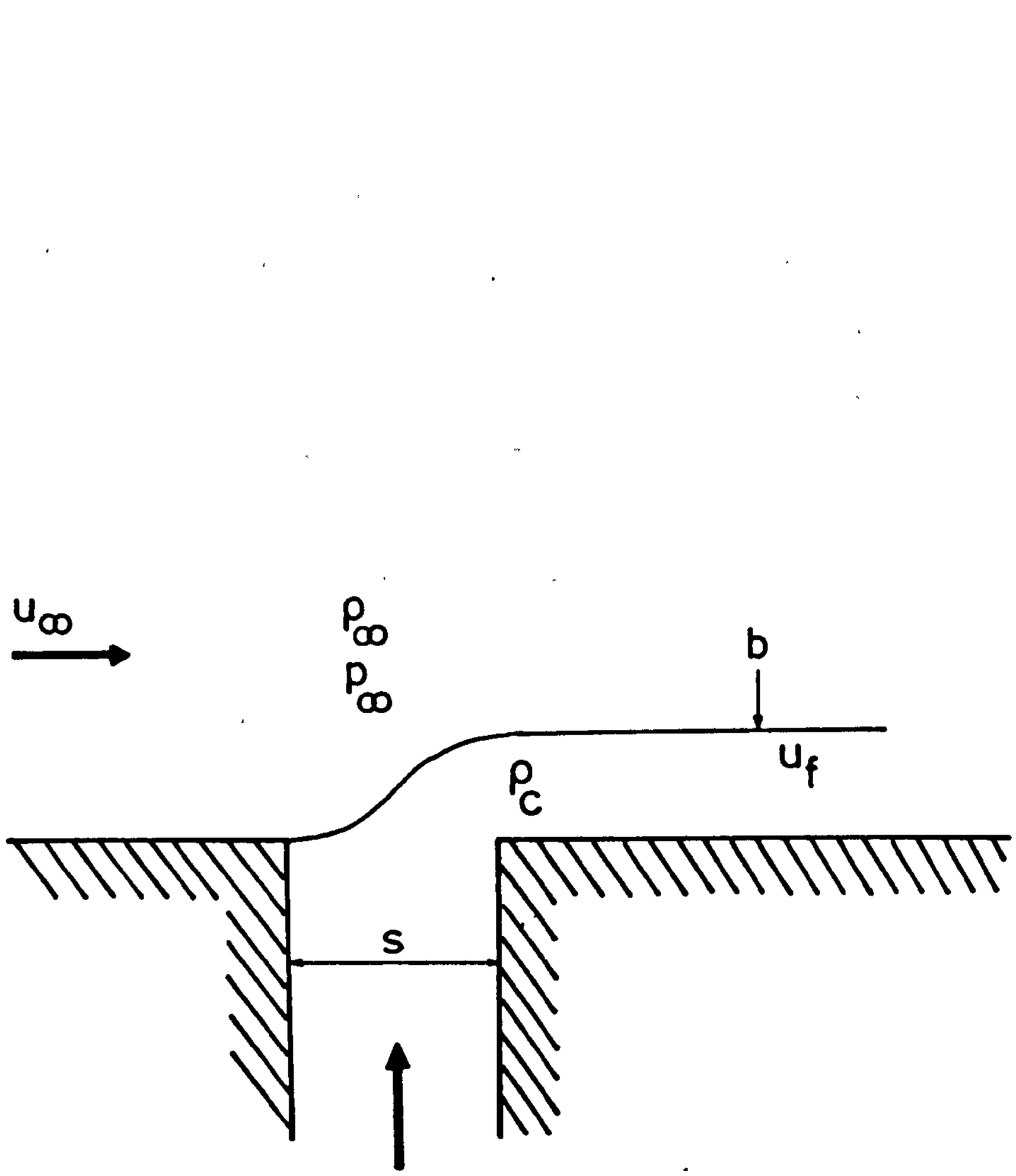

Fig. 2.3 Two-dimensional film cooling model.

depend on x/s and I.

Furthermore, Forth and Jones [32] have identified two broad and distinct flow regimes; the weak injection regime, in which the injection flow remains essentially attached to the surface, as for an angled slot or a double row of holes at 30°, and the strong injection regime in which the injected flow lifts off the surface and penetrates some distance into the mainstream, as for a 30° inclined single row of holes. For the weak injection regime, the heat transfer data with variable density and velocity ratios collapsed well with the newly developed parameter, equation (2.2), whereas for the strong injection regime, satisfactory scaling was achieved with a modified form of eq. (2.2) incorporating the velocity ratio and distance only.

2.5 NUMERICAL WORK

Accurate analysis of the flowfield in the vicinity of injection through discrete holes requires three-dimensional calculation procedures. Patankar et al [57] analysed the injection at high blowing rates from a single normal hole. Their numerical calculation was based on three-dimensional elliptic finite-difference scheme. Bergeles et al [58] calculated laminar flow and temperature fields for injection via a single and multi-row of holes inclined at 90°, 45° and 35° by applying a partially parabolic calculation code. They have also considered a case for which injection was through a row of holes at 30° in the presence of density gradients and strong mainstream acceleration. Their predictions of the spanwise averaged effectiveness for the latter case agreed satisfactorily with some experimental data. Further, in another two publications, Bergeles et al [59, & 60] predicted the film cooling effectiveness for injection through a row and two rows of holes aligned at 30° to a turbulent mainflow. The numerical simulation method presented embodied a semi-elliptic treatment of the flowfield in the vicinity of the holes. The most widely used k-ε two-equation model of turbulence, which assumes an isotropic eddy viscosity, was modified by introducing non-isotropic transport coefficients. The numerical results showed a good agreement for the cases of

low blowing rates (M<0.5). However, the assumptions of symmetrical jet exit conditions, local equilibrium inherent in the turbulence model, and the inability of the semi-elliptic procedure to properly simulate the zone of recirculation downstream of a hole, has produced significant errors at conditions of small boundary layer thickness and large M.

Crawford et al [61] extended their boundary layer program STAN5 by an injection model in which the additional lateral mixing was modelled by augmentation of the mixing length in their turbulence model. The calculated Stanton numbers for full-coverage film cooling at different injection angles and for spacings s/D of 5 and 10 compared well with corresponding experimental data. Using basically the same model of [61], Miller and Crawford [62] presented predictions of St and effectiveness for geometries incorporating single, double and multiple rows of holes. They obtained good agreement with experimental data for M<1.0 and α<45°.

More recently, Demuren, Rodi and Schonung [63] employed a locally elliptic calculation procedure, which could be safely applied to regions with flow reversals even at large M. The standard k-ε turbulence model was used but modified as in [59] to account for non-isotropic eddy viscosities and diffusivities. They analysed the influence of injection angle, relative hole spacing and blowing rate on the effectiveness. Agreement of the effectiveness predictions with systematic data was satisfactory for M up to 1.0 and for small hole spacing, but for high M and large spacing the predicted level of effectiveness was lower than the experimental results. They claimed that the mixing process was crudely simulated with the turbulence model used. In their recent work, Schonung and Rodi [64] used the Lam and Bremhorst [65] modified version of the k-ε turbulence model. In this model, the wall functions for bridging the viscous sublayer are not implemented as the governing differential equations of the flow are solved up to the wall. They have described a two-dimensional boundary layer procedure in which injection and dispersion models were incorporated to account for the elliptic nature and three-dimensionality of the flow respectively. Their calculated heat transfer

coefficients for injection through a row of holes and those measured by Eriksen and Goldstein [22] were in satisfactory agreement at distances far downstream (x/D>30). Near the injection site, somewhat, appreciably lower coefficients were predicted. The authors suggested that this might have been due to an underestimation of the lateral mixing by the model.

2.6 CONCLUDING REMARKS

In the light of this literature survey, a few conclusions relevant to the present investigation can be made,

i) Studies concerning the effects of density ratio have been mainly limited to the film cooling effectiveness. The influence of density ratio on the local heat transfer coefficient is yet to be determined.

ii) The effect of adverse mainstream pressure gradient on the film cooling heat transfer coefficient has been shown to be generally insignificant. However, the effect of favourable pressure gradient is seen to have some contradictory results regarding the level by which the heat transfer coefficient is reduced.

iii) Further development of correlations is needed to allow the application to design of the heat transfer coefficient data from unity density ratio tests.

iv) The current schemes of computing film cooling heat transfer coefficients are, at present, unsatisfactory.

CHAPTER 3

OBJECTIVES AND EXPERIMENTAL METHODS

Chapter 3 outlines the objectives of the present work, explains the various experimental methods used to measure the heat transfer coefficient and the reasons behind the choice of the method used in this study.

3.1 OBJECTIVES OF PRESENT WORK

The review of the existing data on the film cooling heat transfer coefficient in the presence of density and pressure gradients indicates a need for further work.

Film cooling is normally employed in gas turbine practice with large temperature differences between the mainstream and cooling air flows. This results in coolant to mainstream density ratios well in excess of unity. Cost considerations have resulted in many fundamental investigations being carried out at low temperatures, with density ratios near unity. The results of such experiments have shown the order of increase in the heat transfer coefficient produced by injection, and have given some insight into the flow mechanisms. But, since it is evident that the film cooling process depends significantly on density ratio [32, 66], these experiments do not yield data directly applicable in the design process, unless proper scaling is established and applied.

Studies of heat transfer with film cooling under accelerating flow are also of practical concern, since both the pressure and suction sides of vanes and blades are exposed to favourable pressure gradients. Such studies, in particular those with the presence of severe mainstream acceleration are scarce. Firm conclusions on the influence of such conditions on the heat transfer rate have

not yet been reached, and such influence can not be disregarded.

Many of the questions regarding the effect of density and pressure gradients on film cooling heat transfer coefficients, therefore, have remained unanswered.

Furthermore, satisfactory prediction of the cooling film heat transfer coefficient by numerical methods is still lacking, in particular at regions close to the injection site where recirculation takes place. Consequently, further generation of models or improvement of existing ones is of substantial importance if prediction of the film cooling heat transfer coefficients is to be made successfully and more readily.

The current work springs from the above considerations. It is an attempt to provide answers to these intricate questions. However, with time as the major constraint, the experimental results with different flow conditions are obtained only for two configurations of a single row of holes on a flat plate.

The objectives of the present research may be summarized as follows,

i) To investigate the effect of coolant to mainstream density ratio on local and spanwise averaged heat transfer coefficients.

ii) To investigate the effect of mainstream acceleration imposed by moderate and strong favourable pressure gradients on the cooling film heat transfer coefficient.

iii) To examine also the effect of density ratios on the heat transfer coefficient in the presence of mainstream acceleration.

iv) To attempt to formulate heat transfer coefficient data correlations for preliminary design calculations.

v) To identify the optimum cooling conditions based upon the experimental results obtained, in an effort to reduce the penalties associated with excessive usage of cooling air.

vi) To determine the suitability of a fluid dynamics computational program for the solution of three-dimensional film cooling problems.

These objectives imposed the type of experimental apparatus to be employed and the nature of experiments to be performed.

3.2 EXPERIMENTAL METHODS OF ACQUIRING THE HEAT TRANSFER COEFFICIENT

Various experimental methods have been developed by researchers seeking accurate measurements of local and mean heat transfer coefficients under cooling films. Such methods utilize either a heat or a mass-transfer analogue system, and usually employ either a constant surface temperature (constant surface concentration in mass-transfer analogue processes) or a constant heat flux along the surface.

A summary of the most widely used techniques is given in the following. For a more comprehensive review, the reader is referred to Button and Mohamad [67] and Hay [68].

3.2.1 Heat Transfer Techniques

The thermal method is the most common used to determine the heat transfer coefficient. Thermally isolated copper or aluminium strips running spanwise across the test surface are heated electrically, directly or through cemented wire resistors, by passing a measured current through them. The strips, thus, produce a constant heat flux when heated and adiabatic wall when unheated. The heat transfer coefficient is determined from the local surface temperatures measured using a large number of thermocouples embedded in the insulation behind the heater strips or bonded between them, the heat transferred to the working fluids and the associated fluid temperatures. Such systems had been used by Eriksen and Goldstein [22], Foster and Haji-Sheik [54] and Mick and Mayle [69].

Another method utilizing an electrically heated surface uses a thin layer of cholesteric liquid crystals over the heated surface. The crystals display different colours in response to different temperatures. The thermal visualization determines the surface temperatures and consequently the local heat transfer coefficient, as has been used by Hippensteele et al [70].

Kruse [27] used a heat transfer model made of plastic with a poor thermal conductivity. Copper blocks embedded in the model were individually

cooled by internal air flows. The heat flux at different streamwise positions, averaged in the spanwise direction, was determined by the measured mass flow and the inlet and outlet temperatures of the individual internal air flows. The surface temperature was measured by means of a calibrated infra-red pyrometer, and the fluids temperatures were measured by thermocouples, thus giving the heat transfer coefficient.

Such tests are normally performed in steady state wind tunnels at low speed and low temperature. However, Liess [24] with a similar experimental model using heater strips and thermocouples in a blowdown wind tunnel test facility, measured lateral average heat transfer coefficients at Mach numbers and Reynolds numbers representative of gas turbine conditions. The coefficients were obtained by being related to the transient variation of temperature of the heater strips.

Short duration test techniques, such as isentropic light piston tunnels, facilitate a more complete modelling of the engine environment. Air at constant pressure and temperature flows through a working section having a pre-cooled or pre-heated isothermal test surface. The heat transfer rates from the surface are measured using thin film resistance gauges associated with analogue circuits of transient surface temperature techniques. In addition, pressure transducers and thermocouples are used to measure the injection and mainstream flow properties during a test. This method has been used by Forth et al [12] and Ligrani and Camci [34]. However, the size of the gauges dictates that the coefficients measured are spanwise averaged, rather than local.

3.2.2 Mass Transfer Techniques

In view of the difficulty of measuring accurately the local heat transfer coefficient using thermal systems, other workers [71, 72] resorted to an alternative method utilizing mass transfer analogue experiments, primarily the sublimation of naphthalene. In this technique the test surface is made of a removable section made of naphthalene. Local mass transfer coefficients are

determined from the local depth of sublimed naphthalene surface. The latter is obtained by local measuring of the surface profile before and after exposure to the flow field employing an accurate mechanical depth gauge. If average mass transfer coefficients are required, the naphthalene section is divided into segments. The weight of the naphthalene segments before and after exposure to the air streams determines the mass transfer rate.

A relatively new mass transfer method for the acquisition of heat transfer coefficient data from film cooled surfaces is the swollen polymer technique [73]. Instead of a naphthalene coating, a polymer coating swollen to equilibrium by absorption of an organic swelling agent is used. Loss in the swelling agent to the flow field results in a reduction in thickness linearly related to the mass transferred. Use of laser interferometry produces a hologram with a fringe pattern from which the coating recession, and therefore the mass (heat) transfer coefficient, can be deduced at all points on the surface.

3.3 CHOICE OF EXPERIMENTAL TECHNIQUE

In regard to achieving the objectives set for the current research, and after evaluation of the two experimental approaches, the mass transfer approach was favoured over the heat transfer one. It was selected for the following reasons,

i) The mass transfer method offers a good spatial resolution, so that accurate local measurements of mass transfer at the surface are achievable.

ii) A large range of coolant to mainstream density ratio can be easily obtained by using unheated mainstream air and injecting a dense gas or a mixture of gases to achieve the desired density ratio. This avoids the task of heating a large mass of mainstream air to a high temperature or chilling injectant air, which would cause condensation and icing.

iii) Errors produced by heat conduction within the wall in thermal techniques especially when large temperature differences are present close to the

injection location are avoided.

The conventional mass transfer technique of naphthalene sublimation is, however, slow and cumbersome, the naphthalene mass lost by sublimation due to diffusion and convection is deduced from a lengthy and tedious process by mechanically measuring thickness changes of the coating. Corrections accounting for mass losses by free convection during thickness measurement have to be considered. The coating also requires frequent reconstruction to maintain an acceptable smooth hydrodynamic surface.

A more convenient and powerful mass transfer method is the swollen polymer technique. Here, surface restoration requires only immersion of the surface in a swelling agent for a few hours. The very small changes in the coating thickness are accurately, quickly and easily measured using laser holographic interferometry. This yields high resolution and full surface mapping of the mass transfer. The swollen polymer technique is therefore chosen for conducting the present experimental research. A detailed description of this method is given in the following chapter.

3.4 MASS TRANSFER ANALOGY

Analogous mass transfer techniques have been used in many studies for the determination of the influence of injection on the heat transfer coefficient [21, 71]. Using a mass transfer technique dictates that a mass transfer analogy for the film-cooling process must be satisfied. The heat-mass transfer analogy holds if the Sherwood number, Sh, describing the mass transfer coefficient is equivalent to the Nusselt number, Nu, describing the heat transfer coefficient. This can be so if the Schmidt number, Sc, for the mass transfer process is equal to the Prandtl number, Pr, for the heat transfer process. For a turbulent flow, this implies not only the molecular diffusion numbers but the turbulent ones as well.

In addition, similar initial boundary conditions must be maintained and the film-cooling controlling parameters must have the same magnitude.
Further, one boundary condition at an impermeable wall for the momentum

equation is zero normal velocity. However, in a mass transfer situation, there is a finite migration of the mass transferring material to the flow streams normal to the wall surface. This is generally very small so that it does not significantly affect the validity of the analogy [74].

Thus, a constant concentration surface mass transfer correlation Sh=f(Re,Sc) can be utilized as Nu=f(Re,Pr) for an isothermal surface heat transfer calculation. However, if, as is the case in film-cooling experiments, the form of the function is not known, difficulties arise if Sc and Pr are different. Launder and York [75] stated that it is generally acknowledged that the turbulent Prandtl and Schmidt numbers are equal. Eckert and Drake [76] suggested that experimental evidence also point to the fact that the turbulent numbers are equal. By contrast, the molecular Prandtl and Schmidt numbers are usually different; the Sc for naphthalene diffusing in air at ambient temperatures is approximately 2.5, and 2.85 for ethyl salicylate organic compound diffusing in air used in the swollen polymer technique [21]. Both are many times greater than the Pr of air (=0.71).

Fortunately, that particular difficulty has been easy to circumvent. If it is assumed that the form of the functions of Reynold and Schmidt numbers can be written as a product of individual functions of these groups, i.e. $Sh=f_1(Re)f_2(Sc)$, ratios of Sherwood number in the analogue mass transfer experiment will then be equal to Nusselt number ratios in the heat transfer experiment even though Sc and Pr are not matched.

When absolute values of heat transfer coefficients rather than ratios are acquired, researchers [77] generally use the correlation forms derived from the Reynolds' analogy, such as the Chilton-Colburn analogy,

$$h = h_m \rho c_p (Pr/Sc)^{-2/3}$$

where h_m is the mass transfer coefficient, and ρ and c_p are the density and specific heat of the experimental fluid.

Others, for example Goldstein & Taylor [71], Webster & Yavozkurt [72], and Han et al [78] put their results in the following experimentally validated form,

$$Nu = (Pr/Sc)^n Sh$$

where n has a value of the order of 0.4.

However, in this research the heat transfer coefficients are presented as ratios.

An exact analogy for the variable property situation does not exist. However, Eckert and Goldstein [79] have shown that the heat-mass transfer analogy holds with a good approximation when the density ratio of the coolant to the mainstream has the same value for the mass transfer experiment and the analogous heat transfer situation.

CHAPTER 4

THE SWOLLEN POLYMER TECHNIQUE

Description of the swollen polymer technique is provided in this Chapter. Further, the factors determining a suitable choice of polymer-swelling agent system for the present film cooling experiments are outlined.

4.1 THE SWOLLEN POLYMER TECHNIQUE

The experimental technique of swollen polymers is comparatively a novel one devised for the determination of local convective transfer coefficients. This powerful and versatile method has been developed by Macleod and co-workers [80, 81] at Edinburgh University. Swollen polymers supplemented by laser holographic interferometry offer the advantages of precision, rapidity, simplicity and very high spatial resolution over the conventional naphthalene coatings. Further, the polymer can be applied to surfaces of quite complex geometry, which could not be formed of naphthalene.

The technique incorporates a mass-transferring surface of permanent polymer coating such as silicone rubber. The coating, of thickness normally between 0.1 and 1.0mm, has its superficial area maintained nearly constant by adhesion to a rigid test surface. The coating is swollen to equilibrium in a reversible manner by a suitable liquid swelling agent. Equilibrium swelling is achieved simply by immersing the coating in a bath of the swelling agent for a few hours. Because the swelling is to equilibrium the concentration of the swelling agent is constant over the coating surface, simulating isothermal conditions. Convective evaporation of the swelling agent to a flowfield, within designated limits, results in a local change of a few microns in the polymer coating thickness proportional to the local mass transfer coefficient. This is realised only if the following basic conditions hold [80],

i) The reduction in coating thickness is proportional to mass of swelling agent transferred.

ii) The constant vapour pressure of the swelling agent over the surface (or the constant swelling agent concentration at the surface) remains sensibly invariant as the transfer proceeds.

iii) The overall resistance to mass transfer is predominantly in the gas phase.

iv) Lateral diffusion of the swelling agent within the polymer is insignificant.

Satisfactory practical fulfilment of these requirements at certain chosen conditions has been shown to apply by Macleod and Todd [80], who have conducted experimental and theoretical analysis of these requirements. However, the chosen conditions imply that for any swollen coating system the period of experiment "must" be limited to the "constant rate period". During this period, the deviation of convective transfer from the requirements outlined above remains within acceptable limits. A proper choice of polymer-swelling agent system, suitable to the conditions and duration of the specific experimental situation, can therefore generally fulfil the requirements. Such swollen polymer systems can give an accurate measurable loss of mass transfer, and hence mass transfer coefficients, over a convenient constant rate period.

4.1.1 The Constant Rate Period

The constant rate period for any swollen polymer is estimated from the maximum allowable fractional recession of the coating, which can be calculated from the theoretical analysis provided in [80].

It is always desirable to have a constant rate period long enough to minimize start-up and shut-down errors.

The length of the constant rate period depends upon many factors, a discussion of which is given elsewhere [82]. However, the effects of these factors on the constant rate period may be summarized as follows,

i) High rates of transfer and high Reynolds number flows give inconveniently short constant rate periods.

ii) High equilibrium swelling is desirable to lengthen the constant rate period.

iii) The higher the diffusivity of the swelling agent within the polymer phase the longer the period of the constant rate.

iv) The higher the operating temperature the shorter the constant rate period.

v) The constant rate period depends only slightly on the initial swollen polymer thickness when the coating thickness is small, <1mm.

vi) The constant rate period is highly sensitive to the vapour pressure of the swelling agent. The vapour pressure depends both on temperature and composition of swelling agent in the swollen coating. A comparatively low saturation vapour pressure swelling agent increases the constant rate period considerably. Further, a maximum change of 5% of the initial value of the vapour pressure is tolerable during the course of an experiment for it would have a negligible effect on the determination of mass transfer coefficient compared with other sources of error [80].

It is noteworthy that theoretically calculating the constant rate period leads to pessimistic estimates of the permissible duration of an experiment [80]. The time interval at which 5% change of vapour pressure is allowed would be much longer if the mass transferred is time averaged or "integrated" (that is determined by dividing the total weight loss by the total time). Kapur [83] showed by experiment that the measured integrated constant rate periods for some polymer-swelling agent systems to be more than twice the length predicted by the theoretical analysis.

In film cooling experiments, high local mass transfer rates are present near the injection site, the "integrated" constant rate period suggestion could not be accepted, and all of the mass transfer experiments in this research were operated inside the theoretically estimated constant rate period. The latter was calculated based on 5% allowable change in the saturated vapour pressure of the swelling agent used.

4.1.2 Determination of Mass Transfer Coefficients

The local mass transfer coefficient, h_m, at any point on the surface measured using the swollen polymer is,

$$m'' = h_m (C_w - C_\infty) \qquad \text{- - - (4.1)}$$

where m'' is the mass flux at that point, C_w and C_∞ are the concentration of swelling agent vapour at the wall and the free stream respectively. Equation (4.1) is analogous to equation (1.1). However, since the concentration of the swelling agent in the free stream, C_∞, is equal to zero,

$$m'' = h_m C_w \qquad \text{- - - (4.2)}$$

The mass flux, m'', at any point of the polymer surface in time t can also be calculated from the measured change of the swollen coating thickness (i.e. recession), δ_s, at that point,

$$m'' = \rho_s \delta_s / t \qquad \text{- - - (4.3)}$$

where ρ_s is the density of the swollen polymer.

From equations (4.2) and (4.3) we have,

$$h_m = (\rho_s \delta_s)/(C_w t) \qquad \text{- - - (4.4)}$$

Thus local mass transfer coefficients can be determined from measurements of coating shrinkage if C_w and ρ_s are known.

The concentration of the swelling agent vapour in air just above the polymer surface, C_w, is given by [84],

$$C_w = \frac{M_a}{22400} \times \frac{P_a}{760} \times \frac{273}{T} \quad \text{g/cm} \qquad \text{- - - (4.5)}$$

where M_a is the molecular weight of the swelling agent, and P_a is the vapour pressure over the polymer coating swollen to equilibrium, in mm Hg at a temperature T, in Kelvin.

The saturation vapour pressure, P_o, is generally given in the literature for many organic agents as a function of temperature.

As for the density of the swollen polymer, ρ_s, Kapur and Macleod [84] have found experimentally that, for small recessions, the relation between recession and weight loss for the saturated swollen coating is the same as that for a homogeneous subliming solid of the same density. Thus ρ_s is given by,

$$1/\rho_s = (a/\rho_p) + (1-a)/\rho_o \qquad \text{- - - (4.6)}$$

where a is the mass fraction of the swelling agent in the swollen polymer, which is a measured value, ρ_s and ρ_c are the densities of the swelling agent and the polymer coating respectively.

Information on ρ_c and ρ_s is provided by the manufacturer, or may be obtained from data sources.

The diffusivity of the vapour of the swelling agent in the experimental fluid is needed for conversion of the mass transfer coefficient into heat transfer coefficient. It can be calculated reasonably accurately using established empirical correlations if not available in data sources.

Therefore for accurate measurement of mass transfer coefficients using the swollen polymer method it is essential to obtain accurate measurement of coating recession. By using a transparent swollen polymer with a good optical quality maintained before and after sublimation the local shrinkage in coating thickness can be measured accurately and easily by holographic interferometry. It is worth noting that interferometric techniques cannot be employed with conventional coatings.

4.2 LASER HOLOGRAPHIC INTERFEROMETRY

Holographic interferometry is a technique widely used to provide accurate information about surface displacements or deformations of solid objects in the form of interference fringes recorded on a photographic plate, called a hologram. The basic principles of interferometric holography can be found in many text books, e.g. Ostrovsky et al [85].

In the swollen polymer technique holographic interferometry is used to measure accurately the recession at all points of the surface of a transparent polymer coating applied to a diffusely reflecting substrate. To obtain a hologram of the coating recession, a beam of coherent laser light is split into two beams (see Fig. 5.7 in chapter 5). One beam is scattered from the fully swollen polymer coating (object beam) in its initial state and the other illuminates a photographic plate (reference beam). Both beams interfere with each other and fall upon the photographic plate to record a density pattern of

the light reflected from the coating, thus forming a first exposure. A second exposure is then made on the same photographic plate after subjecting the polymer coating to an air stream causing the recession to be examined. When the resulting double-exposure hologram (or interferogram) is developed and reconstructed by illumination with the reference beam, bright and dark fringes are observed to be superimposed on the polymer coating. The interference fringes are produced by the change in optical path length of the object beam created by the coating shrinkage between the making of the two exposures. These fringes are contours of equal recession or equal mass transfer. From the geometry of the optical setup and the physical properties of the swollen polymer it is possible to evaluate the coating shrinkage at any point of the surface, provided the fringe order at that point is identified.

It is important to note that precise relocation of the object on the holographic setup is essential for spurious fringes that could be caused by improper relocation be avoided.

The method of holographic interferometry described above where two holograms corresponding to two states of the polymer coating recorded on one photographic plate is called the "double-exposure" method. The fringes produced are known as "double-exposure" or "frozen" fringes. Alternatively, if a hologram of the polymer initial state is developed in-situ (or precisely relocated in its previous position after being developed elsewhere), and is viewed when illuminated by the reference beam while mass is transferring from the polymer coating, interference fringes will develop in real time. The fringes appearing by this "real-time" method are known as "live" fringes.

4.2.1 Fringe Order Identification

In order to translate the interference pattern to the thickness changes of the polymer coating at all points in the surface, the order of each fringe must be established. In experiments using the real-time method the fringe order can be fairly readily identified by counting the number of fringes passing through a point on the surface. The task may even be simplified further if the

interferogram includes a region of zero fringe order (i.e. zero recession) to which other fringes can then be related.

In other kind of experiments where a wind tunnel is used as in the current work, it is only possible to use the double-exposure method. In this case the zeroth fringe can not be identified on the interferogram as generally it will not appear there since the whole polymer surface would have suffered a mass transfer. Moreover, the way the fringe order changes (increase or decrease) at a given point is not known.

However if the fringe number and direction of increase at a reference point are determined the fringe order at all points of the surface can be deduced. One method of determining the fringe number at a selected reference point is by the use of an air-gauge as a means of measuring the absolute recession at that point. That is by taking two measurements one before sublimation and one after.

The air-gauge is capable of providing very accurate measurements of small changes in displacement at a point. However, evaporation of the swelling agent by the impingement of the supply air of the air-gauge on the swollen polymer surface, and relocation of the air-gauge probe to take the second measurement at the same point produce errors of the order of one or two fringes. It is of advantage, therefore, to make the air-gauge measurement at a point of high recession to reduce the errors associated with such method.

Another method of identifying the fringe order was used by Hay et al [86]. A jet saturated with the same swelling agent as that in the swollen polymer was used to create an area of zero recession on the surface. They found that it was difficult to ensure full saturation of the jet, and success using this method was therefore inconsistent.

An attempt was made to improve on the accuracy of obtaining a region of zero recession. A soft sponge continuously wet with the swelling agent was kept in contact with an area of the polymer test surface during the mass transfer phase in the wind tunnel. An area of no recession was obtained, however, the many fringes around it could not be totally resolved as they

were too close to each other. Further improvement of this method is needed, but it could have been more successful if used at lower Reynolds number flows and/or for shorter exposure times to the flows than have been used in the experiments of this research.

To find whether the fringe order is increasing or decreasing at a point, a hologram of the initial state of the polymer test surface is made and developed in-situ. The polymer surface after being exposed to the flow stream in the wind tunnel is accurately relocated on the holographic table and is viewed through the hologram. Slight displacement of the test surface towards the photographic plate moves the fringes towards an area of high recession (a valley) or away from a low recession area (a hill) on the surface [87]. This information may also be found by the use of two air-gauges separated by a distance in the streamwise direction [21].

The air-gauge was the tool used for fringe order identification in the current work. Modifications to the basic air-gauge system were implemented in an effort to reduce the errors inherent in the tool when used with swollen polymers.

4.2.2 Relationship Between Recession and Fringe Order

From the known geometry of the optical setup the change in optical path-length, S, with recession, δ, at a given point of a transparent coating of refractive index N can be calculated from the following equation given by Kapur and Macleod [88],

$$S = \delta \left[\frac{N\text{-}\cos(i_1\text{-}\alpha)}{\cos\alpha} + \frac{N\text{-}\cos(i_2\text{-}\beta)}{\cos\beta} \right]$$

where i_1 and i_2 are illuminating and viewing angles respectively, $\sin(\alpha)=\sin(i_1)/N$ and $\sin(\beta)=\sin(i_2)/N$.

The difference in optical path length between points on successive fringes is $\lambda/2$ where λ is the wavelength of the laser light. If the fringe order is n then $S=n\lambda/2$, subsequently the recession,

$$\delta = \frac{n\lambda}{2} \Big/ \left[\frac{N\text{-}\cos(i_1\text{-}\alpha)}{\cos\alpha} + \frac{N\text{-}\cos(i_2\text{-}\beta)}{\cos\beta} \right] \qquad \text{- - - (4.7)}$$

Therefore the recession at any point in the polymer surface can be accurately evaluated once n, λ, N and the geometry (i_1,i_2) are known.

The fringe order n can be determined by the use of an air-gauge as explained in section 4.2.1 above. The wavelength λ of the laser light used is known. The variation of the refractive index N with composition of the swelling agent in the polymer was shown by Kapur and Macleod [81] to be very small over the composition range within the constant rate period (<1% for silicone rubber-ethyl salicylate system). The illumination angle i_1 and the viewing angle i_2 are known from the optical arrangement. But, if i_1 and i_2 are large the geometrical factor which involves cosines of these angles may vary over the test surface so that the fringes may not be directly contours of equi-recession. However, Maali [89] has shown that for a flat test surface the variation in the geometrical factor over the whole surface is negligible (<1%, i.e. <1/2 a fringe for a 20x20cm plate and i_1<23°). Maali has also shown that the variation becomes significant for curved surfaces.

The optical setup for the present study is described in the following chapter, while reduction of the experimental data for calculating the film cooling mass transfer coefficient using the swollen polymer method is provided in chapter 6.

4.3 APPLICATIONS

The swollen polymer technique in conjunction with laser holographic interferometry has found applications to a variety of problems in mass transfer. Kapur and Macleod [81] examined the mass transfer coefficients variation over a flat plate surface exposed to tangential and normal impingement of a laminar air jet. Masliyah and Nguyen [90, 91 and 92] used the polymer technique to study mass transfer under laminar conditions for jets issuing from square, rectangular and two-dimensional tubes and impinging on a flat surface. Recently, the technique has been extended by Hay et al [21, 77] to determine heat transfer coefficients and adiabatic effectiveness of film cooled flat plates.

In this work the technique is utilized to convey film cooling heat transfer coefficient data at conditions partly simulating realistic conditions in gas turbines.

4.4 SELECTION OF SUITABLE POLYMER-SWELLING AGENT SYSTEM FOR THE CURRENT WORK

The polymer used in the mass transferring system is polydimethylsiloxane (PDMS) available commercially as RTV615 from the General Electric Corporation (U.S.A.). It has a good swelling properties with respect to many organic agents, adequate optical properties to provide good holograms, relatively easy to prepare and adheres firmly to metal test surfaces (aluminium or stainless steel) with the aid of a thin layer of silicone primer. Furthermore, it is permanent so that it can be reactivated any number of times by re-immersion in the organic compound.

In order to choose a suitable swelling agent it was necessary to conduct theoretical and experimental investigations on some potential swelling agents. Upon the outcome of these investigations, described in Appendix A, it was concluded that n-tetradecane is the most appropriate swelling agent of the options available in the application of the swollen polymer technique to film cooling. However, one drawback was encountered using tetradecane as the swelling agent, the swelling of RTV615 by tetradecane is rather high (≈50% of the initial coating thickness) [93]. Such high swelling was undesirable since it could cause a disturbance to a hydrodynamic boundary layer over a smooth test surface. This effect was minimized by reducing the dry coating thickness to 0.3mm.

The advantages upon which n-tetradecane was chosen are summarized as follows,

i) Long constant rate period at high rates of transfer.

ii) Availability of accurate vapour pressure data.

iii) Its low vapour pressure at ambient temperatures validates the assumption of negligible free convection during air-gauging.

iv) Errors associated with fringe order identification are smaller than those of other potential swelling agents.

v) Consistency and good repeatability of results as shown in chapter 6.

vi) Has a satisfactory shelf-life, it does not degrade rapidly with time.

vii) Readily available at adequate purity.

CHAPTER 5

THE EXPERIMENTAL APPARATUS

In this Chapter, description of the experimental apparatus is provided.

5.1 THE WIND TUNNEL

The experiments were conducted in an existing but modified low-speed, low-turbulence, open-circuit wind tunnel. A general view of the wind tunnel is shown in Plate 5.1, and a layout is shown in Fig. 5.1. Previously, this tunnel, on which the film cooling studies of Foster and Lampard [66] and Afejuku et al [46] had been carried out, was of an open return centrifugal blower type. Later, Hay et al [86] found that the tunnel could only supply low mainstream flow rates in the tunnel working section and was not satisfactory for their work. A laboratory compressor plant which could provide high and constant mainstream flow rates was therefore utilized. However, preliminary tests by the author have shown that the mainstream velocity field over the test surface in the test section was not uniform, this being due to continuous accumulation of dust from the incoming compressed air in the entrance section of the wind tunnel. Major modifications had, therefore, to be made to the entrance section. The floor and roof of the test section, together with the injection system were among other components modified to suit the current work.

The main flow was passed through an entrance section, a test section, a diffuser, and finally through a silencer before being discharged outside the laboratory building.

In addition, a thermostatically controlled heater had been installed in the pipework feeding the pressurised air from the compressor plant, restricting temperature fluctuations in the test section during an experiment to within ±0.2°C. This was necessary in order to determine the absolute mass transfer

Fig. 5.1 General view of the wind tunnel.

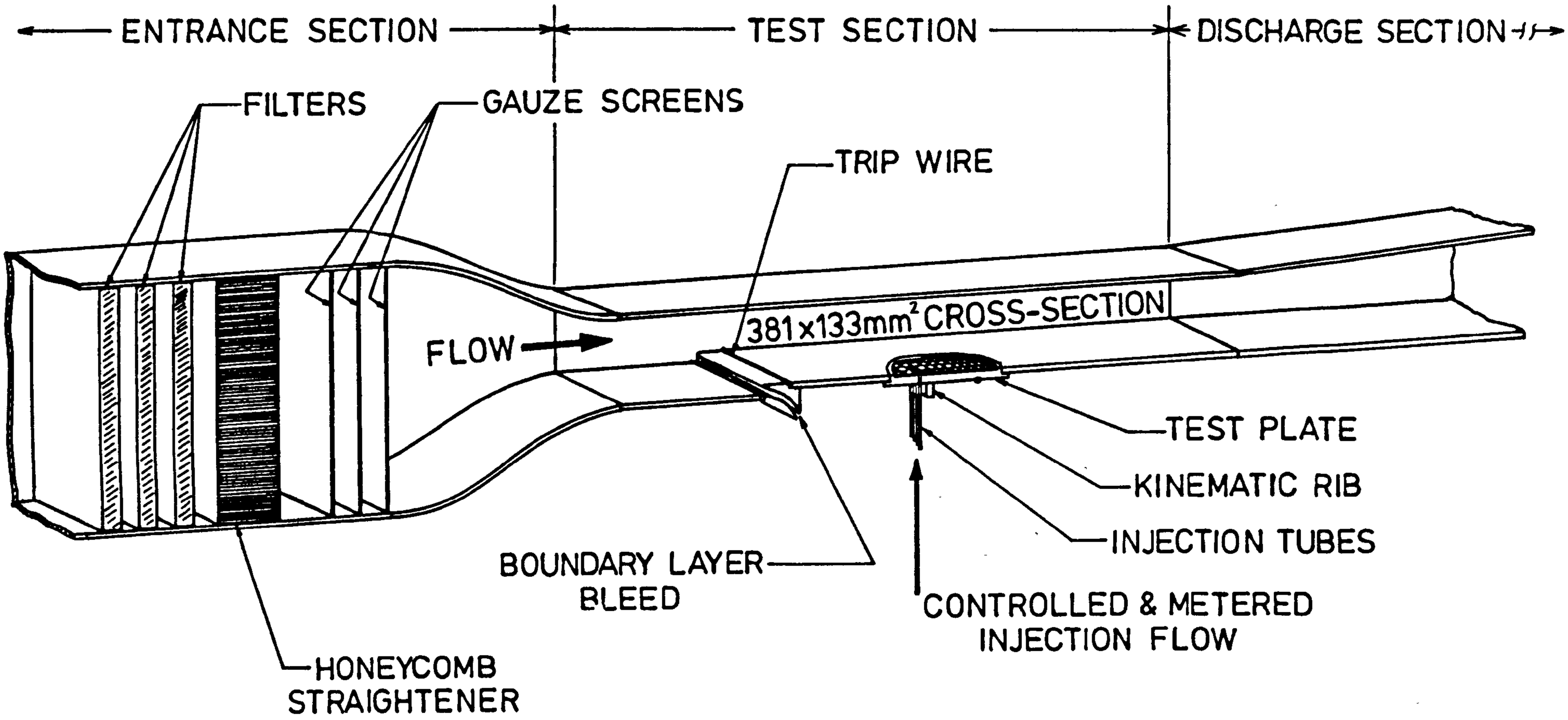

Fig. 5.1 Layout of the wind tunnel.

coefficient accurately using the swollen polymer technique, as the swelling agent partial pressure is strongly dependent on temperature.

The wind tunnel sections are now described proceeding in the flow direction.

5.1.1 The Entrance Section

The entrance section was of rectangular cross-section and consisted of the following components: air filters, honeycomb flow straighteners, gauze screens, and a contraction (see Fig. 5.1).

Three panel type veeglass air filters of 50mm thickness each were fitted 50mm distance apart in the upstream portion of the entrance section. The panels provided adequate filtration and on average arrested 86% of the incoming air dust. The upstream filter was usually replaced every 20 working hours since the compressed air carried relatively large amounts of dust, while the other two were replaced every 40 working hours. Panels were replaced by simply sliding them through grooves made inside the wooden walls of the entrance section, and were moved in or out through a side door.

Directly downstream, an impregnated paper honeycomb straightener of length to diameter ratio of 8 as quoted by Bradshaw and Pankhurst [94] is located to remove any swirl in the flow. The flow turbulence level was reduced and the velocity lateral variation removed by three stainless steel wire mesh screens of 31.4% open area ratio. The screens were placed in the downstream direction more than 500 wire diameters apart [94]. Pressure tappings were embedded in the side wall both upstream and downstream of each screen. Effective blockage of the screens by the mainstream air dust was indicated by the change in pressure drop across a screen. Cleaning of the screens during the experimental phase of the research was required only occasionally, as most of the dust was retained by the upstream air filters.

A contraction of 3:1 area ratio connected the entrance and test sections.

5.1.2 The Test Section

The test section was attached firmly to the end of the contraction part of the entrance section. This section was 928mm in overall length and 381mm x 152mm in cross section at entry. Plate 5.2 and Fig. 5.2 show a general view and detail of the test section respectively.

The bottom wall of the test section was composed of two segments (parts A and B in Fig. 5.2) separated by a boundary layer bleed slot (part C), which reduced the test section height to 133mm. The bleed removed the floor boundary layer and thereby provided a newly-defined boundary layer over the part of the test section floor incorporating the film cooled test surface. Four pressure tappings made from hypodermic tubing were embedded evenly at both sides of the tip of the bleed slot. These taps, combined with a hinged aluminium flap controlling the flow through the bleed, ensured that the location of the stagnation point was at the tip of the bleed slot, and thus the main flow was parallel to the test surface.

A trip wire of 0.70mm diameter was situated 38mm downstream from the edge of the slot bleed. In this way, a fully developed turbulent boundary layer was obtained over the whole of the film cooled surface.

Downstream of the trip wire, the test section floor (part B) of a smooth top surface had a 216mm diameter circular hole cut through it so that a removable assembly of circular flat plates (part D, described in detail later) of the same floor hole diameter could be inserted and spring clamped in position. A steel locating pin fixed to the bottom surface of the floor and a U shape cut in the test plate flange (see Fig. 5.4) assisted similar relocation of the plate axes when fitted to the floor hole. Six spring clamps with rubber pads were located at even intervals around the hole to hold the test plate in position (see Fig. 5.2). The rubber pads were used to alleviate any point stresses at the point of contact between the clamps and the plate. A rubber tube seal was also incorporated into a groove in the bottom surface of the floor around the hole to stop any outward leakage of fluid from around the plate periphery. Furthermore, the wall was equipped with static pressure taps.

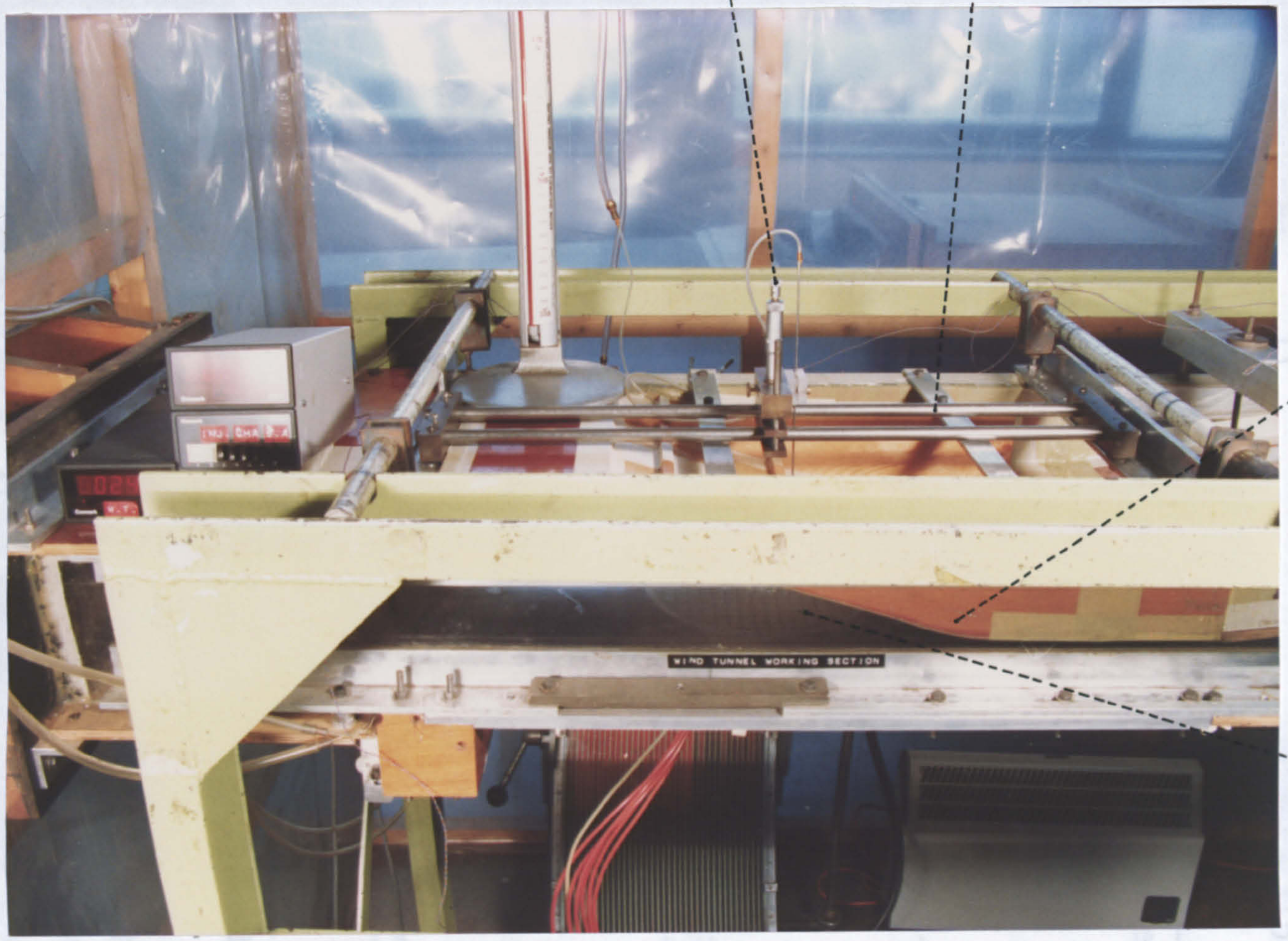

Fig. 5.2 View of the test section.

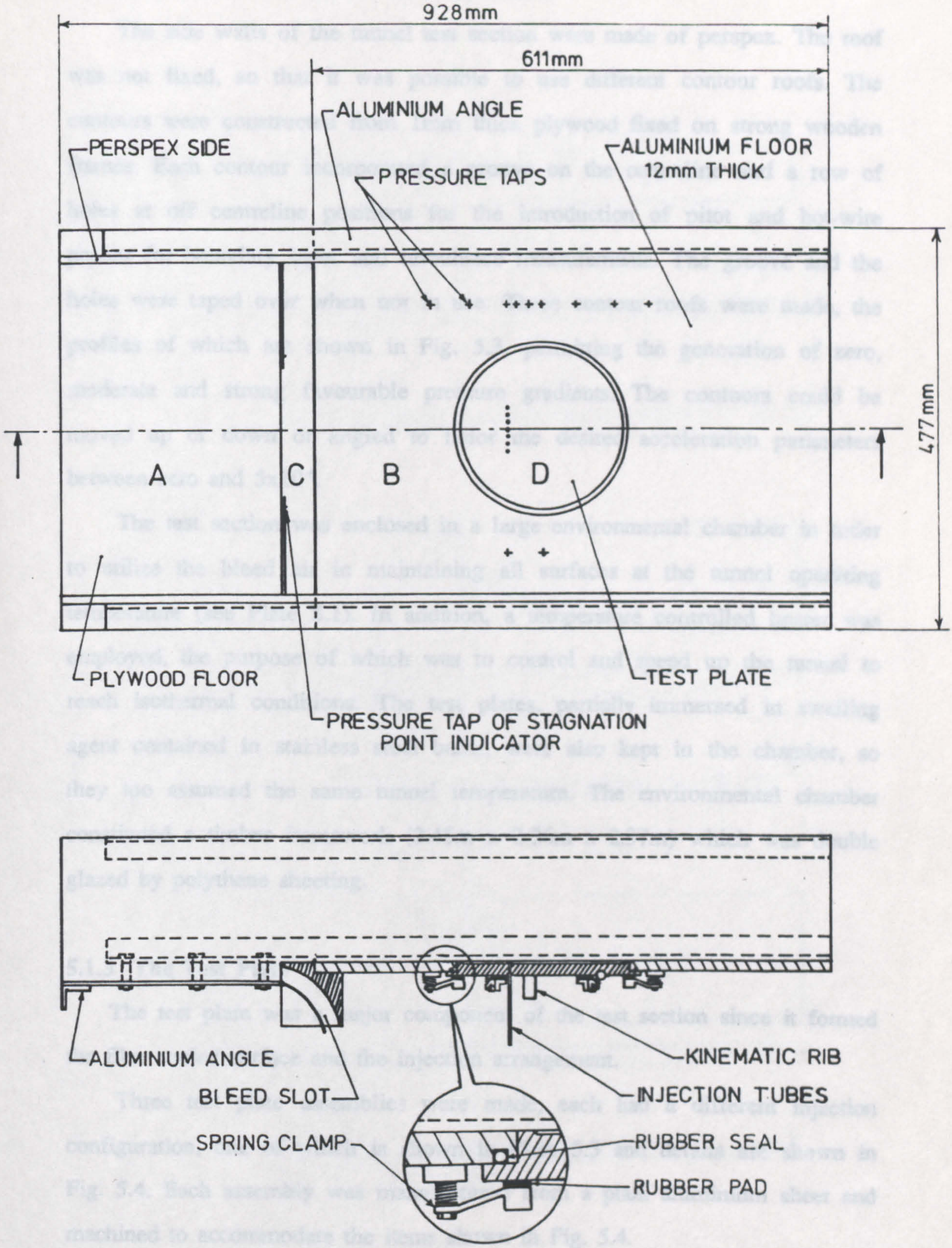

Fig. 5.2 Details of the test section (excluding the roof).

The taps were located in the streamwise direction on both sides of the hole and were connected to a multi-tube manometer.

The side walls of the tunnel test section were made of perspex. The roof was not fixed, so that it was possible to use different contour roofs. The contours were constructed from 1mm thick plywood fixed on strong wooden frames. Each contour incorporated a groove on the centreline and a row of holes at off centreline positions for the introduction of pitot and hot-wire probes for boundary layer and turbulence measurements. The groove and the holes were taped over when not in use. Three contour roofs were made, the profiles of which are shown in Fig. 5.3, permitting the generation of zero, moderate and strong favourable pressure gradients. The contours could be moved up or down or angled to tailor the desired acceleration parameters between zero and 5×10^{-6}.

The test section was enclosed in a large environmental chamber in order to utilize the bleed air in maintaining all surfaces at the tunnel operating temperature (see Plate 5.1). In addition, a temperature controlled heater was employed, the purpose of which was to control and speed up the tunnel to reach isothermal conditions. The test plates, partially immersed in swelling agent contained in stainless steel baths, were also kept in the chamber, so they too assumed the same tunnel temperature. The environmental chamber constituted a timber framework (2.45m x 2.26m x 2.37m) which was double glazed by polythene sheeting.

5.1.3 The Test Plate

The test plate was a major component of the test section since it formed the film cooled surface and the injection arrangement.

Three test plate assemblies were made, each had a different injection configuration, one of which is shown in Plate 5.3 and details are shown in Fig. 5.4. Each assembly was manufactured from a plain aluminium sheet and machined to accommodate the items shown in Fig. 5.4.

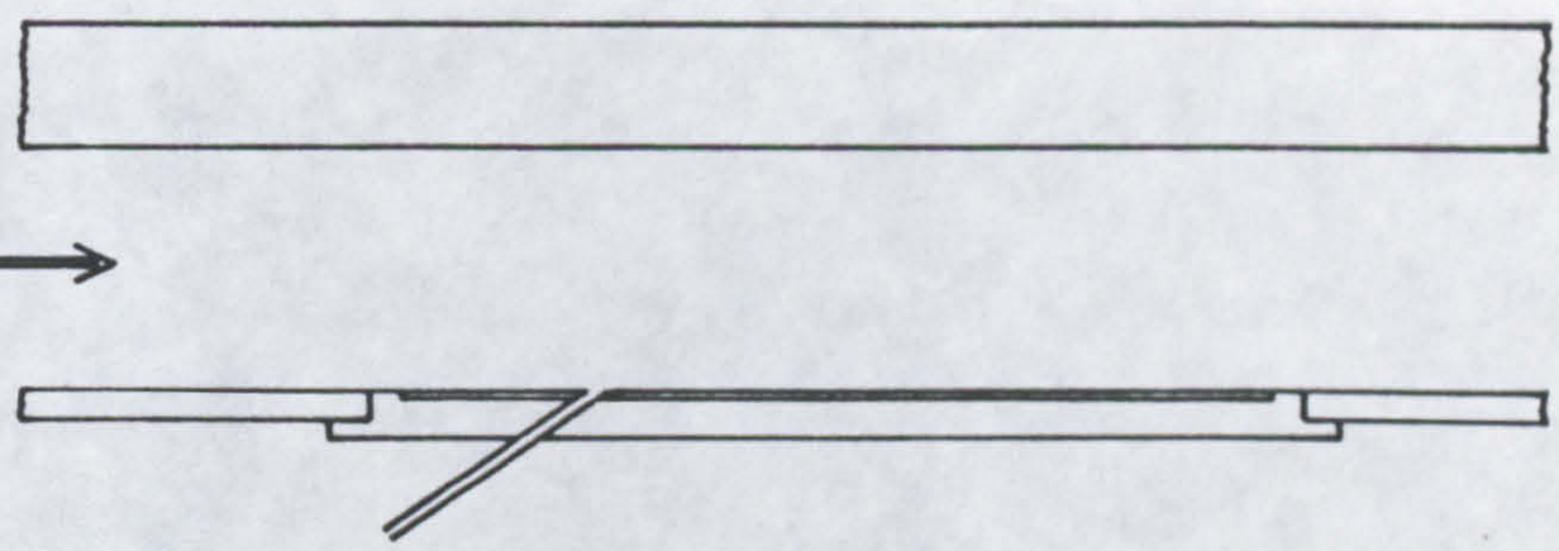

(A) constant mainstream velocity, K=0.0

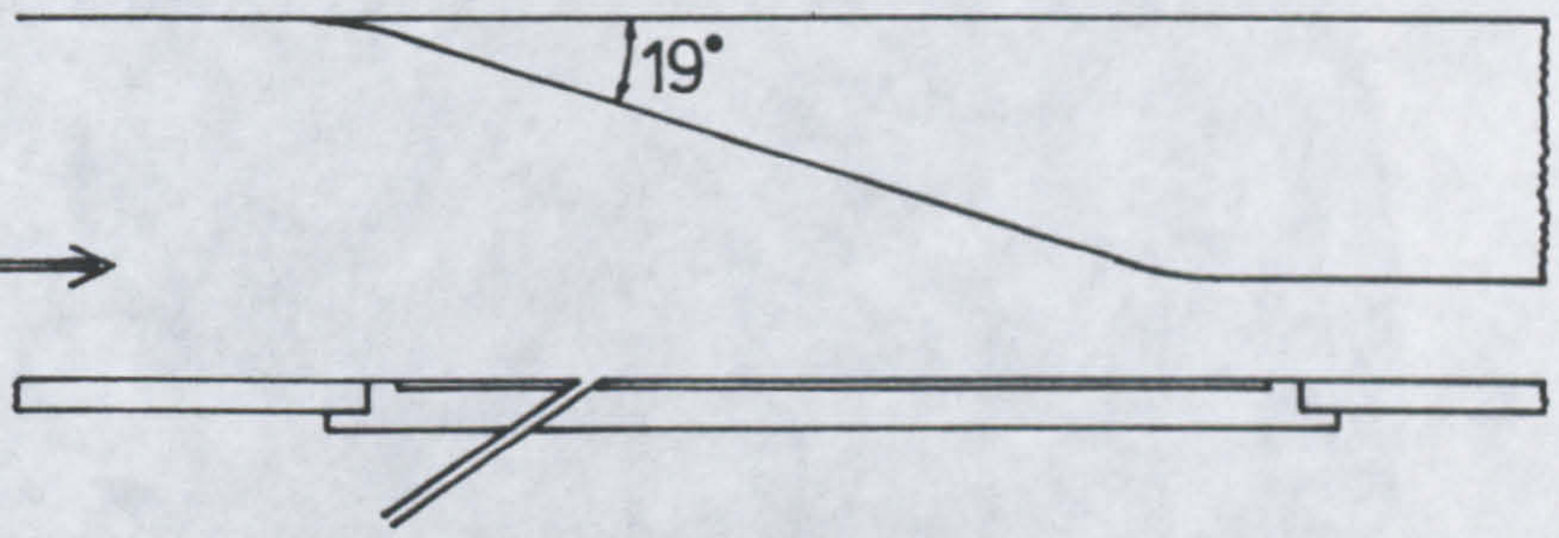

(B) moderate acceleration, $K=1.9\times10^{-6}$

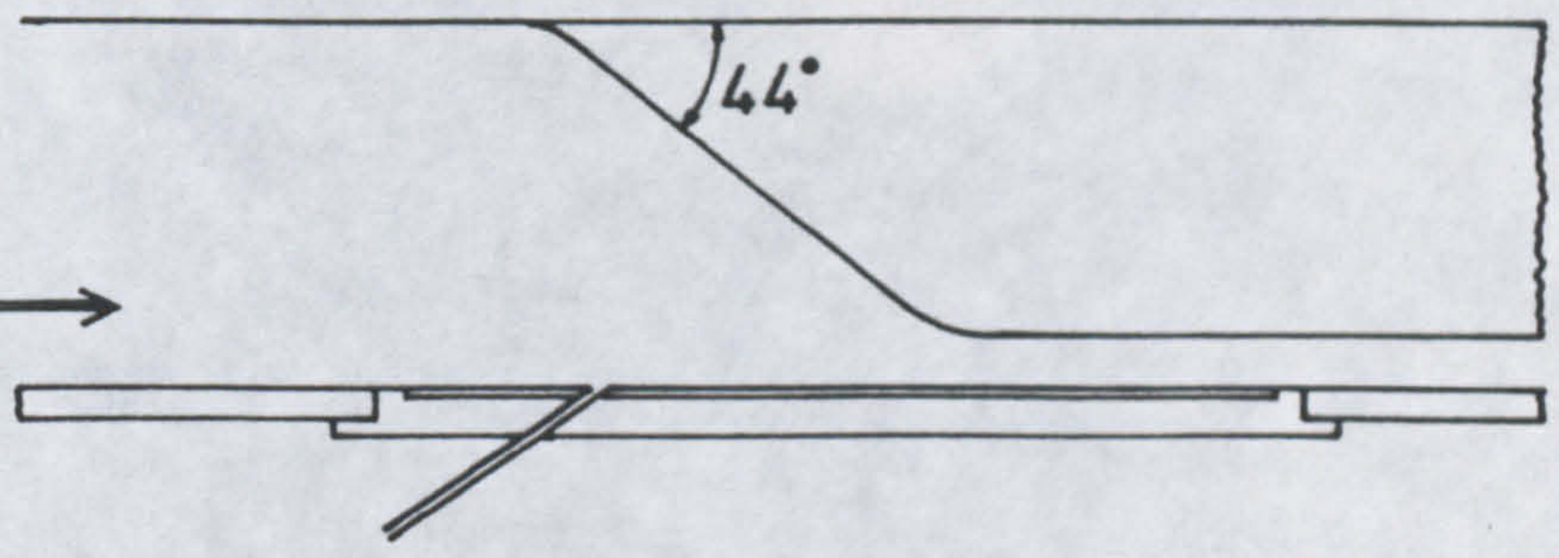

(C) strong acceleration, $K=5.0\times10^{-6}$

Fig. 5.3 Profiles of contours in the test section.

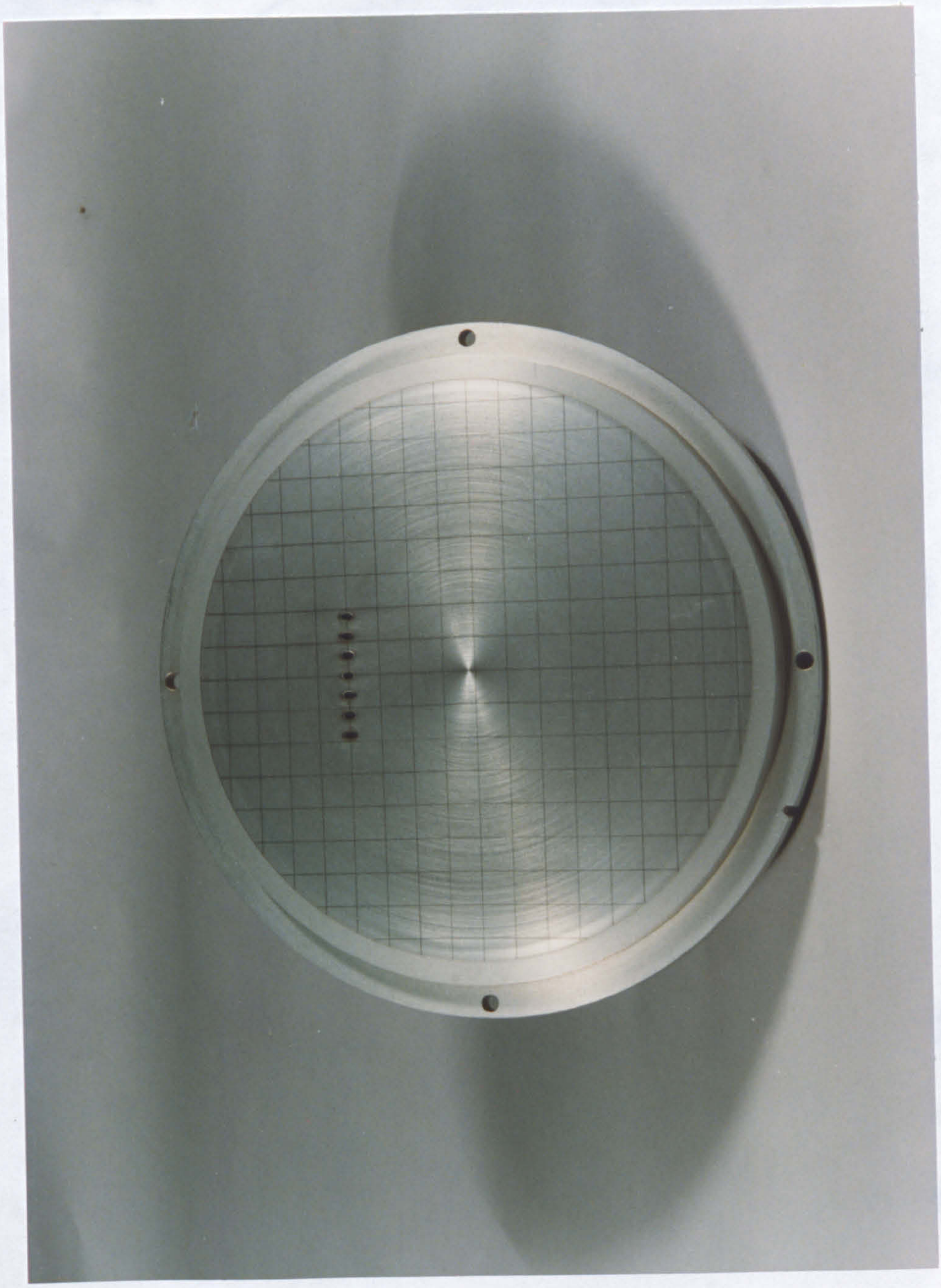

Fig. 5.3 Test plate.

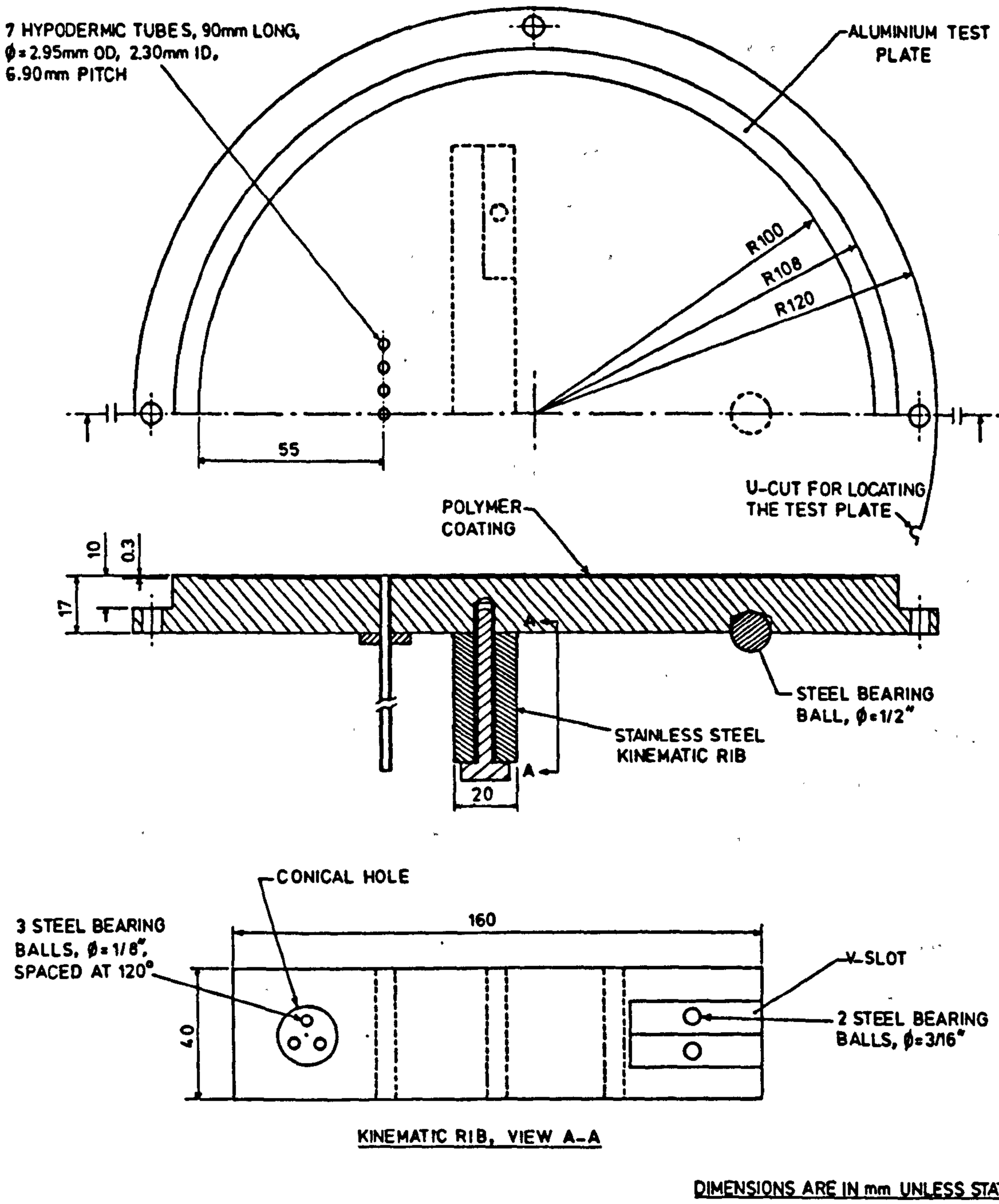

Fig. 5.4 Details of the test plate.

The transparent silicone rubber coating (RTV615) formed the mass-transferring surface after being swollen in n-tetradecane. The coating was applied to the test plate so that its surface and the tunnel floor provided a hydrodynamically smooth surface.

The application of the polymer coating to the recess in the test plate top surface is described in detail in [82].

The stainless steel hypodermic tubes that fed the injectant were fitted flush with the coating surface. The tubes were at 235mm downstream of the trip wire when the plate was fitted in the test section floor.

One test plate incorporated only a single injection tube held normal to its surface, whereas, each of the other two plates contained a single row of seven injection tubes held at three hole diameters between their centres in the lateral direction. One row was normal to the streamwise direction and the other was inclined at 35°, as shown in Fig. 5.5.

The stainless steel kinematic rib screwed to the underside of the test plate, Fig. 5.4, allowed extreme precision of location on a fixed kinematic mount placed on the holographic table (see Plate 5.4). The kinematic rib and the kinematic mount featured the classical fixture of "hole, groove and plane", removing the six degrees of freedom of the test plate by the use of six contact points, a description of which is given by Kapur and Macleod [88].

A dummy aluminium plate (without a polymer coating) of similar size to the coated test plates was also made. The plate had static pressure taps embedded at one side. The dummy plate was used to fill the hole in the test section floor during the time it took the tunnel to reach steady and isothermal conditions before carrying out a test, and was also used when measurements of the boundary layer were made.

5.1.4 The Discharge Section

The whole of the discharge section was retained without any modifications for this work.

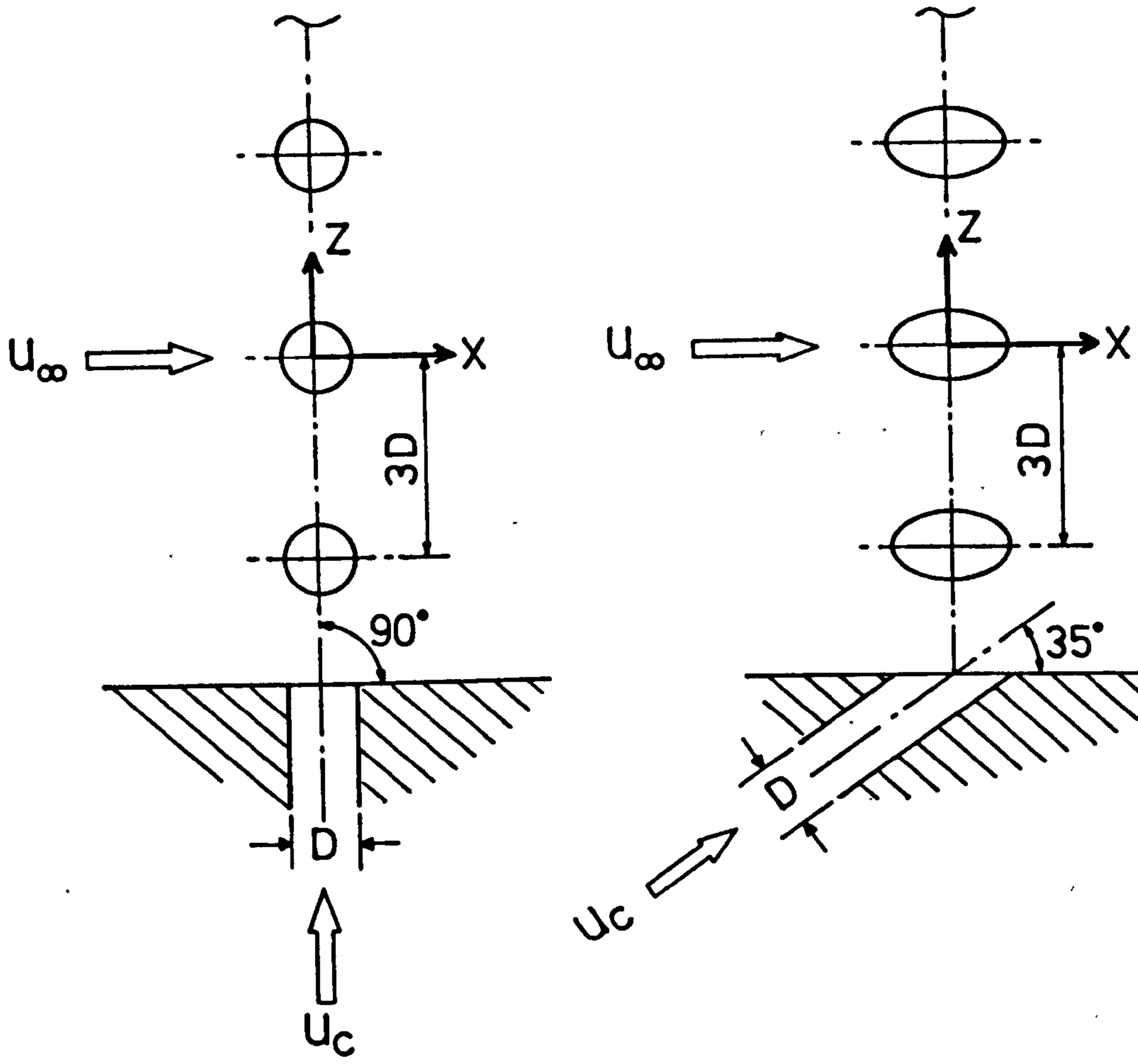

Fig. 5.5 Injection geometry.

A diffuser with an adjustable roof was attached to the downstream end of the test section. The roof was movable and so could be adjusted to match the height of any of the test section contours used, in addition to providing some diffusion.

A second diffuser with an adjustable roof similar to the first was also used to enlarge the diffusion angle. At its downstream end, a 450mm diameter, 5m long flexible circular duct was connected. The other end of the duct was attached to a silencer box for discharging the compressed air outside the laboratory building.

5.2 THE INJECTION SYSTEM

The air injectant was drawn from the laboratory compressor plant supplying the mainstream through a separate supply line. The injectant flow rate was controlled by a needle valve and metered by a calibrated rotameter. Three rotameters were used allowing accurate measurement of both small and large injection rates, the calibration of which is described in [82]. Valves were fitted at both ends of the medium and large flow capacity rotameters to permit the use of either depending upon the desired flow rate.

When a foreign gas or gas mixtures were used as the injectant, it was fed from pressurised bottles through a pressure regulator, which reduced the pressure and eliminated any pressure fluctuations, Fig. 5.6. The foreign gas was then adjusted by the use of a needle valve and passed through about 5 meters of 10mm O.D. coiled copper tube before being metered by the calibrated rotameters. A controlled electric band heater kept the temperature of the pressure regulator steady when carbon dioxide high pressure cylinders were used.

A plenum chamber was connected to the outlet of the rotameters. The chamber contained a straightener and two gauze screens, thereby smoothing out any velocity nonuniformity through it. Seven equally spaced hypodermic tubes of 2.30mm I.D. formed the exit of the plenum chamber. At their exit, seven long flexible nylon tubing were connected to carry the coolant fluid to

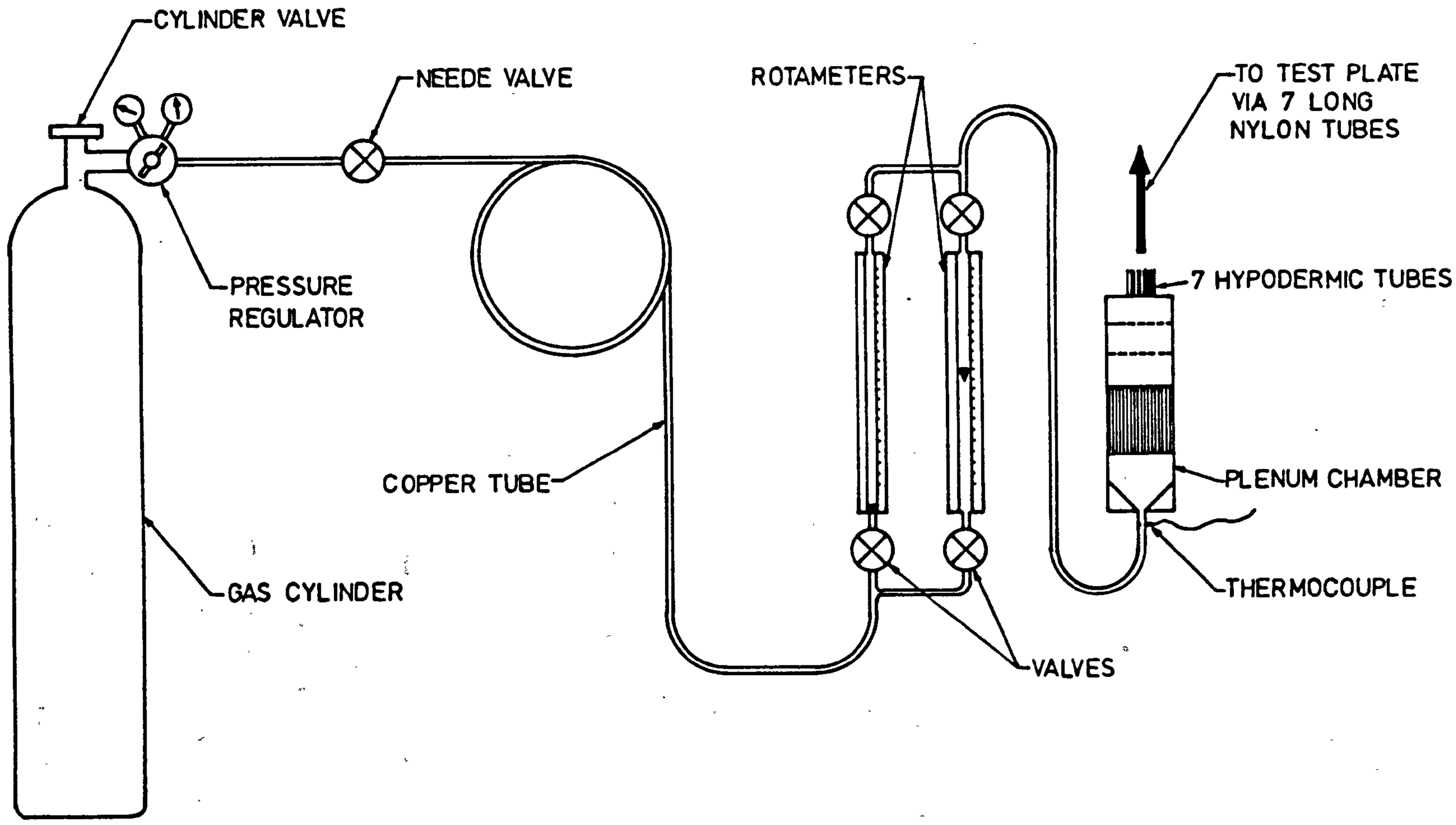

Fig. 5.6 Foreign gas injection System.

the hypodermic injection tubes of the test plate. The long injection tubes ensured having fully developed flow at their exit.

The whole of the injection system was placed inside the environmental chamber to ensure that the secondary fluid was at the tunnel operating temperature when injected.

5.3 INSTRUMENTATION

Instruments were used to measure the boundary layer velocity profiles and turbulence intensities over the test surface both with and without injection, and temperature.

The boundary layer velocity profiles without injection were obtained using a small flattened total pressure probe and the static pressure taps of the tunnel floor of the test section. The probe was mounted on an existing sliding carriage with a micrometer head which provided both axial and vertical positioning of the probe tip for measurements. The probe could be inserted into the flow through either the groove or the holes of the contour roofs.

The variation of longitudinal flow turbulence intensity and velocity profiles with and without injection were also obtained using a DISA 55-D01 constant temperature hot wire anemometer employing either straight or 90° probes. The probe was carried and inserted into the flow as for the total pressure probe.

Precise temperature control and measurements were needed. As stated earlier the vapour pressure of the swelling agent is strongly dependent upon temperature, and more seriously spurious fringes may appear on the film cooling interferograms as a result of thermal effects. Temperature was measured using calibrated chromel/alumel thermocouples (Ni-Cr/Ni-Al) in conjunction with a digitiser which translated the voltages into temperatures (description of calibration is given in [82]). Four thermocouples in all were used; one was embedded in the pipe feeding the plenum chamber to measure the injection gas temperature before injection, another was inserted through the roof of the test section to measure the mainstream temperature, and the

remaining two measured the environmental chamber and the swelling agent bath temperatures. The bath was used to soak the test plate prior to a test and also to ensure that the plate was at the same temperature as the tunnel test section.

5.4 THE HOLOGRAPHIC TABLE

An existing holographic table was situated in a separate darkroom away from the wind tunnel and floor-borne vibrations. The optical components were assembled on a rigid anti-vibration table 1.82m x 1.21m x 0.81m. The table had 0.15m thick cast iron top with T-slots running parallel to its length and breadth to which the various optical components were firmly clamped. The main body of the table was of bricks and supported by four pneumatic springs on which the table was lifted, levelled and isolated from ground vibrations.

Plate 5.4 shows a view of the optical setup, and Fig. 5.7 illustrates the layout of the setup.

A Spectra Physics 124A He/Ne laser of maximum output of 15mW and of wavelength of 632.8 nanometres was used as a coherent light source. A DURST TIM 60 exposure timer was located between the laser and the mains power supply to operate and adjust the exposure time between 1 and 60 seconds. The timer also provided a continuous laser beam to set up the laser table.

The beam from the laser source (1) was raised to a convenient height by a beam steering device (2) and turned by a mirror (3). The light was then split by a beam splitter (4) into reference and object beams with the appropriate desired ratio of intensity. The reference beam was directed by a mirror (5) to pass through a spatial filter (6) consisted of an objective lens with a 25 microns pinhole to remove any fringe patterns from the beam created by dust particles on mirrors. The emergent expanding beam was then received at the photographic plate (7), (Agfa-Gevaert 8E75 HD), which was clamped rigidly in a holder. The plate holder had also a plastic light-proof box used to protect the semi-exposed plate from stray light in between the

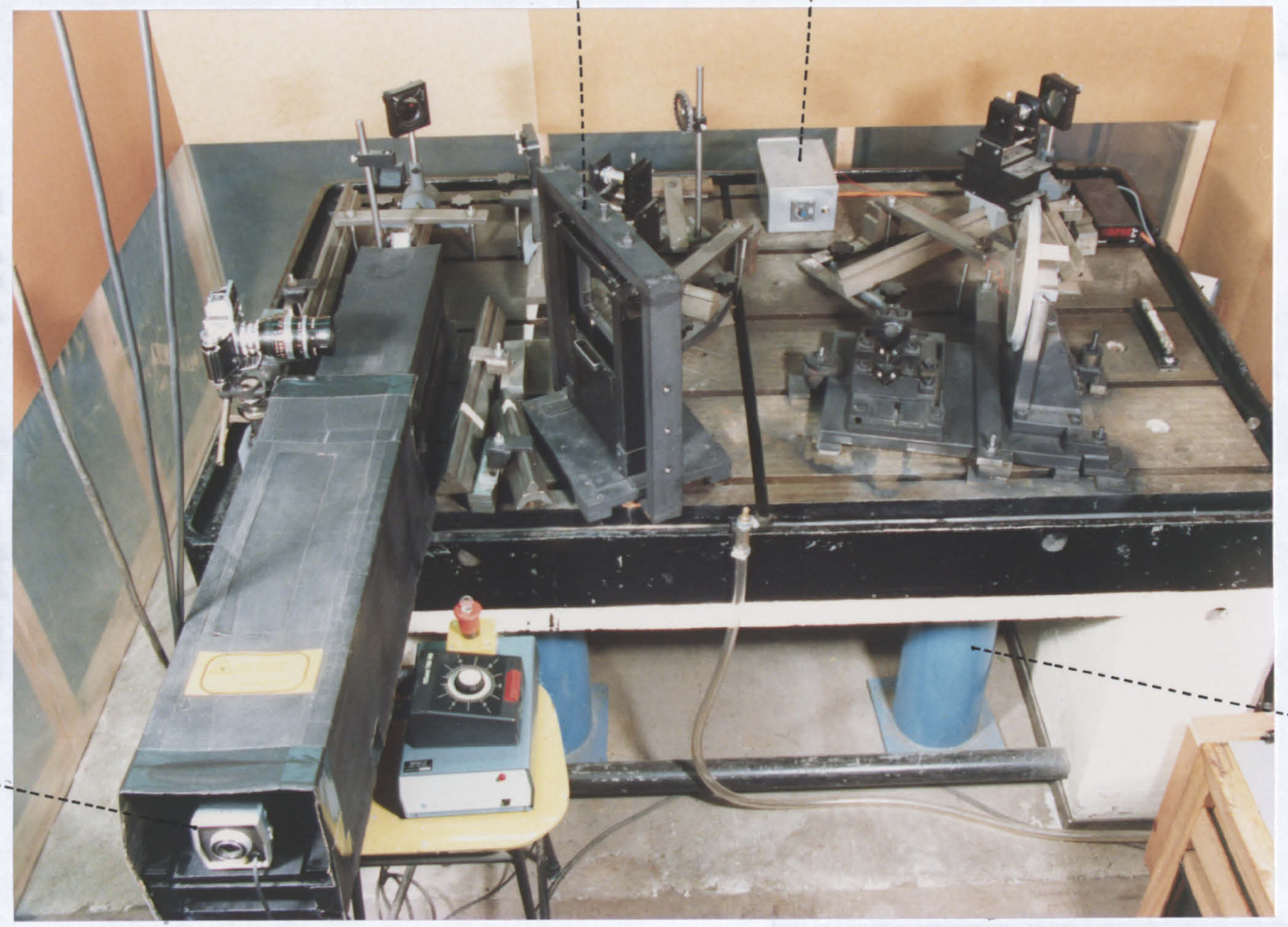

Fig. 5.4 View of the holographic setup.

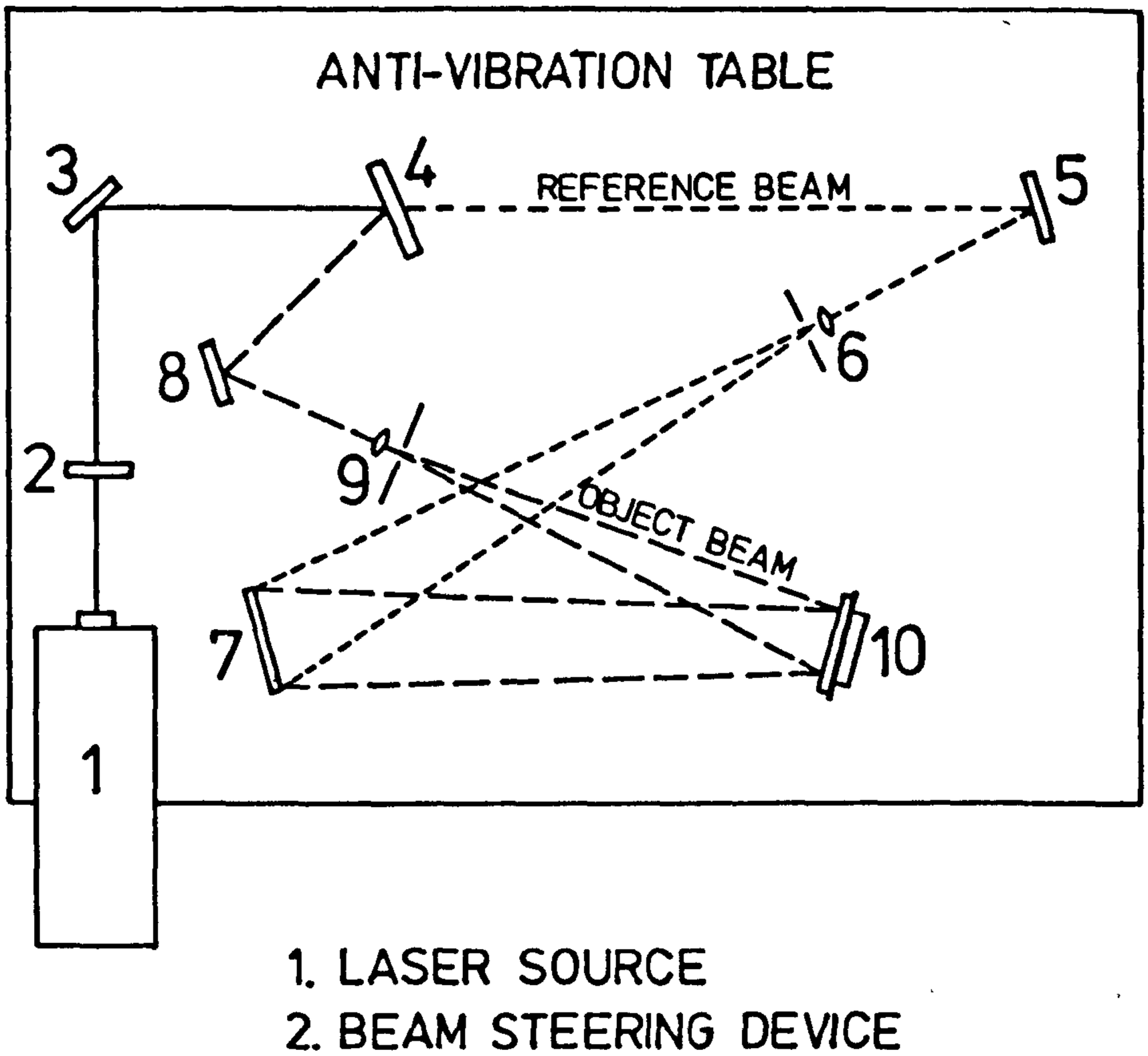

1. LASER SOURCE
2. BEAM STEERING DEVICE
3. MIRROR
4. BEAM SPLITTER
5. MIRROR
6. SPATIAL FILTER
7. PHOTOGRAPHIC PLATE
8. MIRROR
9. SPATIAL FILTER
10. TEST PLATE

Fig. 5.7 Layout of the optical setup.

two exposures. The object beam formed by reflection from the beam splitter was steered by a mirror (8) to pass through a spatial filter (9), identical to (6), onto the coated test plate (10) mounted on a kinematic stand for the precise repositioning of the plate for the second exposure. Part of the beam scattered from the diffusely reflective test plate fell on the photographic plate (7).

The optical setup was arranged so that the difference in path length of the object and reference beams (less than 30mm) was well within the coherence length of the laser light used (about 300mm) necessary to reproduce interference fringes.

It has been observed that a difference in temperature of the test plate of more than 0.5°C between the two exposures produced spurious fringes. Therefore, the holographic table was surrounded by an enclosure made of timber framework (2.72m x 2.80m x 2.11m) covered by polythene sheeting. The enclosure and a controlled electric heater enabled the setting of the table temperature to that of the tunnel test section during a test. Furthermore, to preserve the test plate temperature during a test, the test plate was brought to and from the holographic table in a wooden box kept in the environmental chamber of the tunnel test section.

5.5 THE AIR-GAUGE SYSTEM

The air-gauge was the independent method used to determine the recession at a selected reference point on the swollen polymer surface. The principle of air-gauging simply is that air from a constant pressure supply flows to the atmosphere via two orifices. One is a control orifice inside a tube, while the other is formed by the space between a surface and the tip of a needle probe of the tube. Variation of the space causes pressure changes between the two orifices measured on a manometer. Therefore, in the swollen polymer technique, a comparison of the manometer readings taken before and after the exposure of the swollen polymer surface to the flows in the wind tunnel would reveal the absolute recession at the reference point, if the

relation between the air-gauge back pressure and probe-to-surface distance is known.

An existing air-gauge probe, shown in Plate 5.5, consisted of a 1.5mm O.D. and 1.1mm I.D. hypodermic tubing fixed into a blanked off end of a length of 10.0mm I.D. copper tube. The probe was clamped horizontally to a spring loaded micrometer controlled assembly, the micrometer head of which had graduations of 0.0001in divisions , thus permitting fine adjustments of the probe tip normal to the test plate surface.

The probe assembly was mounted on a kinematic bracket, designed as that described by Kapur and Macleod [88], for removal and accurate relocation of the probe when taking measurements (see Plate 5.5).

Air was supplied to the probe from a laboratory compressor, the pressure of which was regulated and maintained at 105mm H_2O by passing the air through water at a depth of 105mm. The air was then bubbled through two small tanks about half filled with the swelling agent (n-tetradecane) as shown in Fig. 5.8. This was done to saturate the air to minimise evaporation from the swollen polymer surface at the point of measurement. The air partially saturated with the swelling agent from the second tank was passed up through chips of polymer soaked with n-tetradecane and through a layer of glassfibre packing, to remove droplets of swelling agent entrained in the air before it was exhausted to the probe through a plastic tube.

The air-gauge back pressure was measured on a water filled Betz manometer. A quick release valve was located in the air tube to the manometer. This was done to reduce evaporation of the swollen coating during the time it took the manometer to reach a steady reading (normally 0.5-1.0 minute) for the second measurement. By shutting the valve after taking the first reading, the manometer was kept at a pressure close to the expected second pressure reading (i.e. after exposure of the coating to the flow streams) and hence that time was reduced significantly.

To determine the absolute recession at a point, and hence the fringe order, it was necessary to calibrate the probe to obtain the relationship

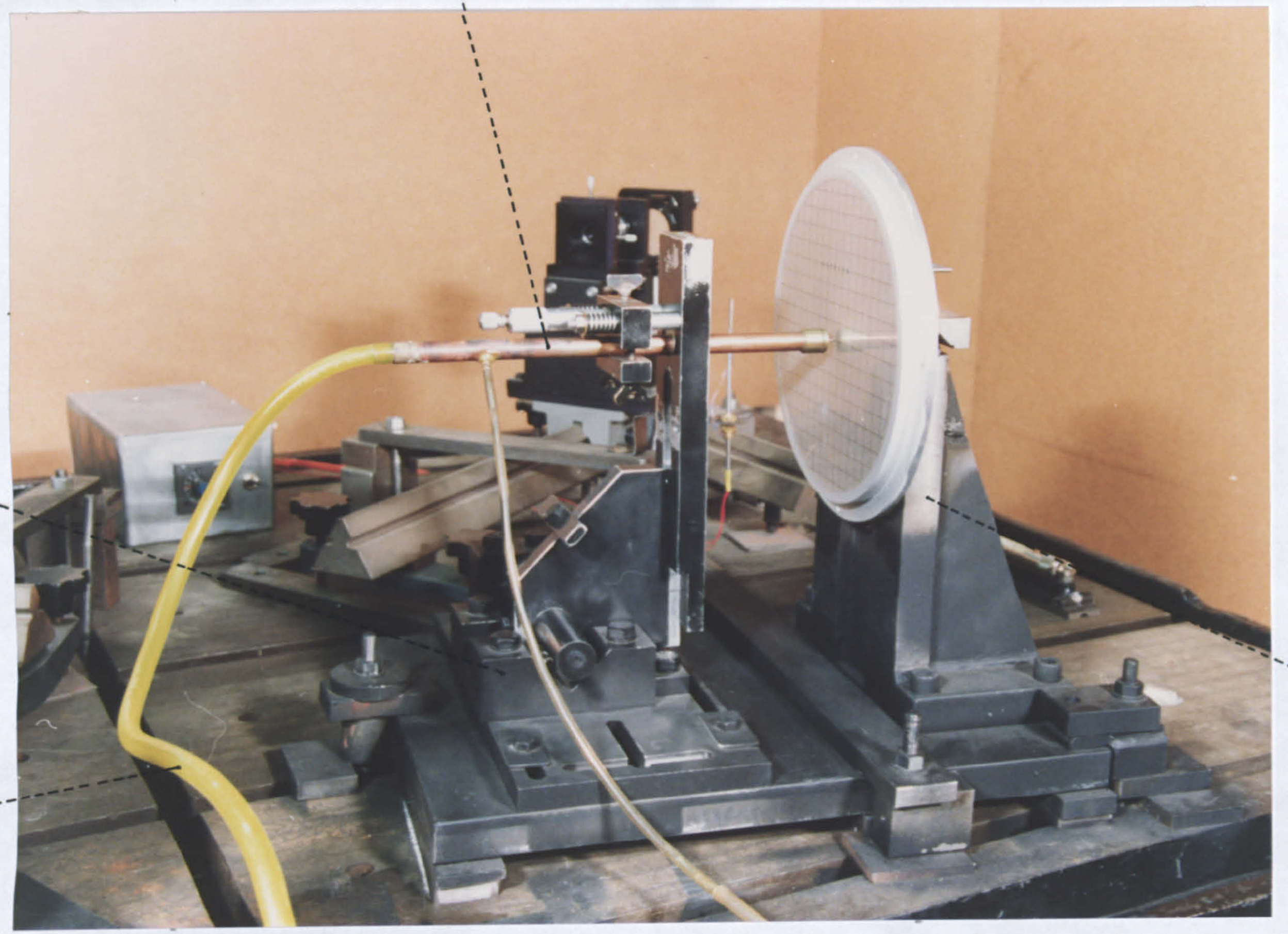

Fig. 5.5 Air-gauge assembly.

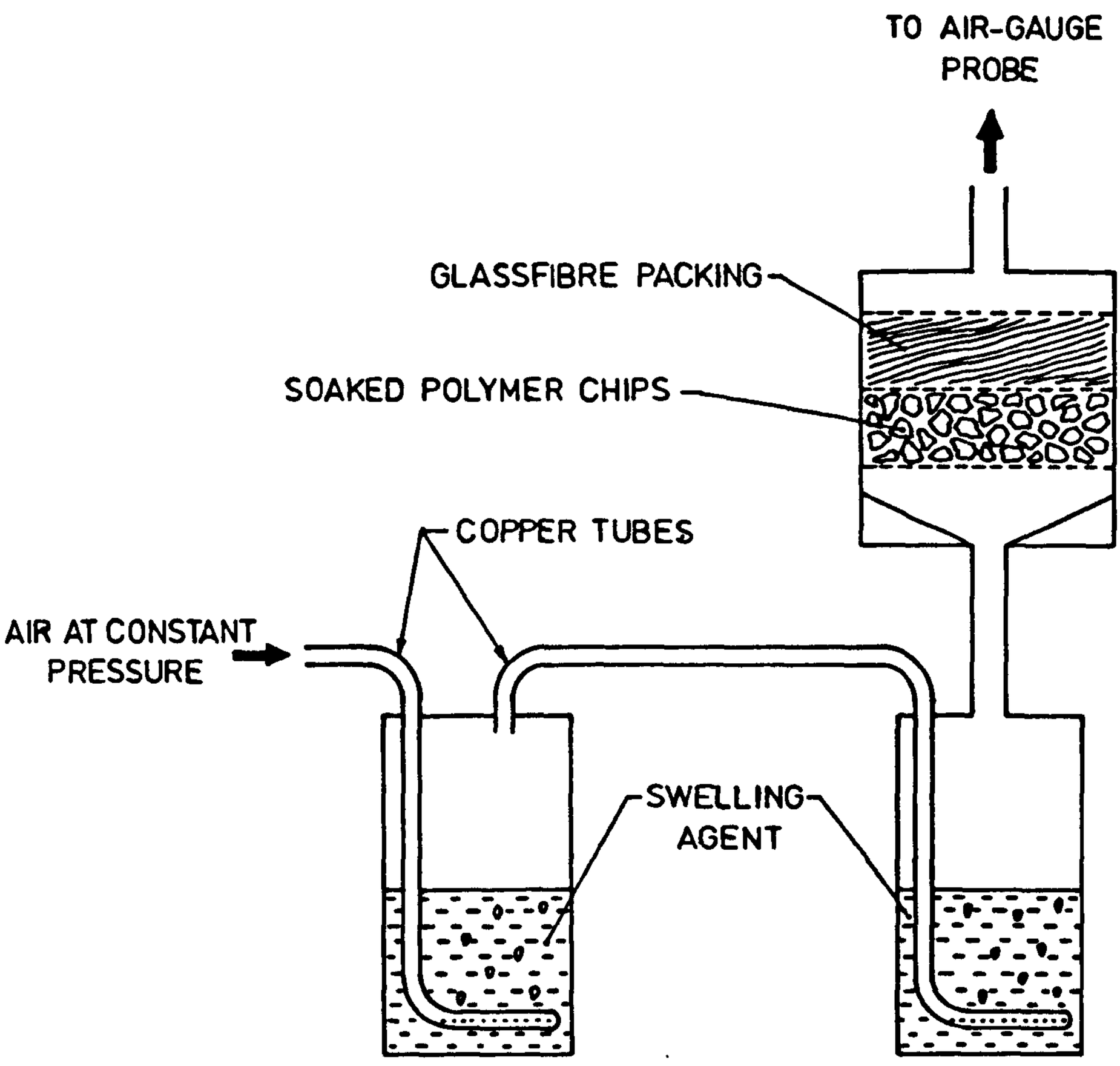

Fig. 5.8 Saturation arrangement of air-gauge air supply.

between the manometer pressure and displacement. This was done as described in Appendix B.

CHAPTER 6

EXPERIMENTAL PROGRAMME, OPERATING CONDITIONS AND PROCEDURES

This Chapter describes the format of the experimental programme and states the range of parameters covered and under which conditions. Moreover, the manner in which the tests were carried out is outlined, and the consistency of the results is assessed.

6.1 EXPERIMENTAL PROGRAMME

After the existing swollen polymer apparatus had been improved through extensive experimentation and subsequent modifications (see Appendix C), preliminary tests were conducted to validate the technique for the determination of mass (heat) transfer coefficients. Initial tests were without injection. Later tests with injection included variation of the coolant to mainstream density ratio. The tests were carried out using the test plate with the single normal tube. The injection hole was sealed by a nylon plug for the zero injection studies. It was thought that testing with varying density ratio using foreign gases having different Schmidt numbers could be validated using a single injection hole rather than a row of holes, since the effect of Schmidt number variation on the mass transfer coefficient was the major concern. This reduced the amount of the expensive foreign gases employed in the investigation.

The validation tests described in chapter 7 were conducted under zero mainstream pressure gradient. However, if Sc influence is found to be insignificant the validation can be assumed to hold in the presence of pressure gradients also.

Once qualification of the present technique had been achieved, the experimental programme for injection via a row of holes was conducted within the range of parameters summarised in Table 6.1.

As can be seen in Table 6.1, the injection hole diameter was fixed at 2.30mm, whereas the diameter of typical film cooling holes are around 0.5mm. Scaling up the hole diameter was necessary to facilitate studying of the lateral distribution of the heat transfer coefficient.

In practice, spacing of film cooling holes to diameter ratio is generally in the range of 2.5 to 5.0, and most of the existing experimental data was for hole spacing of 3.0 diameters. Therefore, a hole spacing of 3.0 diameters was chosen so that a comparison of the present results with the published data could be made.

Two injection hole inclinations were used, 90° injection angle, as encountered around the leading edge of a turbine blade, and 35° angle, as encountered on both the pressure and suction sides.

The number of holes used in a row was 7. This was found to give a central region representative of an infinitely long row of holes over the full streamwise extent of the surface. Edge effects of the mainstream on the cooling film heat transfer coefficients were confined to the holes situated at either end of a row. A similar observation was reported by Pedersen et al [52] for effectiveness measurements.

The effect of density ratio on the heat transfer coefficient was given the primary consideration. Density ratios of 1.0 and 1.52 were studied with the latter approximating real blade cooling situation. The density ratio of 1.52 arose from the use of cheap, readily available carbon dioxide gas as the injectant. Initially, a nominal zero mainstream pressure gradient was employed, blowing rates of 0.5,1.0,1.5 and 2.0 for a density ratio of unity were covered using the 90° holes test plate. The test plate was then replaced by the 35° holes plate and the tests were repeated.

The next series of tests covered the same range of parameters as above but for a density ratio of 1.52.

Geometrical Parameters	
Single row of holes on a flat surface	
Injection hole diameter (D)	**: 2.30mm**
Hole spacing to diameter ratio (s/D)	**: 3.0**
Injection hole inclination (α)	**: 90° and 35°**
Number of injection holes	**: 7**
Data collection area,	
- upstream of injection point	**: 5D**
- downstream of injection point	**: 60D**
Flow Parameters	
Density ratio (ρ_c/ρ_∞)	**: 1.0 and 1.52**
Blowing rate ($\rho_c u_c/\rho_\infty u_\infty$)	**: 0.5, 1.0, 1.5**
	: and 2.0
Mainstream acceleration parameter (K)	**: 0.0, 1.9×10^{-6}**
	: and 5.0×10^{-6}

Table 6.1 Range of film cooling parameters covered in the experimental work.

At this stage, sufficient information had been obtained for comparisons with published work and between the two density ratio results to be made.

Attention was then focused on the influence of mainstream acceleration on the heat transfer coefficient. The flat roof parallel to the floor of the wind tunnel test section was changed for one giving effectively a constant acceleration parameter K ($=\nu(du_\infty/dx)/u_\infty^2$) of 1.9×10^{-6} and subsequently for another giving K of 5.0×10^{-6}. These accelerations are within the range experienced on a turbine blade in regions away from the leading edge. Since it can be shown from continuity that a one-dimensional flow between two convergent flat surfaces yields a constant K, the roof contours were essentially inclined planes. One was inclined at 19° to the streamwise direction and the other was inclined at 44°.

In the application of discrete hole film cooling to turbine vanes and blades, the coolant is usually injected at an angle to both pressure and suction surfaces. Subsequently, only 35° injection was used for the investigation of mainstream acceleration.

For both favourable pressure gradient cases considered the results were taken for the same range of blowing rates of 0.5 to 2.0 for a unity density ratio.

The other significant effect accounted for was the influence of density ratio in the presence of pressure gradient. The tests for density ratio of 1.52 were, however, limited to the strong favourable pressure gradient of $K=5.0\times10^{-6}$. This was done in anticipation that the effect of density ratio would be more pronounced in this case.

For the unity density ratio cases measurements of velocity profiles and turbulence intensities were made for all blowing rates considered in the presence of the different pressure gradients. However, the turbulence intensity measurements were restricted to the root mean square longitudinal velocity fluctuations only. The measurements were taken at three stations in the streamwise direction along the centreline of the centre hole. This was done in an endeavour to deduce explanations for the behaviour of the heat transfer

coefficient with injection at the various conditions investigated.

Table 6.2 indicates the sequence of, and conditions at which the measurements were conducted.

6.2 OPERATING CONDITIONS

The experiments were carried out under the following operating conditions,

a- Steady state, isothermal conditions prevailed during all tests.

b- The mainstream Reynolds number at the injection location, Re_D, was $3.8x10^3$ for all cases considered.

c- The intensity of turbulence of the mainstream without injection was 0.68%.

d- The operating temperature of the wind tunnel test section was controlled to be within the range of 25°-30°C. The injectant temperature was similar to the mainstream temperature during a test. The variation of the mainstream temperature during a test was within ±0.2°C, while that of the injection temperature was within ± 0.3°C.

e- Fully developed turbulent injectant flow existed during all tests with injection.

f- The maximum tube-to-tube variation of injected flow was less than one percent.

g- In absence of mainstream acceleration, the following conditions also existed,

- the mainstream velocity was nominally 25m/s;

- a fully-developed, two-dimensional turbulent boundary layer existed over the entire test plate surface. The effective origin of the turbulent boundary layer was 53mm upstream of the trip wire, 288mm upstream of the injection location. Details of the measurement of the boundary layer are given in [82], and

- the boundary layer displacement thickness to hole diameter ratio, δ^*/D, at the injection location was 0.40.

Injection angle α	Density ratio ρ_j/ρ_∞	Blowing rate M 0.5-2.0	Acceleration parameter K ($\times 10^6$)	Additional measurements: Velocity profiles	Additional measurements: Turbulence intensity
90°	1.0	✓	0.0		
35°	1.0	✓	0.0	✓	✓
90°	1.52	✓	0.0		
35°	1.52	✓	0.0		
35°	1.0	✓	1.9	✓	✓
35°	1.0	✓	5.0	✓	✓
35°	1.52	✓	5.0		

Table 6.2 Sequence of tests conducted, row of holes.

h- In the presence of mainstream acceleration, these conditions were further employed,

- the variation in pressure distribution started upstream of the injection holes; the contour roofs were adjusted so that the mainstream velocity at the injection location was 25m/s, the same as that of the zero mainstream acceleration case,

- the requirement of high mainstream acceleration, and the constraint of fixed height of the side walls of the tunnel test section, restricted the establishment of a constant acceleration parameter to over only a limited part of the test surface, particularly in the case of higher acceleration. The variation of the mainstream velocity, u_∞, normalized by the mainstream velocity at the point of injection, u_{∞_0}, and that of the pressure gradient parameter K as a function of the dimensionless distance x/D are shown in Fig. 6.1. The shape of the resulting boundary layer thickness is depicted roughly in the figure. As indicated by Fig. 6.1 the dimensionless distance covered by effectively constant acceleration was as follows,

case (B), $K \approx 1.9 \times 10^{-6}$, $-5 \leq x/D \leq 50$ and,

case (C), $K \approx 5.0 \times 10^{-6}$, $-5 \leq x/D \leq 30$

case (A) was for the test section roof produced no acceleration where,

$K \approx 0.0$, and $-5 \leq x/D \leq 60$, and

- it has been reported by Moretti and Kays [95] that for $K \geq 3.5 \times 10^{-6}$, complete relaminarization (reverse transition) of boundary layer flow takes place. Reverse transition is indicated by some existing features as, velocity profiles become laminar-like near the wall, and the laminar-sublayer thickness increases [96]. However, this does not imply that reverse transition exhibits a sudden change in the mean properties of the boundary layer flow but rather, a smooth progression [97]. Examination of the velocity profiles in Fig. 6.2 suggests that acceleration has thickened the viscous sublayer at $K=5 \times 10^{-6}$ particularly far downstream. Nevertheless, shape factors determined from the velocity profiles suggest that the boundary layer is still turbulent (Fig. 6.2). It

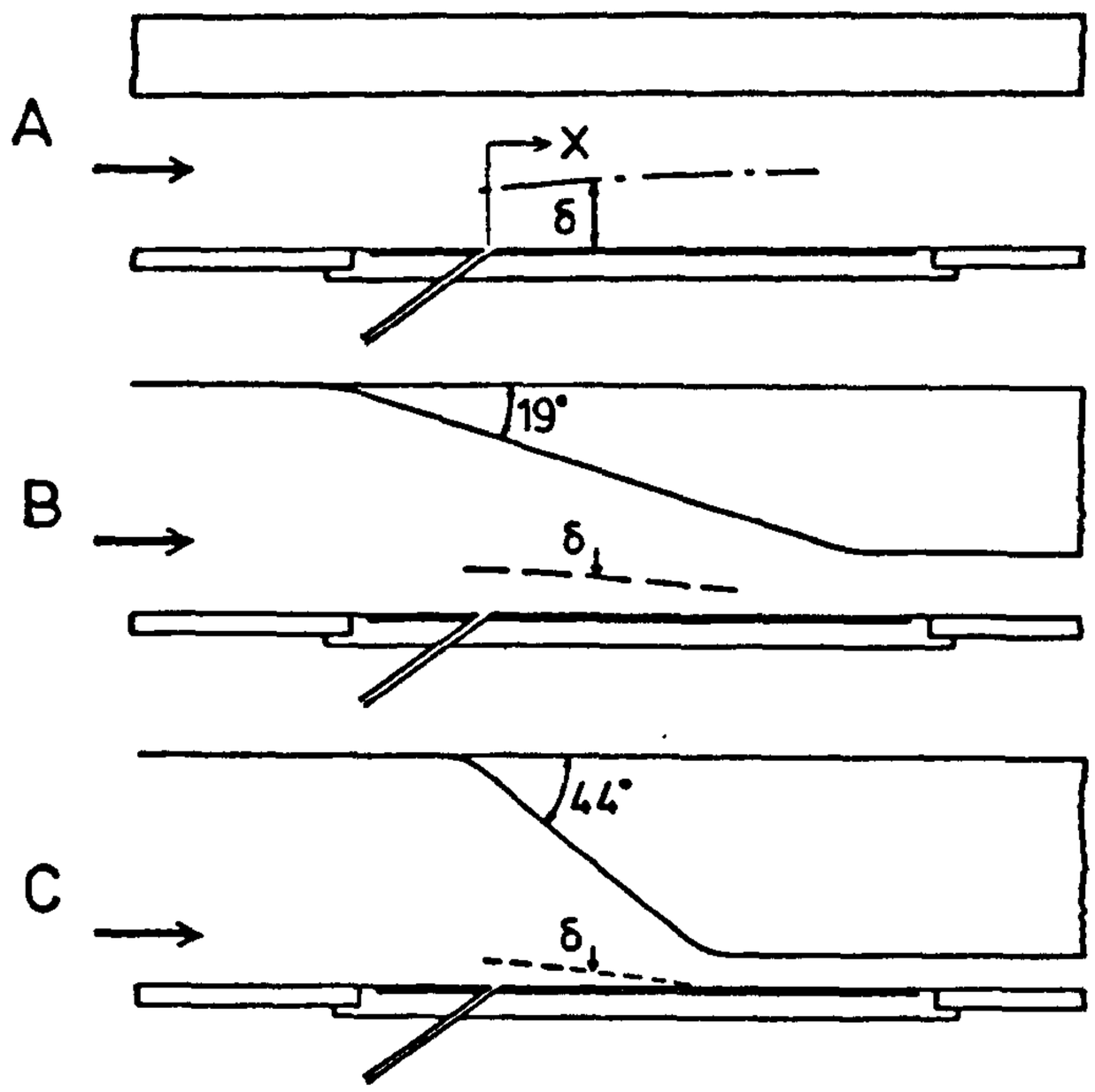

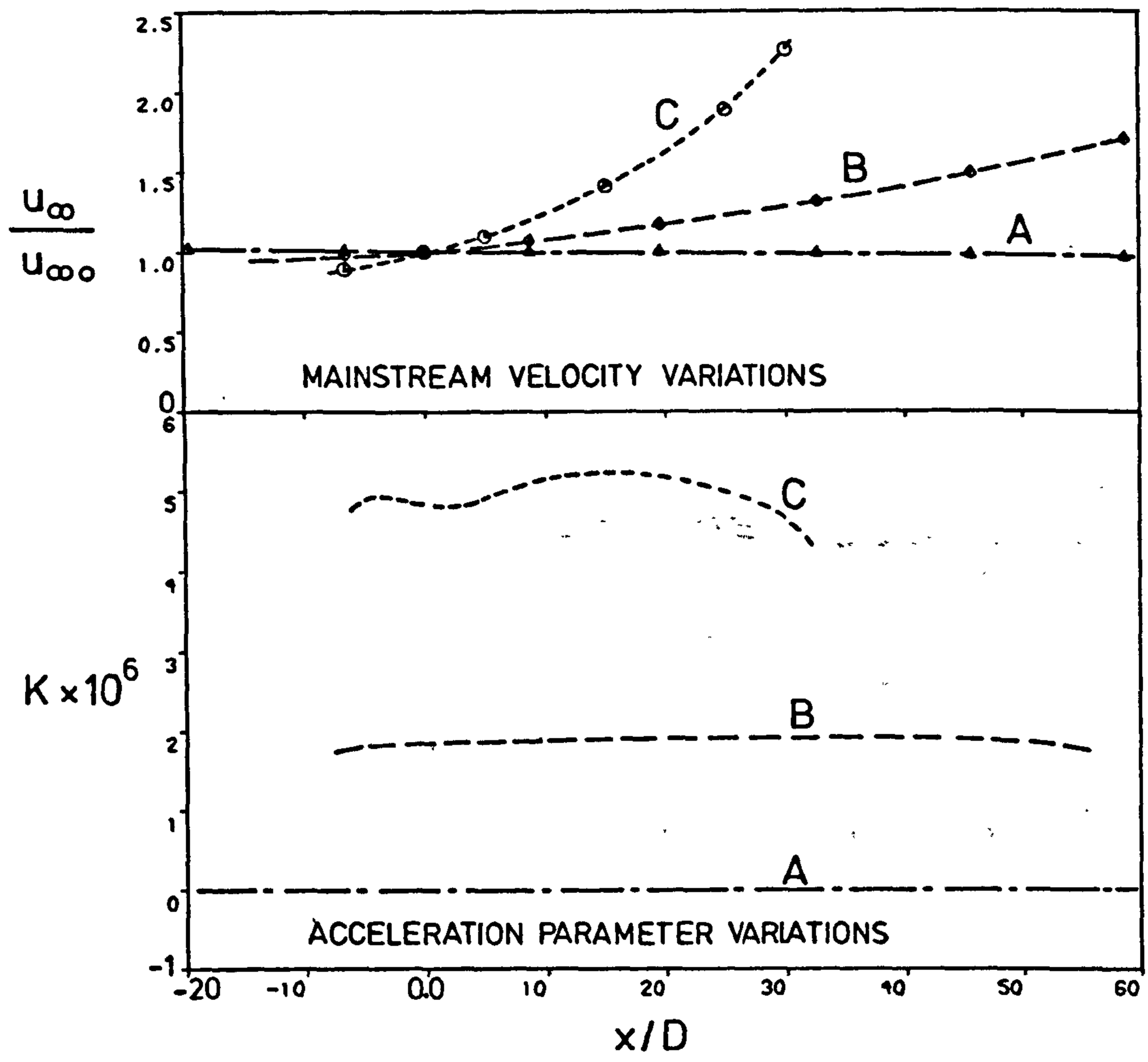

$\frac{u_\infty}{u_{\infty o}}$

$K \times 10^6$

Fig. 6.1 Variation of mainstream velocity and acceleration parameter in absence of injection.

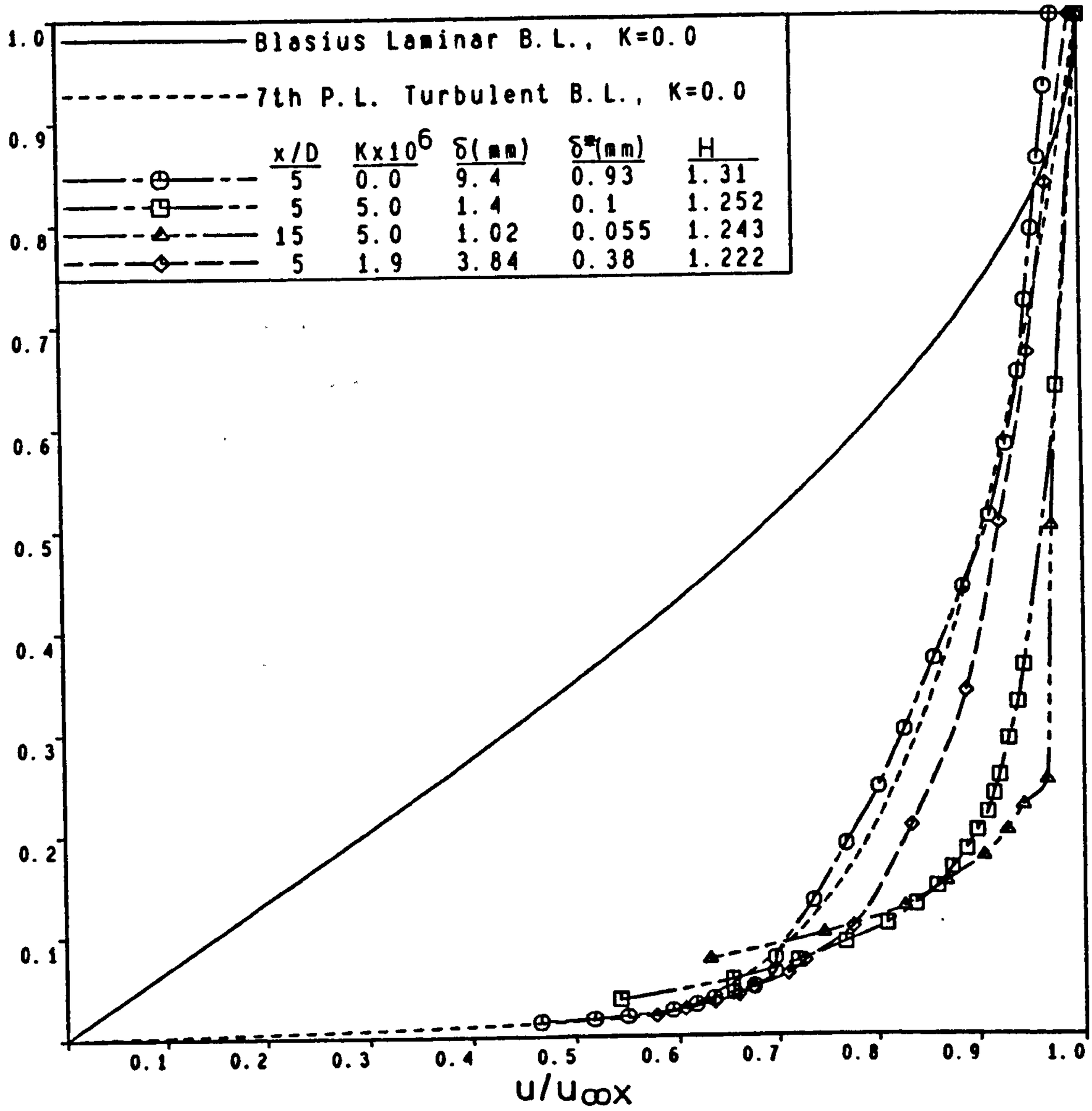

Fig. 6.2 Velocity profiles in absence of injection.

seems that the short distance (x/D up to 30) subjected to the constant K of $5x10^{-6}$ was not long enough to allow the full effect of acceleration in relaminarizing the flow.

6.3 EXPERIMENTAL PROCEDURE

The experimental procedure is best given by a sequential description of the process by which the heat transfer coefficient was measured.

Prior to this, pressure gradients had to be set, and boundary layer measurements had to be made.

6.3.1 Setting of the Pressure Gradients

For the zero pressure gradient case, the flat roof contour was positioned parallel to the test section floor, and adjusted until a uniform pressure was indicated by the floor pressure tappings.

For any of the two favourable pressure gradient cases, the adjustment was carried out while the mainstream velocity at the injection point was about 25m/s. At first, each contour roof was set at a position, the mainstream velocity at different downstream locations was measured, and the acceleration parameter was then calculated. Iterative adjustments of the roof then followed until the desired acceleration parameter was reached.

Once the correct setting of a roof was obtained, it was locked at that position. All of the tests required for that particular pressure gradient were then carried out before changing that roof.

6.3.2 Boundary Layer Measurements

The flattened tip pitot probe was employed to measure the velocity profiles in absence of injection for the zero pressure gradient case as the boundary layer thickness was relatively large. The hot wire probe used to measure the turbulence intensity and the velocity profiles with and without injection was employed in all of the pressure gradient cases.

Both probes were introduced to the flow in the same manner as described in chapter 5. The groove along the roofs' centreline allowed velocity surveys to be made in the streamwise direction. Off centreline holes allowed checking of the lateral uniformity of the mainstream.

The pitot probe was raised from the floor surface towards the bulk of the flow in small steps using the micrometer. An ohmmeter indicated the contact of the pitot probe with the tunnel floor. The hot wire probe was lowered from the mainstream towards the surface until the velocity measured was considerably less than that of the mainstream, or until the wire touched the surface and broke.

Frequent calibration of the hot wire was necessary, normally before and after each set of measurements. Calibration over the range of velocities encountered in the boundary layer measurement was accomplished using the pitot probe as reference.

The boundary layer displacement and momentum thicknesses were calculated from the velocity profiles using the trapezoidal rule.

6.3.3 Test Preliminaries

The wind tunnel was set at the required velocity of 25m/s and the stagnation point set at the lip of the bleed slot.

The electric heaters were switched on and controlled so that the temperature of both the wind tunnel and the holographic laboratory set at around 27°C.

The holographic table was then prepared: jacked up and levelled; the reference and object beams of the laser light adjusted, and the supply to the air-gauge was turned on and adjusted.

Before a test was actually conducted, a waiting time of about two to three hours was required to allow the tunnel test section, test plate, injection system and the holographic table warm up and reach steady, isothermal conditions.

6.3.4 Test Procedure

After it was ascertained that the operating conditions were uniform and isothermal, the test was carried out in the following sequence,

The test plate was removed from the swelling agent bath, dried, and taken to the holographic table for taking the initial exposure. The test plate was then mounted properly on the kinematic support on the holographic table.

The air-gauge assembly was placed carefully on its kinematic bracket and the probe tip was adjusted at the correct distance from the coating surface using the micrometer. After the back pressure measured on the manometer was noted, the probe assembly was removed gently.

The lights were then switched off and an unused photographic plate was placed and secured in its holder on the holographic table with the emulsion side facing the test plate. The photo-plate was then exposed to both the object and reference beams for 15 seconds, after which it was covered by the light-proof box and a polythene cover.

Afterwards, the test plate was taken to the wind tunnel, spring clamped in position and its injection tubes connected to the injection system. The swollen polymer coating was then exposed to the mainstream air and injectant flows for a period between 10 and 20 minutes (normally 12 minutes) which was inside the "constant rate period". During that period the temperature was noted at minute intervals and the injection flow rate required was checked and adjusted if necessary.

The test plate was removed from the tunnel test section and returned to the kinematic support on the holographic table for the final exposure. The half-exposed photo-plate was uncovered carefully and exposed to both the object and reference beams for another 15 seconds. After that the photographic plate was removed from its holder and placed in a light tight box emulsion side up.

With the lights switched on, the air-gauge was replaced on its kinematic bracket and the second air-gauge back pressure manometer reading was noted. Then the test plate was put back in the swelling agent bath to be ready for

the next run (at least 3 hours were allowed for the polymer to reach equilibrium swelling).

The exposed photo-plate was then developed in a darkroom, after which it was repositioned in its holder on the holographic table and illuminated with the reference beam only. The interference fringes superimposed on the holographic image of the test plate were then photographed using a conventional camera. The image printed plus the air-gauge pressure readings were then analysed and processed as outlined in the following section from which the recession, and the heat transfer coefficient, at the entire polymer test surface were determined for that particular run.

The major steps of the test procedure can be summarized as shown in Fig. 6.3. A step by step description of the test procedure is given in [82].

6.4 REDUCTION OF THE EXPERIMENTAL DATA

The local mass transfer coefficient, h_m, from the "film cooled" surface as measured with this technique is equivalent to the heat transfer coefficient, h, measured on an isothermal wall.

The local mass transfer coefficient at any point on the "film cooled" surface is evaluated from equation 6.1 (analogous to equation (1.2)),

$$m'' = h_m (C_w - C_{iw}) \qquad \text{- - - (6.1)}$$

where m" is the mass flux and C_{iw} is the concentration of the swelling agent vapour (n-tetradecane) at an impermeable wall with the same mainstream conditions. As in the case of the heat transfer coefficient, h_f, the mass transfer coefficient h_m is a function only of the flowfield.

In a similar manner to the adiabatic wall effectiveness η_{aw}, eq. (1.3), a mass transfer effectiveness, η_{iw}, based on the impermeable wall concentration [9] is defined as,

$$\eta_{iw} = (C_{iw} - C_\infty)/(C_e - C_\infty) \qquad \text{- - - (6.2)}$$

where C_e is the concentration of the swelling agent vapour in the coolant.

Combining equations (6.1) and (6.2) and eliminating C_{iw}, yields,

$$m'' = h_m [(C_w - C_\infty) - \eta_{iw} (C_e - C_\infty)] \qquad \text{- - - (6.3)}$$

SEQUENCE OF EXPERIMENT

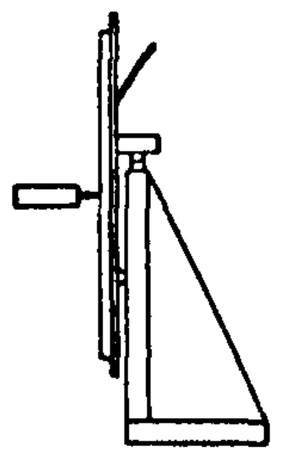

- AIR-GAUGE READING (P1) OF SWOLLEN COATING IS TAKEN AT A REFERENCE POINT

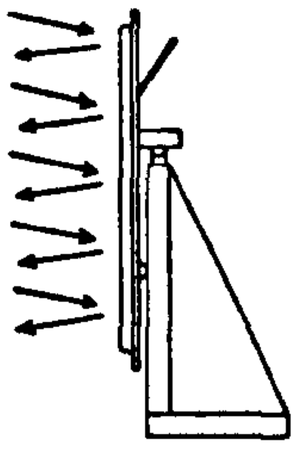

- HOLOGRAM IS FORMED ON A PHOTOGRAPHIC PLATE OF INITIAL STATE OF POLYMER COATING

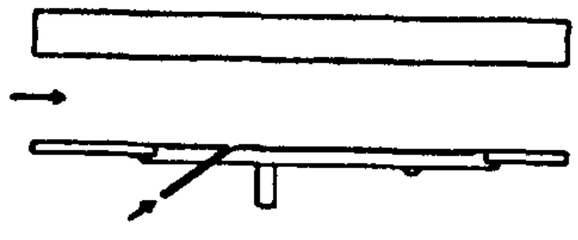

- SWOLLEN POLYMER SURFACE IS EXPOSED TO MAINSTREAM AND COOLANT FLOWS IN THE WIND TUNNEL

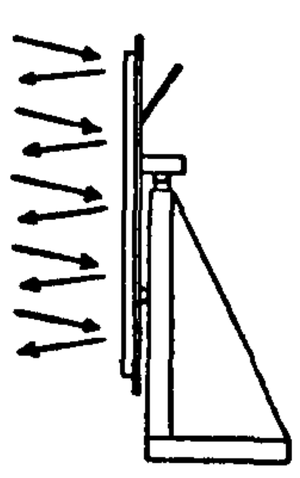

- HOLOGRAM IS FORMED ON THE SAME PHOTO-PLATE OF FINAL STATE OF THE POLYMER COATING

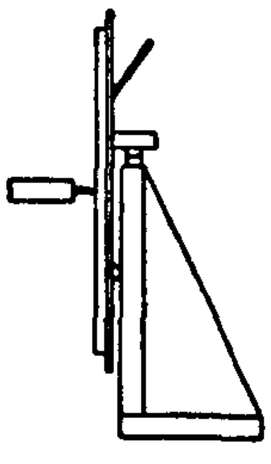

- AIR-GAUGE READING (P2) IS TAKEN AT THE SAME POINT

- THE PHOTO-PLATE IS DEVELOPED AND THE INTERFERENCE FRINGES SEEN WHEN ILLUMINATED BY THE REFERENCE BEAM ARE PHOTOGRAPHED

- THE PRINTED IMAGE OF INTERFERENCE FRINGES IS ANALYSED FOR WHICH:

  RECESSION $\propto$ FRINGE ORDER $\propto$ (P1-P2)

AND, THE MASS TRANSFER COEFFICIENT,

$h_m \propto$ RECESSION

Fig. 6.3 Sequence in a swollen polymer technique experiment.

With the concentration of n-tetradecane in the mainstream and the coolant being equal to zero, i.e. $C_\infty = C_c = 0.0$, equation (6.3) reduces to,

$$m'' = h_m C_w \qquad \text{- - - (6.4)}$$

Since m'' also $= \rho_\infty \delta / t$, eq. (4.3), then,

$$h_m = (\rho_\infty \delta)/(C_w t) \qquad \text{- - - (6.5)}$$

where δ is the coating recession under the film.

The vapour pressure of n-tetradecane over the polymer coating swollen to equilibrium, P_s, needed for the determination of C_w is correlated over moderate temperature ranges using a Clapeyron equation [93],

$$\log P_s = 10.702 - 3738.01/T \qquad \text{- - - (6.6)}$$

here T is temperature in Kelvin.

With the molecular weight of n-tetradecane, $M_s = 198.39$, C_w can be calculated at any temperature from equation (4.5).

The density of the swollen polymer ρ_∞ is calculated from equation (4.6), knowing that ρ_s for n-tetradecane = 0.765 g/cm^3, ρ_c for silicone rubber RTV615 = 1.02 g/cm^3, and the mass fraction of n-tetradecane in RTV615 [93] = 0.378.

The measurement of the coating recession δ is further needed to determine h_m. Evaluation of δ is achieved using equation (4.7) if the following are known:

- the laser light wavelength = 632.8 nanometres;
- the illuminating angle i_1 and the viewing angle i_2. For the current optical setup, $i_1 = 16.5°$, and $i_2 = 19°$;
- the refractive index of the swollen polymer N, and
- the fringe order, n.

The refractive index N is evaluated reasonably accurately by [83],

$$N = N_s v_s + N_c (1-v_s) \qquad \text{- - - (6.7)}$$

where N_s is the refractive index of swelling agent (n-tetradecane) = 1.428, N_c is that of the coating = 1.406, and v_s is n-tetradecane volume fraction in the swollen coating (=0.333 [93]).

The recession using the current optical setup then becomes,

$$\delta = 0.3693\ n \quad \text{microns} \qquad \text{- - - (6.8)}$$

The fringe order n at a reference point is determined by the absolute recession measured at that point using the air-gauge. From the slope of the linear range of the calibration graph in Appendix B (=1.2995 microns/mm H_2O),

$$\delta = 1.2995\ (P1 - P2) \quad \text{microns} \qquad \text{- - - (6.9)}$$

where P1 and P2 are back pressure readings of the air-gauge manometer before and after exposure of the swollen coating to the tunnel flows respectively, in mm H_2O.

From equations (6.8) and (6.9) we have,

$$n = 3.52\ (P1 - P2) \qquad \text{- - - (6.10)}$$

As has been noted earlier in chapter 4, once n at one point of the surface is determined the fringe order at the whole surface is identified, and δ can be evaluated at all points on the surface using equation (6.8).

The local mass transfer coefficient h_m at any point of the film cooled surface is then obtained, using equation (6.5).

The "heat" transfer coefficients in this research are presented as ratios, so that the heat transfer coefficient with injection, h, to that without, h_o, is equivalent to the mass transfer coefficient with injection, h_m, to that without, h_{mo}.

Since the mainstream flow is two-dimensional, the ratio h_m/h_{mo} is obtained from the same interferogram, that is h_m from a location influenced by the film and h_{mo} from the same downstream location at regions not influenced by the film. In this way both coefficients are obtained at the same operating temperature (i.e. same C_w) and time t. Thus, by applying equations (6.5) and (6.8) we get,

$$\frac{h}{h_o} = \frac{h_m}{h_{mo}} = \frac{\delta}{\delta_o} = \frac{n}{n_o} \qquad \text{- - - (6.11)}$$

where δ_o and n_o are the coating recession and fringe order at regions not influenced by injection.

Lateral average heat transfer coefficients normalized by their corresponding no-injection values, $\bar{h}/h_o$, were obtained by numerically

integrating the local coefficients or the fringe order across half the pitch as follows,

$$\frac{\bar{h}}{h_o} = \frac{1}{(s/D)/2} \int_0^{(s/D)/2} \frac{h(x/D,z/D)}{h_o(x/D)}\, d(z/D)$$

In the present work, h is measured from a constant and uniform wall concentration, and absence of the mass-transferring agent from both the mainstream and the coolant flows gives an equivalent condition to the temperature parameter $\theta = 0$. The measured heat transfer coefficient, h, corresponds, therefore, to that measured using the adiabatic wall approach, h_r.

6.5 CONSISTENCY AND REPEATABILITY OF RESULTS

After the technique had been improved, in particular the control of temperature, success in attaining good quality holograms was high. In measurements of similar pertinent film cooling parameters, consistency of the results was excellent. For example, interferograms number 171, 172 and 173 displayed in Fig. 6.4 correspond to normal injection of air at a blowing rate of 2.0. The operating temperature was controlled at 27°C for all of the tests, and the test duration was 14 minutes for the tests number 171 and 172 while it was increased to 16.5 minutes for the test number 173. As can be seen in Fig. 6.4, the pattern and number of constant-recession contours under the film are remarkably identical in tests 171 and 172. Furthermore, the fringe order number as measured by the air-gauge was also similar. Both the number of contours and fringe order are greater in test 173. In similar tests, the number of contours in the double-exposure holograms increased or decreased depending on the operating temperature and test duration, and increased as either or both increased. However, the values of the local heat transfer coefficient ratio, h/h_o, did not differ by more than 3 percent as shown in Fig. 6.5, where the ratio h/h_o of tests 171 and 173 are plotted in contour format. Test 172 is excluded as its data is identical to that of test 171. The small difference observed in the values of h/h_o at a location is attributed to fringe order identification using the air-gauge since the trends are very similar.

Mention should also be made that, during a test, good replacement of

Grid Spacing = 5D

Test Number 171

u_∞ ⟶

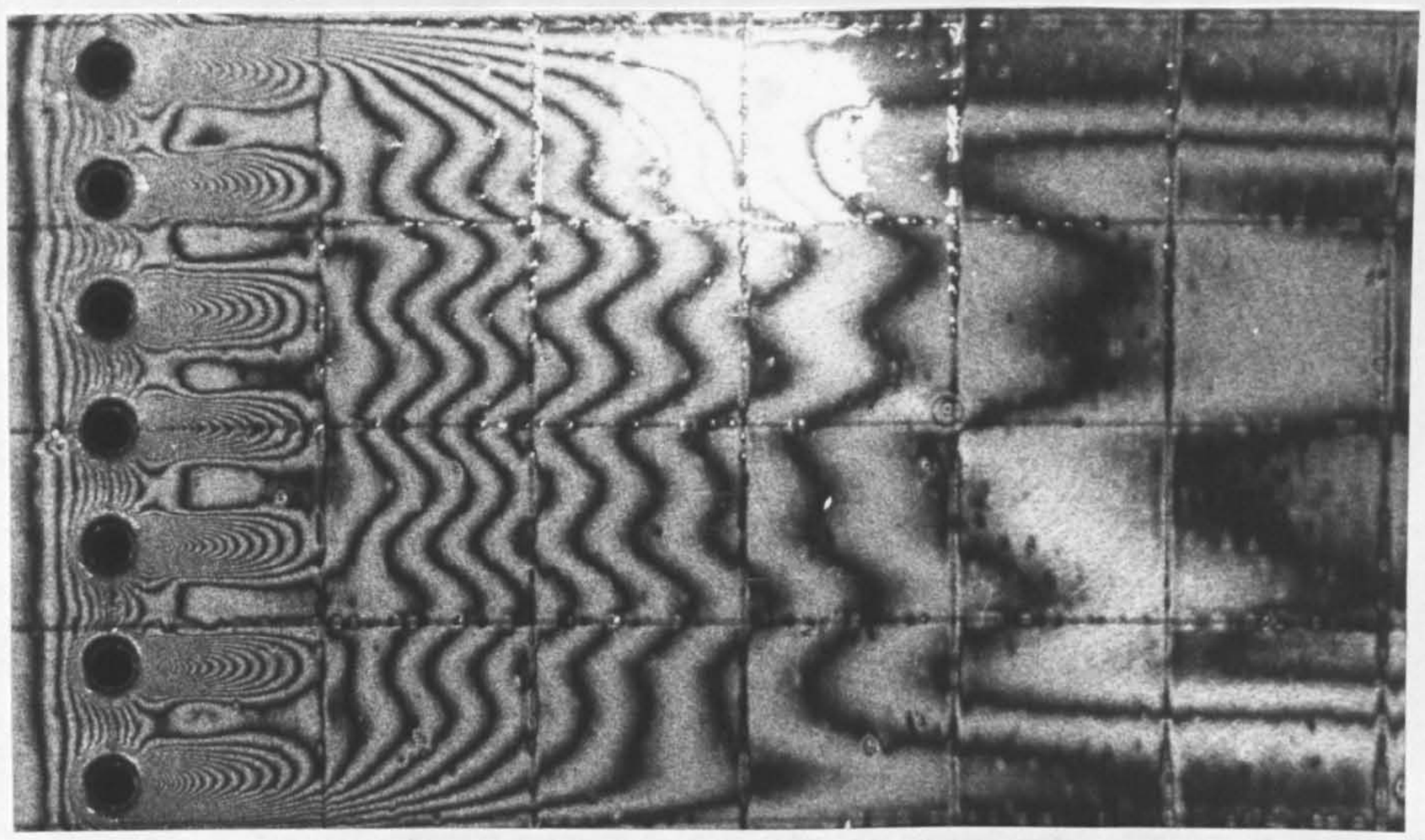

Test Number 172

u_∞ ⟶

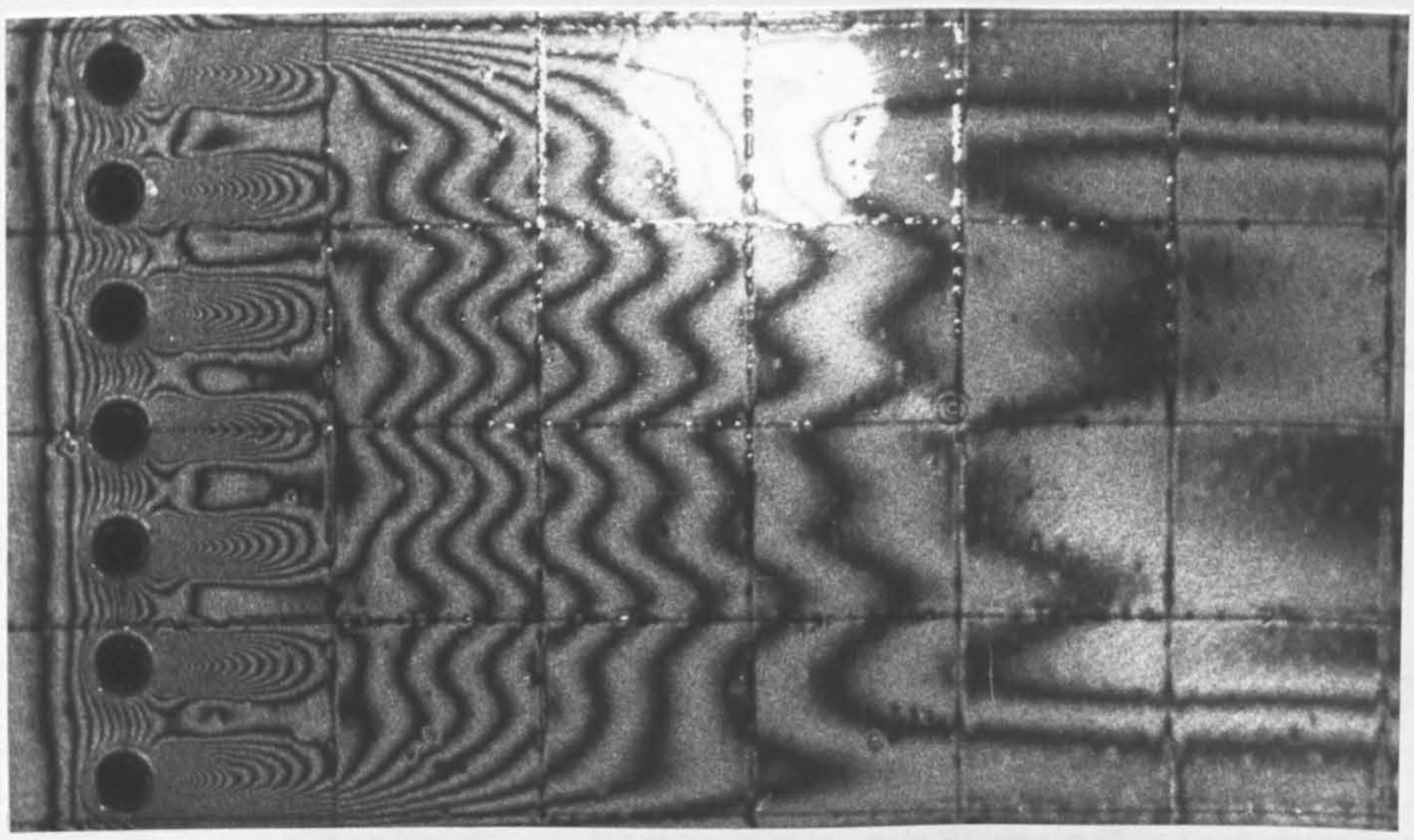

Test Number 173

u_∞ ⟶

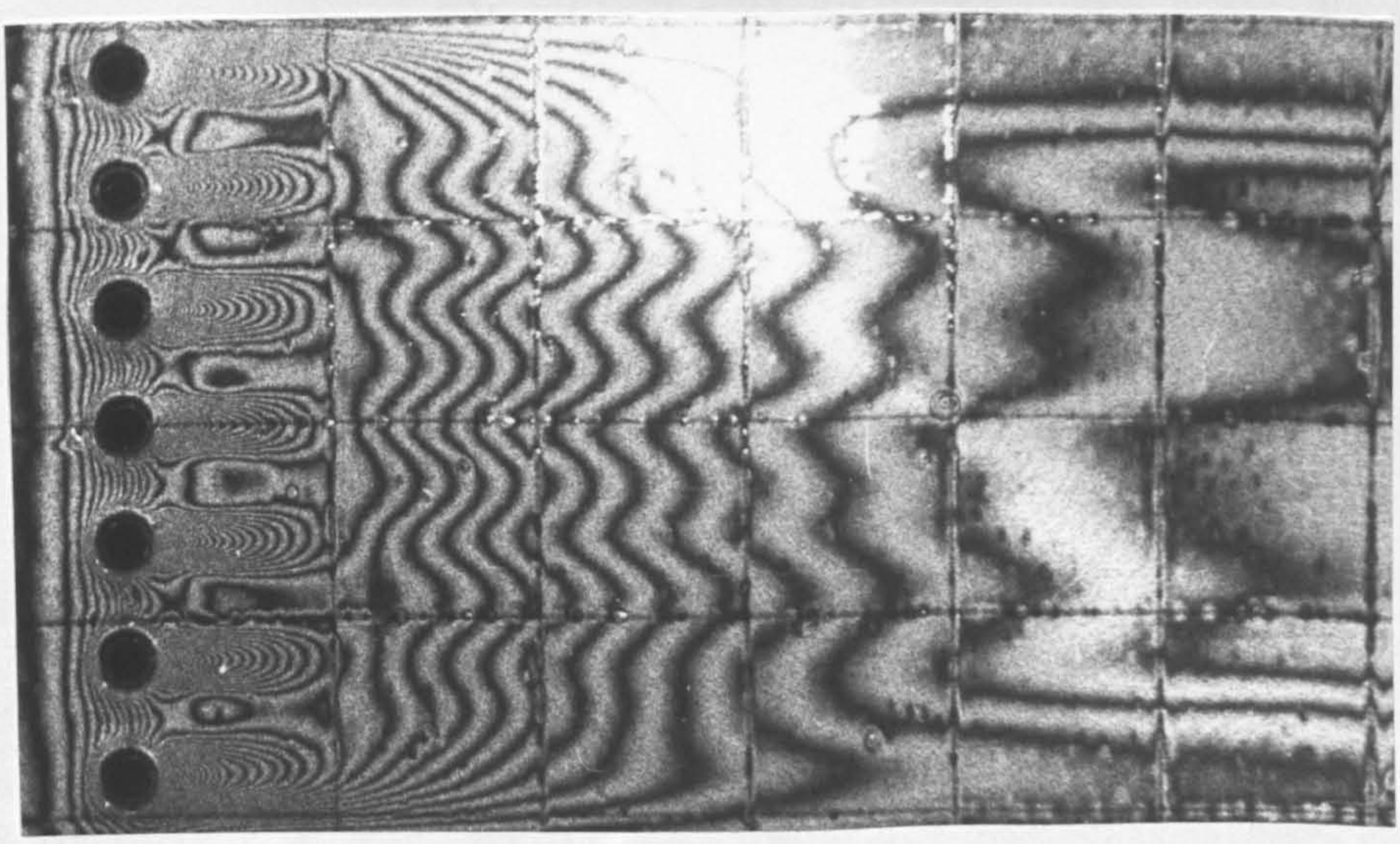

Fig. 6.4 Interferograms depicting contours of constant mass transfer coefficients of normal air injection at M=2.

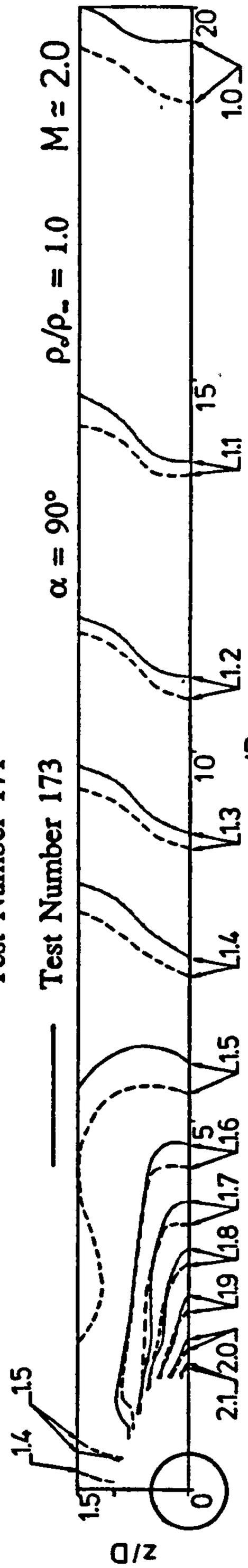

Fig. 6.5 h/h∞ contours downstream of injection through a row of holes.

both the test plate and the air-gauge on their kinematic mounts in addition to a good temperature control throughout is essential for acquiring excellent repeatability of the results.

Uncertainty analysis is carried out in Appendix D according to the method of Kline and McClintock [98]. The uncertainty on the heat transfer coefficient ratio with and without injection, h/h_o, is estimated to be ±4.0% in the nearfield (x/D<10) and ±5.0% in the farfield (x/D>10). The uncertainties associated with the lateral average heat transfer coefficient, $\bar{h}/h_o$, are rather larger, ± 7.9% and ±9.4% in the near and farfields respectively. Uncertainty on the absolute mass transfer coefficient is within ±6.7%, so that the uncertainties on the ratios $\bar{h}_{MF}/\bar{h}$ and $\bar{h}_{SF}/\bar{h}$ in the presence of favourable pressure gradients are even larger at ±9.4% and ±8.2% respectively in the nearfield, and ±13.4% and ±12.4% respectively in the farfield, since the analysis was dependent on division of two averaged absolute heat transfer coefficient values.

CHAPTER 7

VALIDATION OF THE EXPERIMENTAL TECHNIQUE

Chapter 7 qualifies the experimental technique for the determination of the mass (heat) transfer coefficient, and presents and discusses the validation of the technique for the measurement of cooling film mass transfer coefficients at non-unity density ratios with foreign gas injection.

7.1 EXPERIMENTAL QUALIFICATION AT ZERO INJECTION

(i) Zero Mainstream Pressure Gradient

The accuracy of the technique for determining mass transfer rates was verified with a fully developed turbulent boundary layer without injection at zero mainstream pressure gradient. Measured mass transfer Stanton numbers were compared with a standard correlation for a flat plate mass transfer with a step change in surface concentration at a distance L from the virtual start of the boundary layer [99]. The Reynolds number in the correlation was based on the distance from the virtual origin of the tripped boundary layer as determined by extrapolation of the displacement thickness.

The experiments were performed with the hole in the test plate blocked to provide a smooth test surface. Stanton number measurements of three separate tests in addition to the standard correlation are shown in Fig. 7.1. The experimental results obtained show a good agreement with the established correlation within a scatter range of about ± 4.5 percent except for a region upstream of injection location, where the correlation overpredicts the experimental data by a maximum of 7 percent. The scatter band indicates the degree of uncertainty with measured absolute magnitudes inherent in the

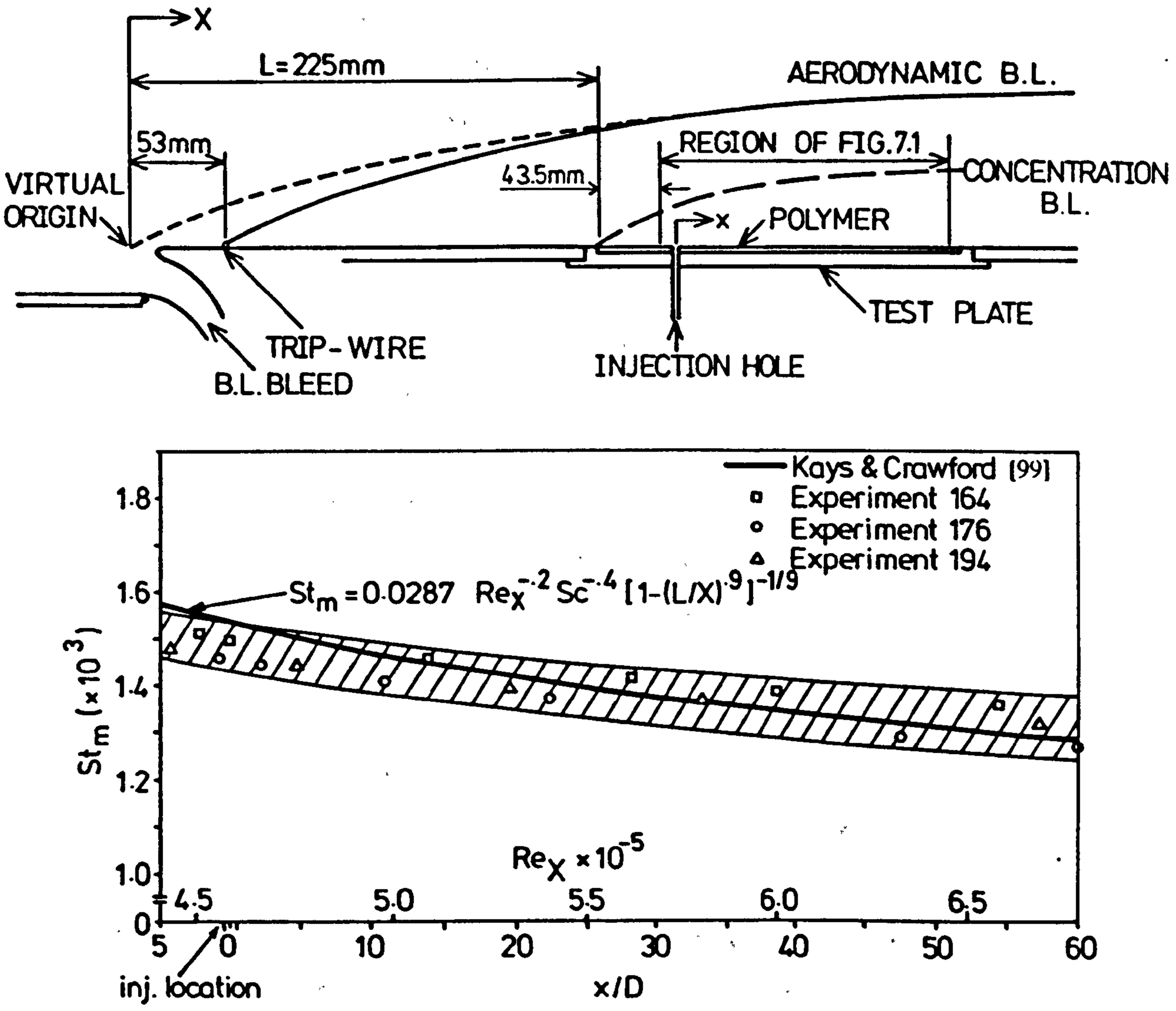

Fig. 7.1 Variation of Stanton number without injection in the streamwise direction.

technique.

(ii) Favourable Pressure Gradients

Experimental data on the heat transfer coefficient on a flat plate in the presence of mainstream acceleration at condition similar to those of the present work does not exist. However, the available data, in general, has shown the heat (mass) transfer coefficient to decrease by the influence of mainstream acceleration.

The strong influence of mainstream velocity acceleration on the mass transfer coefficient is indicated by Fig. 7.2 which shows the local coefficients, h_{m_o}, and the corresponding Stanton numbers, St_{m_o}, without injection. Also shown are the results of zero pressure gradient to provide a base line. Note that acceleration has depressed St_{m_o} below the constant velocity values, with the magnitude of the depression increasing as the acceleration parameter, K, increases. As for the mass transfer coefficient, the reduction at x/D=10 amounts to about 14% for the moderate favourable pressure gradient (case (B)) and 40% for the strong favourable pressure gradient (case (C)) of the zero pressure gradient values. The differences in h_{m_o} values are reduced to about 11% and 33% respectively at x/D=25. The slight recovery of h_{m_o} is due to the great acceleration of the mainstream. In case (C), h_{m_o} tends to decrease after the mainstream velocity returns to constant. The results are in agreement with the findings of Back et al [100] who have reported that heat transfer rates considerably below expected magnitudes for turbulent flow were found for levels of K above $2\text{-}3\times10^{-6}$.

In general, the reduction in the overall heat transfer rate by mainstream acceleration is attributed to the reduction in the generation of turbulent energy, leading to a decay of turbulence in the outer part of the boundary layer, and a consequent decrease in eddy diffusivity for heat transfer [96]. This is evidenced by the turbulence intensity profiles shown in Fig. 7.3. The intensity of turbulence is observed to be lower for the case with acceleration, and decreasing throughout the accelerated zone.

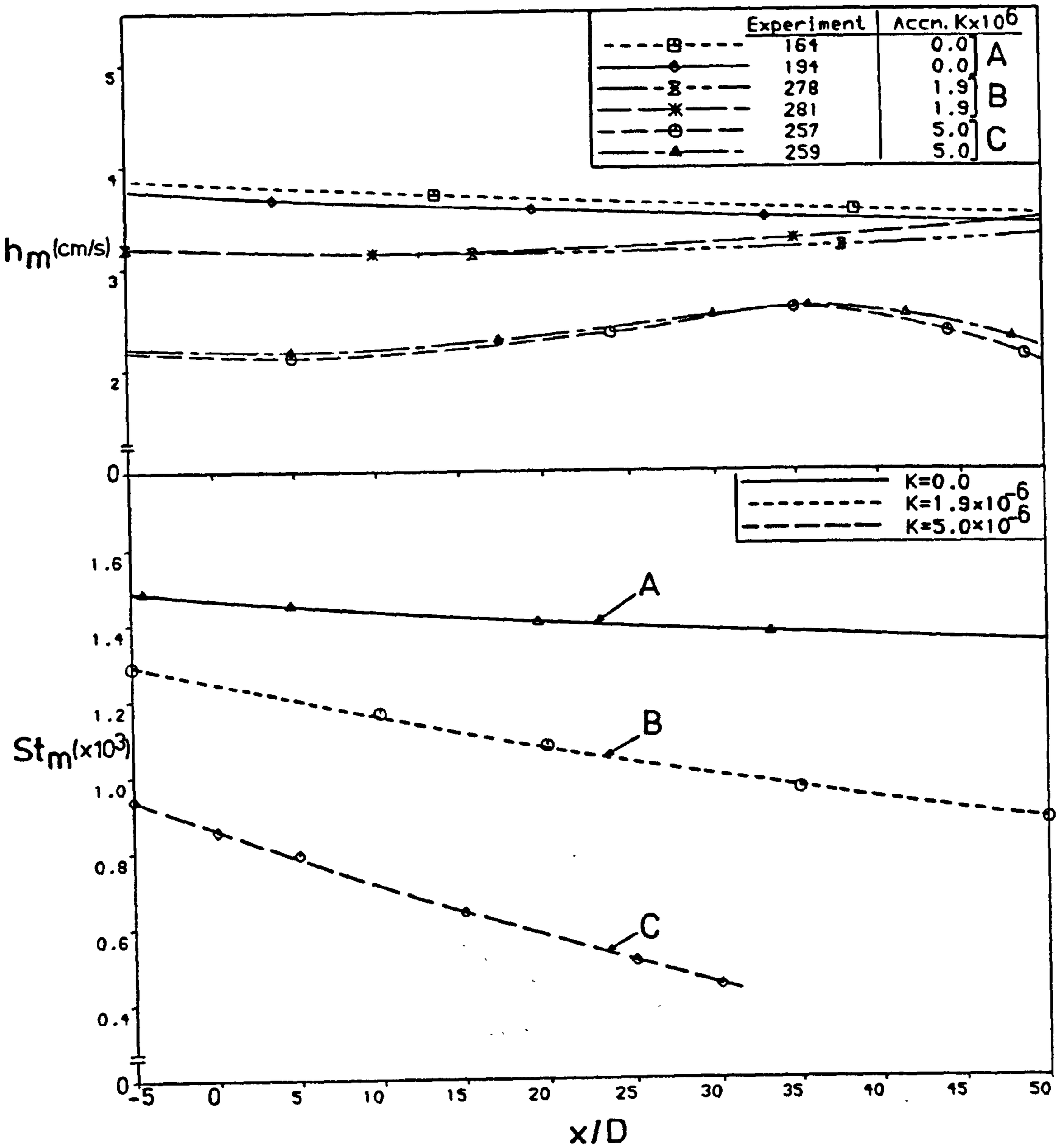

Fig. 7.2 Variation of mass transfer coefficients and corresponding Stanton numbers in absence of injection.

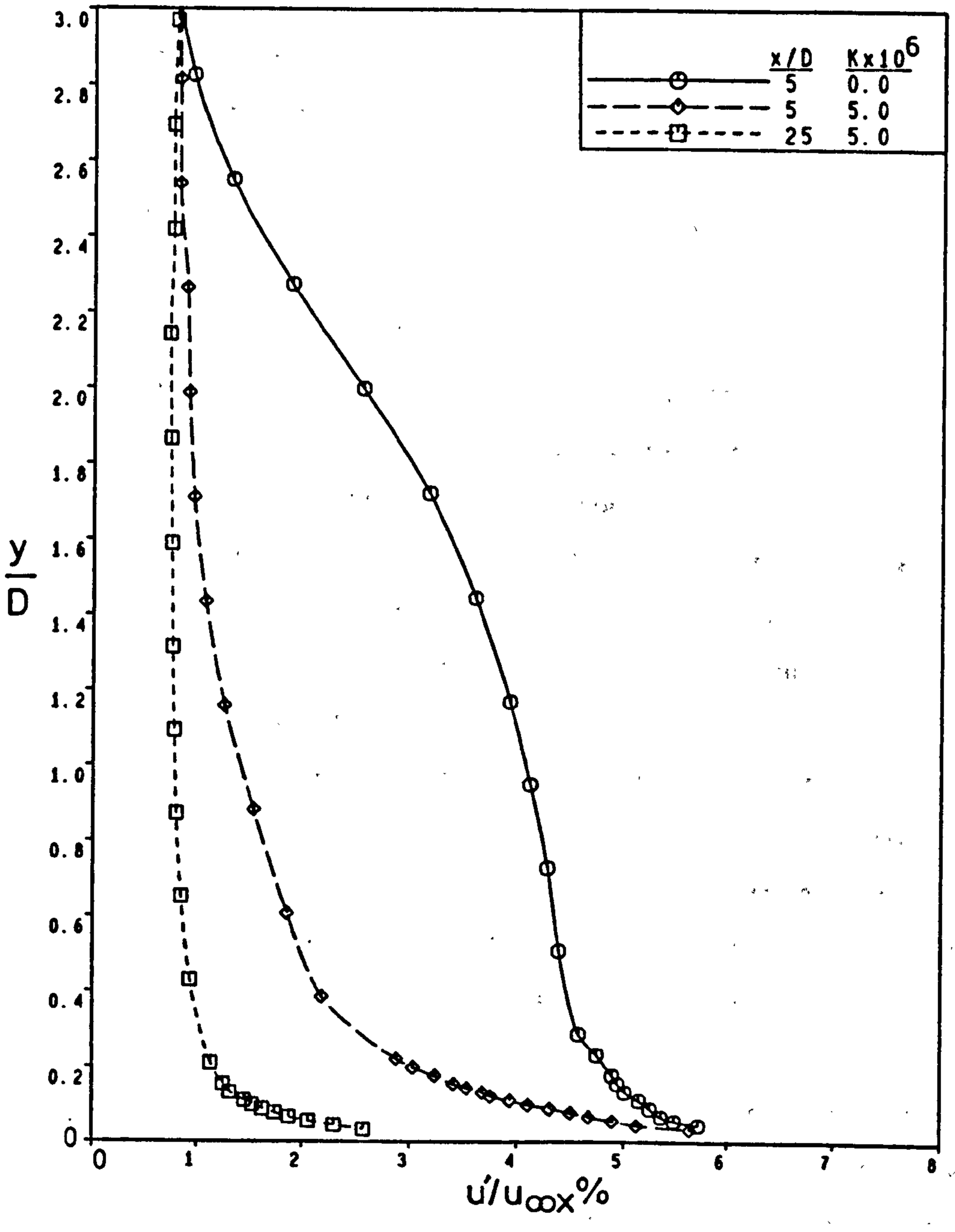

Fig. 7.3 Turbulence intensity profiles without injection.

Apparently, the decrease observed in h_{m_o} has resulted from a combination of the effects of a thicker viscous sublayer and suppression of the generation of turbulence.

Mention should be made of the fact that, in all of the cases investigated, there were also differences in pressure gradient upstream of the injection location. These differences affected the approach boundary layer, and therefore will have influenced the variation of h_{m_o} to some degree.

7.2 EXPERIMENTAL VALIDATION AT NON-UNITY DENSITY RATIOS

7.2.1 Simulation of Density Ratios

The proper modelling of typical gas turbine engine operating conditions dictates a simulation where the coolant to mainstream density ratio is well in excess of unity. In the swollen polymer technique this is achieved by using as injectants foreign gases of higher densities than the mainstream. Concentration fields are taken to correspond to temperature fields, and mass transfer to heat transfer. As stated earlier in chapter 3, this is only strictly true if the ratio of the diffusivities of momentum and mass, the Schmidt number, in the model is the same as that of momentum and heat, the Prandtl number, in the "real" situation. Matching is rarely achieved in practice, and it is necessary to explore experimentally the consequences of this for each new application. The use of foreign gases in film cooling modelling introduces an additional complexity in that the local Schmidt number will vary according to the dilution of the injectant by the mainstream air.

In a cooling film, the bulk of the flow is turbulent, and only in the wall sublayer is molecular transport important. In measurements of adiabatic wall effectiveness, the mass transfer analogue requires an impermeable wall so that both the mass flux and the concentration gradient will be zero at the wall. Such measurements might be expected not to depend on Schmidt number.

When heat transfer coefficients are to be determined the flux and gradient at the wall are finite. The experimental work presented and discussed in this

section is therefore directed towards providing a systematic assessment of the effect of the variation of the molecular Schmidt number on the cooling film mass transfer coefficient. In consequence, the validation of the swollen polymer technique for the measurement of mass (heat) transfer coefficients at non-unity density ratio is addressed.

The experiments were conducted with the test plate having the single normal injection tube. The measurements were taken for a blowing rate of unity at zero mainstream pressure gradient. Experimental data on normal injection with a blowing rate of unity [21, & 22] has shown this to produce high heat (mass) transfer coefficients close to the injection location, so that any probable variation in the mass transfer coefficient due to Sc variation of injectant could be more easily measured.

7.2.2 Preliminary Considerations

On a film cooled flat surface under zero mainstream pressure gradient, the mass transfer coefficient, h_m, depends upon a large number of parameters. However, using a foreign gas injectant introduces the additional problem of property variations, the effect of which is investigated through Schmidt number variation. h_m may be expressed non-dimensionally as a function of these parameters,

$$h_m/h_{m_o} = h_m/h_{m_o}(M, I, Sc, Re, s/D, \alpha, Tu, \ldots) \quad - - - (7.1)$$

where h_{m_o} is the mass transfer coefficient without blowing.

The mass and momentum flux ratios M and I involve the effect of coolant to mainstream velocity and density ratios. For a fixed geometry, if the mainstream conditions are held constant together with the injectant velocity and density, the mass transfer coefficient, h_m, will only be a function of Sc. The effect of Sc can thus be examined experimentally.

Varying Sc in a film cooling experiment using the swollen polymer method can be accomplished via two routes; by changing the swelling agent alone, keeping the injection fluid the same, or by introducing different fluids while keeping the same swelling agent. In the analysis conducted on the

selection of potentially suitable swelling agents for use in film cooling tests, presented in chapter 4, n-tetradecane was found to be the most appropriate. It alone could be used at ambient temperatures for a considerable length of test time at relatively high rates of mass transfer such as occur on film cooled surfaces in regions close to injection location. Thus the first route for varying Sc was ruled out and the second was the only option open and so was used.

In order to vary Sc, mixtures of gases of different diffusivity mixed in volume ratios such that the density was the same were used. Thus in a film cooling context equal density and velocity ratios at fixed values of M and I can be obtained with different values of Sc. The mixtures of gases that were used as injectants were composed from light gases such as Helium and heavy ones such as Xenon.

7.2.3 Estimation of Schmidt Numbers

In the absence of experimental values of molecular Schmidt number for the diffusion of the swelling agent tetradecane in gases and gas mixtures, it was necessary to use empirical relations to predict Sc. In most cases, both the diffusion coefficient and the viscosity had to be calculated. Standard text book methods were used (e.g. [101]). Semi-empirical correlations based on consideration of the kinetic theory of gases and the Lennard-Jones potential of intermolecular forces, described by Brokaw [102], were used in the calculations of diffusion coefficients. An approximate formula based on simple mean-free path arguments cited by Brokaw [102] was used in the calculation of the viscosity of gas mixtures. Description of the correlations used is displayed in Appendix E. The formulae have been extensively tested [102] by comparison with experimental data involving many gas mixtures. The agreement was found to be generally quite good.

An experimental Sc value for tetradecane diffusing in air is given by Paterson et al [93] who performed open-tube experiments from which Sc was determined. The experimental value was 3.51 and the value predicted by the above calculation method was 3.53 thus confirming the accuracy of the

prediction formulae used.

The results of calculations of the Schmidt number of tetradecane in air and in various gas mixtures chosen to simulate various Sc values and density ratios to air are shown in Fig. 7.4. The results span the mixture and Sc ranges that could occur within a cooling film using the gas mixtures (shown in Table 7.1) as coolant. At exit from the cooling hole the Schmidt number is given by the values corresponding to zero mole fraction of air. As the coolant film is diluted with air so the Sc values shift to those for higher mole fraction of air.

7.2.4 Experimental Methodology

Two sets of validation experiments were performed. The first set (see Table 7.1) was intended to reveal the effect of the variation in coolant Schmidt number on the mass transfer coefficient at a density ratio of unity. The maximum difference in Sc between any two experiments was about 11%. The second set of tests (see Table 7.1) was conducted at a coolant to mainstream density ratio of about 1.38. The Sc variation was larger at about 28%.

The effect of moisture in the air was not taken into account in the above calculations of Schmidt number. If the moisture is taken into account the difference in Sc for the first set of tests would change typically to about 13.5%. The values for the second set of tests would not be affected.

7.2.5 Presentation and Discussion of Results

Stanton numbers based on mass transfer coefficients, h_m, measured at the sides of an interferogram in regions not affected by injection were found to fall within the shaded area of Fig. 7.1, indicating similar local Stanton number values as those obtained with the test surface exposed to the mainstream alone. This has permitted the direct calculation of the ratio of mass transfer coefficients with and without injection, h_m/h_{m_o}, from each hologram. When the results are presented in this way rather than absolute magnitudes of the coefficients, the effects of systematic errors, such as occur in the fringe order

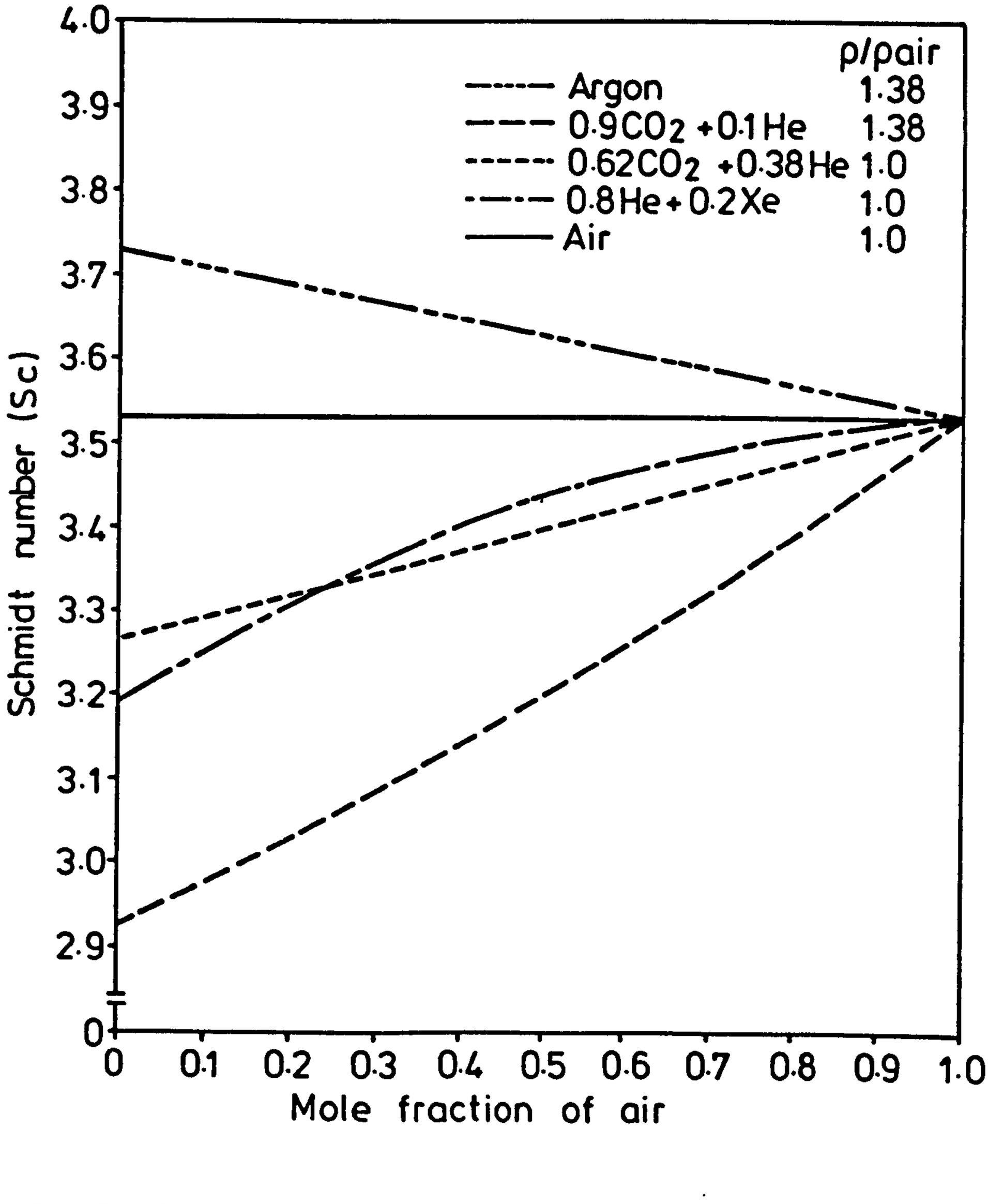

Fig. 7.4 Prediction of Schmidt number of n-tetradecane diffusing in various gas mixtures at 27°C.

Coolant	ρ_f/ρ_∞	Sc	Max. Diff. in Sc
20%Xe+80%He	1.0	3.17	
62%CO_2+38%He	1.0	3.27	11%
Air	1.0	3.53	
90%CO_2+10%He	1.38	2.93	28%
Argon	1.38	3.73	

Table 7.1 Schmidt number of n-tetradecane in air, gases and gas mixtures at 300 K and 1 atm.

identification used in the determination of the coating recession, are reduced.

Fringes in the first 1.5 diameters downstream of the injection location could not be resolved. Measurements within this region would require use of larger injection hole diameter.

For the first set of tests at unity density ratio (see Table 7.1), the Schmidt number was changed by a maximum of about 11% while maintaining the injectant density close to that of the mainstream air. Comparison of the normalized mass transfer coefficient distribution in the streamwise direction is shown in Fig. 7.5. The data are presented for five lateral positions covering all regions affected by injection up to 50 hole diameters downstream. The ratios of h_w/h_{ao} for the three tests do not differ by more than 3 percent at any point on the cooled surface. This is within the accuracy of the experimental technique.

In the second set of tests (see Table 7.1), using different gas mixtures, the density ratio was set to 1.38, and the Schmidt number was varied by 28%. Referring to Fig. 7.6 at the centreline and half a diameter lateral positions the results are practically identical all the way downstream. However, at positions one diameter off the jet centreline a maximum difference in h_w/h_{ao} of approximately 7.5% is noticed near the injection location, whereas at the 1.5D and 2.0D lateral positions smaller differences in the mass transfer coefficient ratio are observed. Although the differences in h_w/h_{ao} at a few lateral positions in this case are a little higher than in the first set of tests with the smaller Sc variation, in general these differences are quite small. As a result, the comparison brings out the fact that molecular Schmidt number variations within the range investigated have a negligible effect on film cooled surface mass transfer rates. Consequently, the experiments have shown that the measurement of cooling film mass transfer coefficients at non-unity density ratios using the swollen polymer technique with foreign gas injection is not sensitive to the change in Sc and is a valid method. This conclusion is corroborated by the following considerations.

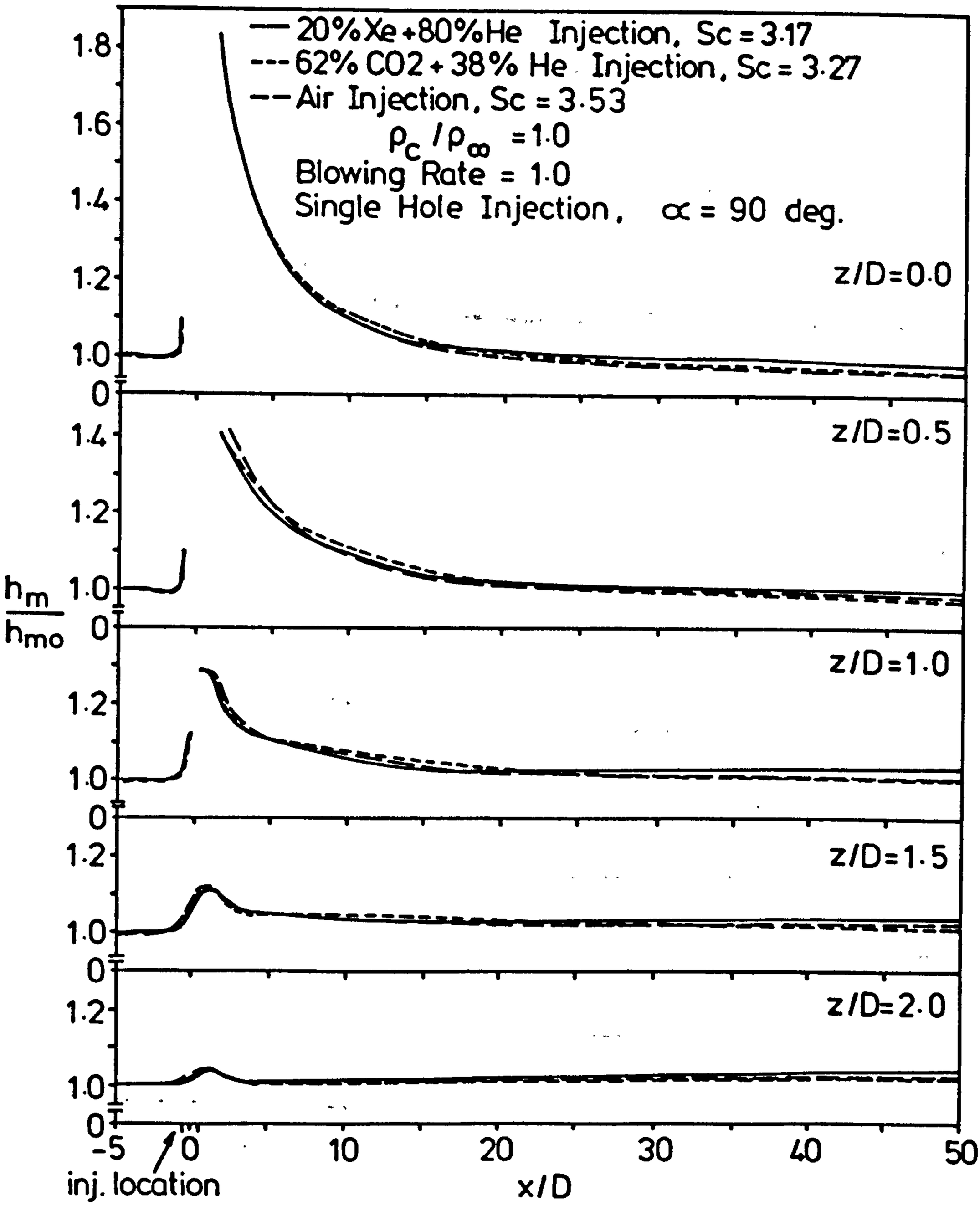

Fig. 7.5 Distribution of normalized mass transfer coefficient for foreign gas injection of equal density but different transport property.

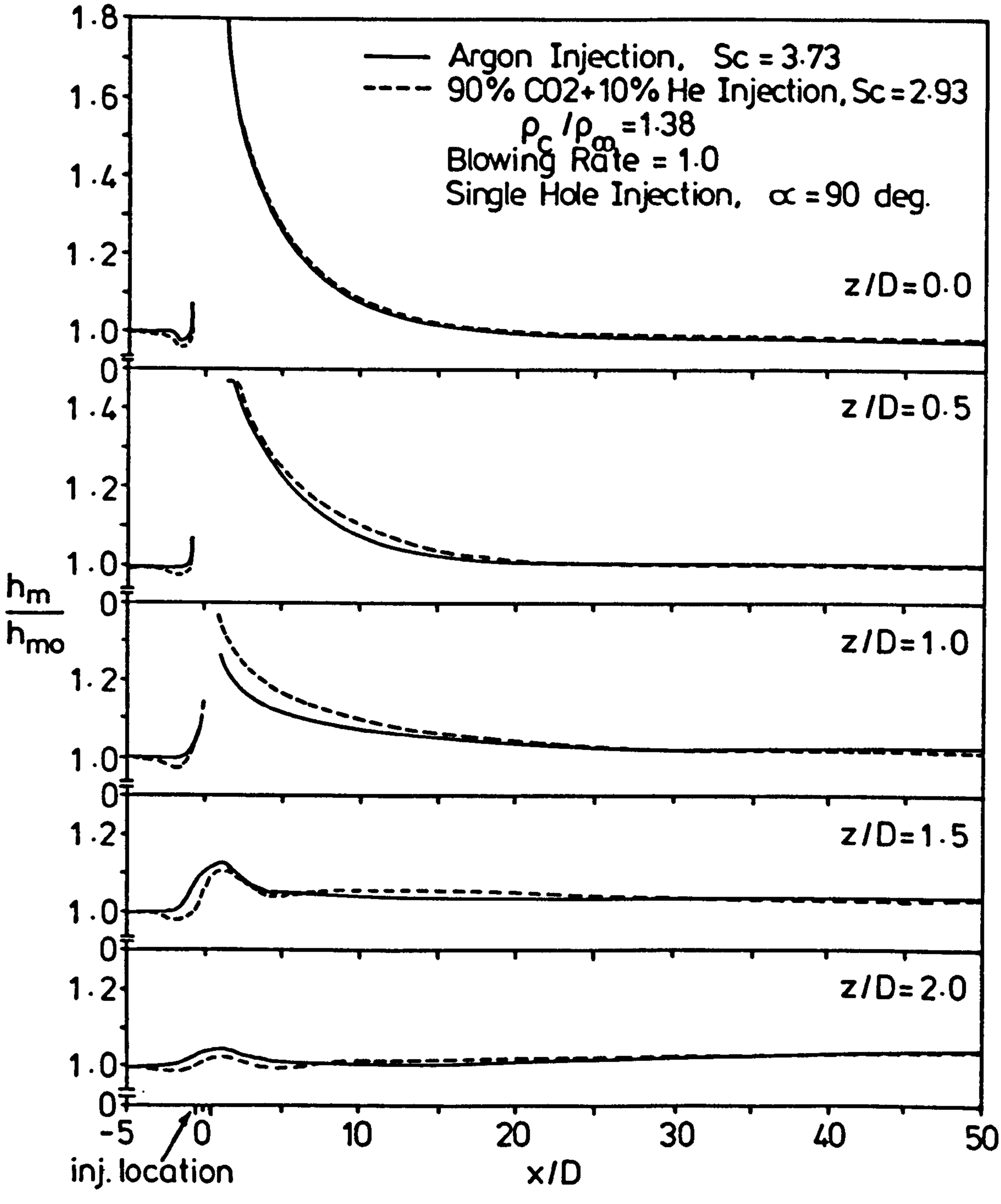

Fig. 7.6 Distribution of normalized mass transfer coefficient for foreign gas injection of equal density but different transport property.

It is generally acknowledged that in convective mass transfer the Stanton number representing the mass transfer coefficient is, to a good approximation, proportional to the power -0.4 of the molecular Schmidt number. But, in the case of film cooling, the relation between Stanton number and Sc is not known. However, if a relation somehow similar to the relation without blowing in regard to Sc is assumed to hold for the film cooling situation, a change in the mass transfer coefficient of about 10 percent at any point on the surface would be expected for a 28 percent variation in Sc. This is so assuming 100% jet fluid is in contact with the surface. But, practically, jet dilution by the mainstream air results in low local jet concentration in most of the flowfield and hence reduced effect of jet Sc.

It is well established that turbulent contribution to mass transport is generally greater than laminar contribution. Injection into a mainstream increases the level and scale of turbulence due to mixing and interaction between the jet and the mainstream [19]. Pedersen [41] found experimentally that injectant molecular Sc had no effect on the downstream wall concentrations for injection through a row of holes. For the injection velocities used in this work, the jets will be detached from the surface and intense turbulent mixing will result. It is thus understandable that a variation of Sc by 28 percent does not have a significant effect on mass transfer coefficients from film cooled surfaces, as demonstrated experimentally above.

Recently, Teekaram et al [36] have conducted thermal film cooling tests using air or CO_2 injectants in an isentropic piston tunnel facility. The row of cooling holes were inclined at 30° as against 90° in the present tests. Their conclusion also was that the gas species did not affect the results obtained and that foreign gas injection can be used to simulate density ratio effects.

7.3 CONCLUSIONS

The experimental method has been qualified for the determination of mass transfer coefficients.

The effect of molecular Schmidt number on the cooling film mass transfer coefficient is negligible for the range of Schmidt numbers examined. Therefore the method of measurement of mass transfer coefficients from film cooled surfaces at non-unity coolant to mainstream density ratios, using the swollen polymer technique with foreign gas injection has been validated.

The experimental film cooling data of the current work are for both air and carbon dioxide injection. The maximum difference in Sc of the injectants is about 21%, which is within the 28% Sc difference examined here.Therefore, the influence of Sc variation between air and carbon dioxide on the measured mass transfer coefficients is neglected.

CHAPTER 8

DISCUSSION OF EXPERIMENTAL RESULTS

In this Chapter representative sets of results from the current experimental programme are presented for analysis and discussion.

The presentation and discussion of the results concentrates on two main bodies of information, the effect of coolant to mainstream density ratios and the effect of mainstream acceleration on the cooling film heat transfer coefficient.

8.1 PRESENTATION OF RESULTS

The results are presented as ratios of local heat transfer coefficients with and without injection, h/h_o. Some are presented as contour plots derived from large numbers of data points read from the interferograms. Individual fringes could not be properly resolved in the first one or two diameters downstream of the holes so contours are not shown there. The plots terminate at 20 diameters since, beyond this point, h/h_o changes very slowly, and is close to unity anyway, for all but the highest blowing rate.

Some of the results are also presented as laterally averaged heat transfer coefficients normalized by the coefficients without injection, $\bar{h}/h_o$.

As noted earlier, in the presence of favourable pressure gradients, the mainstream velocity at the injection location was about 25m/s, i.e. the same as that for the zero mainstream acceleration case. The blowing rate, M, given in the results presented hereafter is related to that local mainstream velocity.

Results are also presented in terms of the ratio of laterally averaged heat (mass) transfer coefficient under the film in the presence of the favourable pressure gradient to that with zero pressure gradient conditions at the same location and blowing rate. In this way, the factor by which the heat transfer

coefficient has been altered due to the imposition of a favourable pressure gradient is quantified.

It has been shown that, by changing the contour roof of the tunnel, for zero pressure gradient in the presence of injection, a large change in the approach boundary layer condition (from thick, turbulent to thin, transitional) produces no measurable change in the cooling film heat transfer coefficient [26]. It would seem logical to assume that the heat transfer coefficient under films injected into regions experiencing nonzero pressure gradients are similarly insensitive to approach boundary layer conditions. In the current work of the effect of mainstream favourable pressure gradient on the heat transfer coefficient, errors associated with different approach boundary layer thickness are neglected.

To avoid confusion, the subscript notations of the heat transfer coefficient are given here,

o zero injection, zero pressure gradient, K=0.0

MF moderate favourable pressure gradient, $K=1.9\times10^{-6}$

oMF zero injection, $K=1.9\times10^{-6}$

SF strong favourable pressure gradient, $K=5.0\times10^{-6}$

oSF zero injection, $K=5.0\times10^{-6}$

8.2 EFFECT OF DENSITY RATIO

The effect of density ratio is now described for each film cooling geometry used in this study.

8.2.1 Single Normal Hole

The single normal hole results used to validate the experimental technique are utilized here to convey the effect of density ratio for this injection geometry.

Contours of the heat transfer ratio h/h_o for the two density ratios 1.0 and 1.38 at a blowing rate of unity are plotted in Fig. 8.1. Increases in the heat transfer coefficient exceeding 10 percent are confined to the first 10 diameters

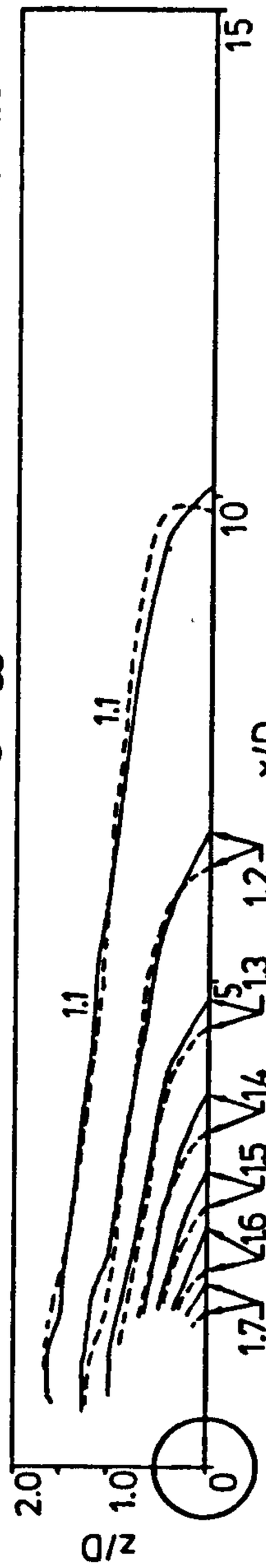

Fig. 8.1 h/h. contours following normal injection through a single hole.

downstream of the holes, and are greatest on the centreline immediately after the hole.

Although the momentum flux is reduced by approximately 28 percent for the denser injectant, the contours for the two densities hardly differ from one another. The fast mixing and high turbulence levels associated with normal injection diminish the influence of jet density as well as momentum variation on the heat transfer coefficient.

One further result to be extracted from the figure is that the blowing rate, M, seems to be a promising correlating parameter in this case.

8.2.2 Single Row of 90° Holes

It seems logical that the result obtained here regarding the effect of density ratio on h/h_o, should be similar to that obtained for a single normal hole since the jet-mainstream mixing is essentially identical in nature. This is confirmed by Fig. 8.2 where the influence of varying the density ratio from 1.0 to 1.52 on the normalized heat transfer coefficient at four blowing rates is shown. Only small differences occur between the contour shapes and levels for the two densities at any position. For most blowing rates, differences do not exceed 3%, although they rise to 5% at large downstream distances at the highest blowing rate. The density ratio thus has no distinct effect on the normalized heat transfer coefficient at a constant blowing rate.

Fig. 8.2 also shows the effect of jet-mainstream mixing on the heat transfer coefficient. Generally, the contour plots for both density ratios indicate that injection causes large increases in the heat transfer coefficient. For M = 2.0, this increase exceeds 100% just downstream of a hole.

There is also a significant lateral variation in the heat transfer coefficient. At a blowing rate of 0.5, the maximum heat transfer coefficient occurs near the edge of the jets all the way downstream where the jets interact with the mainstream. Apparently, due to the low jet trajectory at M=0.5, the jets behave like multiple single jets, until far downstream where injection effects disappear. However, for M of 1 or greater, the maximum is initially on the jet

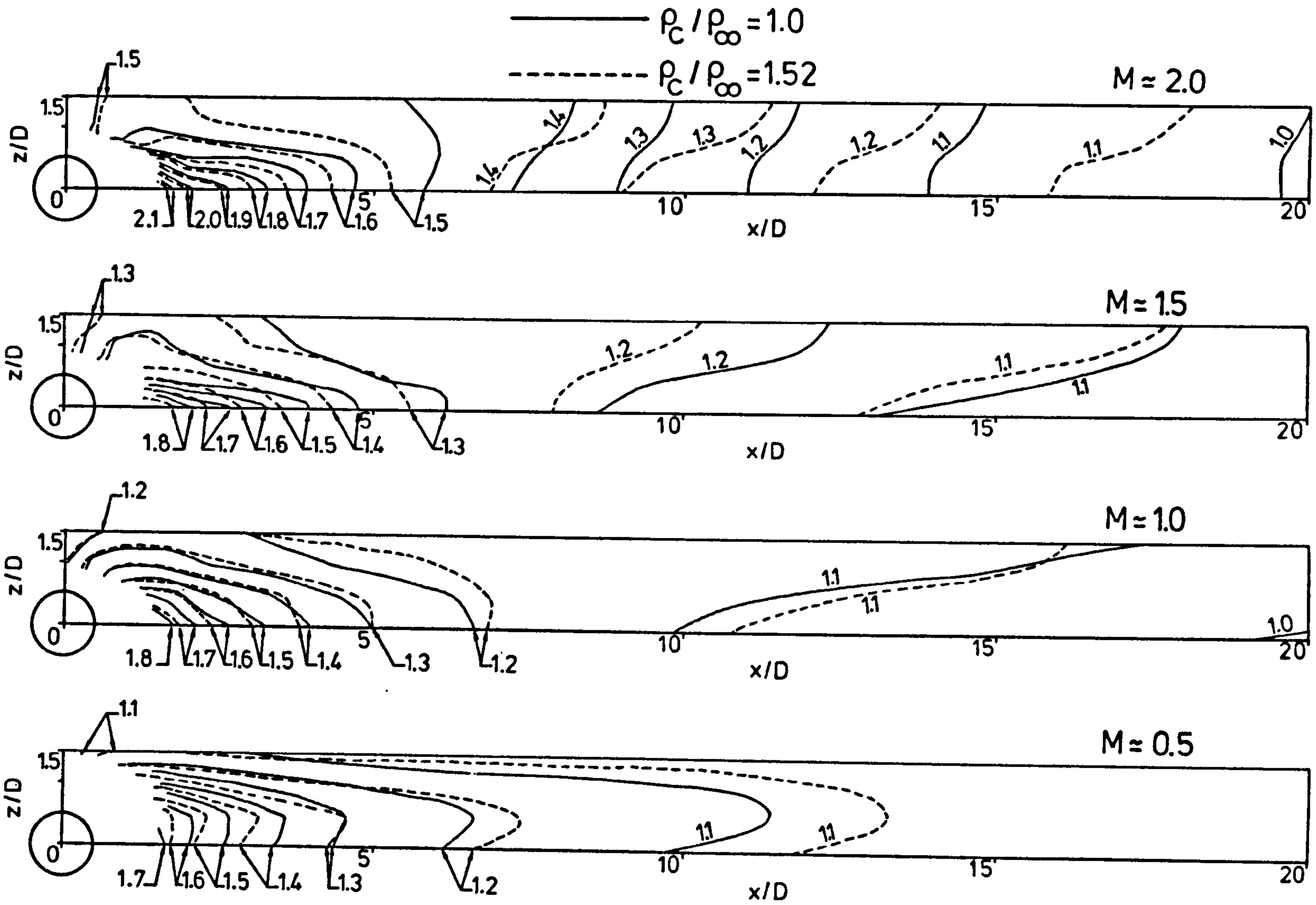

Fig. 8.2 h/h$_o$ contours following normal injection through a row of holes.

centreline, while beyond about x/D of 7, the maximum h/h_o occurs at mid-pitch positions. This behaviour may be due to the fact that, at elevated blowing rates, the jets mix quickly with the mainstream, spread rapidly and coalesce close to the injection location. As a consequence, the lateral distribution of h/h_o at x/D greater than 7 becomes flatter, and is almost two-dimensional at the highest blowing rate.

Comparison of data from Fig. 8.2 with that for injection through a single normal hole at unity density ratio for M of 0.5, 1.0 and 1.5 are presented in Fig. 8.3. The data shows that the heat transfer coefficient following injection through a row of holes is the same or little higher than that for injection through a single hole at centreline positions, whereas it is appreciably higher at locations between the holes at M greater than 0.5. Mixing between neighbouring jets therefore enhances the heat transfer coefficient. Similar conclusions were reported by Eriksen and Goldstein [22] for injection through 35° holes.

The insensitivity to density ratio of the detailed normalised heat transfer coefficient distribution at a fixed blowing rate naturally implies that the spanwise-average distributions will also correlate with M. This is verified in Fig. 8.4, where the laterally averaged normalized heat transfer coefficient $\bar{h}/h_o$ is presented for density ratios of 1.0 and 1.52 as a function of x/D. Upstream of the injection holes, the injection-affected region is at most 3 hole diameters in extent at high M. At these high blowing rates, the jets are seen as solid bars by the mainstream and the interaction gives rise to an increase in $\bar{h}/h_o$ just upstream of up to 16% at M=2. As the blowing rate reduces, so also does the strength of the interaction, until at M=0.5 there is a slight decrease in the heat transfer, probably caused by the slowing down of the mainstream by the jets.

Downstream of the injection location, $\bar{h}/h_o$ increases with M, and decreases monotonically with x/D. Maximum values vary from 1.45 at M=0.5 to 1.75 at M=2.0.

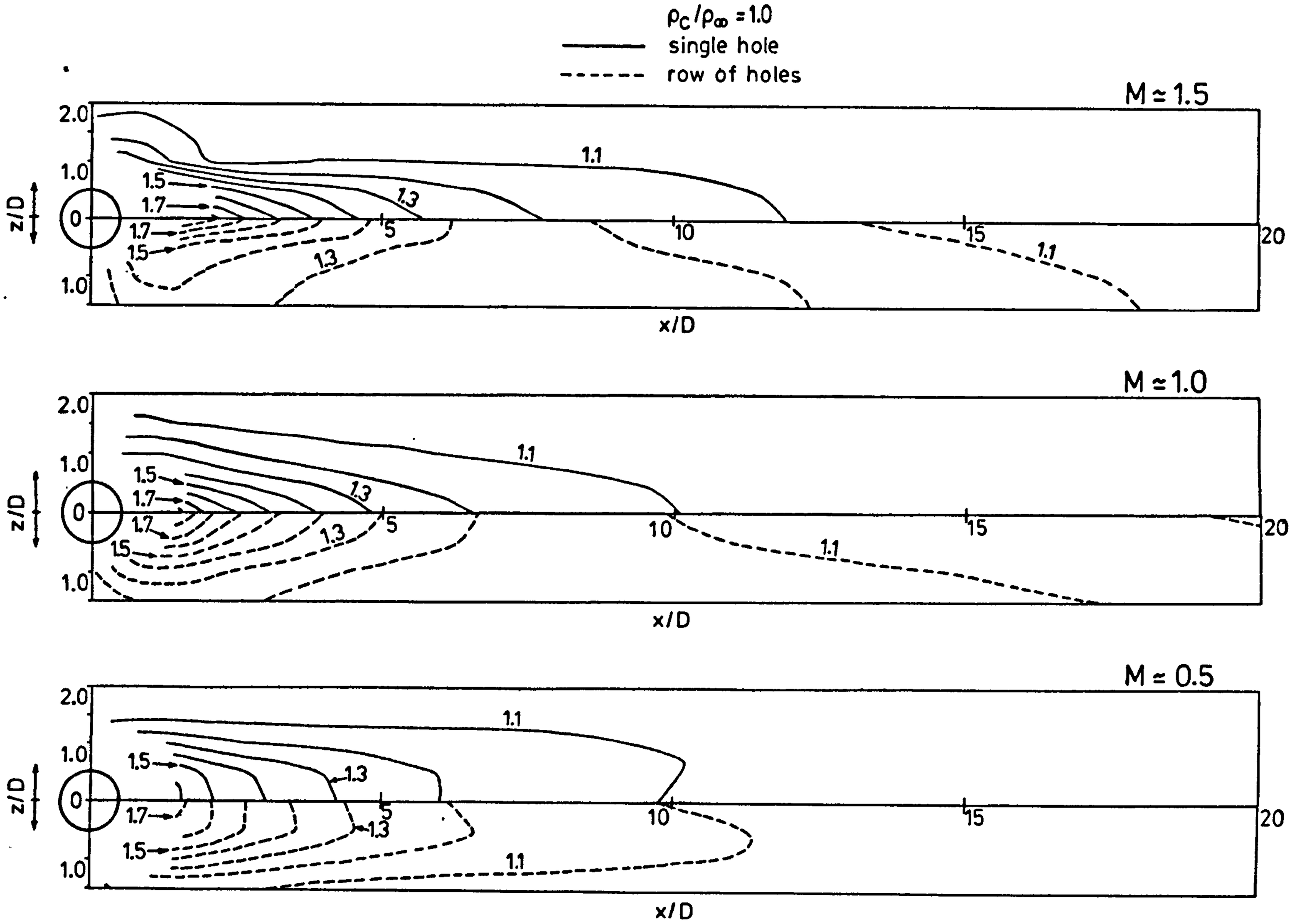

Fig. 8.3 h/h$_e$ contours following normal injection through a single hole and a row of holes

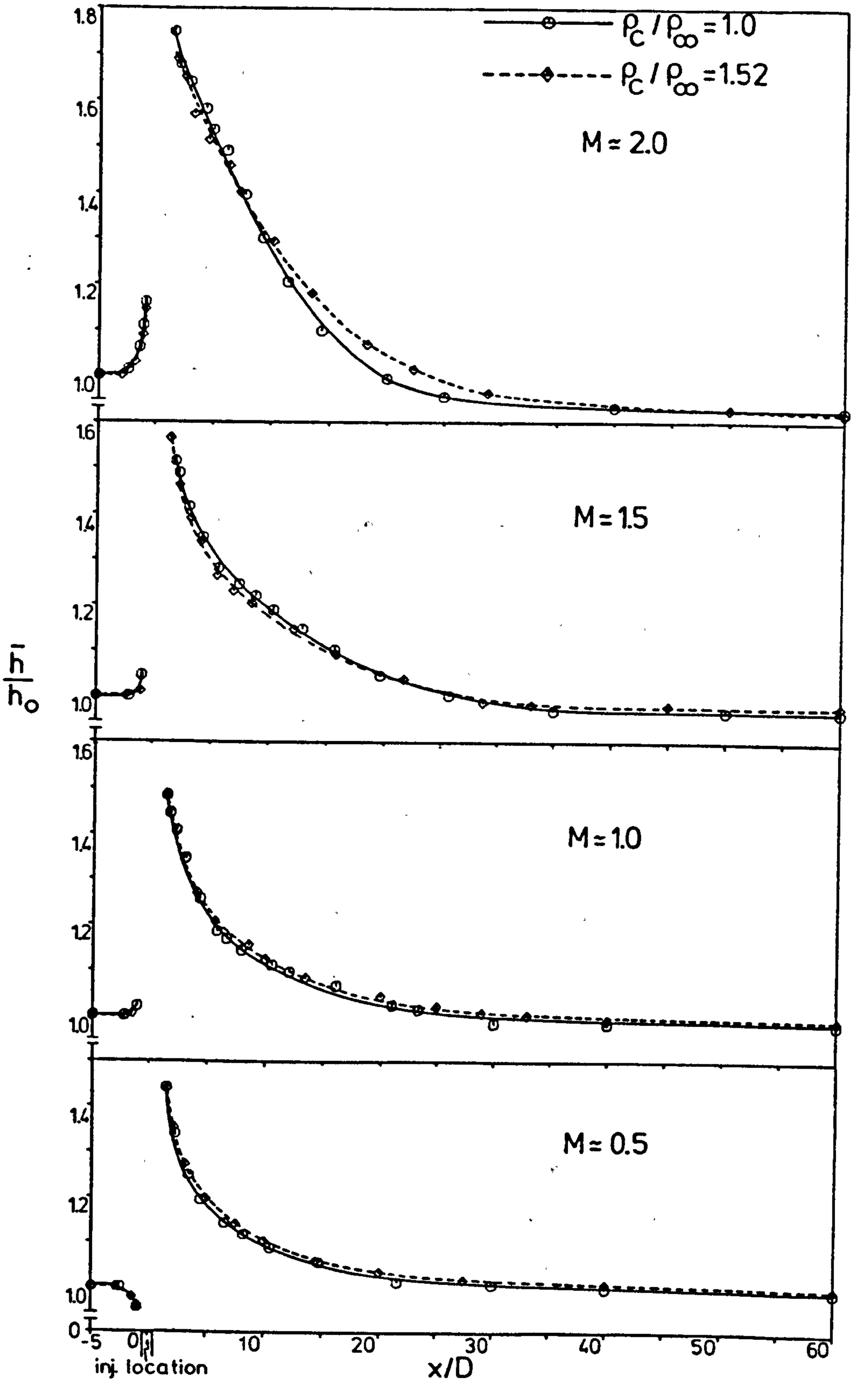

Fig. 8.4 Effect of density ratio on $\bar{h}/h_o$ for normal injection through a row of holes.

8.2.3 Single Row of 35° Holes

Blowing rate does not correlate data from 35° tests, as seen from Fig. 8.5, contour plots of h/h_o for M=0.5-2.0 at density ratios of 1.0 and 1.52. Close to the injection holes ($x/D \leq 5$) differences of the order of 10% occur in h/h_o when the density ratio changes, lower density leading to increased heat transfer. Similar behaviour occurs further downstream, where the difference in h/h_o has increased by 20% at mid-pitch positions for the highest blowing rate.

At any given blowing rate, the lower density injectant has the higher momentum. Because the inclined jets do not mix rapidly with the mainstream, this increased momentum is reflected in the cooling film, and hence Reynolds' analogy leads to the expectation of an increased heat transfer coefficient.

A closer comparison of the data in Fig. 8.5 reveals that there is a slight deviation for the case of M=0.5. At dimensionless regions >5 h/h_o is seen to increase (not exceeding 4%) with the increase in jet density. The denser gas was injected at such low velocity ($u_j/u_\infty \approx 0.33$) that the gross separation from the surface, as seen for the higher injection velocities, did not occur. This point is reinforced by the streakline flow visualisation using helium bubbles made by Colladay and Russell [19] who have shown that the film injected through 30° holes remained attached to the surface as long as the velocity ratio did not exceed about 0.5. This attached film flow is designated by Forth and Jones [32] as the weak injection regime. As the low momentum jets emerge they are knocked over by the mainstream pressure and are kept attached to the surface. The weak jet-mainstream mixing permits the retention of the jets for a longer downstream distance before the jets becoming diffused into the existing boundary layer. This behaviour is indicated by the gradual though small decay of the heat transfer coefficient with downstream distance.

In a recent paper, for injection through a geometry similar to that of the present study, Pietrzyk et al [103] have postulated that the extent of the separation region in the wake of a hole for a high density jet ($\rho_j/\rho_\infty=2.0$) would be similar to that of the unity density ratio jet with equal velocity ratio. Pietrzyk et al have also found that for M=0.5 the turbulence levels at

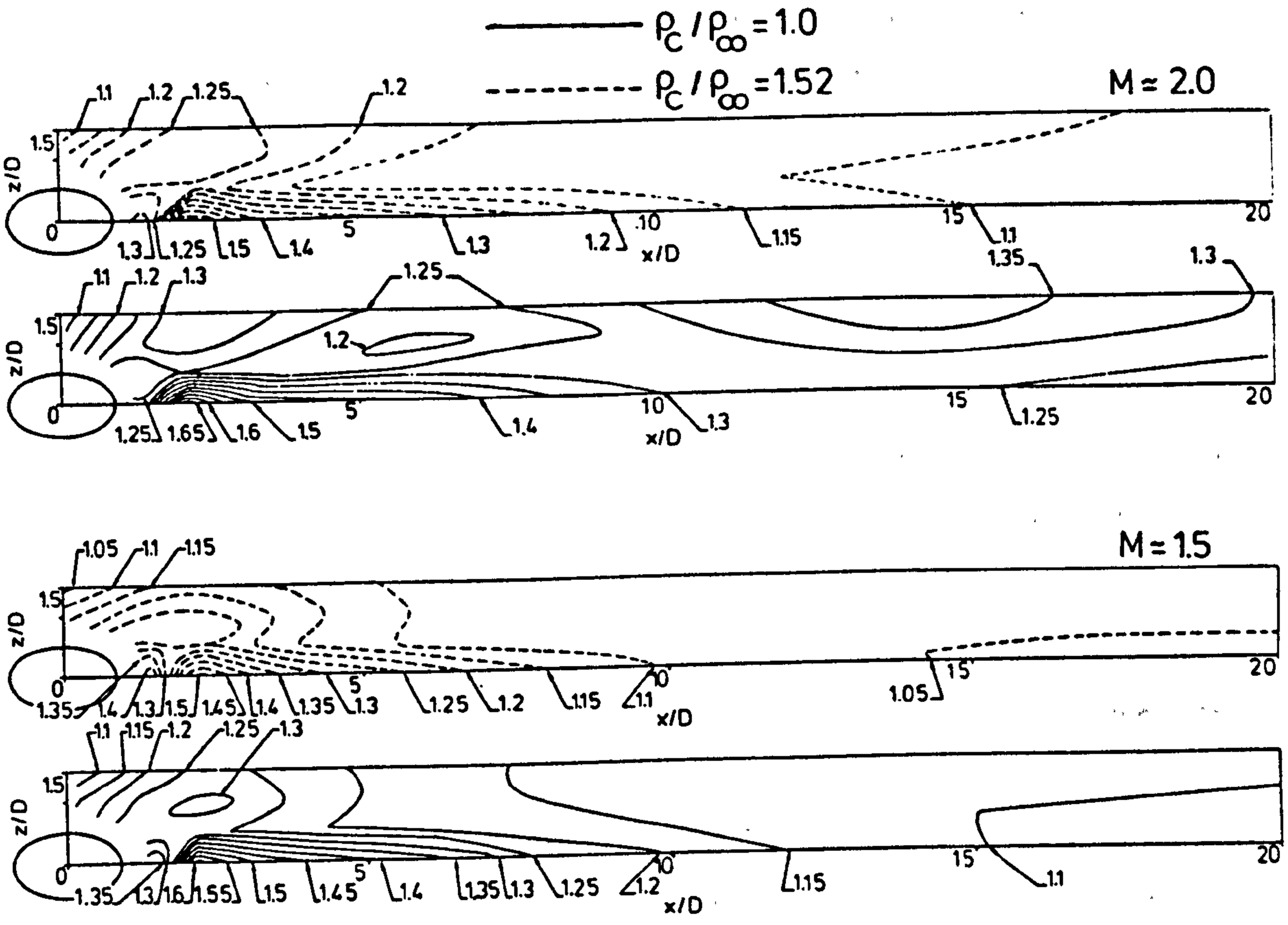

Fig. 8.5 h/h_o contours following injection at 35° through a row of holes.

the exit of a dense jet (ρ_j/ρ_∞=2.0) are less than those for the M=0.5 unity ρ_j/ρ_∞ jet. However, high turbulence levels persisted for greater distances downstream for the dense jet. This supports the present findings at M=0.5.

Regions of high h/h_o close to the holes were observed for all blowing rates examined. The heat transfer coefficient in these regions increased in magnitude with increased M, as did their streamwise extent. For M=0.5 at both density ratios, interaction between the jets and the mainstream, all the way downstream, has increased h near the edges of the jets more than on the jets centreline. This has also been observed by Eriksen & Goldstein [22]. For M≥1.0 and at regions less than about 12 diameters, h/h_o is greater at the centreline than on regions between the holes. This is understandable since, at sufficiently high injection momentum ratios, jet lift off immediately downstream of the holes permits the mainstream to flow beneath the jets creating intense eddies, and increasing the heat transfer. Further downstream, reattachment of the streamwise vortices and interaction between the spreading adjacent jets has apparently enhanced the heat transfer coefficient at mid-pitch positions.

To clarify the influence of density ratio variation on the heat transfer coefficient, the normalized heat transfer coefficient data averaged in the spanwise direction are plotted as a function of the streamwise direction for four blowing rates in Fig. 8.6, with the density ratio as parameter. Upstream of the injection holes (-x/D<3), the heat transfer coefficient is slightly reduced by the presence of the jets. Downstream of the holes, an increase in density ratio is seen to result in a considerable decrease in $\bar{h}/h_o$ at all M's. As M increases, the difference in momentum between the heavier and lighter gas injectants increases, and this is reflected in a corresponding increase in the difference in $\bar{h}/h_o$ between the two sets of results. Differences in $\bar{h}/h_o$ as high as 8 percent at M=0.5 and 18 percent at M=2.0 are observed.

It is of interest to note that the results for the case of M=1.0 are consistent with those obtained using a heat transfer method by Eriksen and Goldstein [22], where an increase in jet density of 15% is accompanied by a

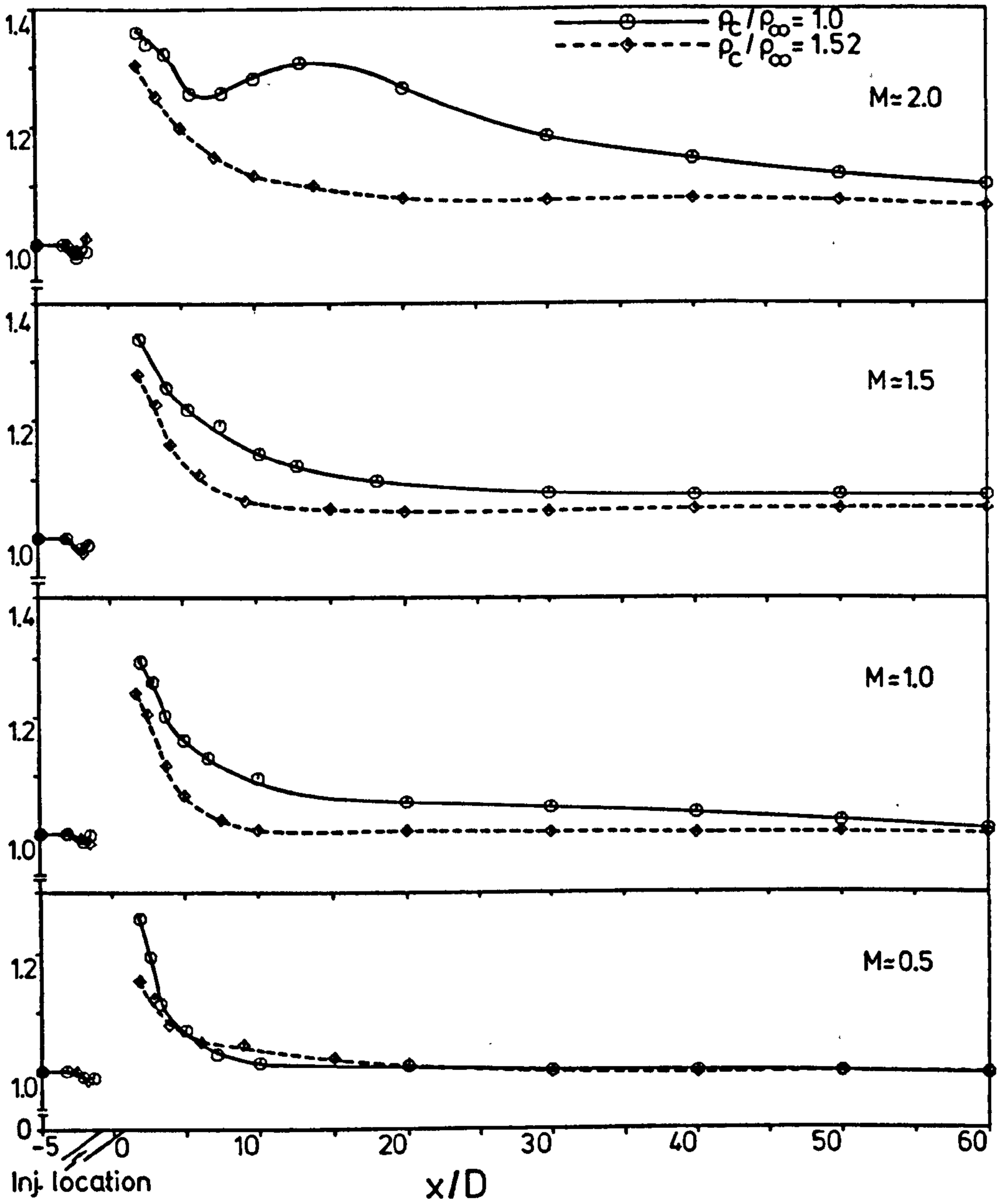

Fig. 8.6 Effect of density ratio on $\bar{h}/h_o$ for 35° injection through a row of holes.

decrease in $\bar{h}/h_o$ of approximately 2%.

Furthermore, Fig. 8.6 reveals that, at the unity density ratio $\bar{h}/h_o$ is always ≥1.0 and increased as M was increased. At density ratio of 1.52, $\bar{h}/h_o$ is also always ≥1.0. However, in the range $5 \leq x/D \leq 25$, $\bar{h}/h_o$ fell by 5% when M was increased from 0.5 to 1.0 as shown in Fig. 8.7. This behaviour is also seen in the results of Forth [31] for injection through 30° holes (see Fig. 8.7). At density ratio of 0.81 $\bar{h}/h_o$ increased as M was increased to ≈1.2 in a similar manner to the present results at ρ_j/ρ_∞ of one. But when the density ratio was about 1.67, at $x/D<30$ $\bar{h}/h_o$ fell as M was raised from 0.4 to about 1.2. The decrease of $\bar{h}/h_o$ in [31], however, was greater probably because of the differences in density ratio, injection inclination and experimental method.

Results of the lateral average effectiveness obtained by Pedersen et al [52] and Forth [31] with injection via 35° and 30° row of holes respectively, have shown that the optimum value of M at which maximum effectiveness occurred increased as the density ratio increased. It is interesting to note that the optimum value of M of about 0.5 at ρ_j/ρ_∞ of 1 increased to about 0.62 at ρ_j/ρ_∞ of 1.5 [41] coincides with low $\bar{h}/h_o$ values at M=0.5 and unity ρ_j/ρ_∞, and lower $\bar{h}/h_o$ values at M=1 than at M=0.5 at ρ_j/ρ_∞ of 1.52. This may be because jet lift-off depends on I, which is higher for smaller ρ_j/ρ_∞ at a given M.

A comparison of the present results for 35° injection with those of other experimenters for a density ratio of unity using a similar injection geometry is shown in Figs. 8.8 and 8.9. The operating conditions for each data set are shown on the figures.

In Fig. 8.8 the $\bar{h}/h_o$ data for x/D less than 10 and for all M covered is compared with that of Goldstein and Taylor [71] obtained using the naphthalene sublimation technique. The agreement is generally good, although the results of [71] show a much steeper initial fall in $\bar{h}/h_o$. This may be due to the differing boundary layer displacement thicknesses and Reynolds numbers.

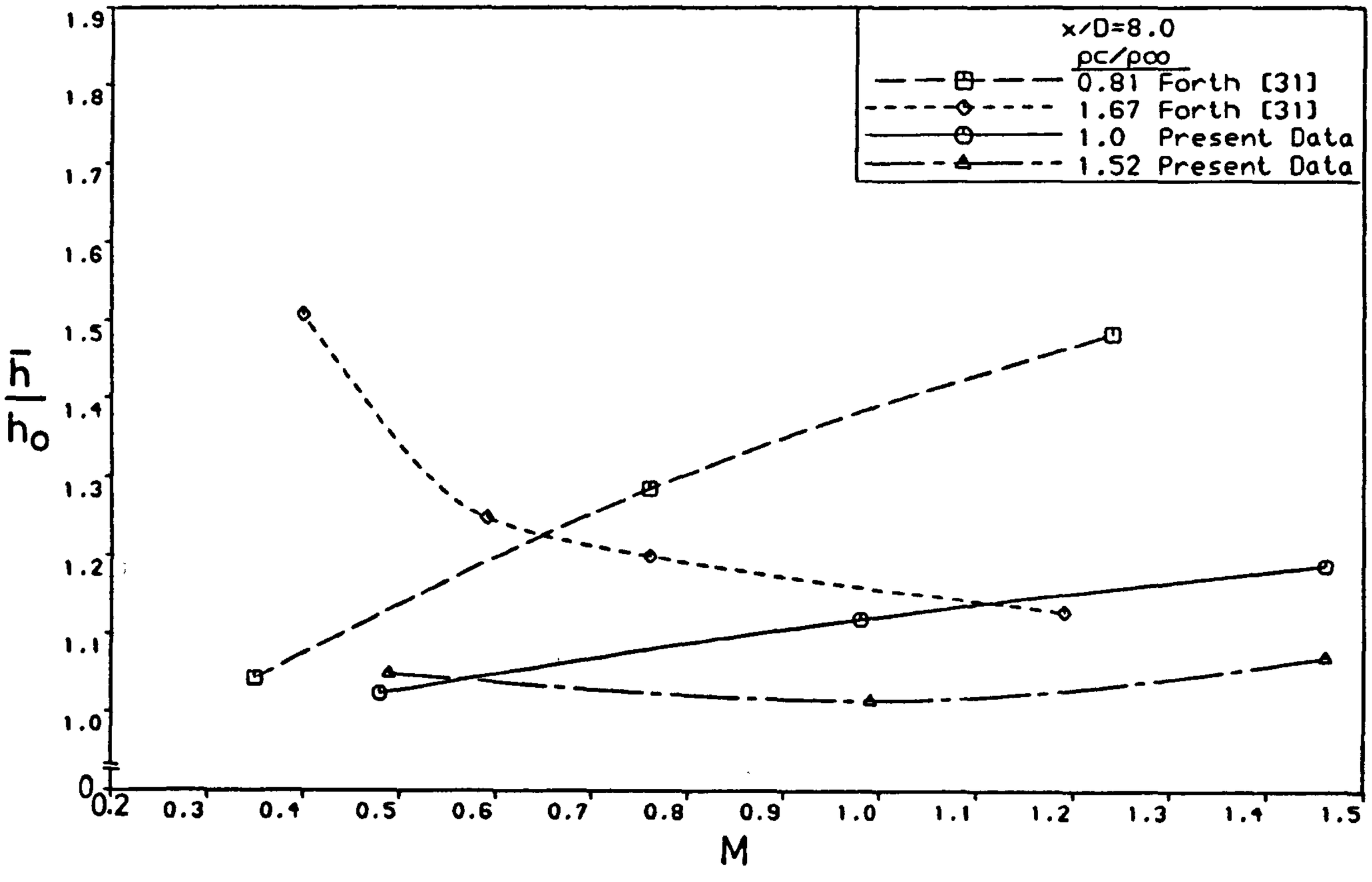

Fig. 8.7 Variation of $\bar{h}/h_o$ with the blowing rate.

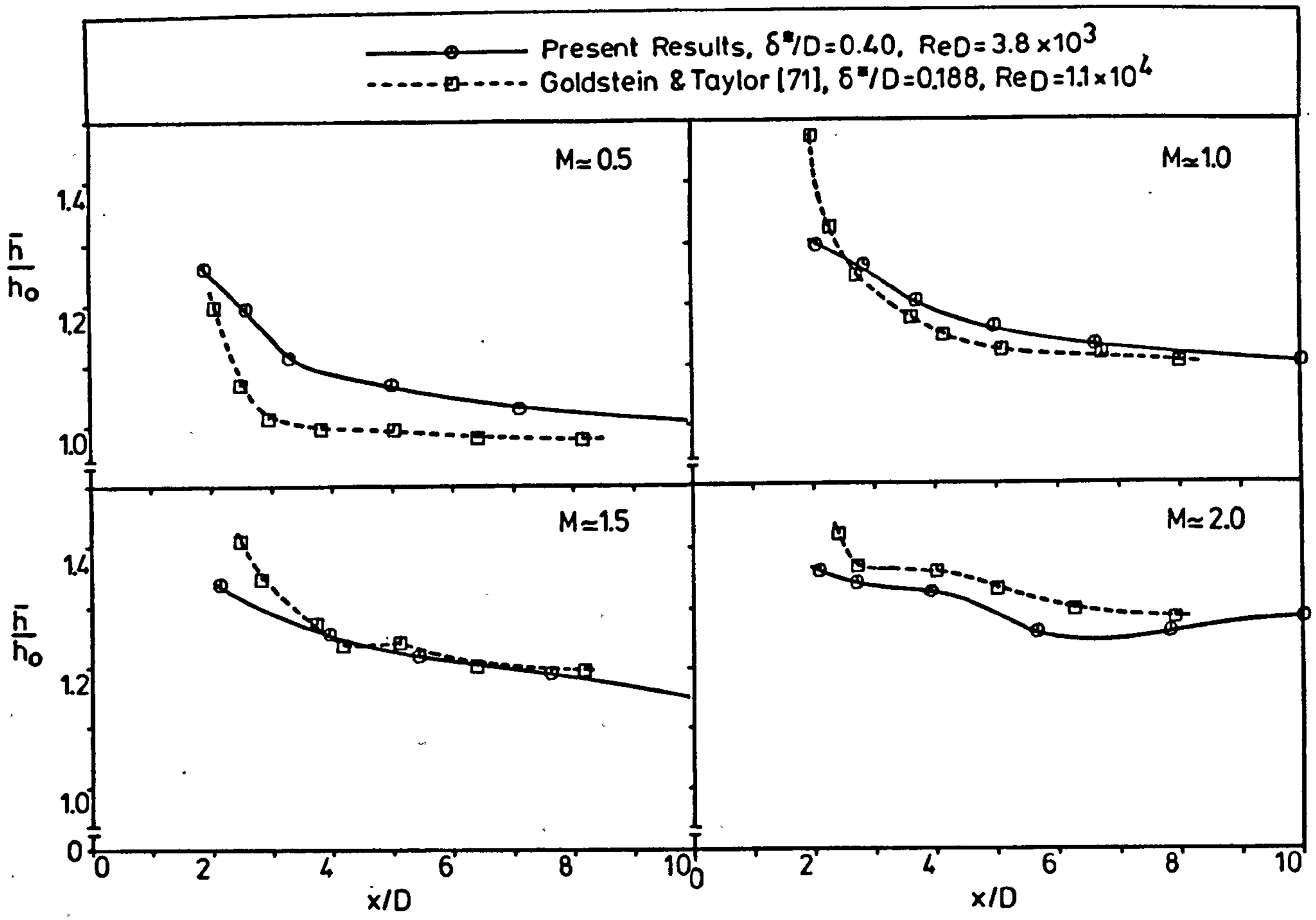

Fig. 8.8 Comparison of $\bar{h}/h_o$ results with those of others for 35° injection.

The results of references [22], [24], [104] and [25] were obtained by thermal methods at different test conditions, and are compared with the present results in Fig. 8.9. At M=0.5, very close agreement is seen between the present results and those of Eriksen [104] and Goldstein and Yoshida [25]. Generally, the difference between the present results and the results of the other experimenters is less than the difference between their results.

8.2.4 Comparison of Data of 90° and 35° Holes

The 90° and 35° results differ markedly in their response to changes in blowing rate and in density ratio. For 90° injection the variation with blowing rate was quite weak at both density ratios, except when M=2. Further, there was little difference between 1.0 and 1.52 density ratio results. By contrast, for 35° injection the heat transfer coefficient rose when the blowing rate increased or the density ratio decreased, indicating a dependence on jet to mainstream velocity or momentum ratio.

Typical double-exposure holograms of 90° and 35° injection at M=1.0 and ρ_j/ρ_∞ of 1.0 and 1.52 are shown in Fig. 8.10. The figure reveals qualitatively the structure of the contours of mass transfer coefficients. Notice the differences in the patterns of the contours downstream of injection, especially immediately after the holes. The difference between the two injection angles is attributable to the difference in nature of jet-mainstream mixing. The difference between the contours of the 35° injection is caused by raising the density ratio from 1 to 1.52.

The retention of the jet structure within the cooling film for the shallow angled injection was noted earlier. This is much less pronounced for the normal injection case. The normal jets penetrate deeper into the mainstream, and strong mixing occurs as they are turned parallel to the wall. This mixing results in a film from which the jet structure is almost completely absent, approaching two-dimensionality within the first 15 diameters. A velocity distribution similar to a turbulent boundary layer would therefore be expected, with the heat transfer coefficient ratio quickly tending to unity as observed in

Symbol	M	δ^*/D	$Re_D \times 10^{-4}$	
—⊖—	0.49	0.40	0.38	Present Results
- - - - -	0.36	0.171		Liess [24]
— — -	0.49	0.171	2.2	Eriksen & Goldstein [22]
— - - —	0.5	0.149	4.4	Eriksen [104]
⊔	0.5	0.14	0.34	Goldstein & Yoshida [25]

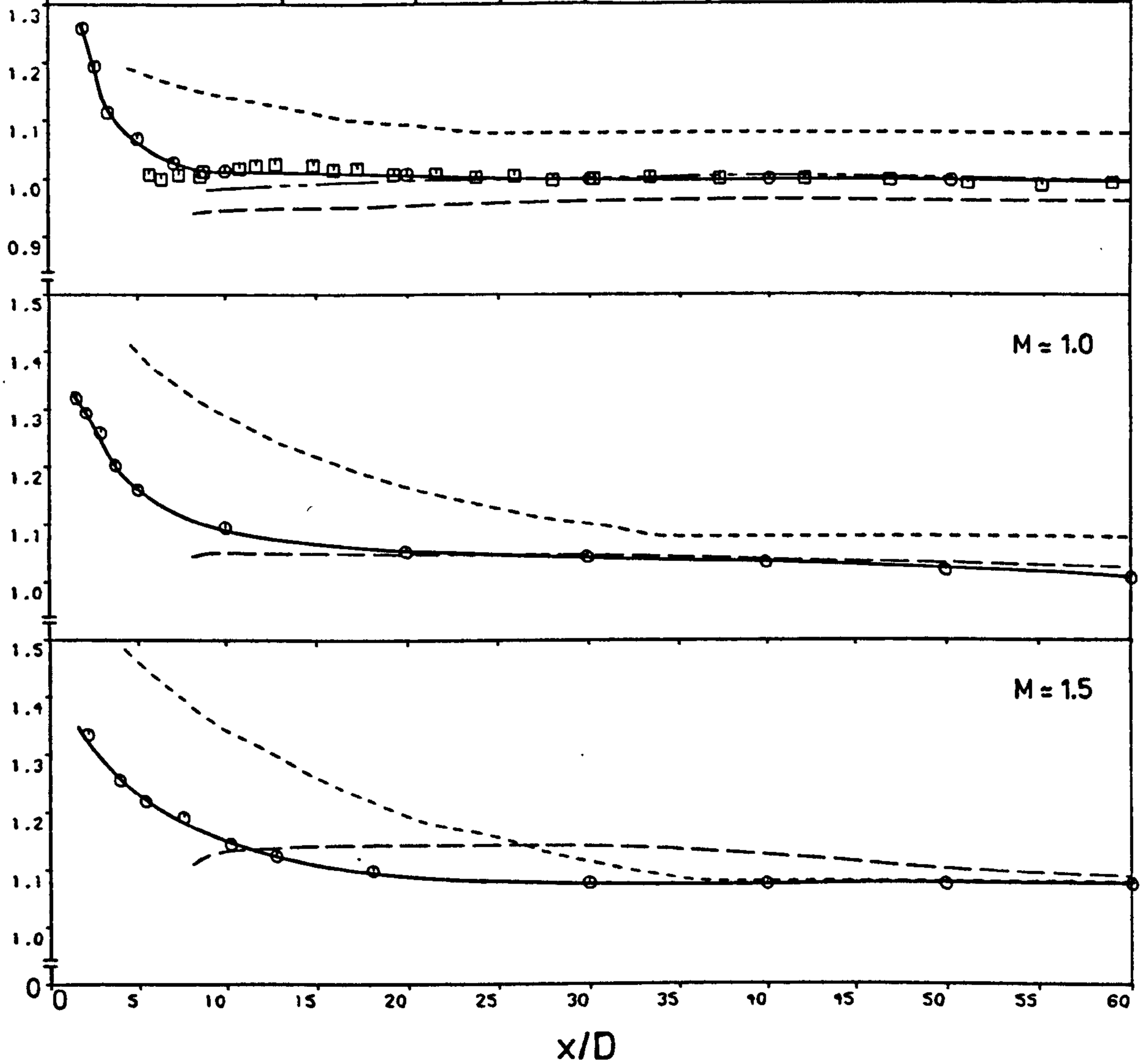

Fig. 8.9 Comparison of $\bar{h}/h_o$ results with those of others for 35° injection.

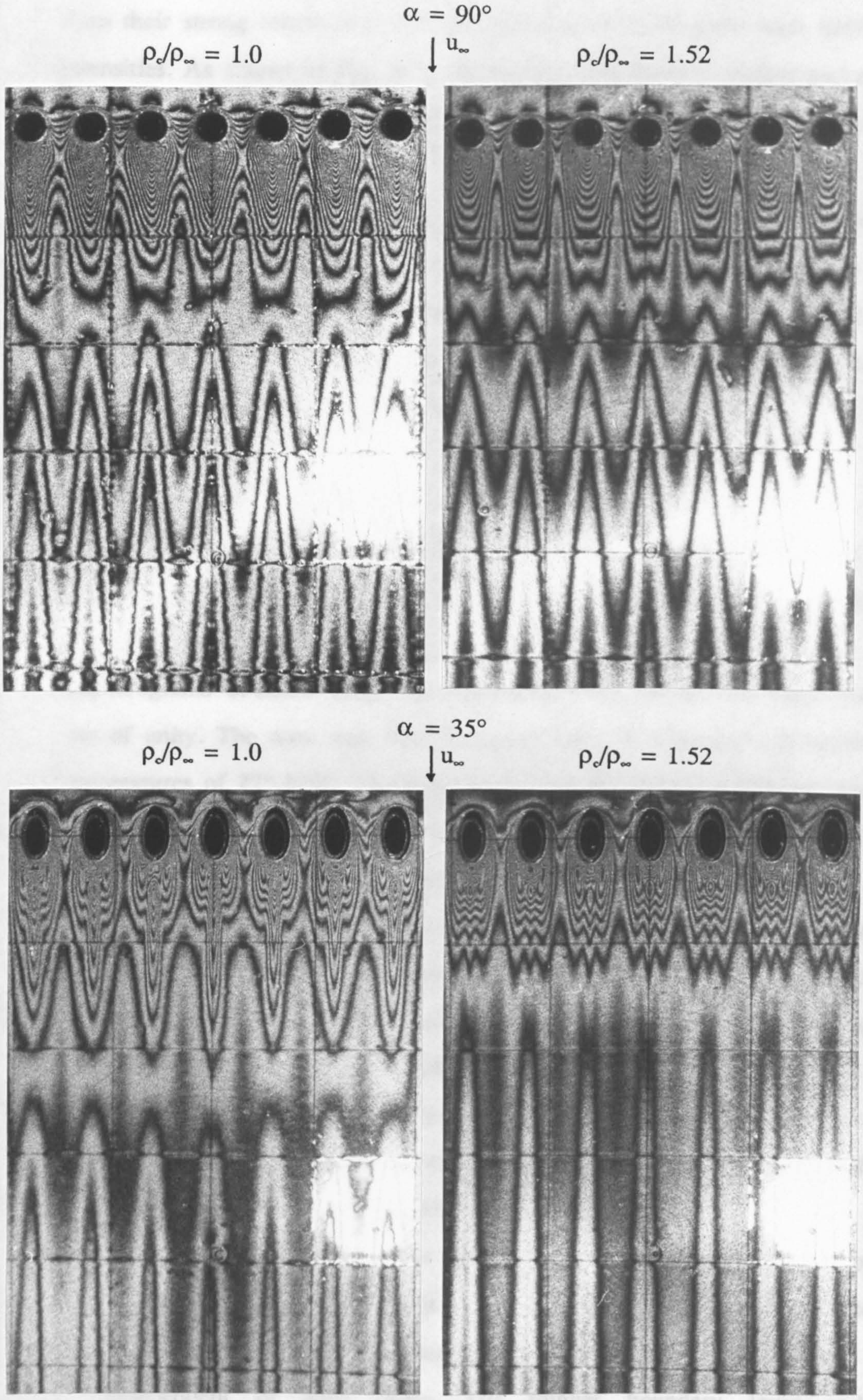

Fig. 8.10 Comparison of contours of constant mass (heat) transfer coefficients for 90° and 35° injection through a row of holes at M=1.

Fig. 8.2. The enhanced heat transfer immediately downstream of the jets arises from their strong interaction with the mainstream which gives high turbulence intensities. As shown in Fig. 8.11 the inclined jets show a smaller increase in heat transfer initially as they disturb the mainstream less, but the decay is slower because of the reduced mixing.

It follows that, from a blade cooling design point of view, employing inclined injection holes rather than normal ones is more beneficial; the lower heat transfer coefficients and higher cooling effectiveness values [17] at a given blowing rate that are associated with inclined injection results in a more efficient film cooling performance.

8.3 EFFECT OF MAINSTREAM ACCELERATION

Observation of interference fringes of constant mass transfer, Fig. 8.12, albeit qualitative, provides a clear picture of the variation in the structure of jet-mainstream intermixing due to acceleration. Fig. 8.12 shows three interferograms obtained from three different tests, but for the same blowing rate of unity. The tests were run for equal time (12 minutes) and operated at temperatures of 27°-29°C. The holograms represent the three different pressure gradient cases; zero (A), moderate favourable (B) and strong favourable (C). The following features may be noted from the figure,

i) Close to the holes, the strong mixing between the jets and the mainstream is faster in the highly accelerating mainstream cases (B) and (C) than in the constant mainstream velocity case (A). The jets travel more rapidly and the strong mixing is marked for a longer downstream distance. As a result, the distinct three-dimensional character of the contours of mass (heat) transfer coefficient is extended from about 10 diameters at K=0.0 to about 15 diameters at $K=5.0\times10^{-6}$.

ii) The lateral spread of the jets downstream of the holes is reduced by the acceleration. The reduction is observed most in case (C). Close to the injection site, the jet flows seem to be more compact and therefore more independent of each other. The thinner boundary layer and the

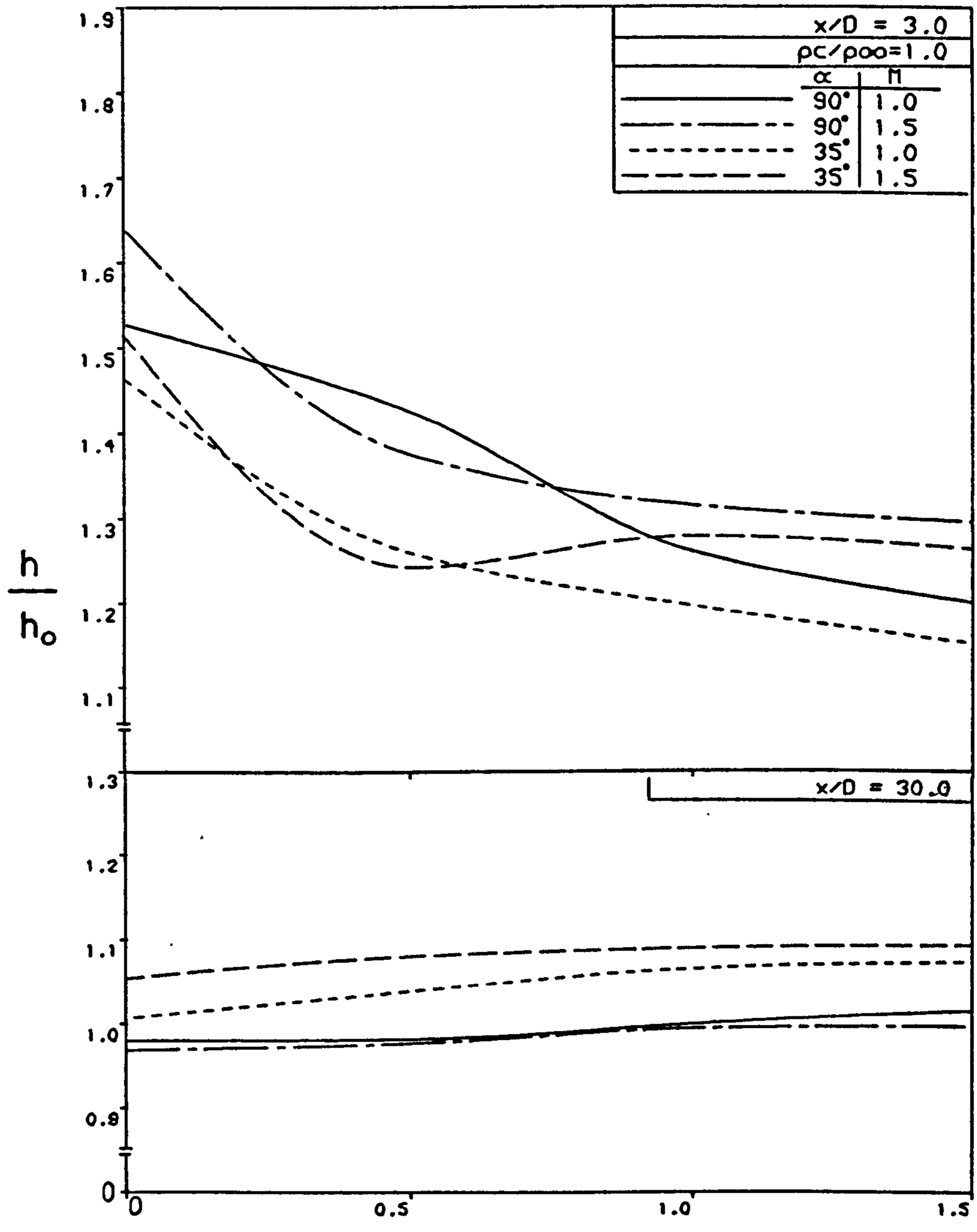

Fig. 8.11 Lateral distribution of h/h_o at two downstream locations for 90° and 35° injection via a row of holes.

Grid Spacing = 5D

K = 0.0

u_∞ ⟶

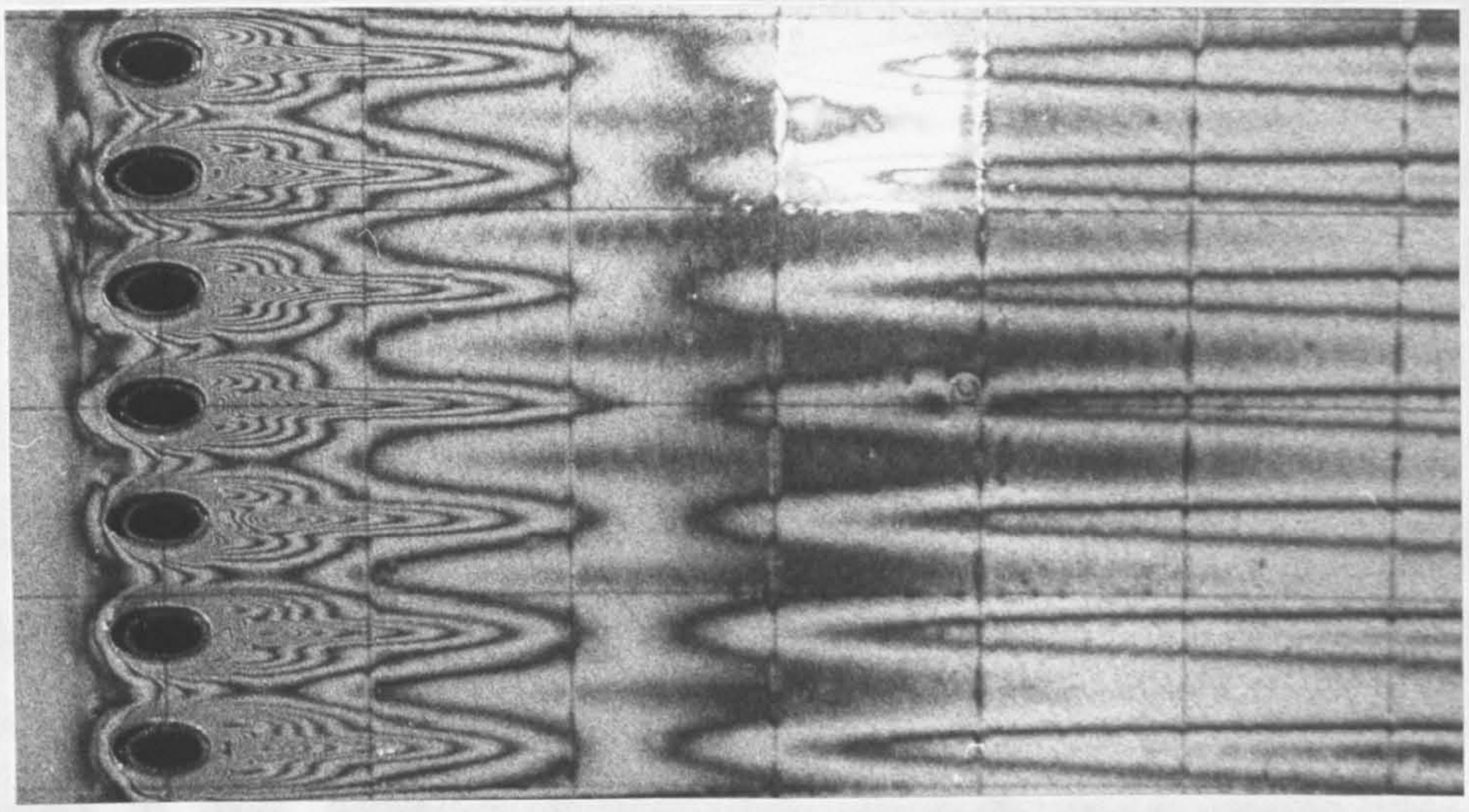

K = 1.9×10^{-6}

u_∞ ⟶

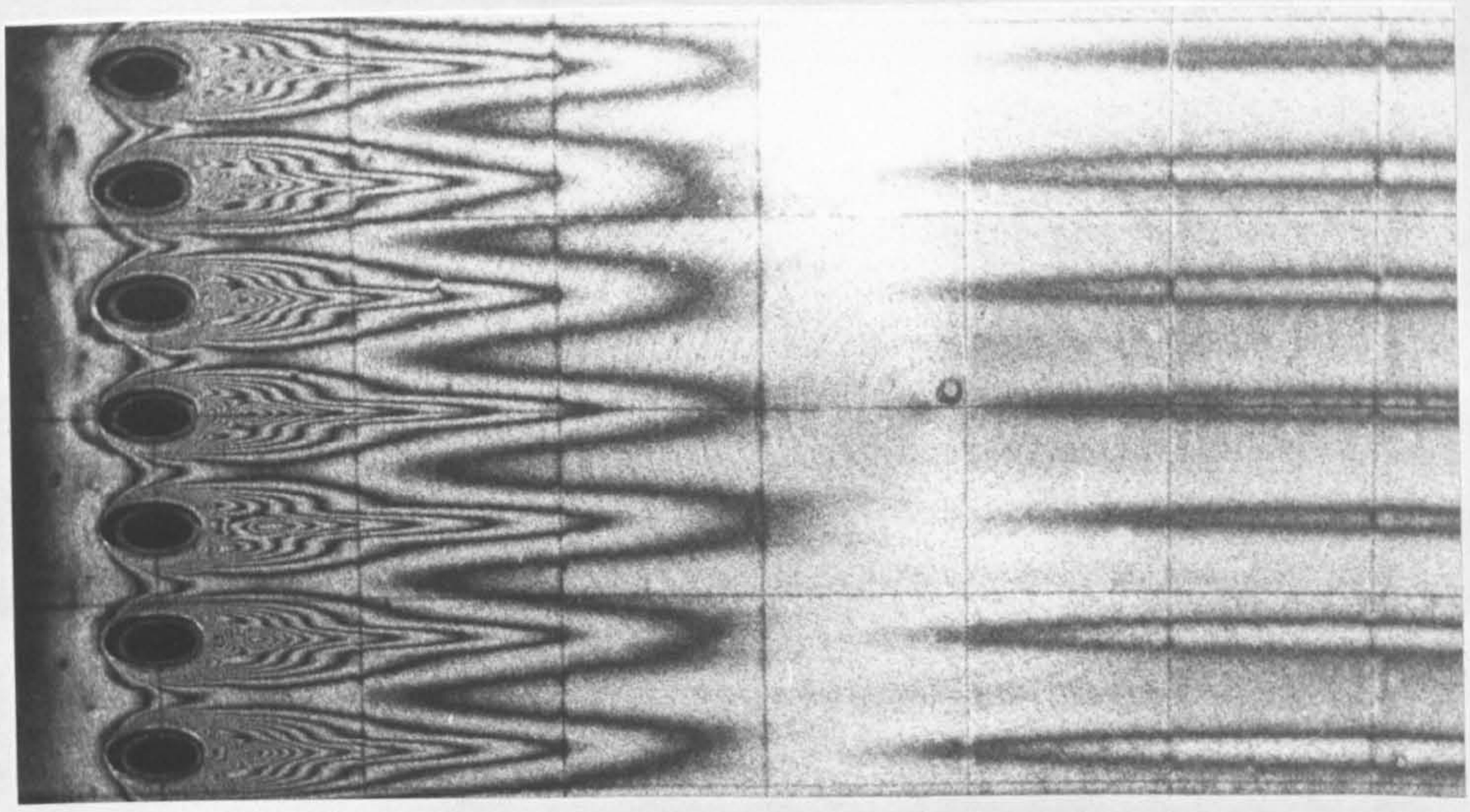

K = 5.0×10^{-6}

u_∞ ⟶

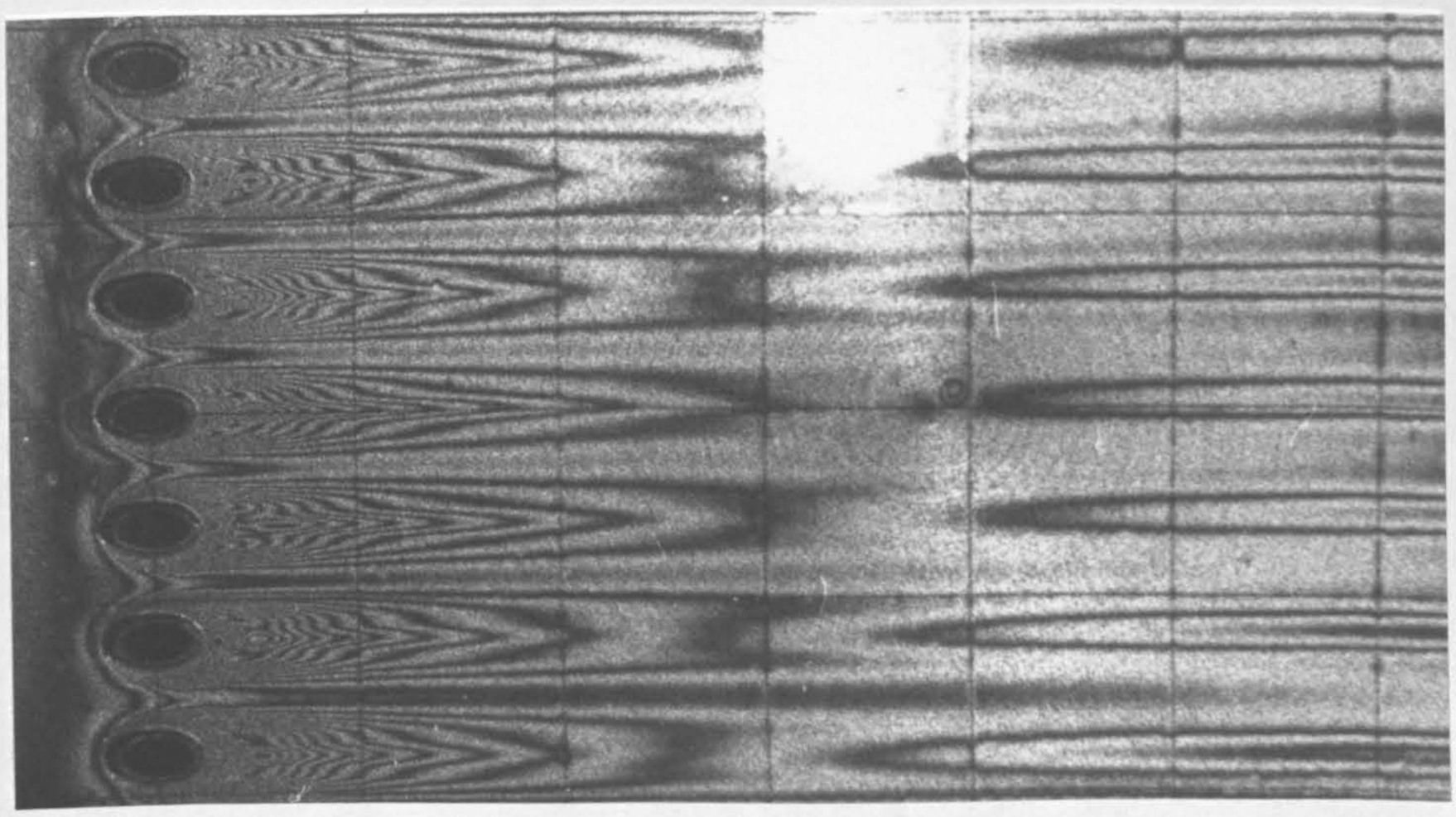

Fig. 8.12 Interference fringes depicting contours of constant mass (heat) transfer coefficients for air injection through a row of 35° holes at M=1.

accelerating mainstream seem to have squeezed the emerging jets quickly into the downstream direction. This behaviour has also been observed by Foster [105] for 90° injection with s/D=3, who measured jet concentrations at x/D=4.25 and z/D=0.0-1.5 above a film cooled wall at zero and strong favourable ($K=8.5\times10^{-6}$) pressure gradients. A reduction in the lateral spread of jets issuing from staggered rows of holes aligned at 45° with s/D=8 by an acceleration parameter of 2.0×10^{-6} was also reported by Launder and York [75].

iii) The pattern of the mass transfer contours is generally similar at all K. The peak in the local mass (heat) transfer coefficient corresponding to the maximum polymer coating shrinkage downstream of the hole centreline appears to have happened at the same position, about x/D=2.4. Thus, separation may have occurred even at $K=5.0\times10^{-6}$, and has taken place almost at the same location.

Similar behaviour to that in Fig. 8.12 was seen at the other blowing rates used in this study.

To provide the aspects of the response of the injected jets to the acceleration, the centreline turbulence intensity (longitudinal velocity fluctuations) and mean velocity profiles with air injection for M=1.5 with and without acceleration are plotted in Fig. 8.13. In general, the mean velocity profiles close to a hole do not differ too greatly from one another, although acceleration tends to press the jets slightly down as the boundary layer is thinned, which results in an increase in the velocities near the wall. The effect of acceleration on the turbulence levels is more pronounced; suppression of injection induced turbulence is increased with increase in acceleration parameter at all downstream positions. It should be noted, however, that the levels at $K=1.9\times10^{-6}$ were measured by a different hot-wire probe (90° probe against 180° probe for the others) and a slight out of line behaviour is observed.

The turbulence levels close to the wall and in all cases are seen in Fig. 8.13 to be decreasing with downstream distance, and larger for the zero

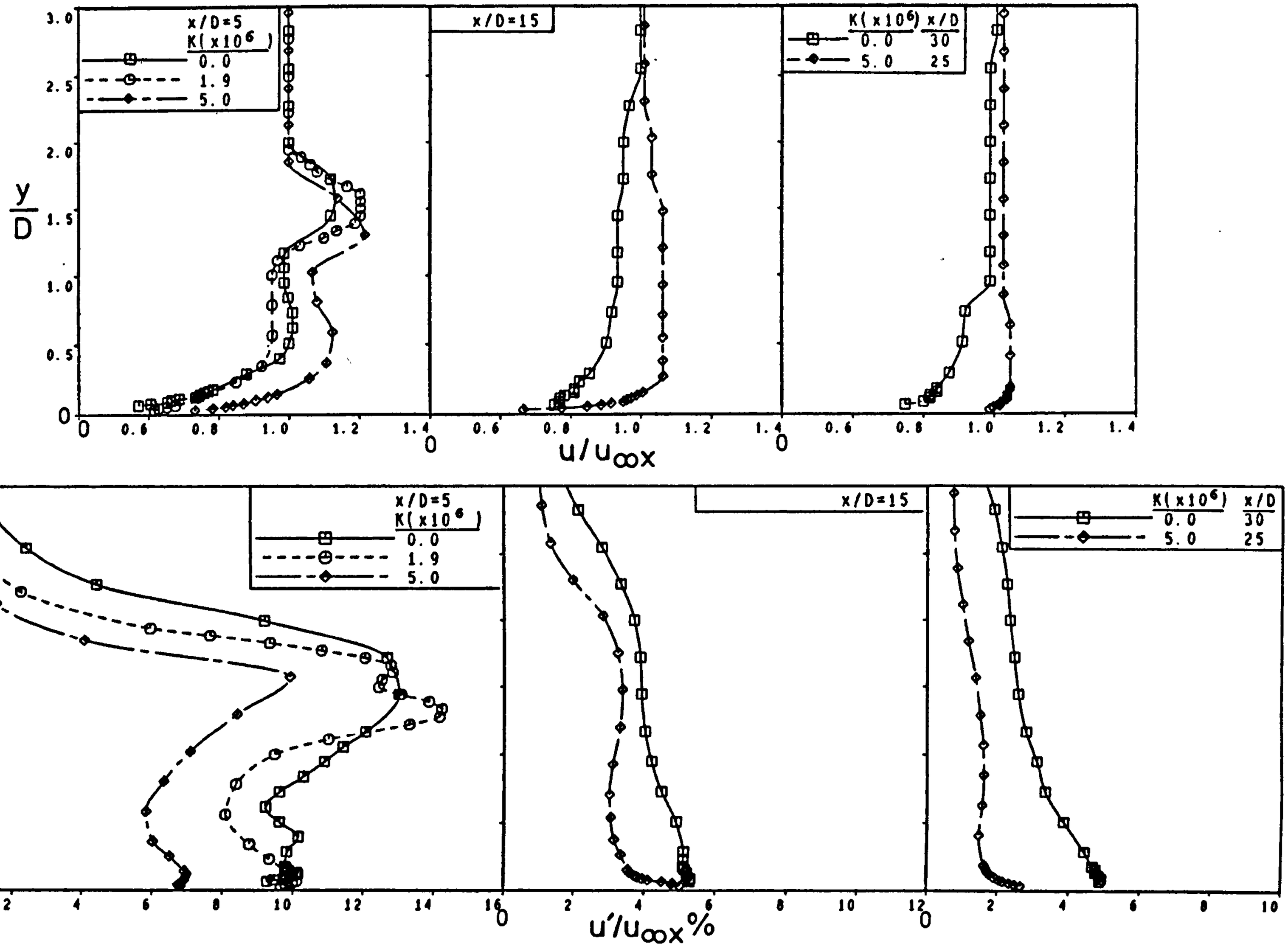

Fig. 8.13 Mean velocity and turbulence intensity profiles in the presence of both injection and acceleration, M≈1.5.

acceleration condition, indicating greater transfer close to a hole and at zero acceleration.

The effect of the cooling jets on the downstream surface heat transfer in the presence of acceleration is shown in Fig. 8.14. The figure shows that injection always causes an increase in the heat transfer coefficient. The laterally averaged heat transfer coefficients with acceleration normalized by their corresponding no injection values are increased largest near the injection location and decreased monotonically with distance downstream, and further enhanced as the blowing rate is raised. This effect is seen to be magnified by acceleration. The curves are generally of similar shape with the exception: the peak in the normalized average heat transfer coefficient observed at K=0.0, at about x/D=15 for M=2.0 is still evident at higher values of K, but has become progressively less distinct with acceleration; the jets close to the holes spread less with acceleration far downstream so that interaction between neighbouring jets is less intensive than at K=0.0.

Apparently, even in accelerating flows injection always reintroduces strong turbulence enhancing the heat transfer coefficient. However, at moderate favourable pressure gradients, full recovery of the enhanced heat transfer coefficients to levels of those at zero pressure gradient does not take place until far downstream (x/D>45), as seen in Fig. 8.15, a plot of the ratio $\bar{h}_{MF}/\bar{h}$ as a function of x/D. The figure shows that the heat transfer coefficient under the film is slightly reduced by acceleration, but the effect diminishes from about x/D=30. At locations close to the holes, the heat transfer coefficient with acceleration, $\bar{h}_{MF}$, is reduced by 3 to 8 percent of that for zero acceleration, $\bar{h}$. Beyond about 5 diameters downstream, the reduction in $\bar{h}_{MF}$ for almost all of the blowing rates used increases further to about 10 percent of $\bar{h}$. Farther downstream, $\bar{h}_{MF}$ rises and becomes of similar magnitude to $\bar{h}$ as the region subjected to the constant acceleration ends. As mentioned above, the mainstream acceleration suppresses the injection induced turbulence, Jabbari and Goldstein [39] using two staggered rows of holes observed a slight drop in the laterally averaged heat transfer coefficient of cooling films

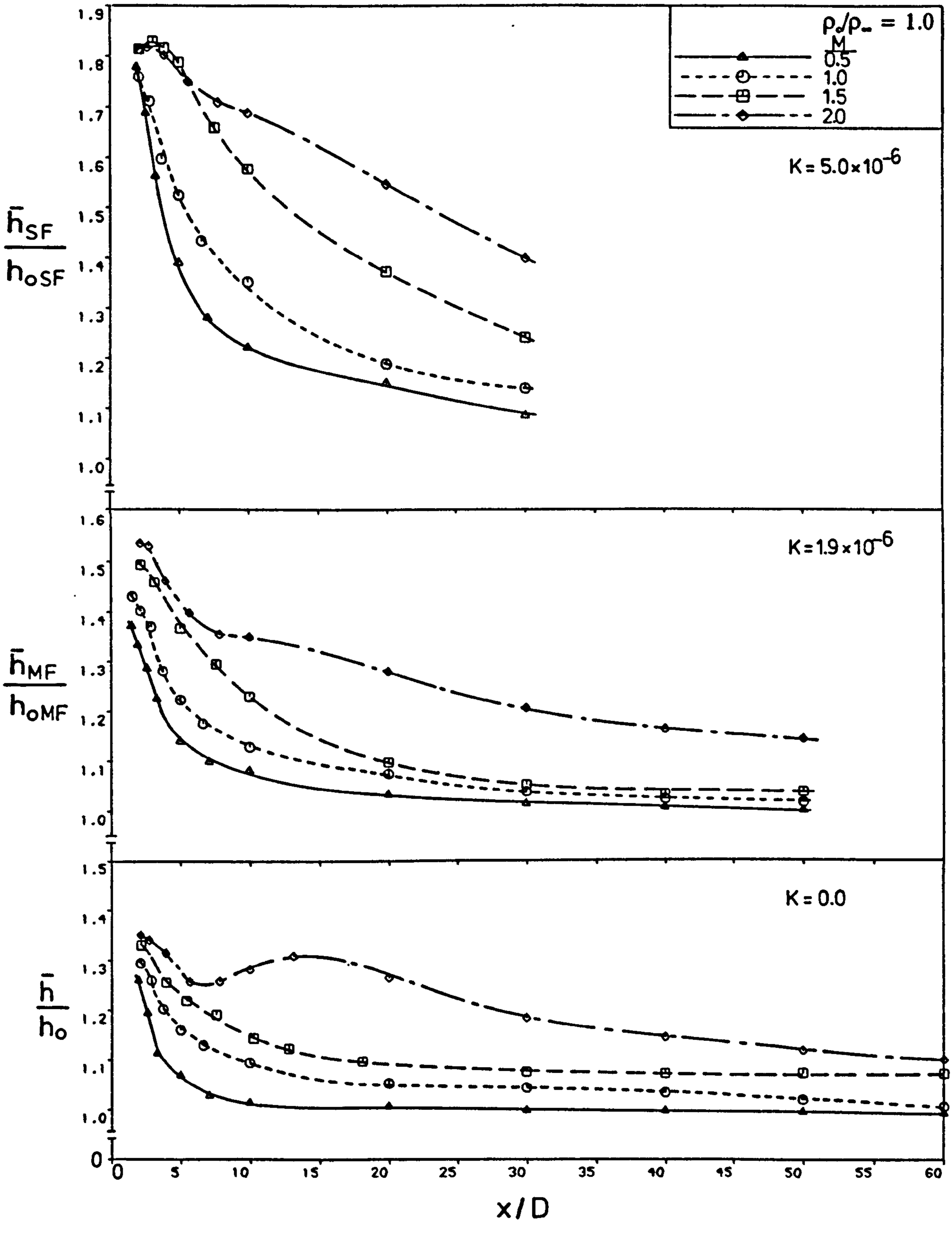

Fig. 8.14 Variation of the laterally averaged heat transfer coefficient downstream of injection at 35° through a row of holes.

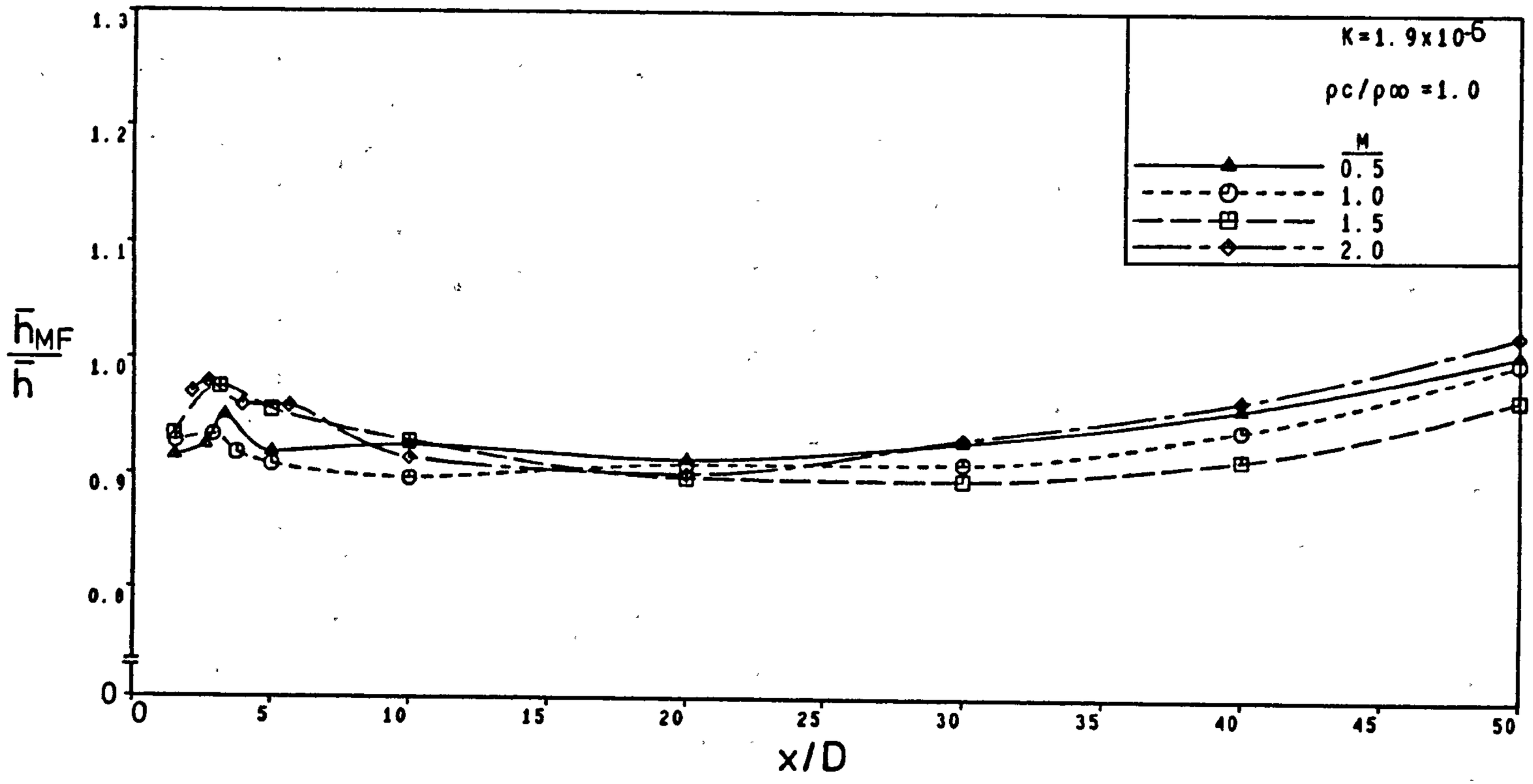

Fig. 8.15 Effect of moderate mainstream acceleration on the laterally averaged heat transfer coefficient, row of holes, α=35°.

for M>1.0 by an acceleration of about $1.0x10^{-6}$. Liess [24], and Hay et al [26], both employing similar injection configuration to the one in the current study, reported a decrease in the spanwise averaged heat transfer coefficient in the presence of a mild pressure gradient.

It can also be seen in Fig. 8.15 that in the presence of a moderate favourable pressure gradient, the variation of the ratio of the heat transfer coefficient $\bar{h}_{MF}/\bar{h}$ with the blowing rate is small and is within the inaccuracy of the experimental measuring technique. Firm conclusions regarding M are therefore difficult to draw. Close to the holes the disparity in behaviour of $\bar{h}_{MF}/\bar{h}$ between the blowing rates may be explained by the complex characteristics and steep gradients of the three-dimensional heat transfer coefficients under the film. The trends indicate that close to the injection site, the effect of acceleration is most pronounced at weak injection rates, whereas farther downstream, the opposite occurs. An exception to this is the case for M=2.0, but as seen in Fig. 8.14 the heat transfer coefficient $\bar{h}_{MF}$ was distinctly high for M=2.0 far downstream.

As the patterns of interference fringes of equi-recession at zero and favourable pressure gradient conditions do not differ greatly (see Fig. 8.12), one would expect the trends of the ratios of local and lateral average heat transfer coefficients downstream of injection would generally be somewhat similar as verified in Fig. 8.16, a plot of the distribution of the centreline coefficients ratio, $\hat{h}_{MF}/\hat{h}$, in the streamwise direction, where the centreline coefficient is little reduced by acceleration.

In the presence of strong favourable pressure gradient ($K=5.0x10^{-6}$), a more definite variation of the reduced cooling film heat transfer coefficient with M is observed (Fig. 8.17). In general, the strong mainstream acceleration appears to significantly lower the heat transfer coefficient with injection all the way downstream particularly at lower M's. This behaviour was also observed by Hay et al [26]. The lateral average heat transfer coefficient is now reduced by about 20% and falls further, by 27%, for low blowing at locations farther downstream. As the blowing rate is increased, $\bar{h}_{SF}$ ranges

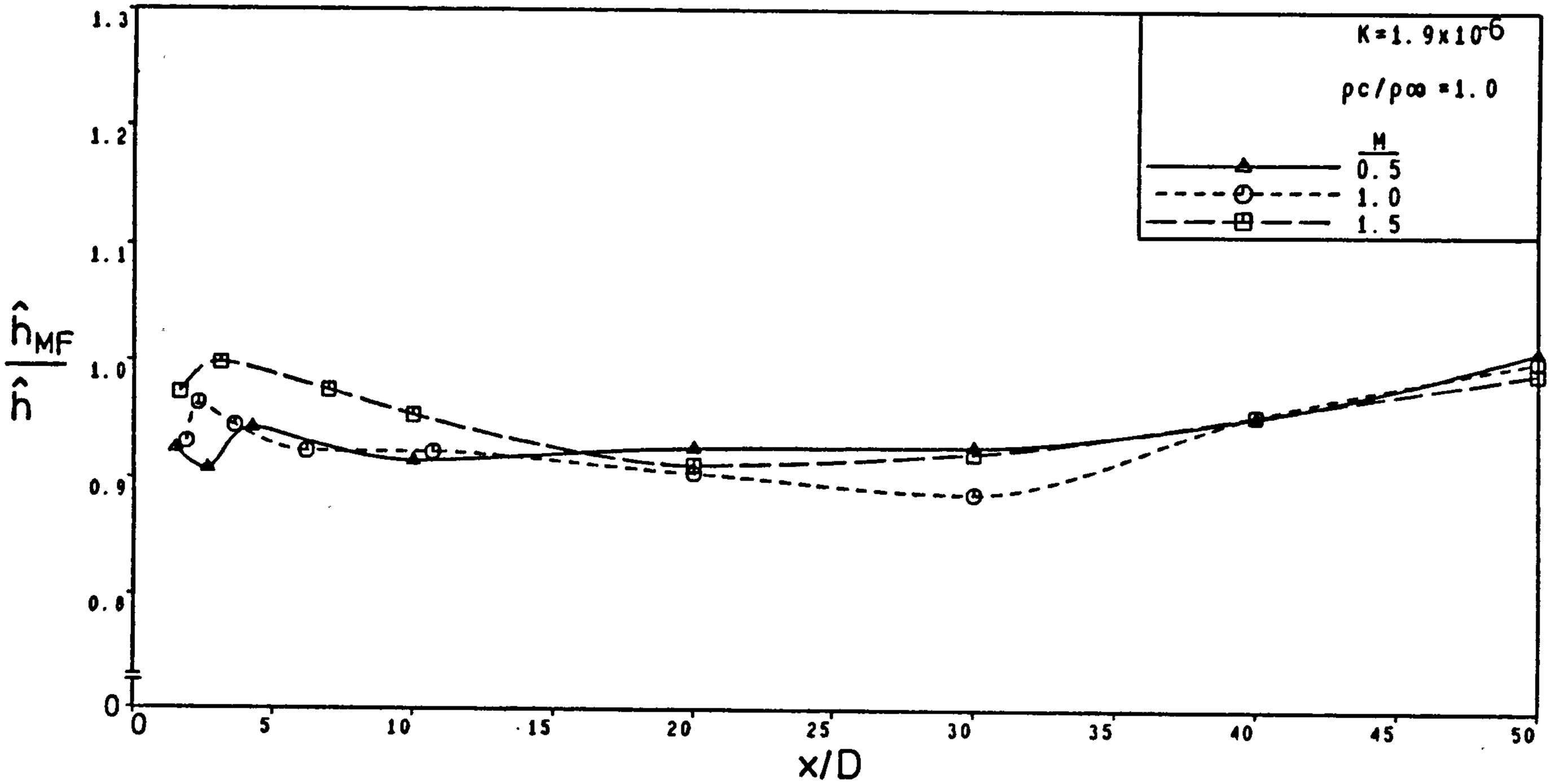

Fig. 8.16 Effect of moderate mainstream acceleration on the centreline heat transfer coefficient, row of holes, α=35°.

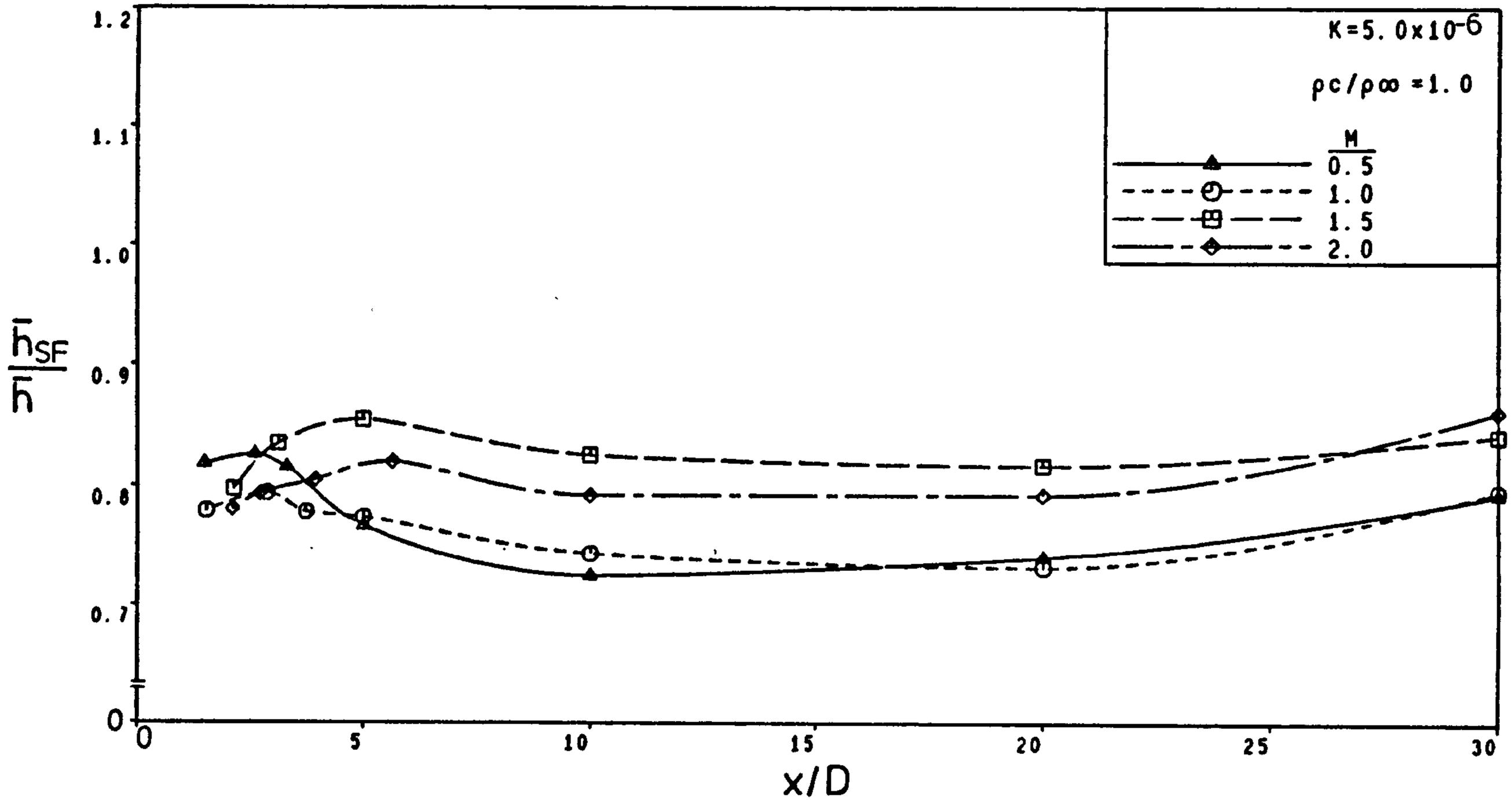

Fig. 8.17 Effect of strong mainstream acceleration on the laterally averaged heat transfer coefficient, row of holes, α=35°.

between 80% of the value for the zero pressure gradient close to the injection point to 86% far downstream. This distinct behaviour of $\bar{h}_{sp}/\bar{h}$ with M may be interpreted by the fact that at $K=5.0\times10^{-6}$ the jets penetrate the thin boundary layer ($\delta/D\approx0.6$ at $x/D=5$) and encounter the high mainstream velocity. As the blowing rate is raised, injection creates greater disturbance in the mainstream boundary layer, and therefore resists more strongly the domination of the imposed pressure gradient in suppressing the injection induced transport eddies close to the wall. It is worth noting also that the differences in the values of $\bar{h}_{sp}/\bar{h}$ resulting from varying M are at most 10%, which are not far from the uncertainties associated with the curves themselves.

In order to study the influence of mainstream acceleration on the cooling film heat transfer coefficient more effectively, the average coefficient at the various pressure gradients normalized by that at zero pressure gradient, $(\bar{h})_{o,MF,SF}/(\bar{h})_o$, is plotted in Fig. 8.18 as a function of K with M as parameter at fixed downstream positions. The figure reveals that the laterally averaged heat transfer coefficient approximates to a linear behaviour with the mainstream acceleration parameter; the data do not vary significantly from the fitted line at all downstream positions (within about ±7%). The development of the induced streamwise vortices and mixing between adjacent jets are suppressed with acceleration, resulting in direct reduction in the ratio $\bar{h}/(\bar{h})_o$ with increased K. The overall average reduction in the coefficients ratio for all M tested is about 8% at $K=1.9\times10^{-6}$, and increases to about 19% for $M\geq1.5$ and 23.5% for $M<1.5$ at $K=5.0\times10^{-6}$.

In addition, Fig. 8.18 shows that the influence of blowing rate on $\bar{h}/(\bar{h})_o$ is not so obvious everywhere at $K=1.9\times10^{-6}$, while the influence becomes substantial when K is further increased to 5.0×10^{-6}, particularly at $x\geq5$ diameters downstream.

Suppression of injection induced turbulence by the mainstream acceleration is clearly shown in Fig. 8.19, where the effect of acceleration on the centreline turbulence intensities is seen to be larger than on the centreline mean velocities. Further noteworthy features are,

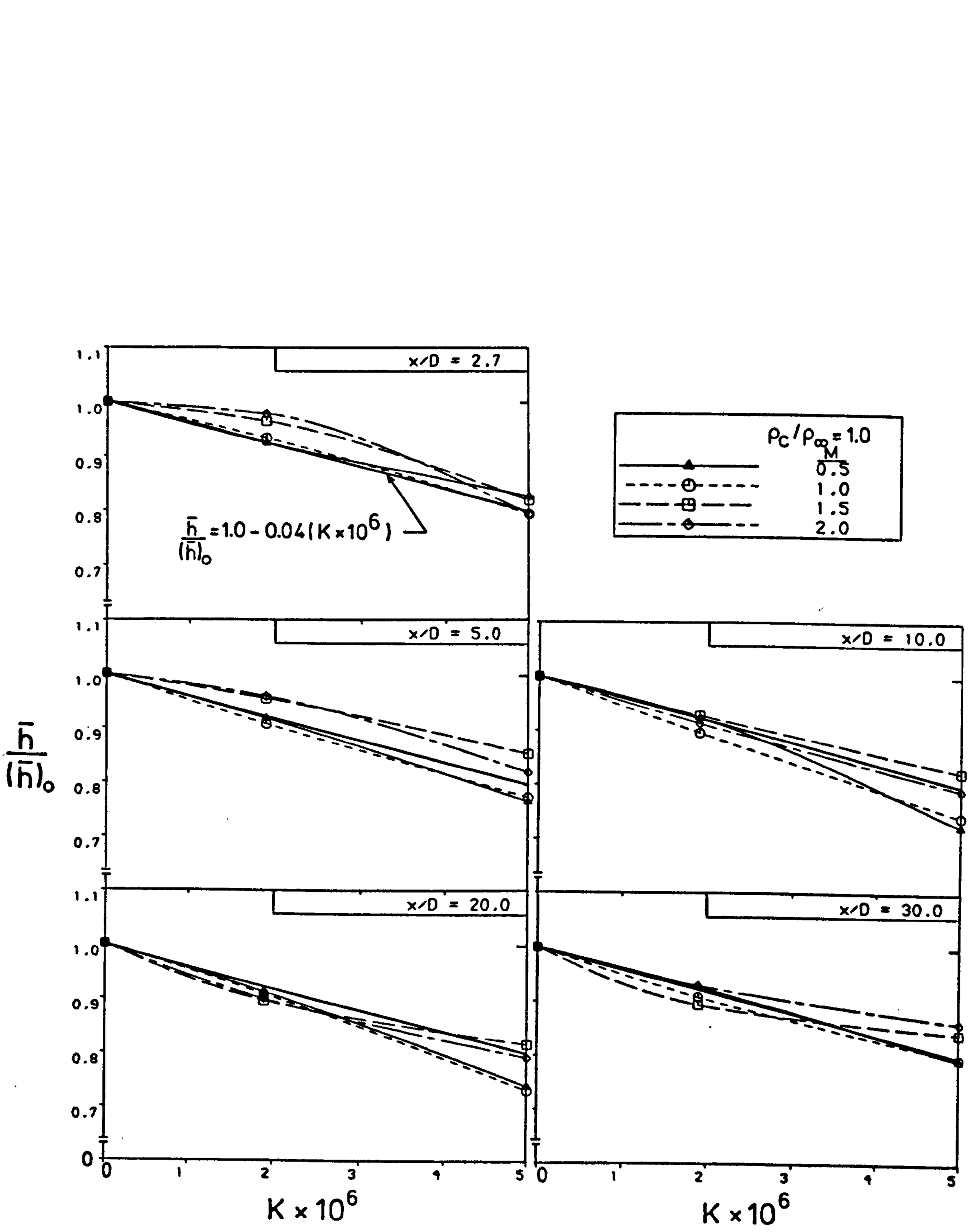

Fig. 8.18 Effect of acceleration parameter on the laterally averaged heat transfer coefficient, row of holes, α=35°.

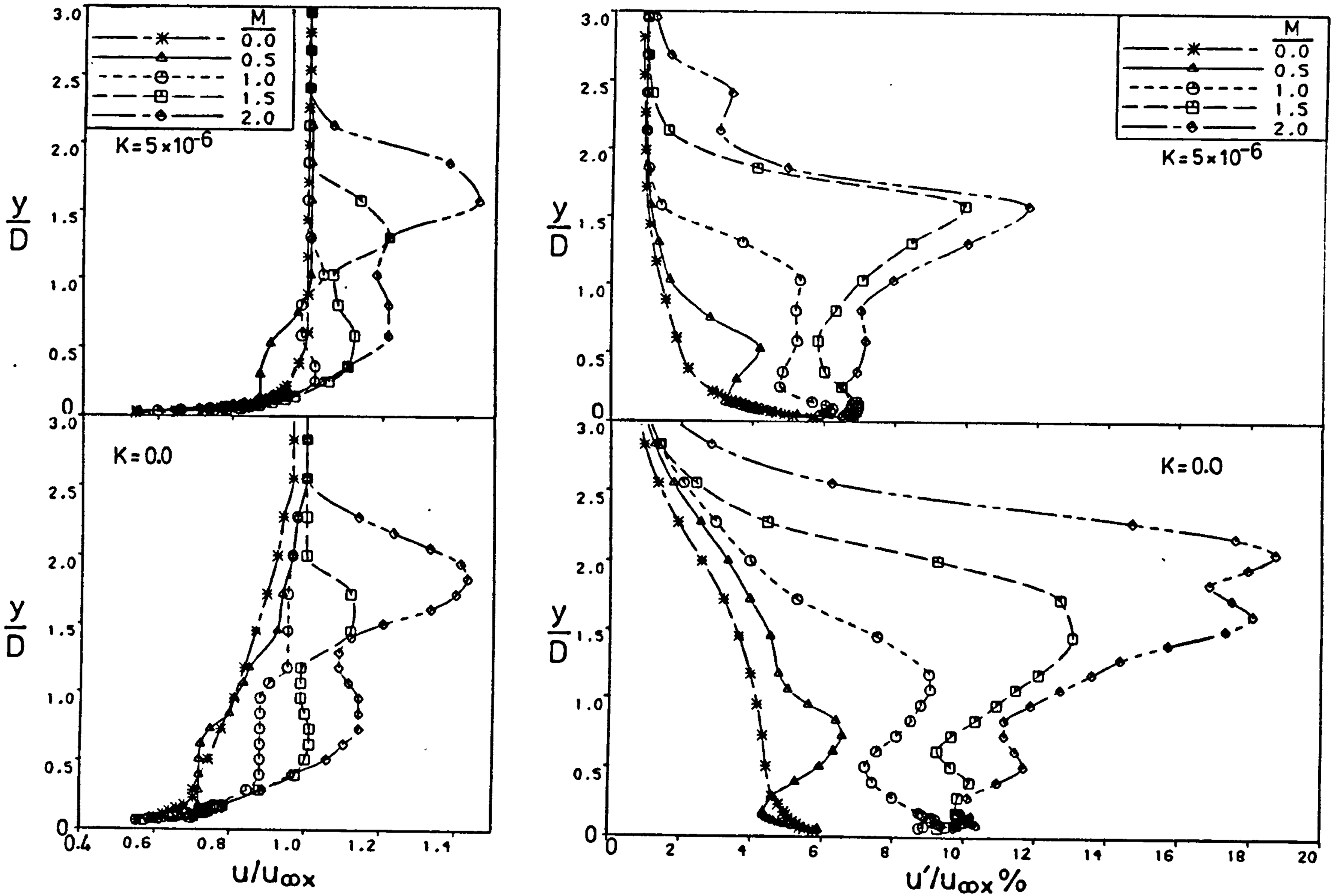

Fig. 8.19 Mean velocity and turbulence intensity profiles at x/D=5 following injection at 35° through a row of holes.

i) The mean velocity peaks appear to have been slightly pushed down closer to the wall by acceleration as the boundary layer is thinned.

ii) The peaks appearing in the turbulence intensity profiles correspond to upper or lower edge of a jet core where intensive jet-mainstream mixing takes place.

iii) As M is increased, jet penetration is higher and the turbulence intensity is enhanced as observed in the mean velocity and turbulence intensity profiles.

The most striking acceleration effect of all is the amount by which the injection introduced turbulence, and hence heat transfer, is reduced, including the region close to the wall.

8.4 COMBINED EFFECTS OF ACCELERATION AND DENSITY RATIO

The preceding discussion of the film cooling data in the presence of a favourable pressure gradient was for coolant to mainstream density ratio of unity. The cooling film heat transfer coefficient decreased with increase in K. Further, it was seen that the influence of K on h at a magnitude of 1.9×10^{-6} was relatively small; one would expect a similar behaviour when the density ratio is raised by 52% created by carbon dioxide injection. Hence, it was felt that the combined influence of K and ρ_c/ρ_∞ on h can be more effectively revealed at the higher value of K ($=5.0\times10^{-6}$), and the investigation was carried out only in the presence of strong favourable pressure gradient.

The tests with $\rho_c/\rho_\infty=1.52$ at $K=5.0\times10^{-6}$ showed the same general trends as those at K=0.0 (Fig. 8.20). The laterally averaged ratio $\bar{h}_{sf}/h_{osf}$ for $M\geq1.0$ increases significantly in the vicinity of the holes with M and decays monotonically with x/D. This time with the pressure gradient, however, the effects of the absence of gross separation on the heat transfer coefficient at M=0.5 after 5 diameters downstream are more pronounced. The attached low-momentum jets, at M=0.5, were maintained in the thin boundary layer, flattened by the strong acceleration, mixed with neighbouring jets and

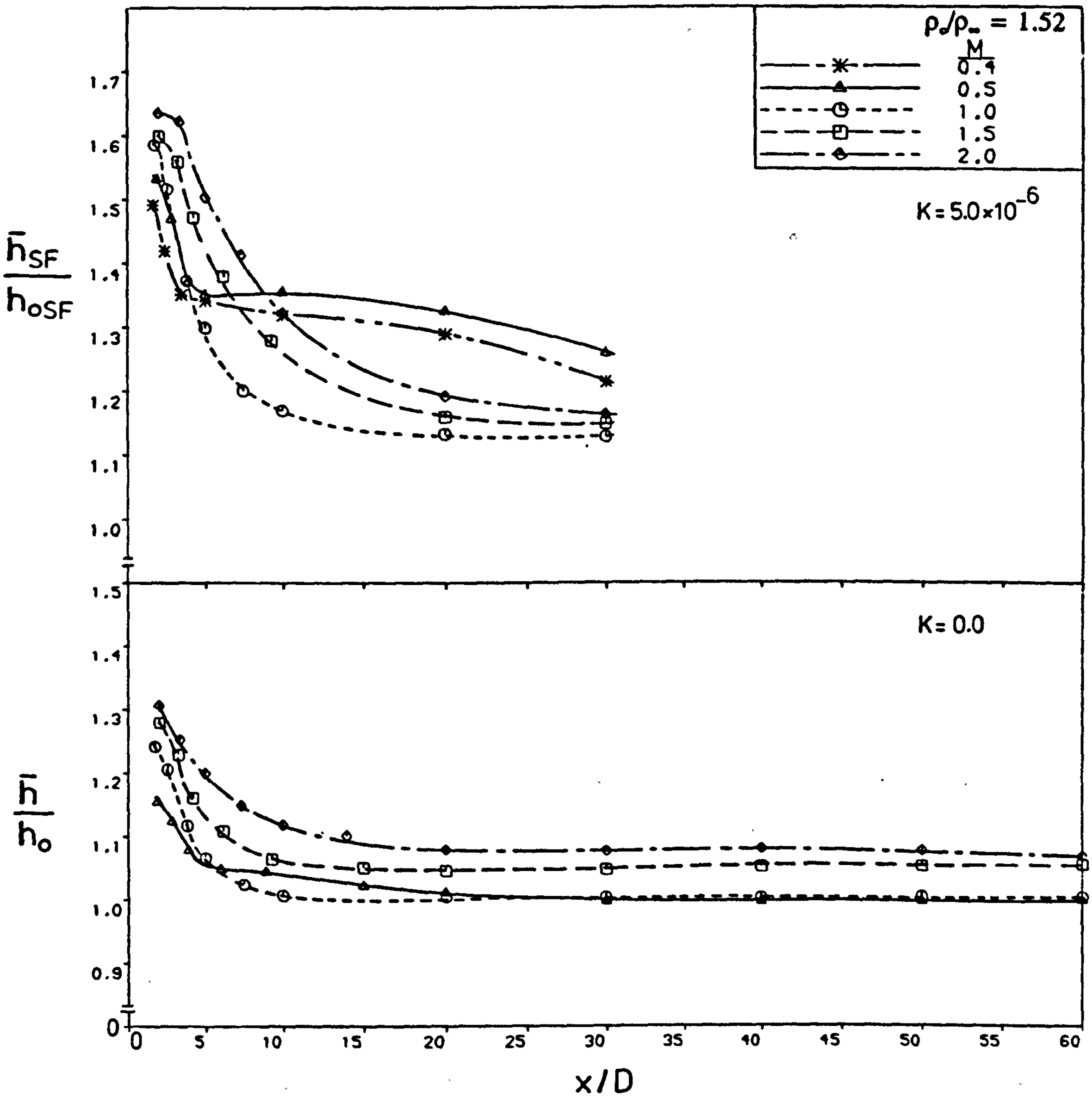

Fig. 8.20 Variation of the laterally averaged heat transfer coefficient downstream of injection at 35° through a row of holes.

persevered longer far downstream. To confirm the behaviour at M=0.5 further tests at a blowing rate of 0.4 were conducted and the results are also shown in Fig. 8.20. The behaviour is identical to the case of M=0.5. However, $\bar{h}_{SF}/h_{oSF}$ have lower values than those for M=0.5. This points to further reduction in jet velocities producing further decrease in the heat transfer coefficient. This also suggests that jet blow-off in the present experimental setup occurs at a momentum flux ratio, I, around 0.16 corresponding to M=0.5.

The dimensionless heat transfer coefficient $\bar{h}_{SF}/\bar{h}$ for carbon dioxide injection as a function of x/D with M as parameter is given in Fig. 8.21. In general, the curves for $1.0 \leq M \leq 2.0$ with CO_2 injection have the same form as those with air injection (Fig. 8.17) at the blowing rates M<1.5. This is probably because the velocity ratio, u_j/u_∞, rather than M or I is the correlating parameter for the heat transfer data in the strong injection regime [32], which is <1.5 for the highest M covered with CO_2 injection ($u_j/u_\infty \approx 1.3$). The factor by which acceleration has now reduced the cooling film heat transfer coefficient is about 28.5% at regions of 10 to 20 diameters downstream. The influence of K on $\bar{h}$ is only slightly stronger than in the case of $\rho_j/\rho_\infty=1.0$ at M<1.5 where the factor reached about 27%. However, the small recovery of $\bar{h}_{SF}/\bar{h}$ close to the injection location observed for air injection is not as strong for carbon dioxide, whereas its recovery beyond x/D=20 is almost identical. The overall average reduction in $\bar{h}$ is about 27%. It has been shown earlier that the characteristics of the heat transfer coefficient at $\rho_j/\rho_\infty=1.52$ for M=0.5 belong to the weak injection regime. The distinct behaviour of $\bar{h}_{SF}/\bar{h}$ of remarkably reduced influence of acceleration for M=0.5 in Fig. 8.21 at locations further than 5 diameters downstream, is explained by the substantial increase in $\bar{h}_{SF}$ at M=0.5 observed in Fig. 8.20. A further comment should be made that the ratio $\bar{h}_{SF}/\bar{h}$ at $\rho_j/\rho_\infty=1.52$ appears to be insensitive to the blowing rate for strong injection.

The effect of acceleration of $K=5.0\times10^{-6}$ on the heat transfer coefficient at density ratios above unity is shown to differ only slightly in manner and

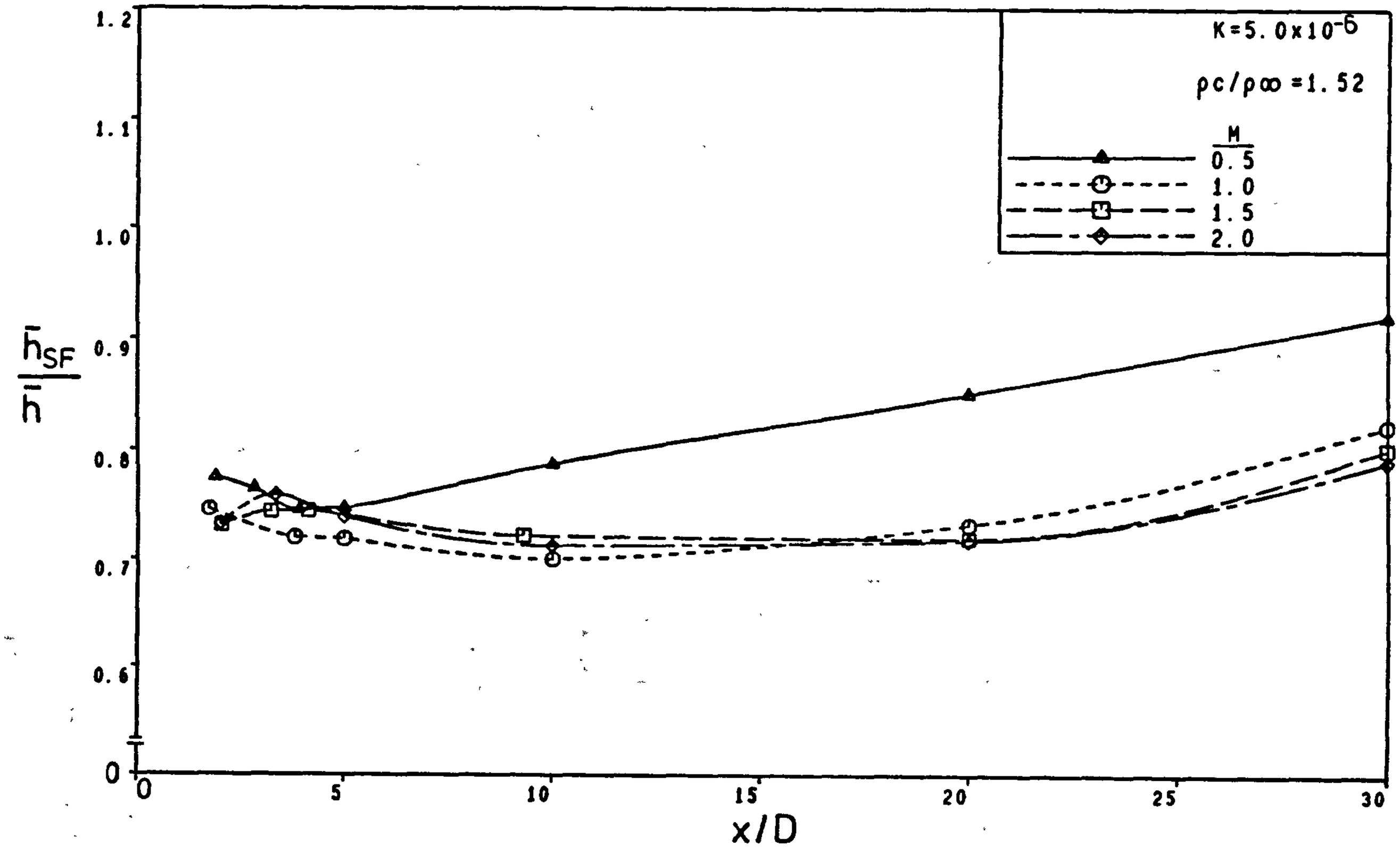

Fig. 8.21 Effect of strong mainstream acceleration on the laterally averaged heat transfer coefficient, row of holes, α=35°.

magnitude to the effect at density ratio of one. An acceleration of $1.9x10^{-6}$ would, therefore, be expected to yield effects which also do not differ too greatly when ρ_j/ρ_∞ is raised from 1.0 to 1.52.

The influence of varying the density ratio from 1.0 to 1.52 at constant acceleration $K=5.0x10^{-6}$ on the heat transfer coefficient is shown in Fig. 8.22. The data are presented as lateral distribution of the local heat transfer coefficient for M ranging from 0.5 to 2.0 at x/D locations of 3 and 25. Fig. 8.22 also gives some insight into the influence of strong favourable pressure gradient on the spanwise distribution of local heat transfer coefficient with injection. The noteworthy points from the figure are summarized as follows,

i) At x/D=3, and for $0.5 \leq M \leq 2.0$, a substantial decrease in the heat transfer coefficient ratio h_{SF}/h_{oSF} of around 20% occurs when ρ_j/ρ_∞ is increased by 52%. As stated earlier at K=0.0, this behaviour is interpreted by the fact that the heavier gas injectant has a lower momentum at a fixed value of M, which is reflected in the heat transfer coefficient.

ii) At x/D=25, the decrease in h_{SF}/h_{oSF} when using the denser injectant is observed to be gradual with M, and reaches about 20% at M=2.0. On the other hand, an increase in h_{SF}/h_{oSF} with increase of density ratio is evident for the weak injection regime ($I \approx 0.16$) at M=0.5. This is similar to what was observed at K=0.0, although here, the increase in the heat transfer ratio is greater.

iii) Close to a hole, a peak in the heat transfer coefficient for M=0.5 is observed at about z/D=0.5 at both density ratios. This is characteristic of low trajectory jets at zero pressure gradient conditions [22, 71], where the centreline value of the heat transfer coefficient is lower than the value near the edge of the jet. As M was increased the peak moved to the centreline and remained there for all M examined.

iv) Far downstream from a hole, the relatively high values of h_{sp} at the edges of a jet for M=0.5 at both density ratios, moved to z/D=1.5 for larger M; an effect of jet spreading, interaction with adjacent jets, and the induced streamwise vortices.

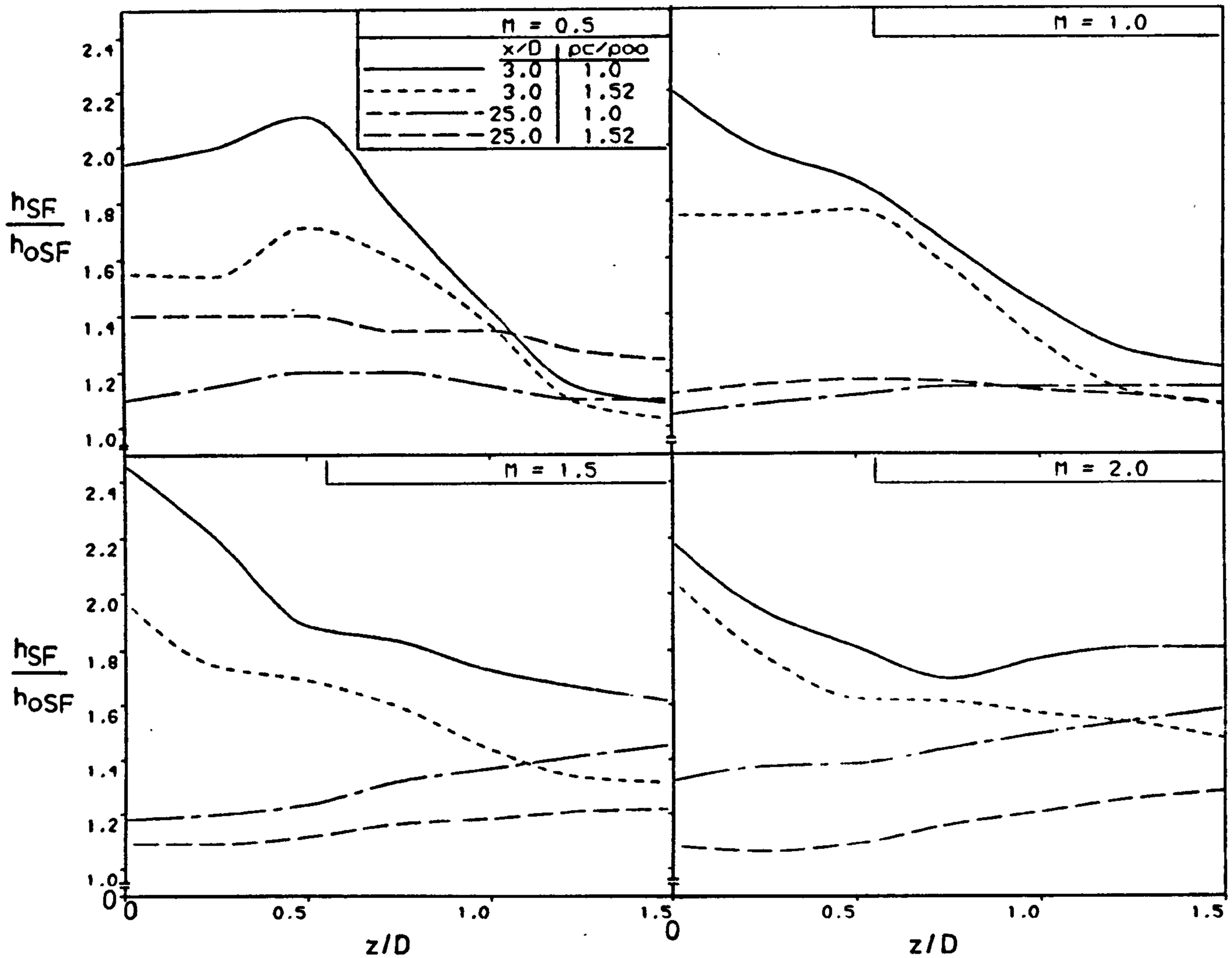

Fig. 8.22 Effect of density ratio on the heat transfer coefficient in the presence of strong mainstream acceleration, $K=5x10^{-6}$, row of holes, $\alpha=35°$.

The results are seen to be consistent with those found at zero mainstream pressure gradient although the strong mainstream acceleration seems to have exaggerated the influence of density ratio.

So far, the influence of mainstream acceleration at fixed density ratios of 1.0 and 1.52, or that of density ratio at fixed acceleration of zero and $5x10^{-6}$ on the heat transfer coefficient are discussed. However, the simultaneous effect of both acceleration and density ratio is further needed as data collected at unity density ratio in the absence of pressure gradients can be converted into data at condition partly characteristic of gas turbines. Fig. 8.23 presents a plot of the ratio of lateral average heat transfer coefficients, $\bar{h}_{sr}/\bar{h}$, as a function of x/D. $\bar{h}_{sr}$ was obtained at $\rho_\infty/\rho_\infty=1.52$ and $K=5x10^{-6}$, and $\bar{h}$ at $\rho_\infty/\rho_\infty=1.0$ and K=0.0. The reduction in the ratio $\bar{h}_{sr}/\bar{h}$ is seen to be comparatively larger than in any preceding condition considered, as both density ratio and acceleration act to reduce the heat transfer coefficient. The conversion factor of h for $M\geq1.0$ is on average about 30% close to a hole ($x/D<5$), with this average increasing to about 35% further downstream. The singular behaviour of $\bar{h}_{sr}/\bar{h}$ at M=0.5 is again explained by the change of injection regime from strong at the low density jets to weak.

8.5 CORRELATING PARAMETERS

(i) 90° Injection

The parameter correlating film cooling heat transfer coefficient ratio for normal hole injection appeared to be the mass flux ratio, M. Confirmation of this is seen in Fig. 8.24 in which $\bar{h}/h_\infty$ is plotted against M, I, and u_∞/u_∞ for x/D=5 and 20, with the density ratio as the varying parameter. For x/D=20, data collapse at the two density ratios is achieved in all three plots, but for x/D=5, only M gives a satisfactory correlation.

Data correlation is taken a stage further in Fig. 8.25 where $\bar{h}/h_\infty$ is plotted against $(x/D)M^{-0.5}$. Significant deviation from a mean curve occurs only for the highest blowing rate. The decay in $\bar{h}/h_\infty$ looks exponential, and this is confirmed by the log-linear plotting of Fig. 8.26, from which M=2 data are

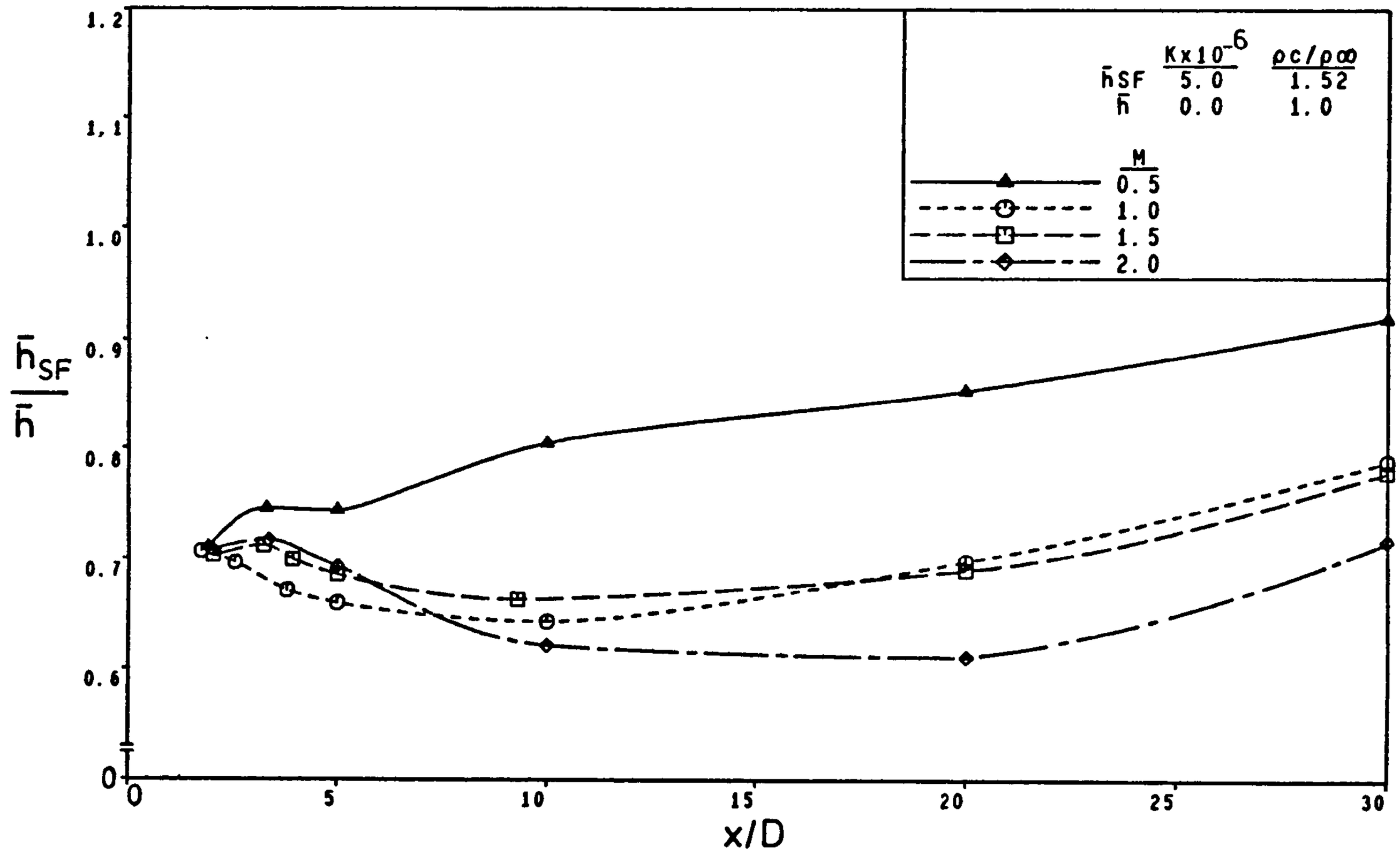

Fig. 8.23 Effect of both the density ratio and strong acceleration on the laterally averaged heat transfer coefficient, row of holes, α=35°.

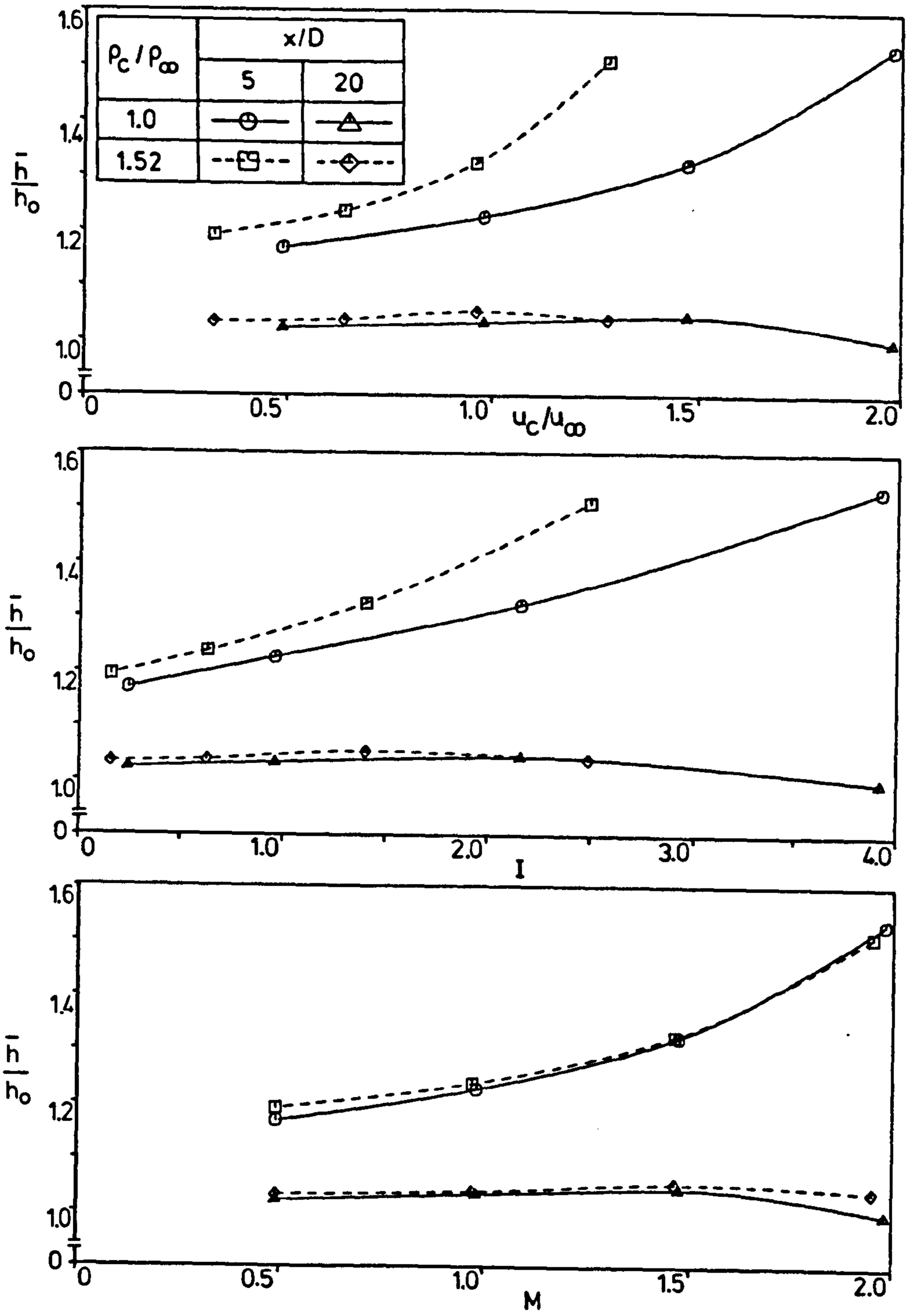

Fig. 8.24 Effect of injection parameters on $\bar{h}/h_o$ for normal injection through a row of holes.

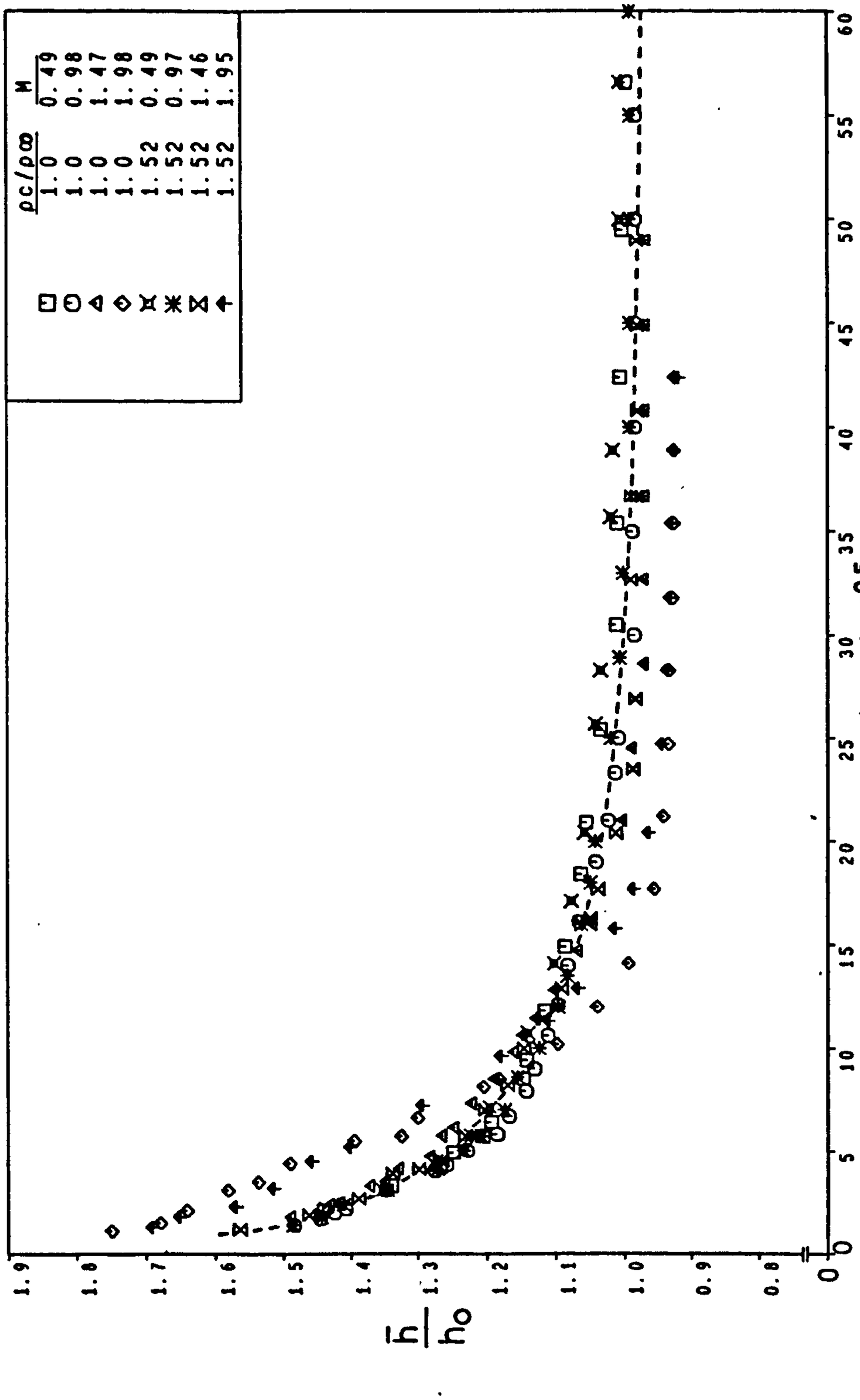

Fig. 8.25 Correlation of $\bar{h}/h_\infty$ for normal injection through a row of holes.

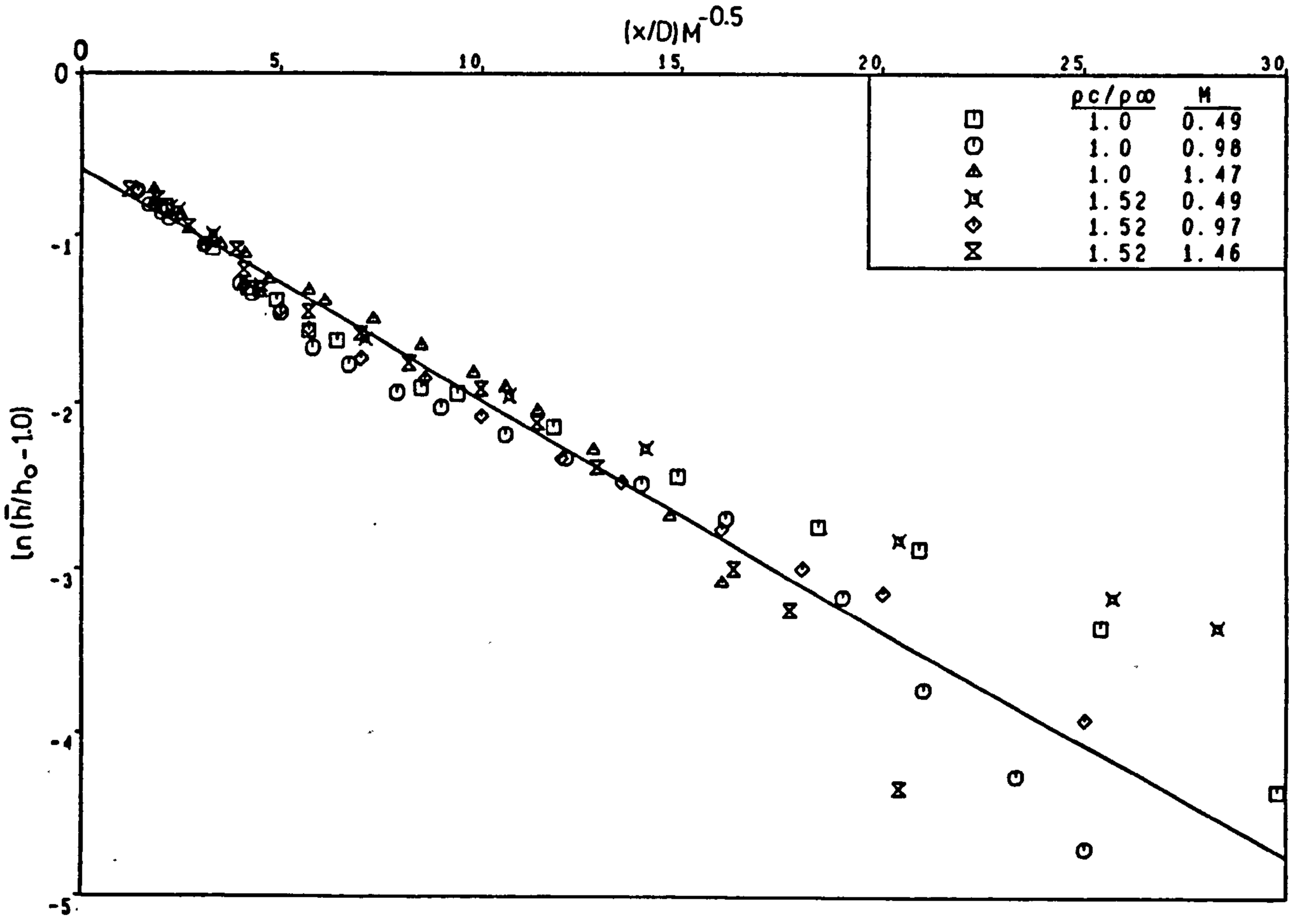

Fig. 8.26 Correlated $\bar{h}/h_o$ data for $x/D \leq 25$ and $0.5 \leq M \leq 1.5$ for normal injection.

omitted. A best-fit line yields a correlation for single row 90° injection as,

$$\bar{h}/h_o = 1.0 + 0.555 \exp\{-0.14(x/D)(M)^{0.8}\}$$

This correlation is applicable to variable coolant to mainstream density ratios, a blowing rate range from 0.5 to 1.5 and for the important dimensionless downstream distances in film cooling of x/D<25. The correlation could also be applied to downstream distances further than 25D as the influence of injection on the heat transfer coefficient there is rather weak.

A measure of the accuracy of the correlation is shown in Fig. 8.27, the experimental results of M=0.5, 1.0 and 1.5 at the density ratios of 1.0 and 1.52 are compared with the curve predicted using the correlation. Good agreement between the experimental data and the correlation is observed. The uncertainty associated with $\bar{h}/h_o$ using this correlation is at most of the order ±5 percent.

(ii) 35° Injection

As has been previously noted, M is not a good correlating parameter for 35° data. With the data at x/D of 5 and 20 plotted in Fig. 8.28 against the injection parameters, u_c/u_∞ is seen to give a better data collapse than either M or I.

The velocity ratio u_c/u_∞ therefore appears to be the key correlating parameter for the 35° data. This is corroborated by the findings of Forth [31], who has reported that for a row of holes at a given velocity ratio, u_c/u_∞, the influence of density ratio, ρ_c/ρ_∞, in the "strong injection" regime is small. Accordingly, if the correlation of the "weak injection" regime, equation (2.2), is written in the following form,

$$\frac{x}{s}\left[\frac{\rho_c}{\rho_\infty}\right]^{-2/3}\left[\frac{u_c}{u_\infty}\right]^{-4/3}$$

and the density ratio term for strong injection conditions is dropped as implied, we are left with,

$$\frac{x}{s}\left[\frac{u_c}{u_\infty}\right]^{-4/3}$$

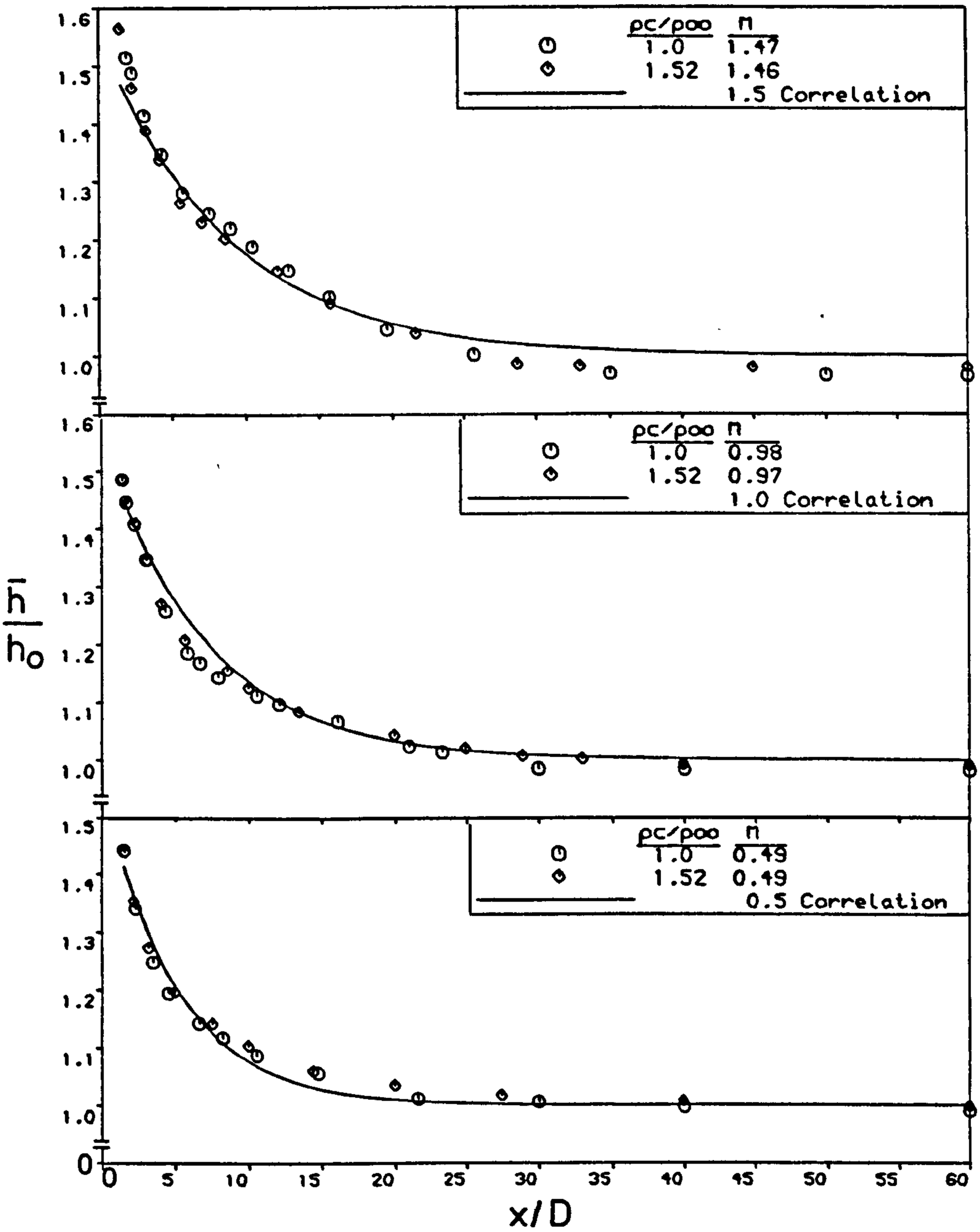

Fig. 8.27 Comparison of predicted and experimental data of $\bar{h}/h_o$ for normal injection.

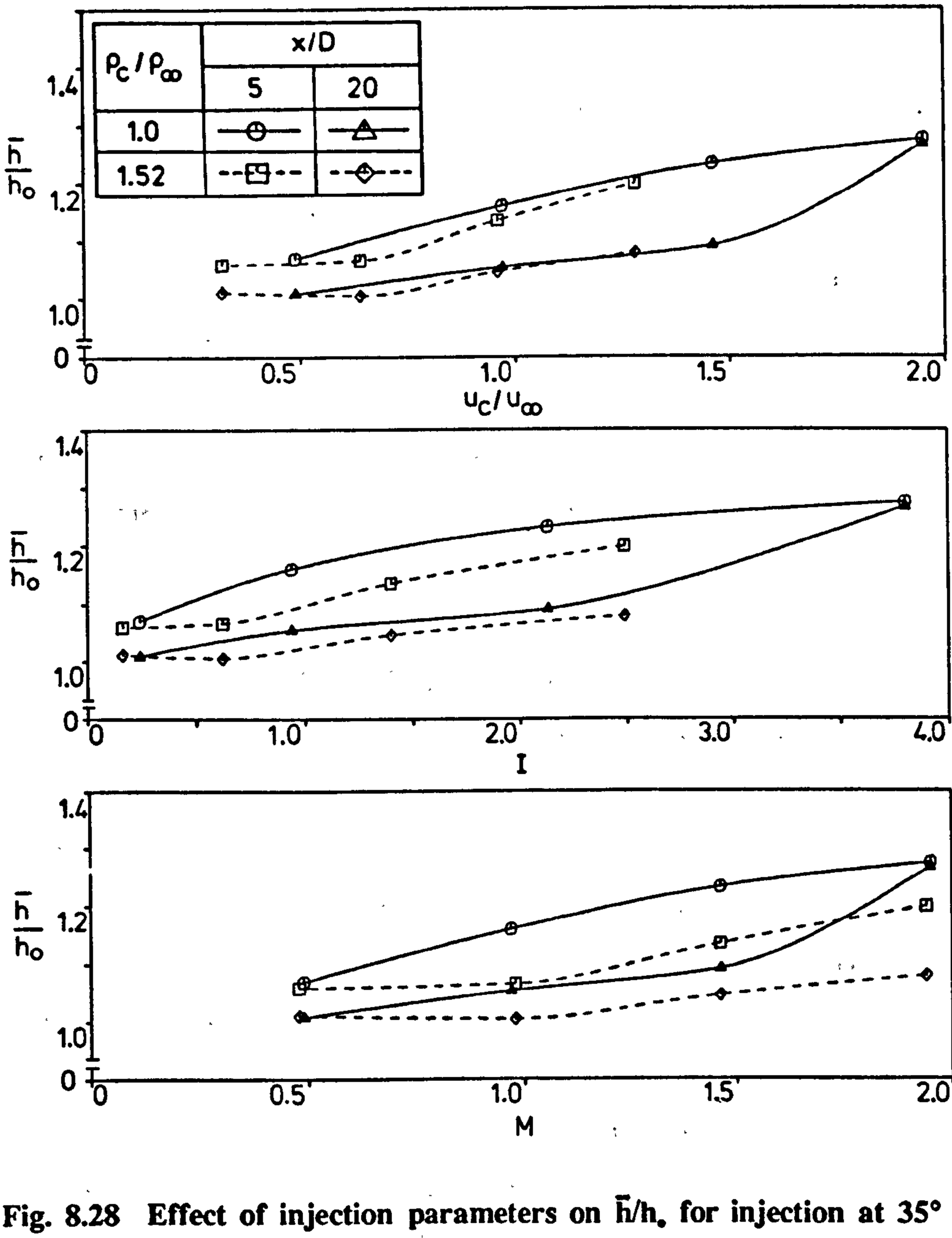

Fig. 8.28 Effect of injection parameters on $\bar{h}/h_o$ for injection at 35° through a row of holes.

Forth and Jones [32] have correlated some single row, inclined hole heat transfer data using $(x/D)(u_\infty/u_-)^{-4/3}$ for the "strong injection" regime (note that the hole diameter, D, was used instead of the slot width, s). This is associated with jet lift-off, which they state will occur above about I=0.1. Below this limit, i.e. in the weak injection regime, data were found to correlate on I (eq. (2.2)).

For the tests reported here, jet lift-off occurred at I about 0.16, and a minimum blowing parameter of 0.5 was used, so that I≥0.16. Strong injection conditions, therefore, prevailed throughout except for the high density injection at M=0.5 where I=0.16. The correlation $(x/D)(u_\infty/u_-)^{-4/3}$ would therefore be expected to apply, and this is verified in Fig. 8.29. This figure also includes results from [22] and [25] which corroborate the use of the velocity ratio as a correlating parameter. The correlation is seen to work best for low values of the parameter, with significant deviation only for the highest blowing rate, low density condition. The dotted mean curve indicated in the figure can be represented by,

$$\bar{h}/h_\infty = 1.025 + 0.35 \exp\{-0.15(x/D)(u_\infty/u_-)^{-4/3}\}.$$

The recommended correlating curve collapses the experimental data excluding the highest velocity ratio case of 2 to within ±7 percent uncertainty as shown in Fig. 8.30.

However, the success of blowing rate, rather than velocity ratio, as a correlating parameter for 90° injection data seems to indicate that a subdivision of the strong injection regime may be needed.

Since the general behaviour of the cooling film heat transfer coefficient under favourable and zero pressure gradients are shown to be somewhat similar (see Figs. 8.14 and 8.20), it would seem logical that the pressure gradient data should correlate with the zero pressure gradient correlating parameter, $(x/D)(u_\infty/u_-)^{-4/3}$. This is clearly shown to be so in Fig. 8.31, where a reasonable collapse of the pressure gradient heat transfer data is achieved.

A correlation attempt which includes the acceleration parameter K to bring together all of the experimental data excluding those at u_∞/u_- of 2 is

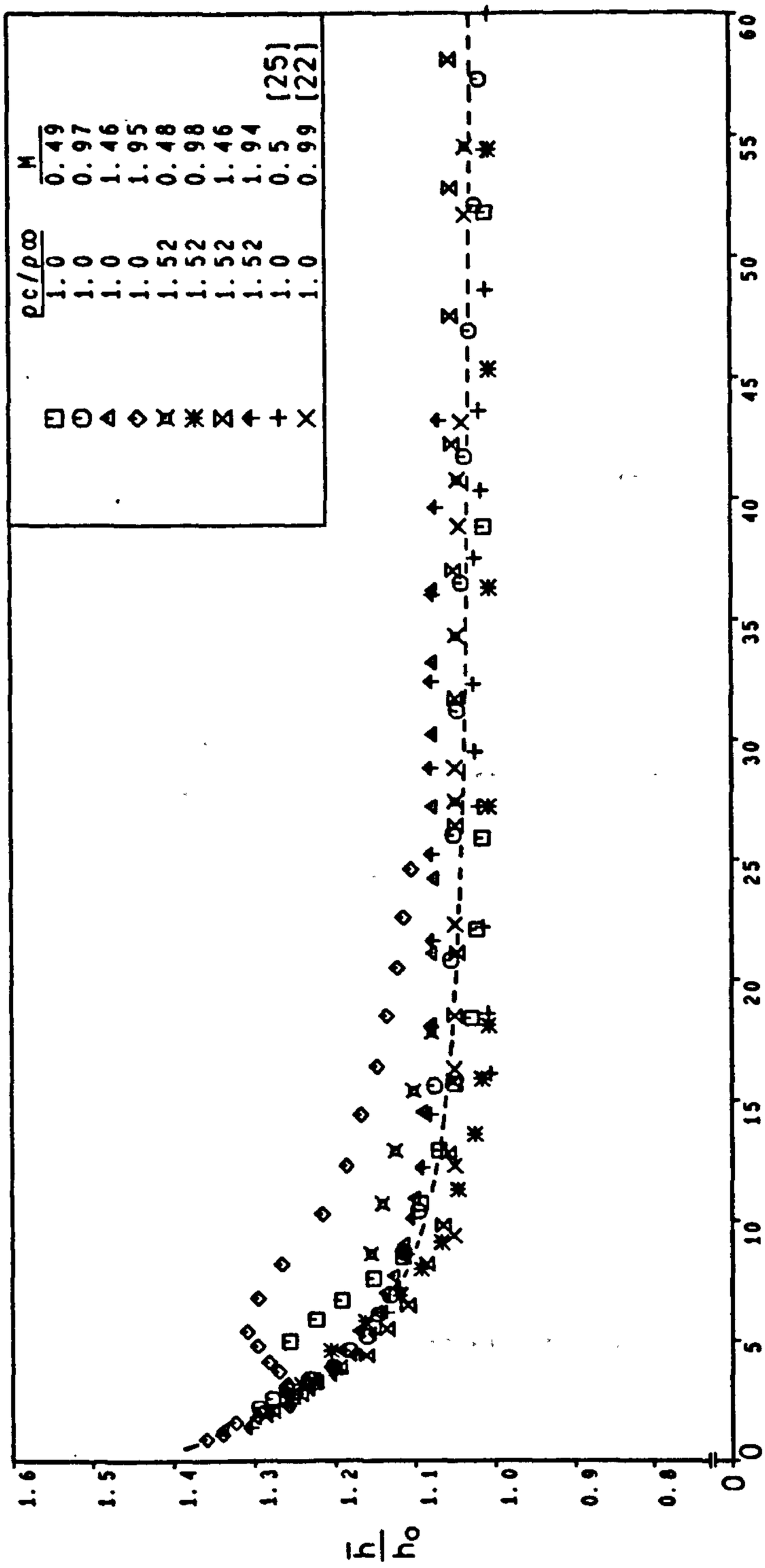

Fig. 8.29 Correlation of $\bar{h}/h_\circ$ for injection at 35° through a row of holes.

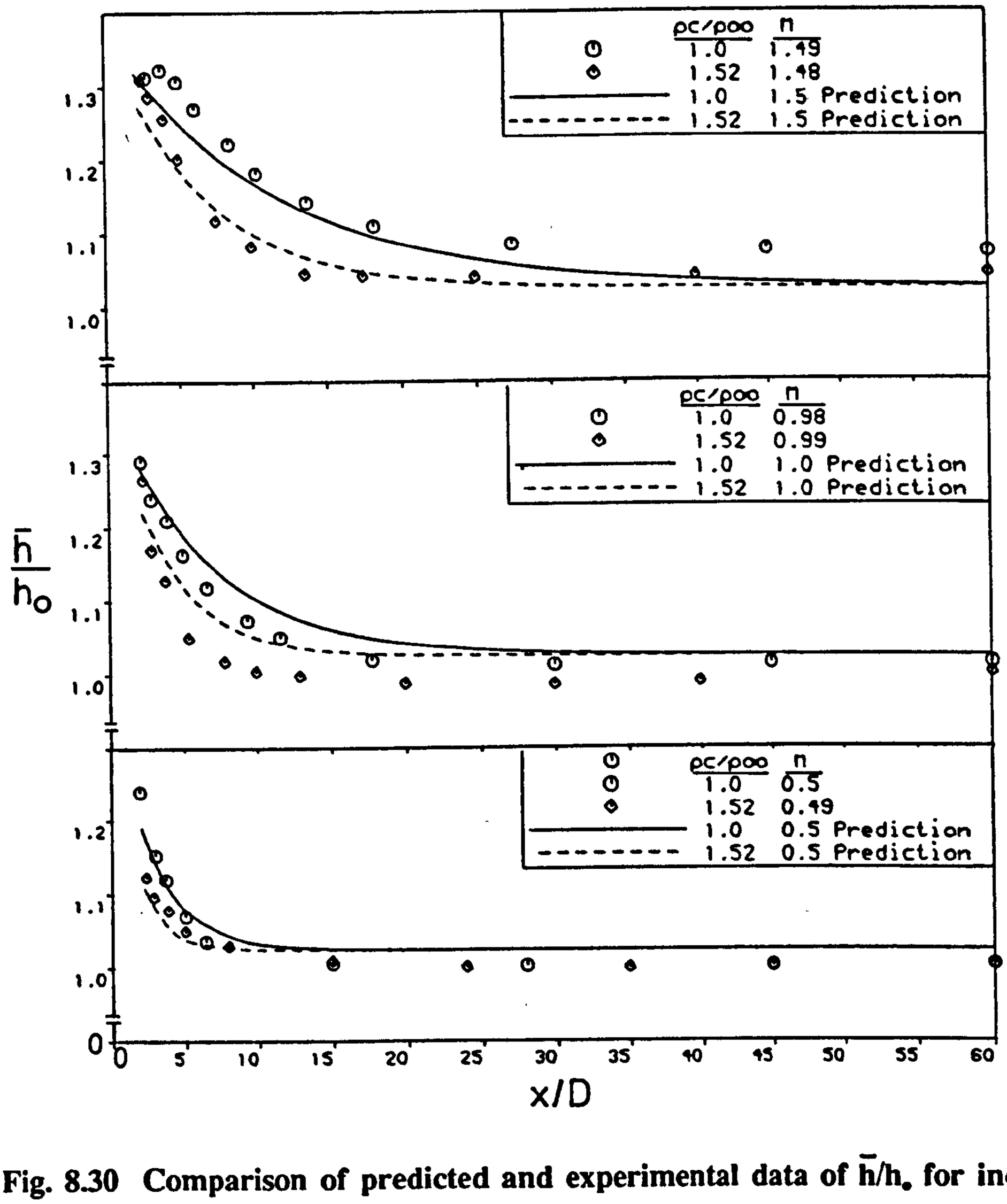

Fig. 8.30 Comparison of predicted and experimental data of $\bar{h}/h_o$ for inclined injection.

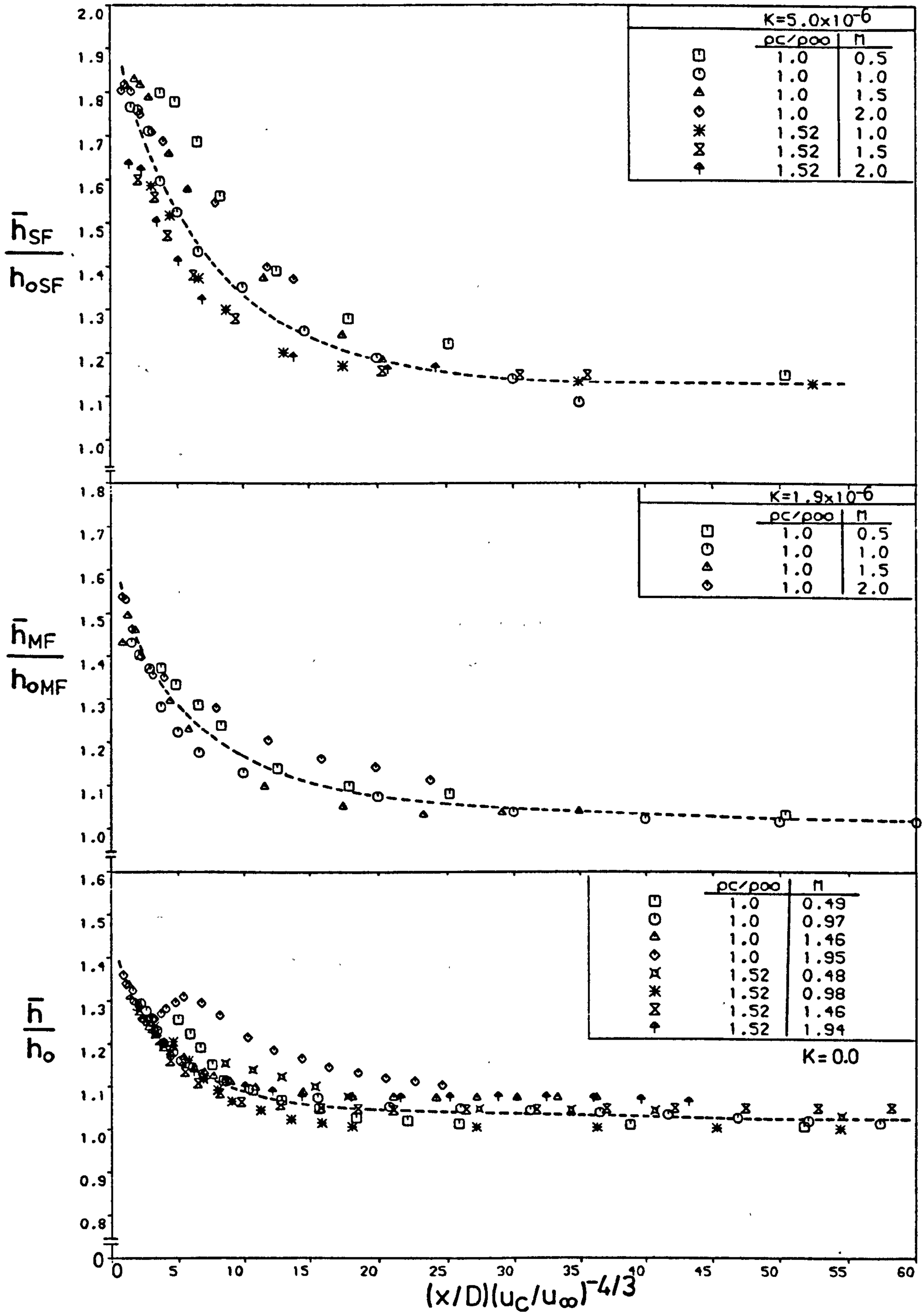

Fig. 8.31 Correlation of the laterally averaged heat transfer coefficient in the presence of mainstream acceleration for injection at 35° through a row of holes.

shown in Fig. 8.32. The correlation incorporates the scaling parameter, $(x/D)(u_\infty/u_-)^{-4/3}$, and that expressing the effect of acceleration at unity density ratio, $[1-0.04(Kx10^6)]$. The scatter, however, is seen to be large particularly for the data of density ratio in presence of acceleration.

8.6 APPLICABILITY OF CURRENT WORK

The importance of the present results is not only in identifying and assessing the effects of density and pressure gradients on the cooling film heat transfer coefficient, but also the possibility of direct application of the results in its current form in turbine blade film cooling calculations.

The range of parameters at which the heat transfer coefficient was measured mostly were within those existing on. a turbine blade: the acceleration parameters $K=1.9x10^{-6}$ and $5x10^{-6}$; the blowing rates M=0.5-2.0 and density ratio $\rho_\infty/\rho_-=1.5$ covered; and the mainstream Reynolds number $Re_D=3.8x10^3$ at the injection location are as found in practice, although the boundary layer displacement thickness ratio at the injection position with zero pressure gradient, $\delta^*/D=0.40$, is rather larger than that typical of blades and vanes, Hay et al [26] have shown that this should have little effect upon the heat transfer coefficient.

The angles of film cooling holes in turbine airfoils on both the pressure and suction surfaces are often in the neighbourhood of 35°, and close to 90° near the leading edge. Furthermore, the spacing of holes to diameter ratio of 3 is as encountered on a blade.

However, the mainstream turbulence intensity of 0.68% was many times lower than experienced on an airfoil, and the results were obtained only over a flat surface rather than a curved surface of a typical blade.

Nevertheless, the present heat transfer data, h/h_o $(=h_f/h_o)$, can be utilized with some available flat plate effectiveness data, η_{aw}, to convey the optimum film cooling conditions for the injection geometries used.

To achieve this, calculation of the change in the local and lateral average heat load distribution created by film injection are required. For a film cooled

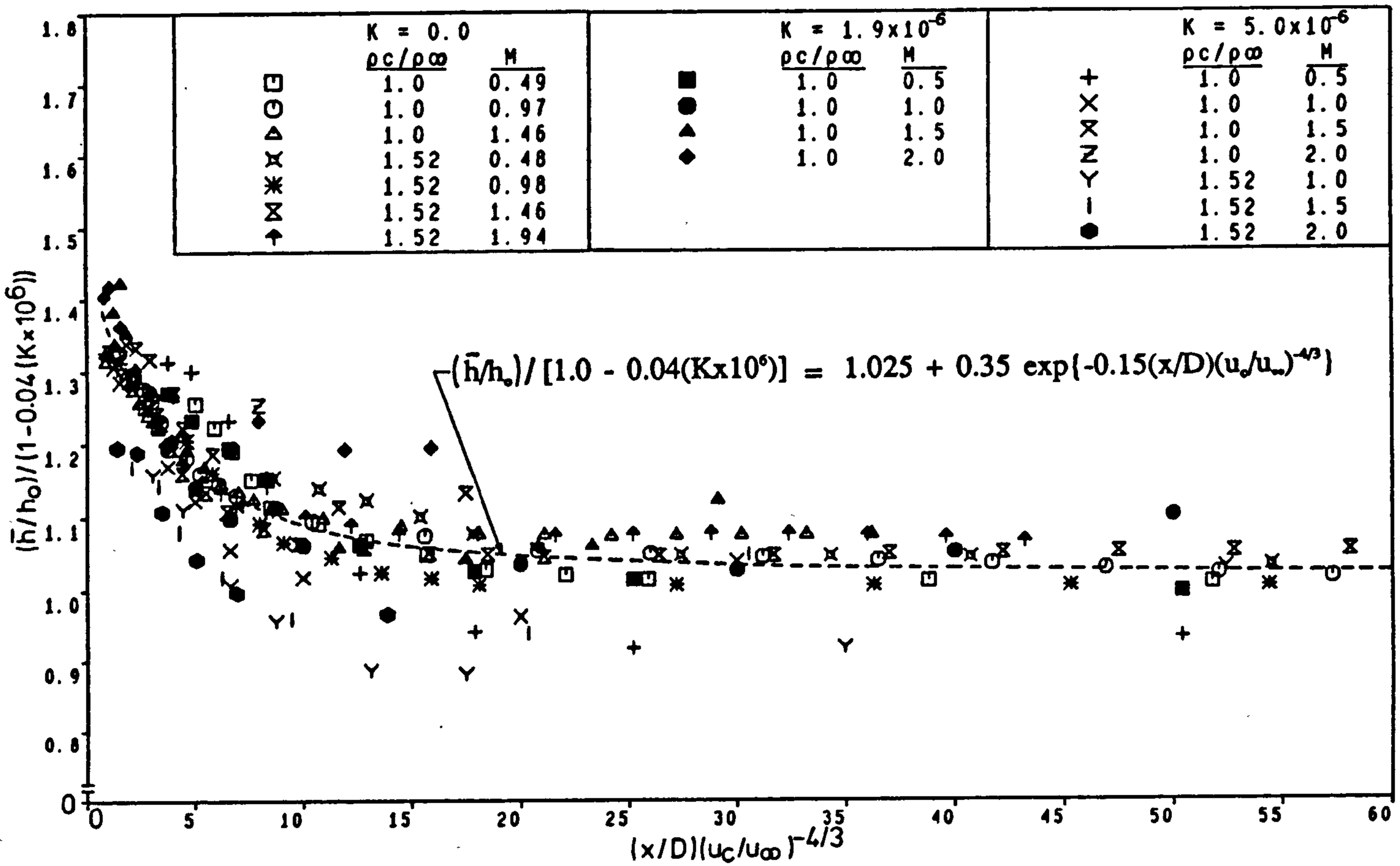

Fig. 8.32 Correlation of $\bar{h}/h_o$ data for $0.0 \le K \le 5x10^{-6}$ and $0.5 \le u_c/u_\infty \le 1.5$, row of holes, $\alpha=35°$.

surface, the heat flux, q_f, expressed as a ratio to that without injection, q_o, is given by equation (1.5),

$$\frac{q_f}{q_o} = \frac{h_f}{h_o}(1 - \eta_{aw}\theta)$$

For modern gas turbine components, the temperature parameter, θ, (equation (1.6)), is typically about 1.67 [106].

The lateral average heat flux ratio, $\bar{q}_f/q_o$, is obtained by numerically integrating the average of the product of the local heat transfer coefficient and the local film effectiveness (equation (1.5) with θ=1.67), and not the product of their averages. Using the latter can produce errors of ±100% in the calculated heat flux near injection locations [106].

Unfortunately, published local effectiveness data downstream of injection through a geometry similar to that of the present work are limited.

Effectiveness data of row of 35° holes acquired from Goldstein et al [40] for a density ratio of 0.85 with zero mainstream pressure gradient, δ^*/D=0.124 and Re_D=2.2x10^4 (Fig. 8.33), is used with the current heat transfer data of unity density ratio to calculate $\bar{q}_f/q_o$. A difference in the density ratio of 15% has been shown by Eriksen and Goldstein [22] to have a small effect on the heat transfer coefficient (of the order of 2%). The displacement thickness and Reynolds number also have a small effect on the heat transfer coefficient [26] and [22] respectively.

Distributions of $\bar{q}_f/q_o$ for the row of 35° holes are displayed in Fig. 8.34 for the four blowing rates covered. The heat flux depends strongly on the blowing rate near the injection location. At M≤1.0, the heat flux is reduced over the whole downstream surface. The largest reduction is about 30% at M=0.5 close to the holes. Further increases in M become detrimental over about the first 20 diameters where an increase of up to about 25% in $\bar{q}_f/q_o$ is seen at M=2. However, further downstream, injection always reduces the heat flux.

The data of Forth [31] for M=0.4 shown in Fig. 8.34 agrees qualitatively with the present data at M=0.5, bearing in mind that Forth's data were obtained for θ=1.0 and $\bar{q}_f/q_o$ calculated from lateral averages of h and η rather

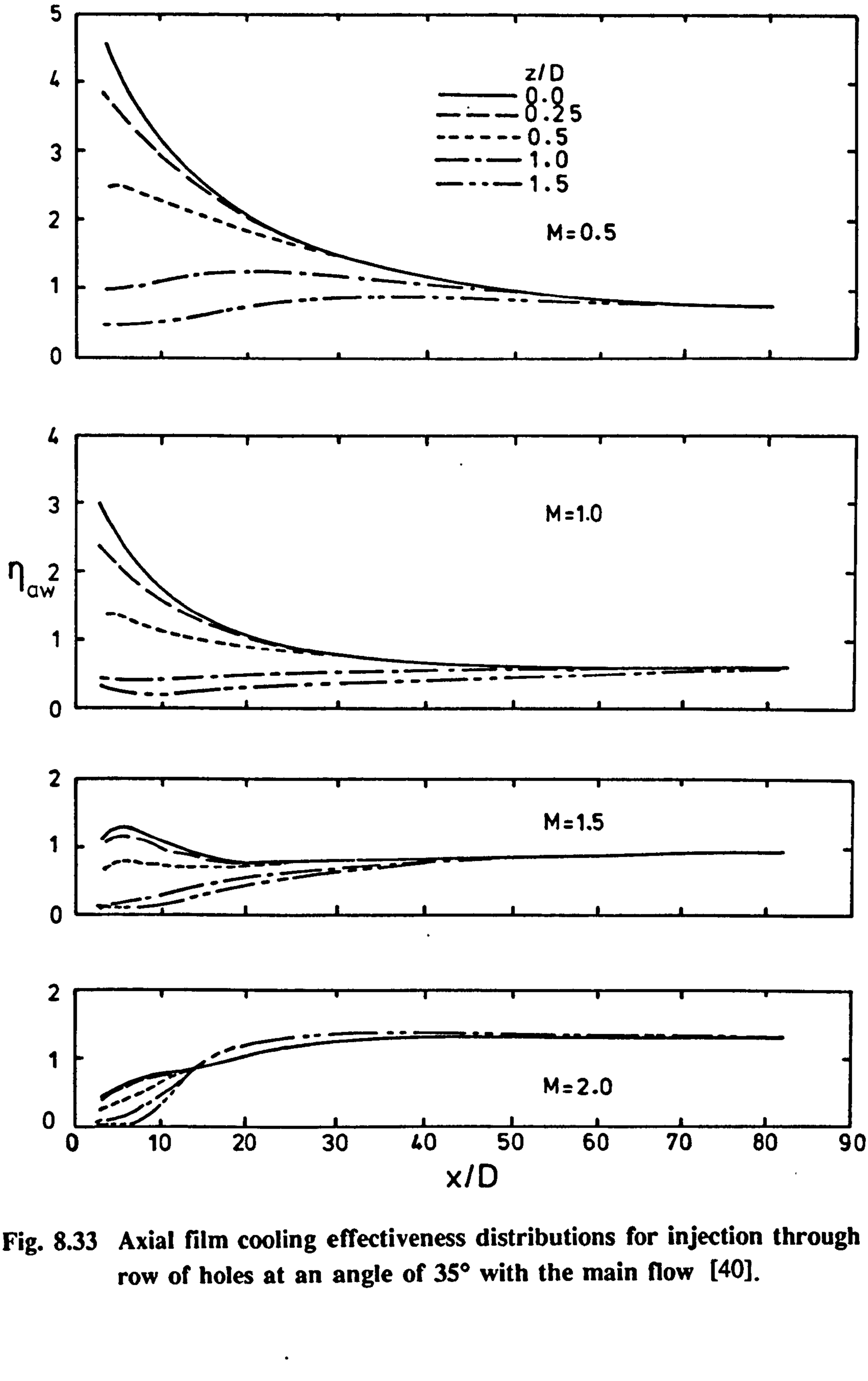

Fig. 8.33 Axial film cooling effectiveness distributions for injection through a row of holes at an angle of 35° with the main flow [40].

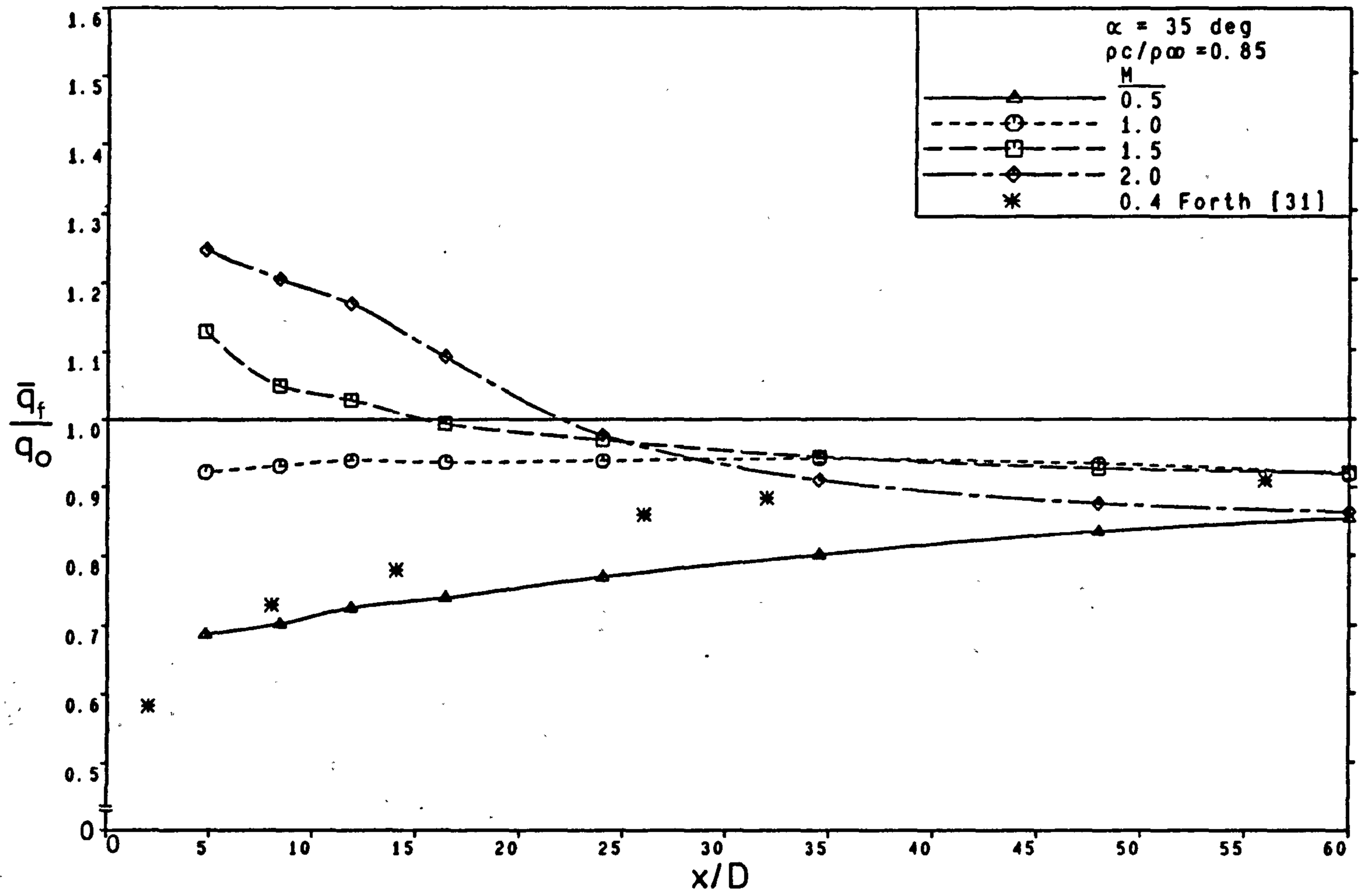

Fig. 8.34 Heat load distribution downstream of injection at 35° through a row of holes.

than local.

Injection at larger coolant to mainstream density ratios, as occurs in practice, is expected to be more beneficial due to lower heat transfer coefficients and higher effectiveness. The order of improvement can be gauged from Fig. 8.35, a plot of the heat flux ratio downstream of the centreline of 35° holes at density ratios of 0.96 and 1.5 for M=0.5, 1.0 and 2.0. The effectiveness data are those of Pedersen et al [52] measured at zero pressure gradients, $\delta^*/D=0.163$ and $Re_D=1.1x10^4$. Improvement in centreline cooling effectiveness of the order of 30% occur when the density ratio is increased by 50% at the higher blowing rates. In addition (see Fig. 8.35), at the lowest blowing rate the centreline heat flux is appreciably reduced that near the injection site heat flow from the surface to the coolant film is observed. However, at M=2.0 for the lower density ratio case, the high heat transfer coefficients close to the holes offsets the film effectiveness and an increase in the heat flux is found.

Existing effectiveness data for injection from a row of 90° holes with s/D=3 are very limited. Fig. 8.36 shows the centreline heat flux ratio, $\hat{q}_r/q_o$, for 90° and 35° injection. The normal injection heat flux ratio is based on Foster's [105] zero pressure gradient effectiveness data at the centreline for $\rho_c/\rho_\infty=1.45$ and $\delta^*/D=0.63$, whereas the 35° injection heat flux data is based on that of Pedersen et al [52]. Close to the holes, the higher heat transfer coefficients and lower effectiveness associated with normal injection as compared with angled injection are reflected in the heat flux ratio curves.

The analysis above indicates that better film cooling performance may be accomplished when coolants are injected at a streamwise angle, with relatively low blowing rates and high density ratios.

The effect of acceleration on the heat load to a film cooled surface could not be assessed as effectiveness data at values of the acceleration parameter similar to those investigated here are not available.

Although some controversy exists on the detailed behaviour of the adiabatic effectiveness of single rows of holes in the presence of acceleration;

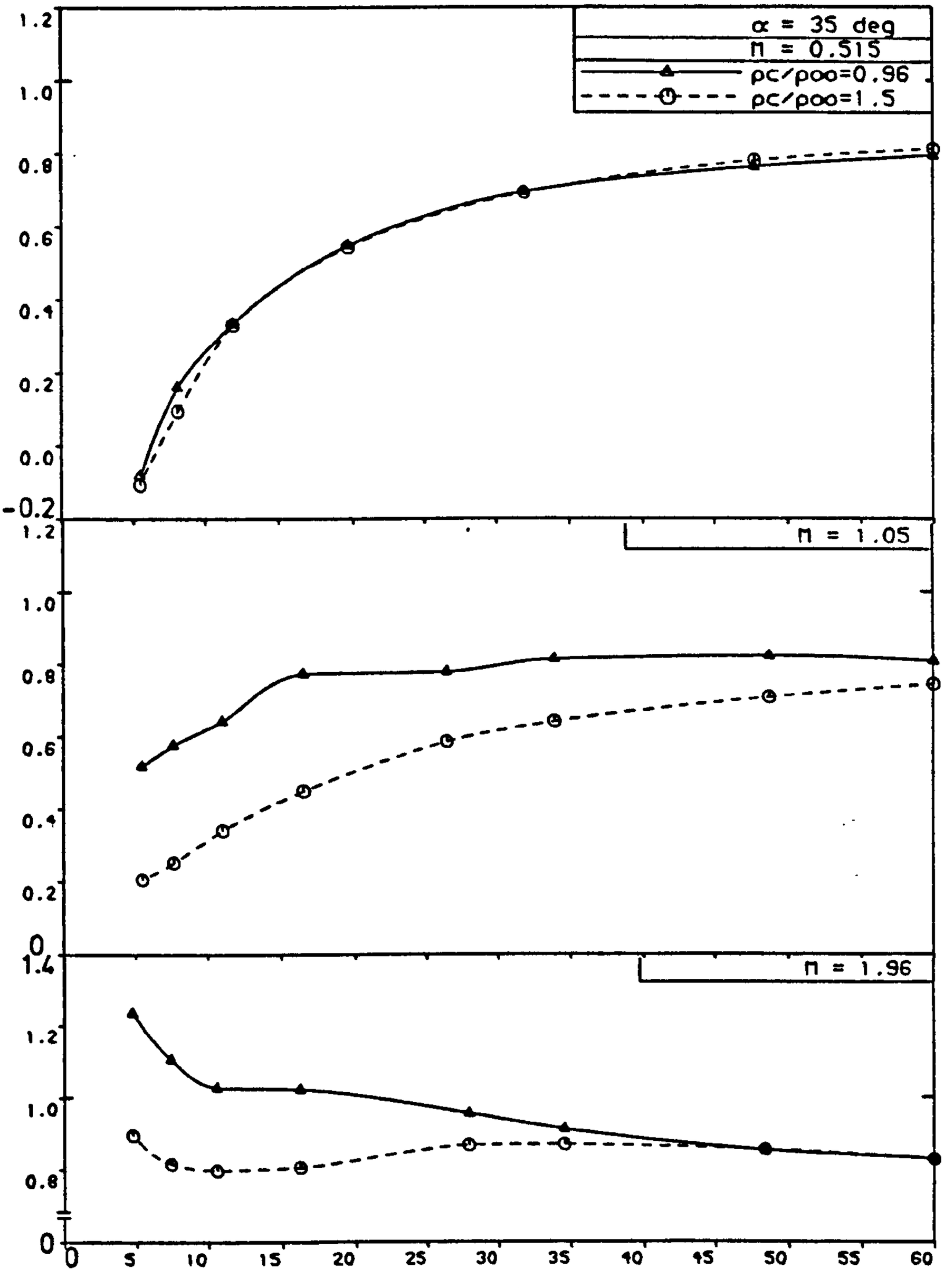

Fig. 8.35 Centreline heat load distribution downstream of injection at 35° through a row of holes.

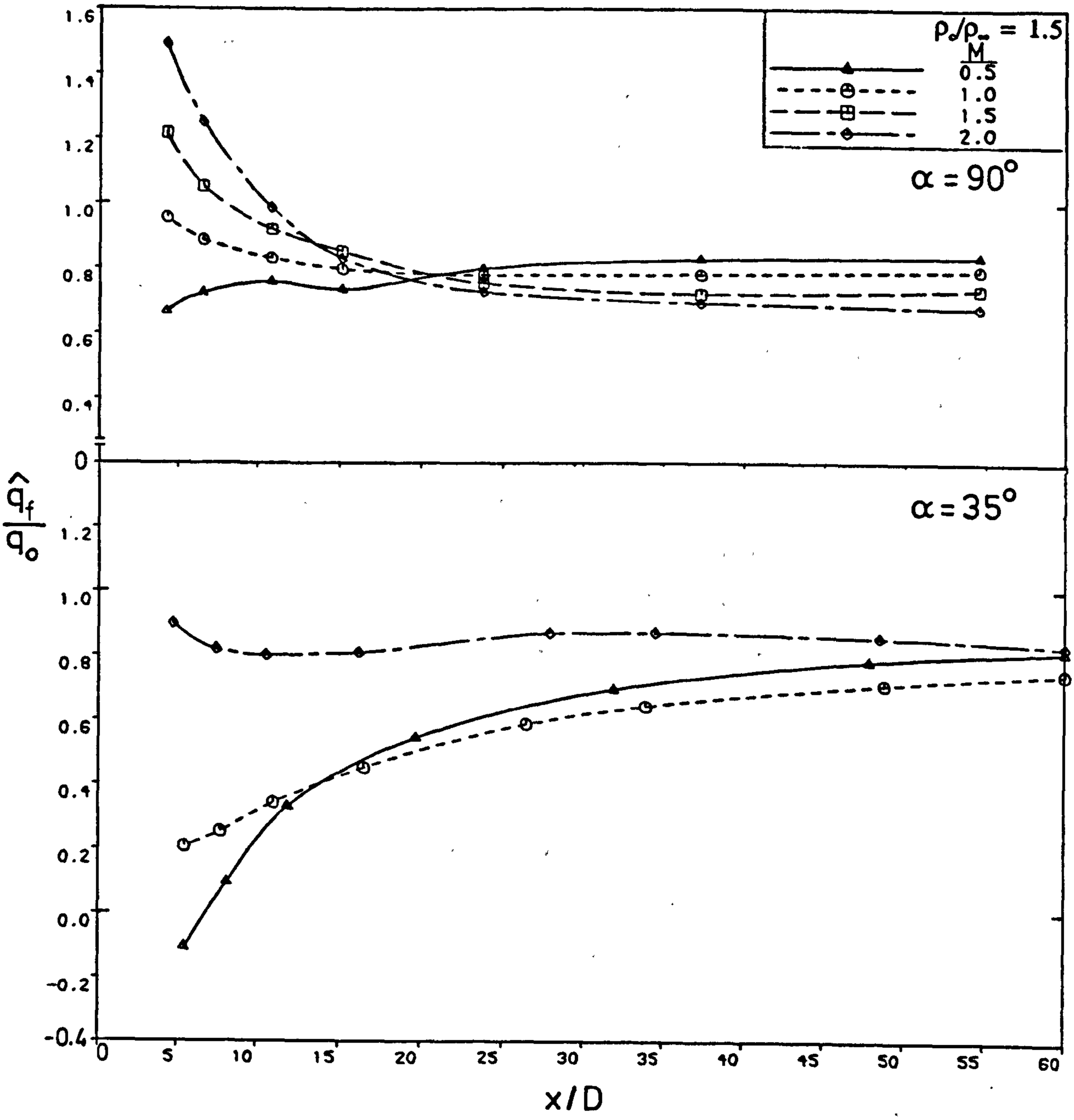

Fig. 8.36 Centreline heat load distribution downstream of injection at 90° and 35° through a row of holes.

for example Kruse [27] found a slight decrease in η by mainstream acceleration of $K=2\text{-}4\times10^{-6}$, while Brown and Saluja [42] reported a modest decrease in η at $K=1.14\times10^{-6}$, on the whole the effect was shown to be rather small and negative, ie leads to an increase in the heat load to the film cooled surface. On the other hand, the present study has shown that acceleration is accompanied by a decrease in the heat transfer coefficient and is substantial at high K. Low to moderate acceleration, therefore, would be expected to have on balance little or no influence on the net heat load, whereas high acceleration on balance would be beneficial particularly at lower M's.

8.7 FINAL DISCUSSION

The present experimental study has some degree of compromise because of the difficulty in matching the values of the various parameters in systematic conditions to those occurring in actual blade film cooling situations. Although the maximum coolant to mainstream density ratio studied in this work of 1.52 is found in practice, ideally more experiments at density ratio of 2.0 should be made to cover the whole range. However, as the results of Forth and Jones [32] for injection through a row of inclined holes which include data at $\rho_c/\rho_\infty=2.0$ corroborate the present findings in regards to correlation of the heat transfer data, one would expect the current results to hold over the whole range of density ratios found in practice.

Acceleration of K values greater than 5×10^{-6} occur in realistic blade conditions, more experimentation is therefore needed. However, the present results have indicated, in general, an approximately linear effect of K on the heat transfer coefficient, and it is possible that the trend may continue at higher values of K.

It is not sufficient, however, for the individual parameters to be investigated; their complex interaction must also be examined. Here, the combined effects of density ratio and acceleration has been studied, but the other film cooling parameters such as turbulence level, curvature and rotation may also have some influence on the cooling film heat transfer coefficient.

The present results may remain valid under these conditions to a certain extent, but further investigations under conditions representative of those over blades may still be needed.

CHAPTER 9

NUMERICAL STUDIES

In this Chapter, a general purpose computer scheme is described and its capability for predicting the heat transfer associated with film cooling by a row of holes is tested.

9.1 INTRODUCTION

Numerical simulation of physical processes has been gaining in importance recently as systematic investigations are usually expensive and time consuming under realistic conditions. By numerical simulation new model concepts and parameters are varied speedily, and comprehensive information is obtained at little cost in time and money. On the other hand, computer simulation is limited by imperfect basic theories and computer capacity, and besides a numerically optimised solution always needs experimental verification in the end.

Application of computational schemes to the film cooling process which has been noted in chapter 2 was of limited success. Most of these schemes were developed to predict the complex flow field generated by injection through discrete holes, and the film cooling effectiveness. The very little work considering the film cooling heat transfer coefficient has been as yet unsatisfactory especially close to the injection holes. The predictions of even the best numerical procedures applied to complex flows such as film cooling often deviate from the experimental data [61]. A computational procedure that could successfully solve the film cooling problem without experimental testing would, therefore, be of considerable value.

The objective of the work in this chapter is to investigate the ability of a numerical procedure to predict the flowfield and heat transfer associated with

film cooling. In addition, this work includes predictions of the heat transfer coefficient at variable coolant to mainstream density ratio. The physical model studied is the present experimental geometry of a row of holes. Comparisons of the computed results with the corresponding experimental data are made to assess the accuracy of the scheme and to explore its use as a design tool for film cooling analysis.

The computational procedure employed is described in the following section. Description of the problems simulated, physical models and computational details is given in section 9.3 followed by a presentation and discussion of the predicted results in section 9.4. Finally, general remarks on the computer code are concluded in section 9.5.

9.2 DESCRIPTION OF THE COMPUTER SCHEME

9.2.1 General

The computer scheme used, called PHOENICS (Parabolic, Hyperbolic or Elliptic Numerical Integration Code Series), is a general purpose Computational-Fluid-Dynamics program designed for simulating fluid flow, heat transfer, chemical reaction and combustion process.

PHOENICS was created by CHAM Ltd. in 1979-80 and was first released in 1981. A major upgrade was effected in 1984; and since that time, there have been numerous re-issues to supply new features, rectify errors or facilitate use.

PHOENICS-1981 was used in the first two years of this research, whereas version 1.4, which incorporates the changes that have been made up to June 1987, was used in the remaining period of the research. Both versions are installed on the University's VAX 11/780 system.

The program solves the discretized versions of the differential equations expressing the physical laws of conservation of mass, momentum and energy (or species concentration). The equations are solved by a "finite-volume" method involving integration over the grid cells of a calculation domain, followed by iterative solutions of the resulting non-linear algebraic equations.

A general description of the solution of the differential equations of conservation is provided in [107]. However, the exact solution procedure implemented in PHOENICS is "conservative" and "fully implicit", although additions or modifications requiring interaction with the solution schemes are possible via subroutines accessible to the user.

9.2.2 Components of PHOENICS

A brief summary of the structure of PHOENICS version 1.4 is given here. Full description of the main features is provided in [108]. Details of the nature of PHOENICS-1981 can be found in [109]. Both versions incorporate essentially the same solution schemes.

PHOENICS comprises two essential computer codes and two auxiliary ones.

The essential ones are a pre-processor called SATELLITE and a processor called EARTH. The auxiliary ones are a post-processor called PHOTON and a separate self-instruction program called GUIDE. Here, emphasis is centred on the essential codes as they set up and solve the simulated problems.

(1) SATELLITE, is a program supplying problem-defining data to cause EARTH to simulate the required process. The input data such as geometry, velocities, fluid properties, initial and boundary conditions, number of sweeps and printout required are inserted in several ways by,

- creating an instruction file called Q1, or modifying an existing one.
- using an interactive input mode, designed to assist new users.
- loading or amending an instruction file from the PHOENICS input library, containing over 500 input-file examples.

SATELLITE also possesses a subroutine called SATLIT with which data-settings by FORTRAN statements can be inserted to establish the problem specifications. However, here, the input data of the simulated problems are set up in a created Q1 file.

(2) EARTH, is the central program of PHOENICS containing the main flow-simulating software. It incorporates the coding sequences representing the relevant laws of physics applied to each cell of the discretised calculation domain.

EARTH reads the data provided by the SATELLITE input file, executes the computations of each variable solved for and produces the required output file of the solutions.

It provides the full solution capabilities, including,

- one-, two- or three-space dimensions, either steady state or transient.
- single-phase and two-phase options.
- equipped to solve for up to 50 variables, and as many more as the user cares to specify. Typical variables are,

  - the pressures and specific enthalpies of both phases.

  - the three velocity components in the three space directions of both phases.

  - the volume fractions of both phases.

  - the k-ε turbulence model properties of either phase.

  - concentration variables of both phases as many as required.
- solves for auxiliary variables derived from algebraic equations rather than from differential ones, such as laminar viscosity, Prandtl number, density etc.
- handles a flow in space of which parts are inaccessible to the fluid caused by partial or total blockage by solid material.

Furthermore, EARTH contains subroutines which are accessible to the user. The major subroutine is GROUND which is in fact a collection of subroutines. Its main function is to assist SATELLITE program to complete problem specifications, so that it enables the user to insert the necessary boundary conditions, fluid properties and output-control features that are not contained within EARTH.

A second important subroutine, GREX2 (GRound EXample 2), contains numerous built-in property and boundary condition options together with

physical models, which are available to the user.

In the current work, GREX2 is accessed to provide the generalised wall functions necessary to calculate the heat transfer. GROUND is used to calculate the temperature, density and other auxiliary variables.

(3) PHOTON, is the interactive graphical program, displays the results from EARTH calculations as,

- two- and three-dimensional representations.
- vectors or contours of any variables.
- solution geometry and grid systems.

PHOTON is based on a graphic software not available at Nottingham University. Therefore, the graphical representation of one of the computed results in the current work was plotted using a similar graphical program called GRAFFIC. The latter was used with PHOENICS-81.

(4) GUIDE, which contains extensive instructional material acts as a source of helpful information about PHOENICS and its use.

9.3 APPLICATION OF PHOENICS IN THE PRESENT WORK

9.3.1 The Problems Simulated

The physical problems concern film cooling by injection from a single row of 90° or 35° holes of s/D of 3 across a flat plate exposed to a mainstream. The flowfield, heat transfer coefficient and cooling effectiveness are investigated for different blowing rates and density ratios. Examples of the computed results are presented and compared with the present and available experimental data.

As the emerging jets from the discrete holes interact with the two-dimensional oncoming mainstream flow, a complex three-dimensional flow is generated in which flow reversal can occur near the injection site [19 & 20]. Therefore, a three-dimensional and elliptic calculation was essential to simulate realistically the flow and the associated heat transfer processes. The

turbulent stresses and heat fluxes are evaluated by the most widely used K-ε model of turbulence implemented in PHOENICS. Furthermore, a modified version of the standard numerical scheme was necessary to predict heat fluxes at flow separation regions.

The jet velocity distribution at the hole exit in reality are asymmetric resulting from the interaction between the jet and the mainstream flows, the calculation domain was chosen, therefore, to include the flow region inside the injection hole as well. This way, the influence of the jet-mainstream interaction near the hole is determined as part of the final solution, without the need for simplifying assumptions, such as specifying two-dimensional uniform jet flow velocity distribution at the hole exit.

9.3.2 Mathematical and Physical Models

The well established differential equations of conservation of mass, momentum and energy (or species concentration) are used in PHOENICS. These are solved approximately using methods of numerical mathematics, as there are no exact analytical solutions of these equations for applications of practical interest.

The equations of conservation retain their fundamental validity also for turbulent flows. Consequently, the turbulence time-averaged properties (turbulent shear stresses and heat fluxes) are considered via "turbulence models". PHOENICS version 1.4 has several models exemplified in GREX2, one of which is the most widely used and accepted model known as the "k-ε" turbulence model which utilises the eddy (turbulent) viscosity concept and calculates two quantities k, the kinetic energy of turbulence and ε, its dissipation rate.

The eddy viscosity is related to the turbulent kinetic energy k and to its rate of dissipation ε through the Kolmogorov-Prandtl relation as,

$$\mu_t = 0.09\ \rho\ k^2 / \varepsilon \qquad (9.1)$$

The distribution of k and ε over the flowfield using PHOENICS is determined from the basic k-ε turbulence model semi-empirical transport

equations as given by [110] in Cartesian tensor notation,

$$u_i\frac{\partial k}{\partial x_i} = \frac{\partial}{\rho\partial x_i}\left[\frac{\mu_t}{\sigma_k}\frac{\partial k}{\partial x_i}\right] + \frac{\mu_t}{\rho}\left[\frac{\partial u_i}{\partial x_j} + \frac{\partial u_j}{\partial x_i}\right]\frac{\partial u_i}{\partial x_j} - \varepsilon \qquad (9.2)$$

$$u_i\frac{\partial \varepsilon}{\partial x_i} = \frac{\partial}{\rho\partial x_i}\left[\frac{\mu_t}{\sigma_\varepsilon}\frac{\partial \varepsilon}{\partial x_i}\right] + \frac{C_1\varepsilon\mu_t}{k\rho}\left[\frac{\partial u_i}{\partial x_j} + \frac{\partial u_j}{\partial x_i}\right]\frac{\partial u_i}{\partial x_j} - \frac{C_2\varepsilon^2}{\rho k} \qquad (9.3)$$

For fully developed turbulent flows, the empirical constants appearing in this standard k-ε model take these values,

$C_1=1.44$, $C_2=1.92$, $\sigma_k=1.0$, $\sigma_\varepsilon=1.3$

It is worth noting that the standard k-ε model, suffers from the following simplifying assumptions,

i) It adopts an isotropic turbulent viscosity. This simplification is not encountered in three-dimensional film cooling situations.

ii) The model is valid only for fully turbulent flows where viscous diffusions are neglected.

iii) In the near wall region the model overestimates the generation of turbulence k [65]. Additional destruction terms in the k-transport equation near the wall region are therefore required to yield reasonable predictions to match available experimental data.

9.3.3 PHOENICS Near-Wall Treatment

As viscous diffusions are neglected, the k-ε model is used in conjunction with empirical wall functions to bridge the viscous sublayer. This is accomplished by relating the velocity components at the first grid node outside this layer to the wall shear stress via the logarithmic law of the wall. A uniform shear stress prevails in this viscous layer, and generation and dissipation of energy are in balance there via the assumption that the turbulence is in a state of equilibrium.

The methods which include integration right up to the wall are better than those assuming the wall functions [111] since they are valid throughout the fully turbulent, semilaminar and laminar regions. However, the computing time is increased considerably due to the fine mesh required to resolve the immediate near-wall region adequately. Wall functions economize computer

time and storage.

Improvements in near-wall behaviour through the incorporation of extra terms to account for the viscous effects and for the anisotropy effects on the eddy viscosity are discussed elsewhere [82].

(i) PHOENICS Standard Wall Functions

GREX2 in version 1.4 of PHOENICS contains the built-in standard wall-function options for both laminar and turbulent flows, namely,

i) the Blasius law,

$C_f = 0.009 / Re^{0.25}$; and

ii) the logarithmic law,

$C_f = [k_v / \ln(E\ Re\ C_f^{0.5})]^2$, for $Re > 132.5$ (9.4)

$C_f = 1 / Re$, otherwise.

where C_f is the skin-friction factor ($=\tau_w/\rho u^2$, τ_w is the wall shear stress and u is the velocity parallel to the wall), k_v is the Von Karman constant, taken to be 0.435, and E is the smooth-wall value of 9.0. The Reynolds number, Re ($=uy/\nu_l$), is based on the resultant velocity parallel to the wall, on the distance from the wall to the grid node, y, and on the laminar kinematic viscosity, ν_l. The limit of Re of 132.5 is that at which the laminar and turbulent wall-functions intersect.

The Stanton number, St, is given by the empirical law of Jayatillika [112],

$St = C_f / [Pr_t(1 + P_m\ C_f^{1/2})]$, for $Re > 132.5$ (9.5)

where, P_m is the smooth-wall sublayer resistance function, a semi-empirical formula given by [110],

$P_m = 9(Pr/Pr_t-1)(Pr_t/Pr)^{1/4}$

For $Re \leq 132.5$, St is simply $= C_f / Pr$.

The heat flux at the wall, q_w, is then deduced from,

$q_w = St\ \rho\ u\ (h_p - h_w)$

where h_p is the enthalpy at the grid node in question, and h_w is the enthalpy corresponding to the prescribed wall temperature.

The heat transfer coefficient was then evaluated from the heat flux q_w using equation (1.4),

$$q_w = h\,(T_\infty - T_w)$$

If the flux of other variables is in question, such as velocity resolutes, the enthalpy values in the above equation are replaced by the in-cell value and that at the wall of that variable. St is then the skin-friction factor.

In addition, the near-wall grid node values of k and ε are fixed to the following empirical correlations via the incorporated logarithmic-law option applicable to smooth walls,

$$k_w = u_\tau^2 / 0.3, \text{ and} \qquad (9.6)$$

$$\varepsilon_w = u_\tau^3 / (k_v\, y) = 0.09^{3/4}\, k_w^{3/2} / (k_v\, y) \qquad (9.7)$$

here, u_τ is the friction velocity ($=(\tau_w/\rho)^{1/2}=uC_f^{1/2}$).

The activation of the wall-function options is given in the PHOENICS reference manual [108]. However, the wall functions of the wall heat transfer could not be accessed directly from the EARTH program in PHOENICS version 1981, and at that time the above implicit equations were implemented in GROUND which had to be solved iteratively for the friction factor C_f.

However, this treatment in which the heat transfer coefficient is calculated via a friction factor manipulation, was found to be appropriate for the case where there was no injection, ie boundary-layer type flows where the near-wall layer is in local equilibrium. For flows with recirculation, as occurs immediately downstream of discrete hole injection to a mainstream, the predicted heat transfer coefficients there were found negligible. The present experimental data has indicated that the heat transfer coefficients are actually at maximum in the separated regions. This deficiency in the standard wall functions is due to the fact that in regions where the flow separates from the wall the shear stress and hence friction velocity is zero. Since the computed Stanton number was directly proportional to the friction velocity the calculations resulted in an incorrectly predicted zero heat flux and heat transfer coefficient.

It was desirable, therefore, to employ a more adequate wall-function treatment of heat transfer. Transfer to the latest version of PHOENICS (version 1.4) was necessary as implementation of improvements is much easier and more straightforward.

The deficiency in the standard wall-function options was the main reason behind the installation of PHOENICS version 1.4 at the University, although time was short for familiarization with the new version and implementation of improved wall functions.

(ii) PHOENICS Generalised Wall Functions

The generalised wall functions adopt the method of Launder and Spalding [110], the main feature of which is based on a modified log-law that uses the turbulent kinetic energy as the characteristic velocity scale, rather than the friction velocity.

Adoption of the practices in [110] leads to the prediction of finite values of k and of wall heat flux at a reattachment point.

Furthermore, the wall functions account for the effects of wall roughness, and the criteria for transition from the turbulent wall function to laminar ones is modified.

The standard log-law of the wall for C_f is generalised by expressing u_τ in terms of a velocity scale calculated from the local k, thereby finite fluxes are predicted, even where the fluid velocity is zero.

The C_f log-law, eq. (9.4), can be written as,

$$C_f = k_v\, C_f^{1/2} / \ln(E\ Re\ C_f^{1/2})$$

since $C_f^{1/2}=u_\tau/u$, and $u=Re\ \nu_l/y$ it follows,

$$C_f = k_v\, (u_\tau/u) / \ln(E\ u_\tau\ y/\nu_l)$$

and since $u_\tau=0.3^{1/2}k^{1/2}$ from the near-wall cell value of k, eq. (9.6), substitution for u_τ gives the generalised log-law of the wall,

$$C_f = k_v\, 0.3^{1/2}k^{1/2} / [u \ln(E\ 0.3^{1/2}\ k^{1/2}\ y / \nu_l)] \qquad (9.8)$$

Substitution for $C_f^{1/2}$ and u_τ in the Stanton number formula, eq. (9.5), gives the generalised form of St,

$$St = C_f / [Pr_t(1 + P_m C_f u / 0.3^{1/2} k^{1/2})] \qquad (9.9)$$

The value of k at the near-wall grid cells is not fixed in this option, and is calculated from its regular transport equation. However, in the source term for k (eq. 9.2), the dissipation rate for the near-wall cells is fixed to,

$$\varepsilon = 0.09^{3/4} k^{1.5} \ln(E\ 0.3^{1/2} k^{1/2} y / \nu_l) / (2 k, y)$$

When the turbulence is in local equilibrium, away from separated regions, the above expression recovers the near-wall empirical correlation of k in the standard wall functions.

Details of activation of the generalised wall functions are given in [113].

Mention should be made that the generalised wall functions were implemented in version 1.4 late 1988.

9.3.4 Computational Details

(i) Geometry and Grid

Three-dimensional computational grids in Cartesian coordinates were employed. The z-direction was taken as that of the mainstream for all of the computations performed as recommended by PHOENICS. The bottom side of the rectangular-box shaped domains was considered solid, the other sides were all fluid as illustrated in Fig. 9.1. The lateral boundaries were 1.5D apart, where D is the hole diameter, and located at planes of symmetry; one bisecting a hole, and the other bisecting the space to its neighbour. The solid wall region in the vertical extent (y-direction) was placed to occupy 2D so that the effect of the mainstream on the jet inside the hole was accounted for; preliminary computational tests with the wall located to 4D had shown that the mainstream effect extended to about 1D only below the hole exit. The other boundary of the y-direction was adjusted to 6D above the wall surface, just sufficiently to encompass the region of undisturbed flow, so that uniform mainstream conditions were assumed there.

The domain extended upstream some 3D from a hole origin where the oncoming flow was undisturbed by injection according to the present experimental measurements. The position of the downstream boundary from

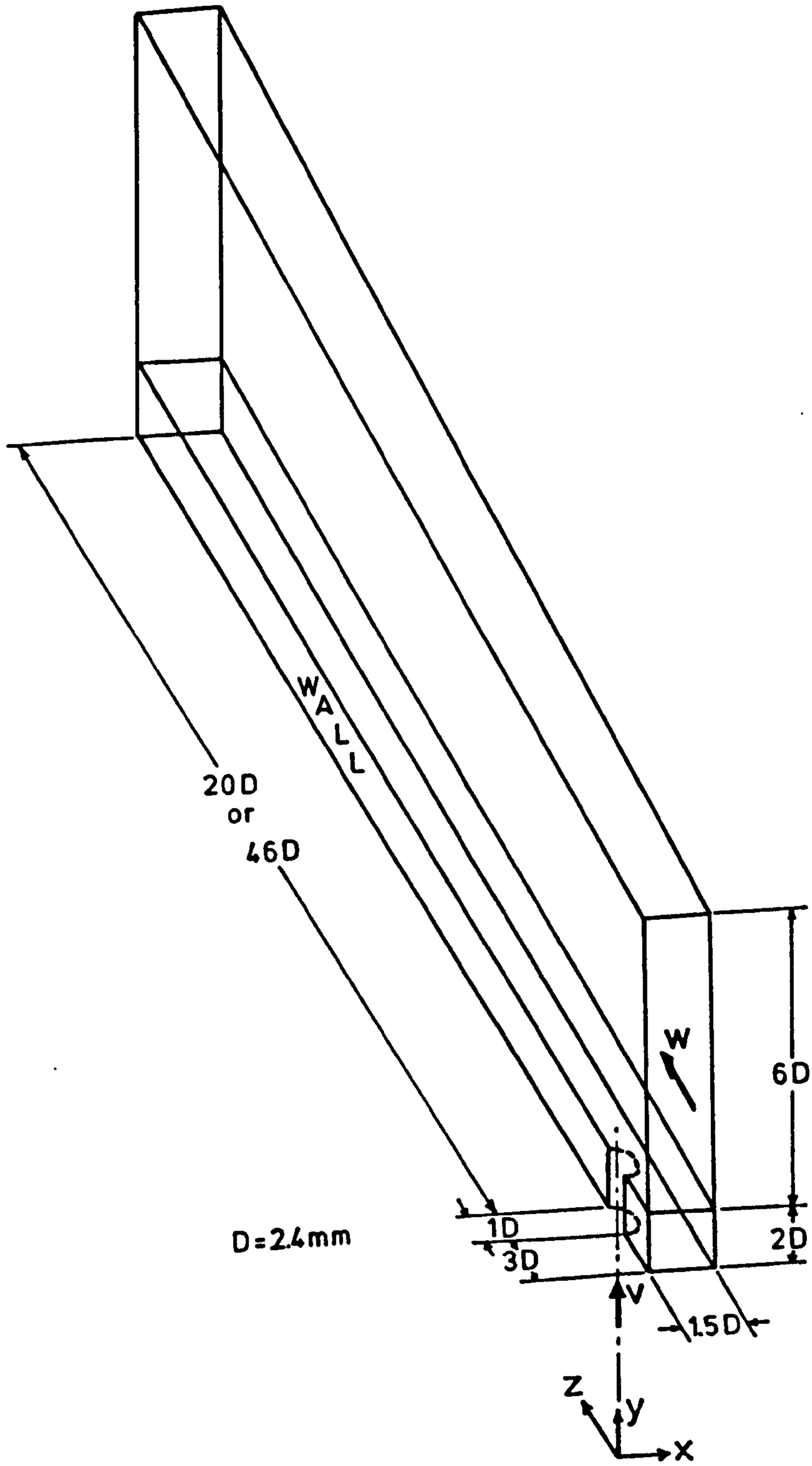

Fig. 9.1 Geometry used.

the hole origin was adjusted so that z = 20D when heat transfer was computed, and z = 46D when cooling effectiveness was calculated due to computer run time and storage considerations.

The number of grid nodes used in the x, y and z-directions were 9, 15 and 30 respectively. Fine-grid spacing near a hole was employed and gradually increased for locations away from it so as to give a good resolution of the solution in the area of interest as shown in Fig. 9.2. The first grid node away from the wall was chosen that it sufficiently bypassed the viscous sub-layer as required by the wall-functions. This was based on calculations using an established sub-layer thickness relation expressed in terms of the Reynolds number, with the current experimental boundary layer thickness and Reynolds number values used as input.

One half of the circular injection hole included in the domain of 2.4mm diameter (approximately similar to that used in the experimental phase of this research) was represented by 18 cells in cross-section. The circular shape of the hole inside the wall was specified by fractional volume and area porosities, thus determining the proportion of the hole periphery in each cell open for flow, as shown in Fig. 9.2. Extensive calculations by integration over finite areas and volumes were made to determine the area and volume fraction porosities for the 35° inclined round hole as they differ from one cell to another depending on the cell location.

(ii) Variables Solved

The variables selected for solution were,

- the velocity resolutes u, v and w in the x, y and z directions respectively,
- the pressure P,
- the two turbulence model parameters k and ε,
- the specific enthalpy h, and
- the mainstream and coolant mass fractions c_m and c_c respectively, when the effectiveness was computed.

The auxiliary variables solved via the GROUND subroutine were,

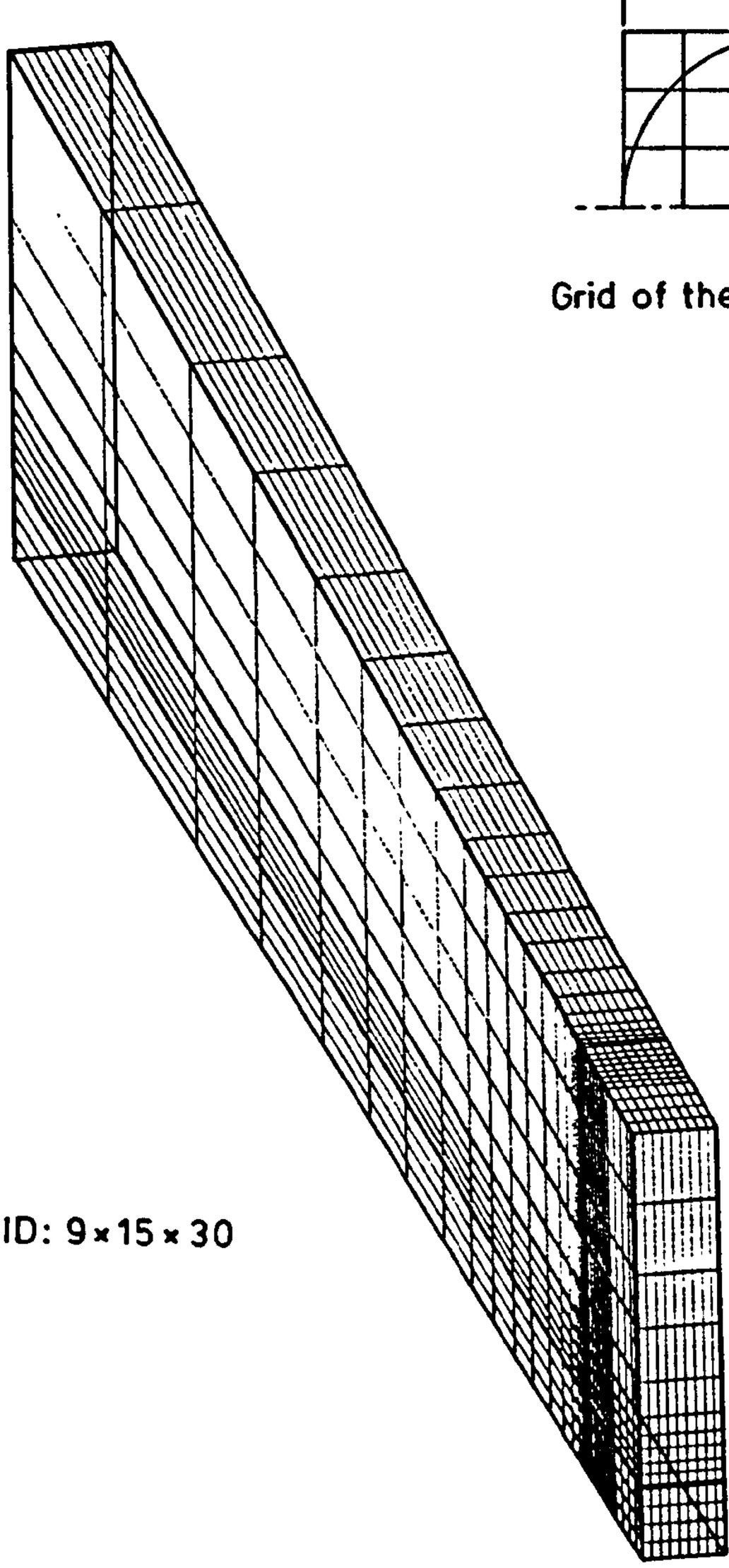

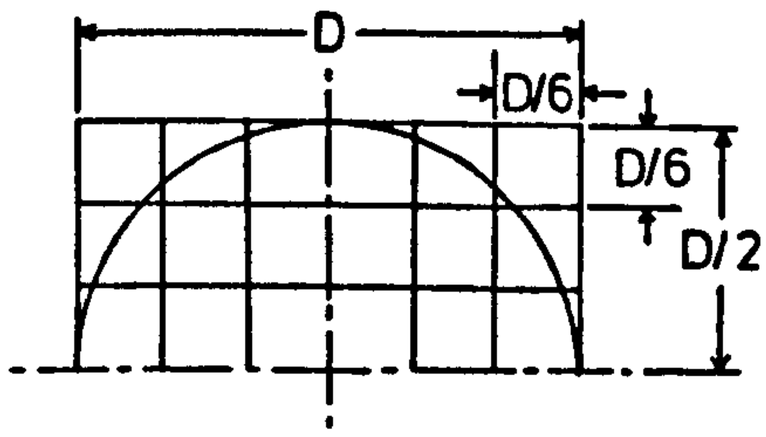

Grid of the Cross-Section of a Hole

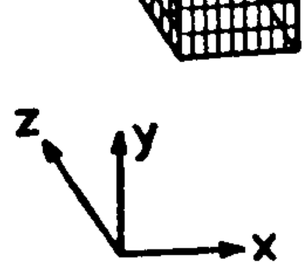

Fig. 9.2 Grid used.

- the temperature which was calculated in terms of the enthalpy; the enthalpy computed in EARTH was called for each grid node for computing the temperature in GROUND by means of a temperature-enthalpy polynomial curve fit.
- the local density was linked to the temperature and pressure by the perfect gas law, $\rho = P / R\,T$

where R is the gas constant and T is the temperature,

- the molecular weight for each cell calculated by a relation consequence of Dalton's Law of mixture of gases for effectiveness calculations involving density gradients, and
- the laminar kinematic viscosity when large density gradients were present. The viscosity was computed in terms of the enthalpy in a similar way as that of the temperature.

(iii) Fluid Properties

In all cases considered, the mainstream and coolant were both air. The property values were all obtained from tables of properties of fluids.

For heat transfer calculations, and unity coolant to mainstream density ratio, the temperatures of both the mainstream and the coolant were considered at 325K while that of the wall was set to 275K. This way the temperature parameter θ, eq. (1.6), was equal to zero, and therefore, was equivalent to that of the experimental work. Note that, in PHOENICS temperature is specified in terms of the corresponding enthalpy.

The density of the mainstream air at inlet was therefore taken as 1.086 kg/m^3 and then calculated throughout the cells of the domain.

Since the temperature difference between the mainstream and the wall was relatively small in this case, the laminar kinematic viscosity was considered as constant and was taken as that corresponding to the mean of both temperatures, ie 1.568×10^{-5} m^2/s at 300K. Similarly, the Prandtl number was taken as 0.707 at 300K. The turbulent Prandtl number was given a value of 0.9.

The effective viscosity, represented by μ_{eff}, was calculated by,

$$\mu_{eff} = \mu + \mu_t$$

where μ_t was obtained through the activated k-ε turbulence model.

In the case where density ratio was present, the temperature of the mainstream was assumed to be at 400K. Both the coolant and the wall temperature were at 275K, resulting in a density ratio of 1.46 and θ=1.0. Here, the laminar kinematic viscosity in addition to the temperature and density were calculated in GROUND via the enthalpy solved for. The Prandtl number was taken as 0.70 since its variation with temperature is small.

For the cases of calculating the cooling effectiveness, a mass transfer process was assumed and a uniform temperature of 300K everywhere in the flow domain was considered. The corresponding mainstream and coolant densities at 300K were 1.177 kg/m^3 when ρ_c/ρ_∞=1.0, and the laminar viscosity was taken as 1.846×10^{-5} at 300K. For the cases when ρ_c/ρ_∞=2.0, the coolant density was set to 2.354 kg/m^3.

(iv) Initial Conditions

The oncoming air was assumed to have no swirl and parallel to the streamwise z-direction, so that the velocity components u and v were prescribed as zero, and the component w was set to 25m/s analogous to that used in the experimental work.

The pressure value was initialised to zero. The enthalpy, h (= c_p T), was prescribed at the mainstream temperature; at 325K h was specified to 3.27×10^5, and at 400K h was set to 4.054×10^5. The turbulent kinematic viscosity of the mainstream was given the initial value of 1.0×10^{-5}.

Initial conditions needed also to be specified to the mainstream turbulence quantities k and ε. The value of k was set to 0.7% of the mean flow kinetic energy. The value of ε was computed assuming that production and dissipation of turbulence were in balance.

For the effectiveness computations, the mass fraction of the oncoming air was set to 1.0.

(v) Boundary Conditions

At the mainstream inlet, part of the plane above the wall started with a turbulent boundary layer characterised by the seventh power law. The boundary layer thickness was set to about 3.3D, analogous to that in the experimental situation.

Initial profiles were prescribed for the following,

- the mean velocity, $w = w_\infty (y/\delta)^{1/7}$

where, w_∞ is free stream conditions velocity, y is vertical distance from the wall and δ is the boundary layer thickness,

- the enthalpy, $h = h_w + (h_\infty - h_w)(y/\delta)^{1/7}$

where, h_w and h_∞ are the enthalpies at the wall and the freestream respectively,

- the mass flux, $m'' = w \cdot \rho$

where ρ is the density corresponding to the enthalpy profile, and

- the turbulence kinetic energy, k, and dissipation rate, ε, through the following empirical profile [108],

$$k = k_w - 3k_w(y/\delta)^2 + 2k_w(y/\delta)^3$$

$$\varepsilon = 0.09^{3/4}\, k^{3/2} / (k_\infty\, y)$$

where k_w is k at the wall.

For $y > 3.3D$, uniform mainstream conditions were set, ie,

$w=w_\infty$, $h=h_\infty$, $m''=w_\infty\rho_\infty$, $k=k_\infty$ and $\varepsilon=\varepsilon_\infty$.

the subscript ∞ denotes freestream conditions.

At the exit of the flow domain, a uniform pressure close to zero gauge was fixed. The top side of the domain was treated as having mainstream conditions.

The wall boundary (bottom region excluding the hole exit) was treated by activating the generalised wall functions for u, w, ε and h. The enthalpy h_w ($= c_p T_w$) was set to 2.76×10^5 corresponding to a uniform temperature of 275K. When standard wall-functions were used for effectiveness predictions, activation of the wall functions for k was also required as k was fixed at the

wall in this option.

The variables at the hole entry were specified as follows,

- injection velocity v for 90° holes, velocity components v and w for 35° holes,
- the mass flux, given by: the injection velocity . ρ_c
- the enthalpy $h_c = c_p T_c$, and
- the turbulence quantities, k and ε, given by,

  $k = 0.007$ (injection velocity)^2, and

  $\varepsilon = 0.09^{3/4} k^{3/2} / (D/2)$.

- the coolant mass fraction = 1.0 when the effectiveness was computed.

(vi) Iteration Control and Convergence

PHOENICS whole-field solver was activated since the pressure field was expected to exhibit substantial elliptic effects close to the hole.

Convergence was procured within 120 iteration sweeps for the situations solving for the effectiveness. The calculations took 60 to 90 minutes CPU time on the VAX. At this stage, velocities, mass fractions and pressure were invariant to within 1%. The sum of the absolute mass errors was less than 1% of the total mass flow rate.

Under-relaxation for all of the variables solved were prescribed to improve convergence.

However, when the generalised wall functions for heat transfer calculations were employed, reasonable convergence was achieved after 300 sweeps which took about 7 hours CPU time.

Excessive under-relaxation was used for the velocity resolutes u, v and w, the enthalpy h and k and ε. The pressure was relaxed by a linear factor of 0.3. Linear under-relaxation was also specified for both the density (a factor of 0.1) and turbulent viscosity (0.4).

9.4 PRESENTATION AND DISCUSSION OF RESULTS

Detailed information in the form of fields of the variables solved for were obtained. However, since the aim here is to test the ability of PHOENICS to simulate the film cooling situation, only selected computed results are presented in the form of velocity profiles, heat transfer coefficients or Stanton numbers and adiabatic wall effectiveness. Note that the heat transfer coefficient was predicted using the generalised wall functions.

Comparisons of the predictions of the heat transfer coefficient are made with the current experimental data of zero mainstream pressure gradient. The experiments of Goldstein et al [40] and Pedersen et al [52] provided the data for testing the simulations of the laterally averaged and local adiabatic wall effectiveness for injection through a row of 35° holes. The former measured the effectiveness by heating the injectant and surveying the surface temperature, while the latter measured the surface concentration of a foreign gas introduced into the injectant. For the case of normal injection, the measurements of surface concentrations by Foster [105] provided the effectiveness data. In PHOENICS, the effectiveness could be predicted by calculating either the adiabatic temperature or the mass fraction of the injectant at the wall. Preliminary tests have shown that there was little difference (<5%) between the effectiveness values predicted by the two methods. Here, however, the predicted data was based on the mass fractions of the injectant at the wall.

The experimental conditions of [40], which were: s/D=3, α=35°, u_∞=30.5m/s, δ^*/D=0.124, Re_D=2.2x10^4, Tu=0.5% and ρ_j/ρ_∞=0.85, were approximately simulated in the computer program for the inclined injection cases, and those of Foster [105]: s/D=3, α=90°, u_∞=30.5m/s, δ^*/D=0.33, Re_D=0.45x10^4 and ρ_j/ρ_∞=2.0, were simulated for the normal injection cases.

(i) <u>Heat Transfer Coefficient</u>

The distribution of the calculated heat transfer coefficient without injection is plotted in Fig. 9.3 along with the experimentally obtained

coefficient (from Fig. 7.1). Both predicted and measured coefficients decrease in the streamwise direction. The calculated heat transfer coefficient overpredicts the measurements by as much as 25% at upstream locations. The disparity is probably caused by the inability to simulate closely the experimental concentration boundary layer, since the latter started downstream of the hydrodynamic boundary layer and was not measured. Furthermore, the calculated heat transfer coefficient was based on the kinetic energy of turbulence, k, the shape of the inlet profile of which was difficult to simulate accurately near the wall.

Nevertheless, the hydrodynamic boundary layer profile is reasonably calculated as shown in Fig. 9.4. The measured velocity profile is that obtained by the hot-wire traverses (see Fig. 6.2). Near the wall, the predicted velocities are lower than measurements, probably caused by overestimation of production of turbulence by the model. This point could further explain the high predictions of the Stanton number (Fig. 9.3).

Fig. 9.5 compares the predicted and measured lateral average coefficients ratio with and without normal injection, h/h_o, for different blowing rates at ρ_j/ρ_∞=1.0. It can be seen that the overall level of agreement of calculations with experiment is reasonably good. Upstream of a hole, the heat transfer coefficient is predicted correctly. Downstream, the trend of the measured results is reasonably predicted, but quantitative agreement with measurements is best for M=0.5. As M was raised, the agreement with the measurements reduced progressively. The predictions were lower than the measurements at z/D<4 and higher further downstream. The discrepancies with measurements for M=1 were less than 10%, and at most 15% for M=1.5 at some downstream locations. For the cases of high M, detachment of jets from the surface was greater so that it was probably harder for the standard k-ε turbulence model to simulate accurately the more complex three-dimensional mixing character.

The lateral distribution of predicted and measured heat transfer coefficient at two streamwise locations is shown in Fig. 9.6. In general, the agreement of

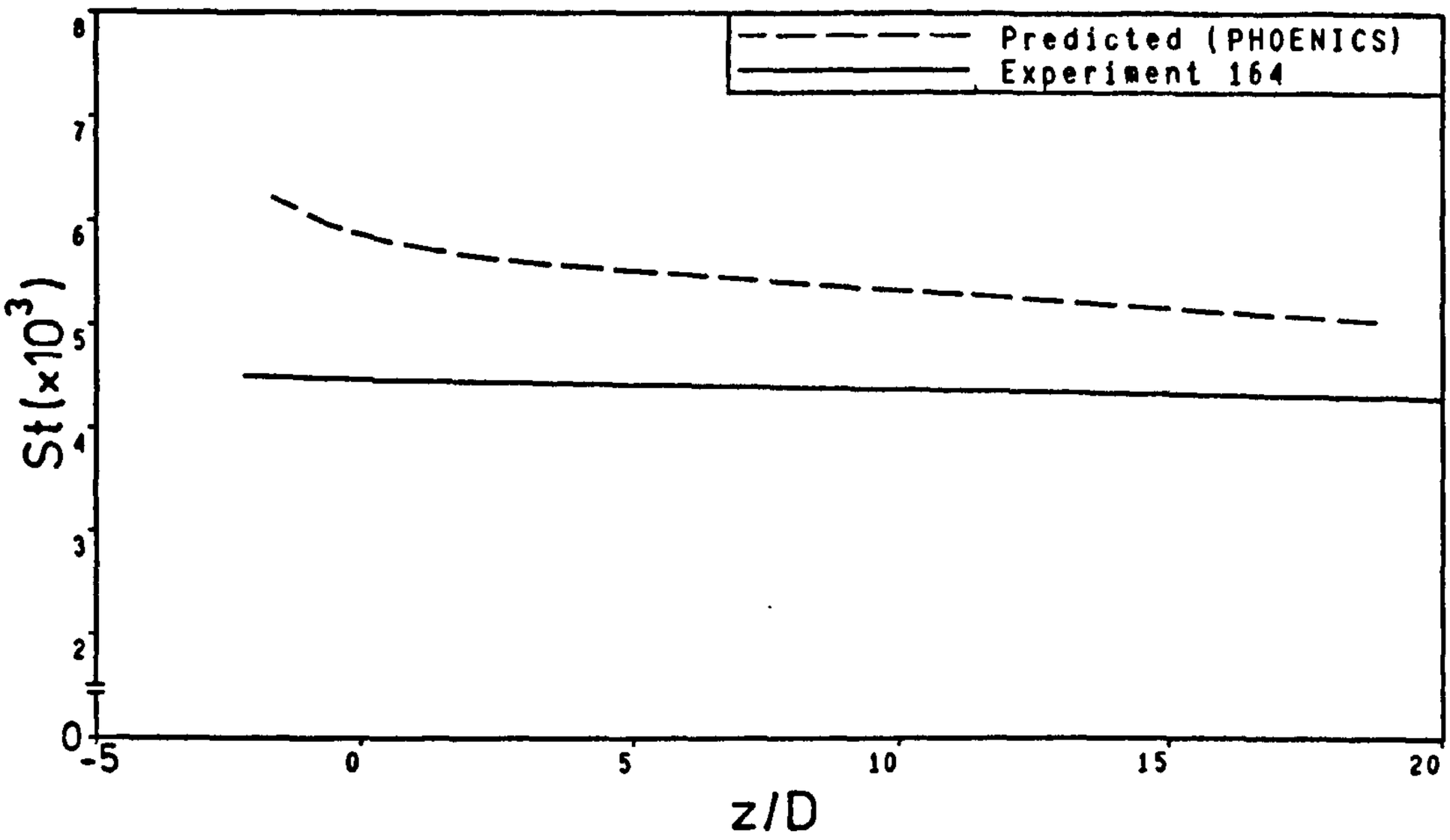

Fig. 9.3 Comparison between predicted and measured Stanton number in the streamwise direction in absence of injection.

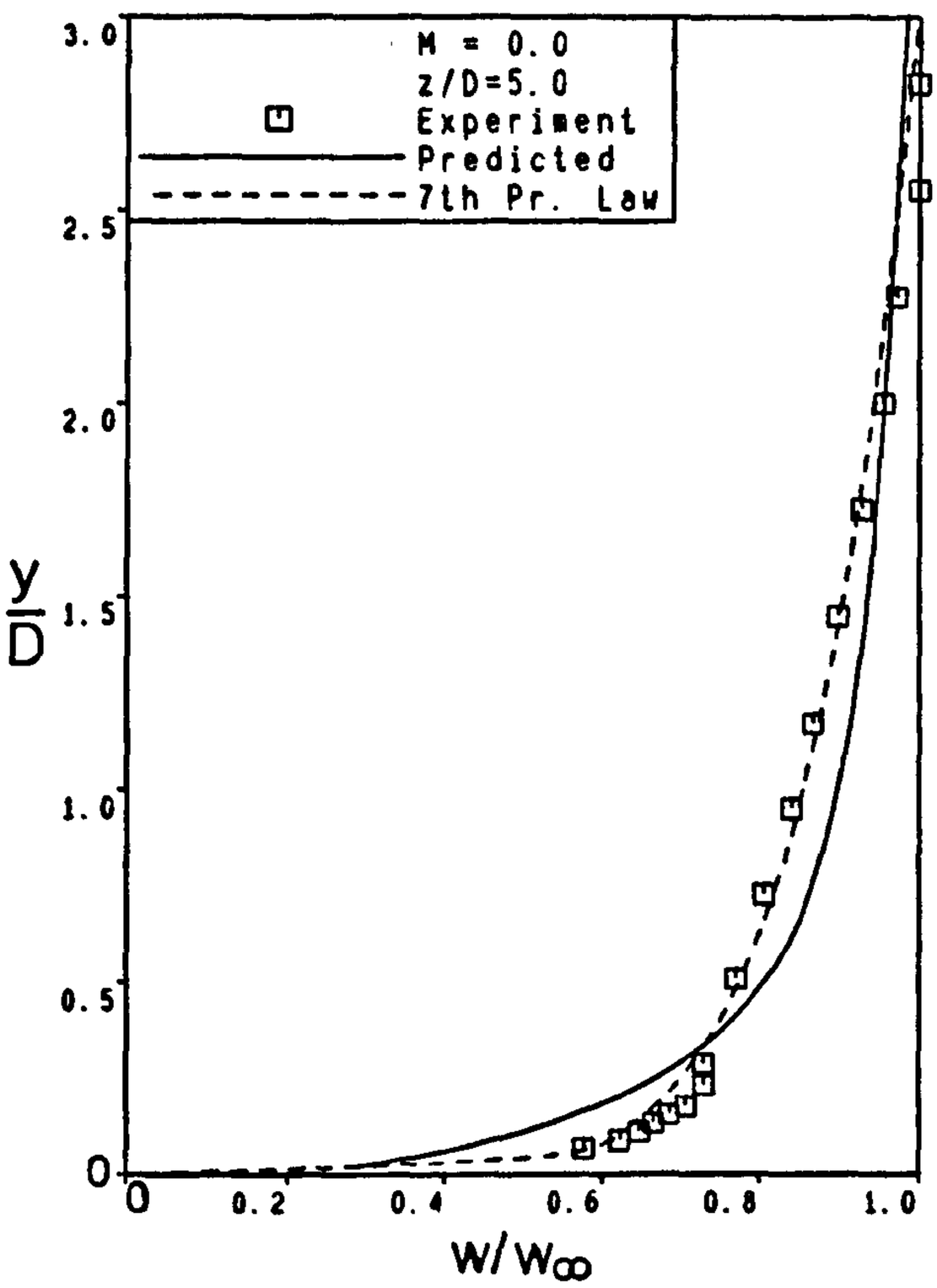

Fig. 9.4 Comparison between predicted and measured velocity profiles in absence of injection.

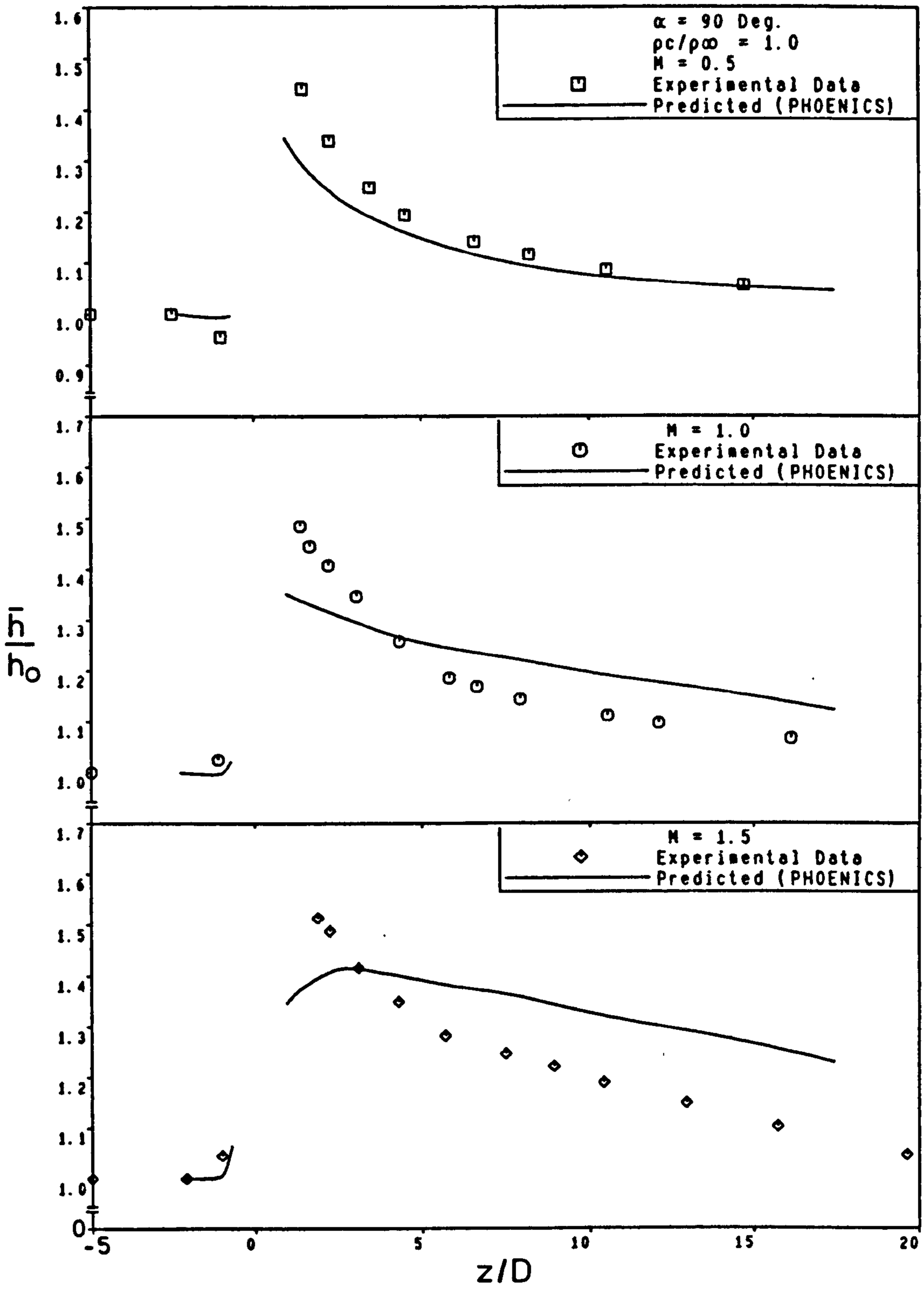

Fig. 9.5 Comparison between predicted and measured $\bar{h}/h_o$ following injection through a row of holes.

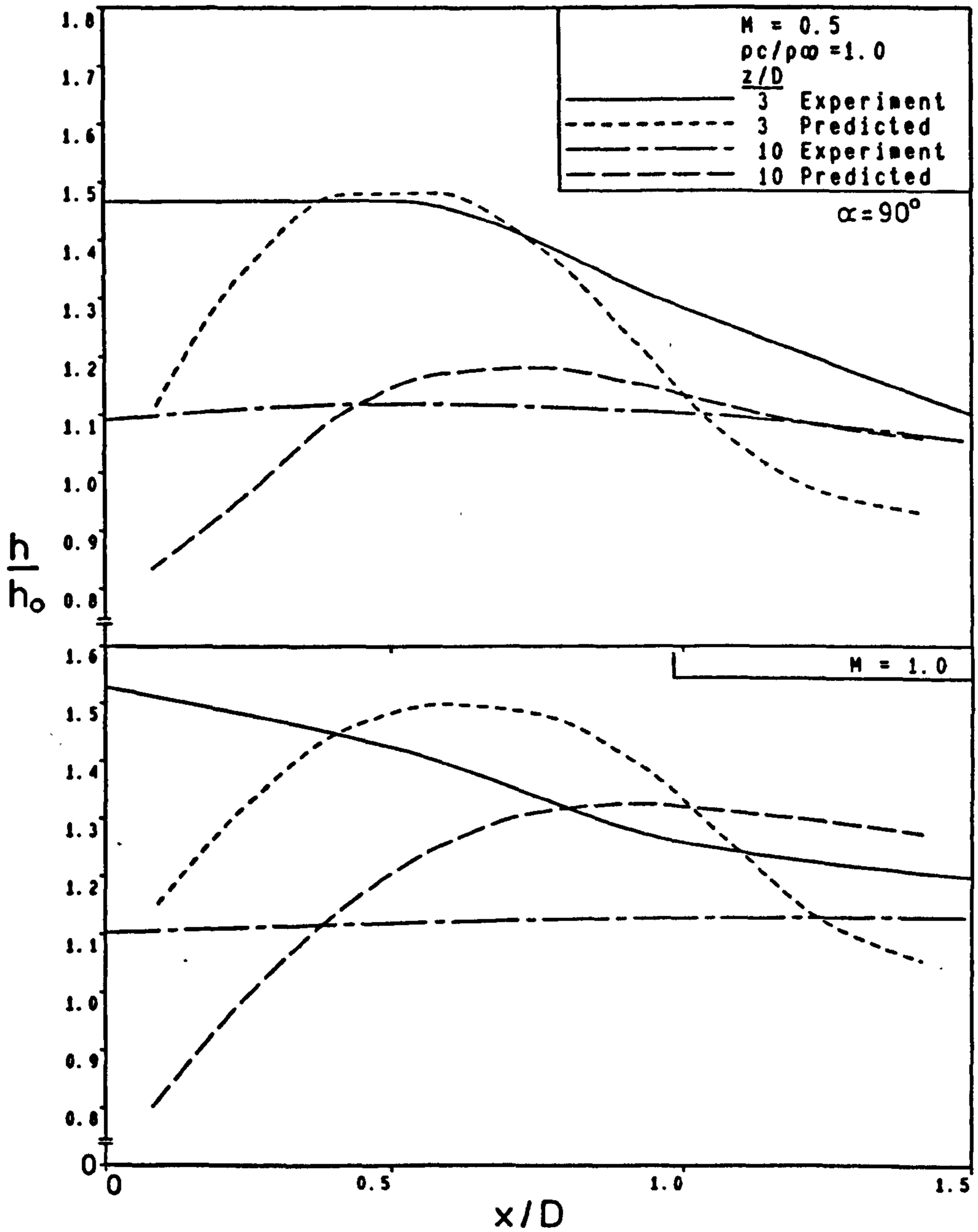

Fig. 9.6 Lateral distribution of predicted and measured h/h$_o$ following normal injection through a row of holes.

the calculated coefficients with experiment is fair. Close to a hole, the predictions of the heat transfer coefficient were found to be minimum in between the holes, and maximum at about the edges of a hole. The greatest disparity with experiment is seen to be downstream of the hole centreline; a sharp drop of the coefficients is predicted even at M=1 where the data shows a maximum. The low predictions at the centreline are probably due to underestimation of the lateral mixing by the turbulence model.

The prediction of $\bar{h}/h_o$ for normal injection at ρ_j/ρ_∞=1.46 and for M=0.5, 1.0, and 1.5 are displayed in Fig. 9.7 along with the present measurements at ρ_j/ρ_∞=1.52. Note that there was a difference in the temperature parameter θ between the predicted and measured heat transfer coefficients, θ=1 & 0, respectively. Such difference may be expected to cause disagreement in the heat transfer coefficient of the order of 10% [32]. For the cases of M=0.5 and 1.5, satisfactory predictions were obtained at z/D≥5. For the case of M=1, the predicted results show, somewhat, lower values of $\bar{h}/h_o$ than experiment everywhere. It can also be seen that the predictions are always low close to a hole indicating underestimation of turbulent mixing by the model. This is in contrast with the experimental data which has shown strong mixing for normal injection regardless of injectant density for M≥0.5.

The lateral distribution of h/h_o for ρ_j/ρ_∞=1.46 are compared with the experimental data in Fig. 9.8. The agreement is fair at M=0.5, but large discrepancies are observed at M=1 particularly close to the hole centreline at both downstream locations.

Similar predictions for injection through a row of 35° holes were made using PHOENICS, but convergence was more difficult to attain so that under-relaxation had to be increased heavily. Time, however, was not available in the current research to test all of the necessary cases.

Fig. 9.9 compares the calculated and measured laterally averaged heat transfer coefficients for 35° injection, M=0.5 and 1.0 and unity density ratio. The numerical predictions of Schonung and Rodi [64] are also shown in the figure. The conditions simulated by [64] were: row of 35° holes, s/D=3,

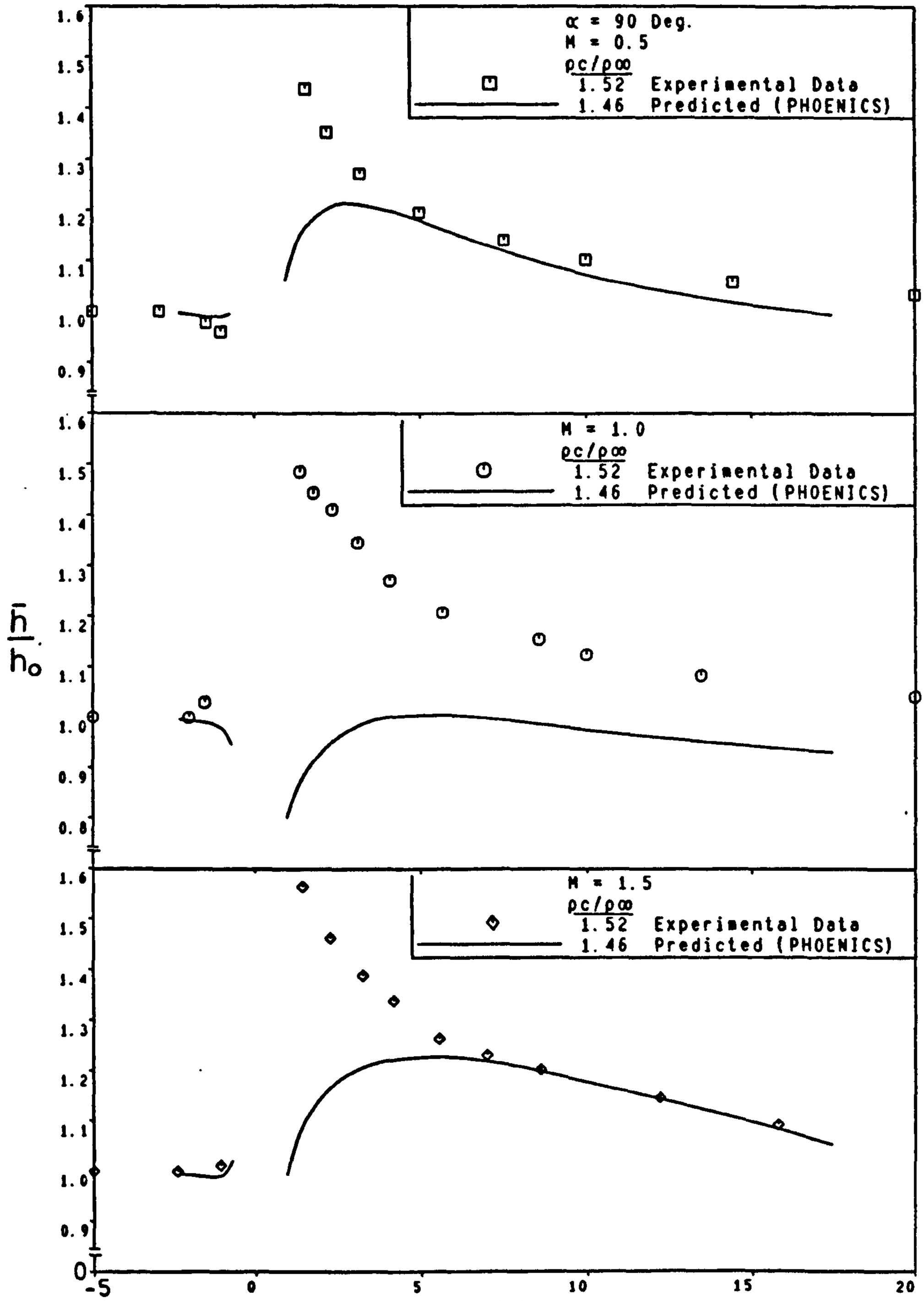

Fig. 9.7 Comparison between predicted and measured $\bar{h}/h_o$ following injection through a row of holes.

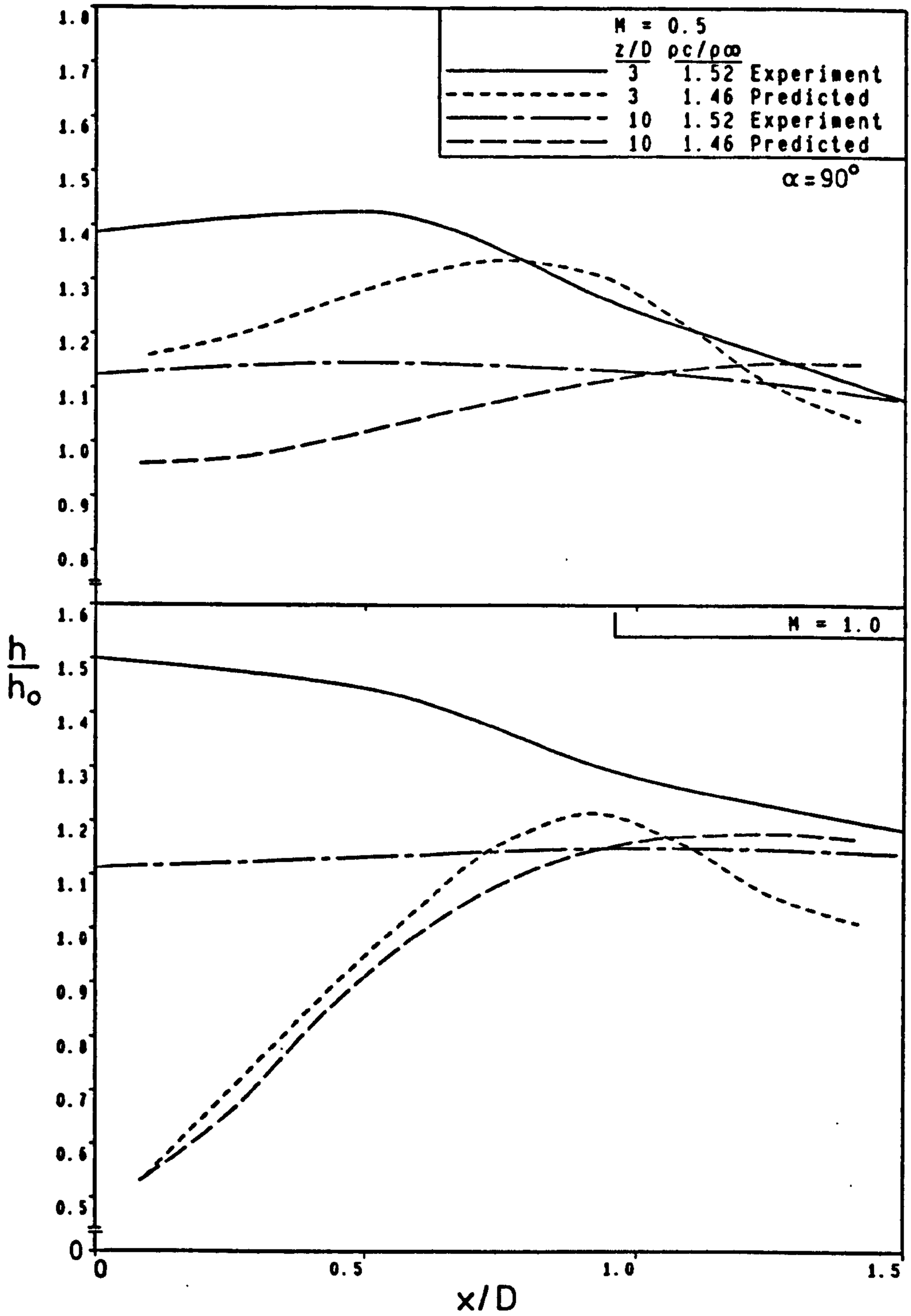

Fig. 9.8 Lateral distribution of predicted and measured h/h$_o$ following injection through a row of holes.

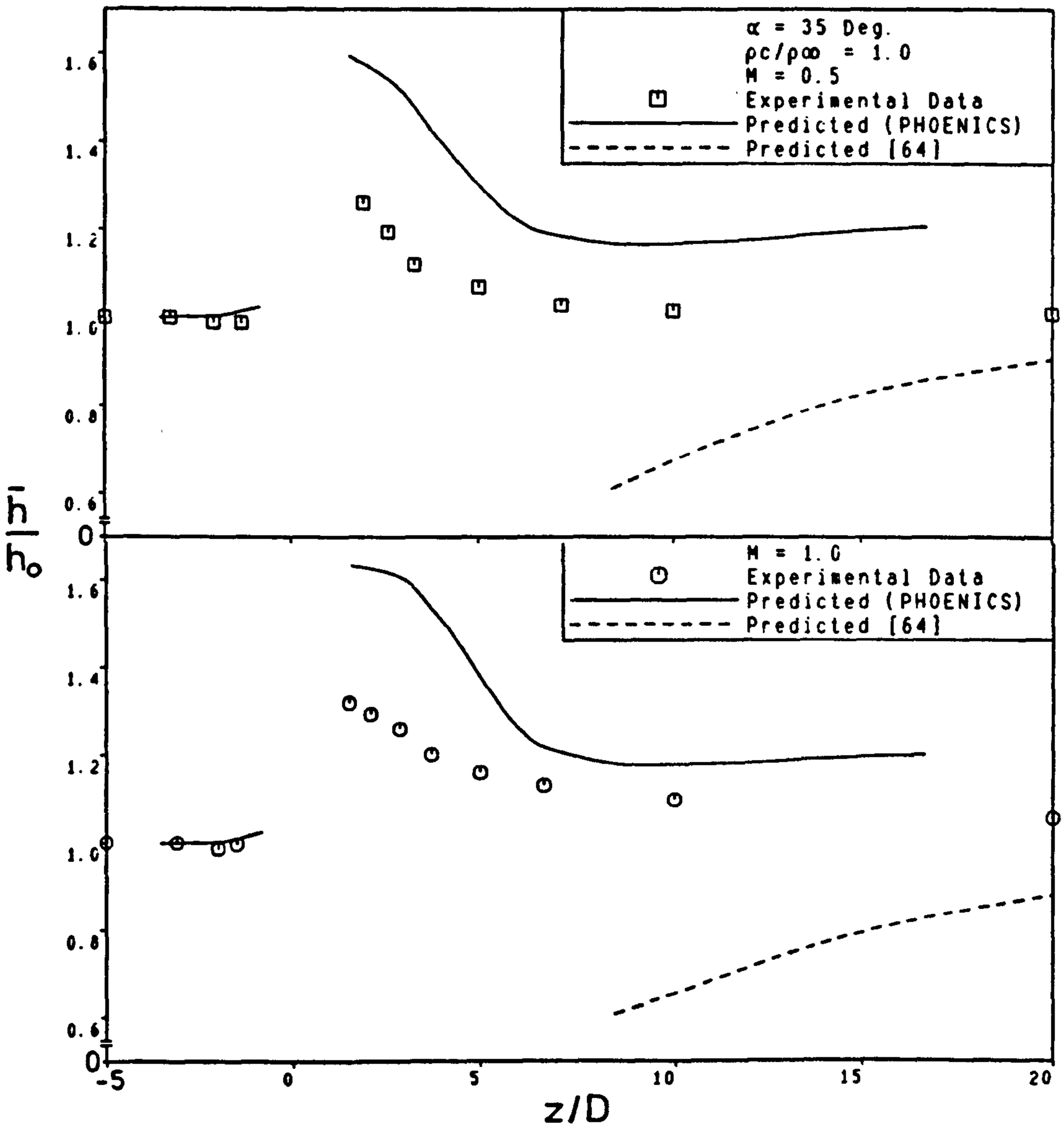

Fig. 9.9 Comparison between predicted and measured $\bar{h}/h_o$ following injection through a row of holes.

u_∞=30.5m/s and Tu=0.5%; the differential equations were solved right up to the wall, and the turbulence model was the k-ε version modified by Lam and Bremhorst [65] which uses a damping function that simulates the influence of molecular viscosity. It can be seen that qualitative agreement between the predicted and measured $\bar{h}/h_o$ is satisfactory. Quantitative agreement, however, is not as good; the calculated coefficients are seen to exceed the measurements by as much as 24% close to a hole (z/D<4), and as much as 15% farther downstream. This may indicate an overestimation of generation of turbulent kinetic energy near the wall. On the other hand, the predictions of [64] are seen to be considerably lower than the measurements, probably caused by underestimation of the turbulent mixing. Apparently, the predictions of film cooling heat transfer coefficient by the general purpose code, PHOENICS, are seen to be in closer agreement with experiment than those obtained by the computer program of [64], which was developed especially for solving the problem of film cooling.

The discrepancy of the predictions with experiment could be illustrated by examining the "w" velocity profiles. Plots of the predicted velocity profiles along with those measured during the experimental phase of this research at streamwise locations z/D=5 and 15, and x/D=0.0 for M=0.5 are shown in Fig. 9.10. Close to a hole, agreement between the predicted and measured velocity profiles in the jet region near the wall is unsatisfactory. The low velocity predictions are probably due to overestimation of turbulent mixing, which may also explain the high predictions of the heat transfer coefficient. Further, the predicted velocity profile may also have been influenced by the difficulty of representing accurately the inclined hole inside the wall by means of porosities, so that the jet velocity profile at the hole exit was possibly poorly predicted. At z/D=15, the discrepancy with measurement extended to the outer region of the boundary layer.

Overprediction of the heat transfer coefficient is clearly shown in Fig. 9.11, a plot of the lateral distribution of h/h_o along with those of experiment. The behaviour of the predicted heat transfer coefficient at z/D=3 appears to be

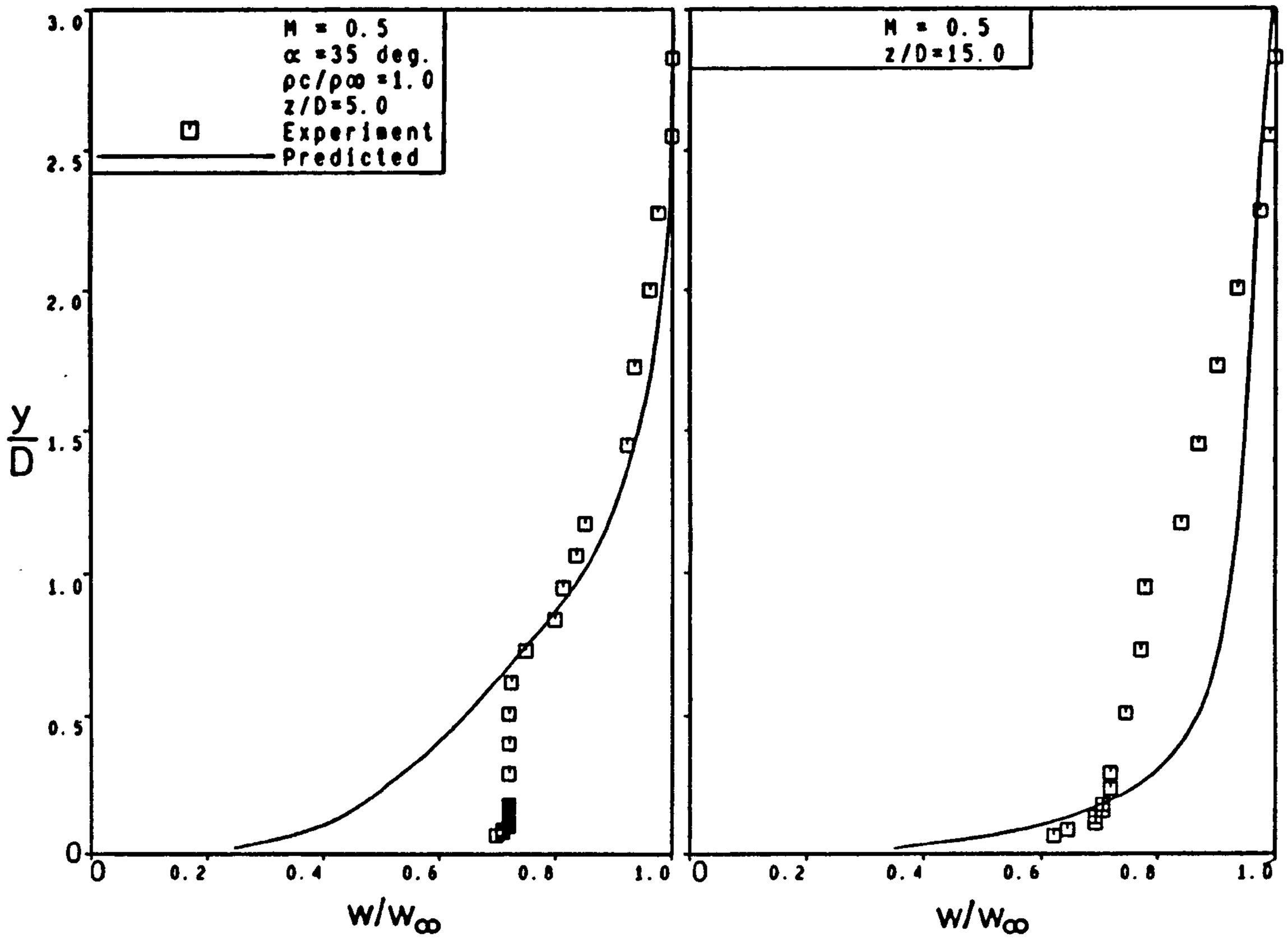

Fig. 9.10 Comparison between predicted and measured velocity profiles downstream of the centreline of a hole.

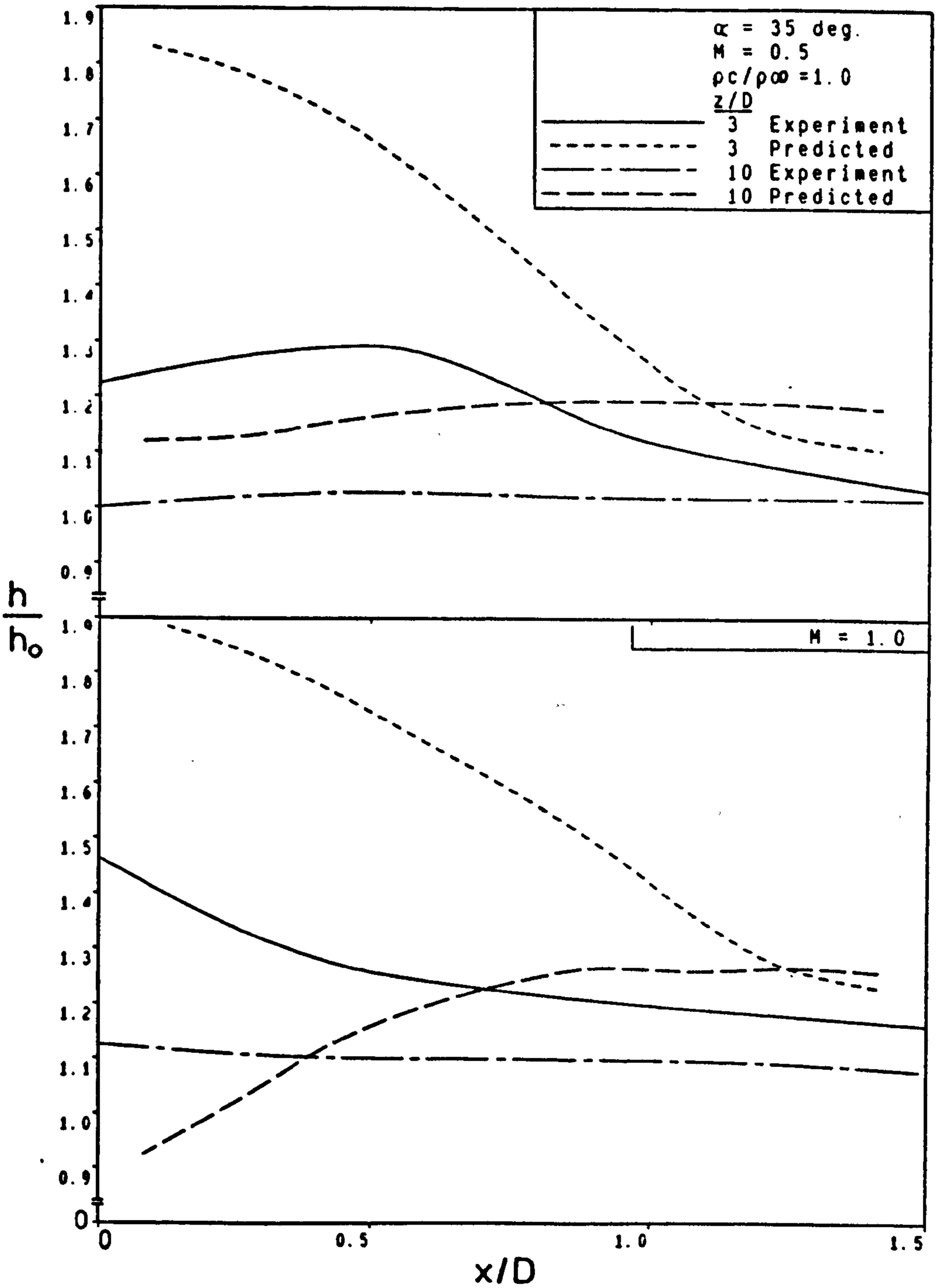

Fig. 9.11 Lateral distribution of predicted and measured h/h_o following injection through a row of holes.

similar to that of experiment, though large differences between predicted and measured values of h/h_∞ are seen everywhere. Farther downstream, at z/D=10, the behaviour is less well predicted. The quantitative differences between calculated and measured h/h_∞ can possibly be reduced if damping terms are implemented in the turbulence model.

(ii) Adiabatic Wall Effectiveness

Fig. 9.12 depicts the averaged effectiveness predictions for M=0.5, 1.0 and 2.0 against the experimental data of [40] and [52]. The numerical predictions of Demuren et al [63] for a hole spacing s/D of 3 but α of 45° are included in the figure. The three-dimensional partial differential equations governing the flow and temperature distributions in [63] were solved with a locally elliptic finite volume technique developed by Rodi and Srivatsa [114], the turbulent stresses and heat fluxes evaluated with the nonisotropic version of the k-ε model proposed by Bergeles et al [59], and the wall function approach described in Launder and Spalding [110] was adopted. The general trend of the $\bar{\eta}$ development is predicted correctly in all cases. Furthermore, halving the grid size has produced negligible change in the predicted effectiveness indicating the independence of the predictions of grid size. The agreement with the measurements is seen to be best for the unity blowing rate, but for the highest blowing rate, $\bar{\eta}$ is underpredicted by as much as 30% downstream of x/D=10. Note that the values of $\bar{\eta}$ are generally small which compound the error. The effectiveness level predicted by [63] is observed to follow the measurements better for M=0.5 and 2, although there is a difference in the angle of injection. However, the enhancement of the nonisotropic variant in the k-ε turbulence model in [63] probably has improved their $\bar{\eta}$ predictions.

In Fig. 9.13, Goldstein et al [40] effectiveness data for M=0.5 are displayed with the predictions along four lateral positions. The general trend of the predicted η is in fairly good agreement with the measurements, although the lateral variation is seen to be higher along the centreline and

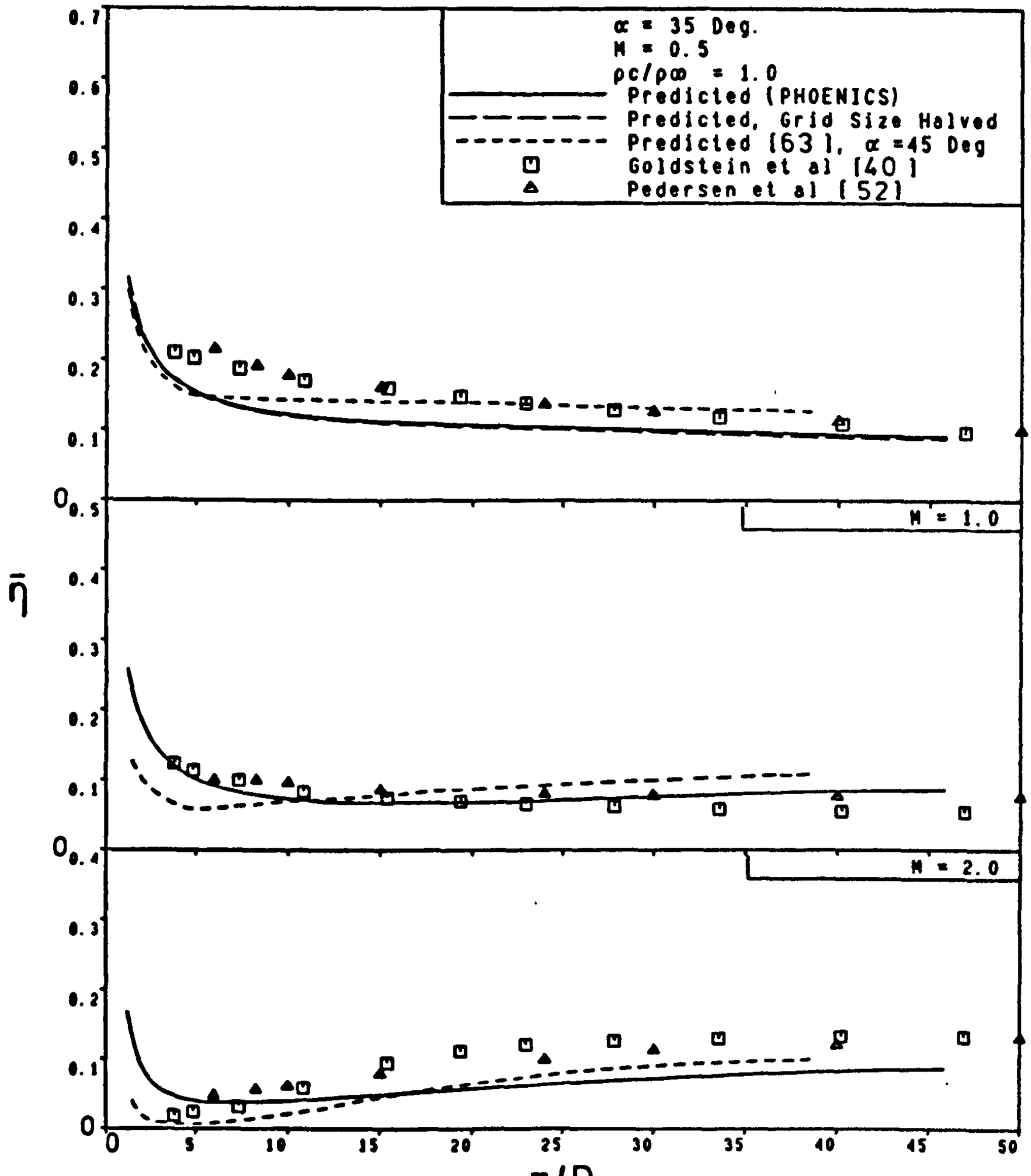

Fig. 9.12 Comparison between predicted and measured laterally averaged effectiveness following injection through a row of holes.

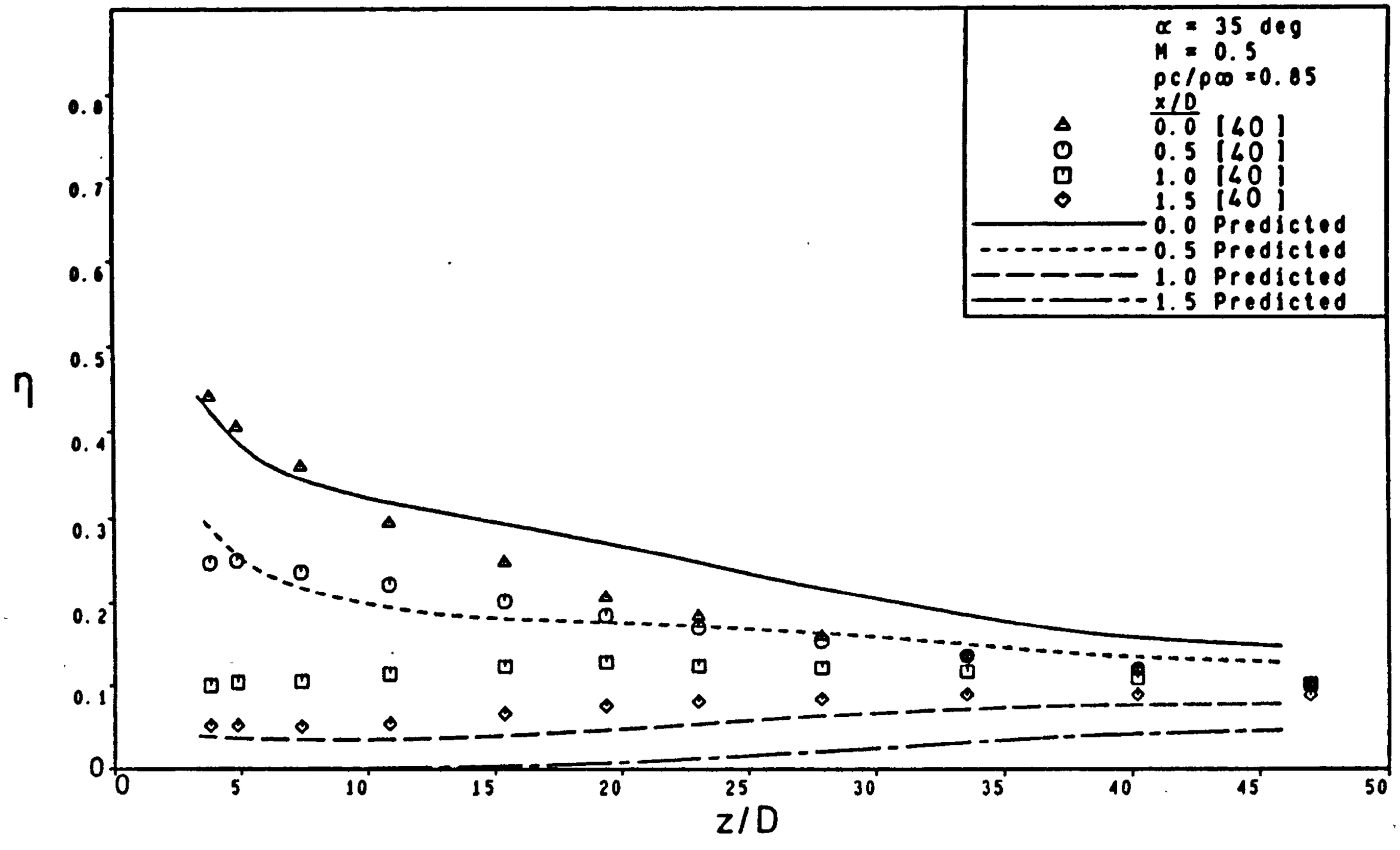

Fig. 9.13 Comparison between predicted and measured effectiveness following injection through a row of holes.

considerably lower in between the holes.

The general picture of the lateral average effectiveness for the case of normal injection as predicted by PHOENICS is much the same as for inclined injection as shown in Fig. 9.14. The initial behaviour, however, is less well predicted; differences with measurements up to 30% are observed. The farfield behaviour is fairly well predicted. The measurements in the figure are those of Foster [105] at a jet-to-mainstream density ratio of 2. The predictions of Demuren et al [63] for normal injection at unity density ratio are also shown. The prediction of Demuren et al are seen to be of the same manner as those predicted by PHOENICS, but at M=1 the level of $\bar{\eta}$ as predicted by [63] is seen to be lower than the measurements presumably caused by the lower density of the jets.

Figs. 9.15(a) and (b) compare predicted and measured [105] lateral distribution and centreline effectiveness respectively for normal injection at density ratio of 2 for different blowing rates. It can be seen that the predicted η is higher than the measurements at centreline positions and appreciably lower in between the holes as has been observed for the case of 35° injection (Fig. 9.13). Nevertheless, the trends agree reasonably well with the measurements.

9.5 CONCLUDING REMARKS

The computer code PHOENICS has been applied to simulate the effects of film cooling by a row of holes. In general, the overall performance is shown to agree reasonably well with the effectiveness measurements. The predicted heat transfer coefficients are also in fairly satisfactory agreement with the measurements. However, simulation of the effectiveness using PHOENICS was more successful than that of the heat transfer coefficient as was the case with the other computer schemes.

The improvement in predictions of the heat flux are solely due to the implementation of the generalised wall functions in PHOENICS.

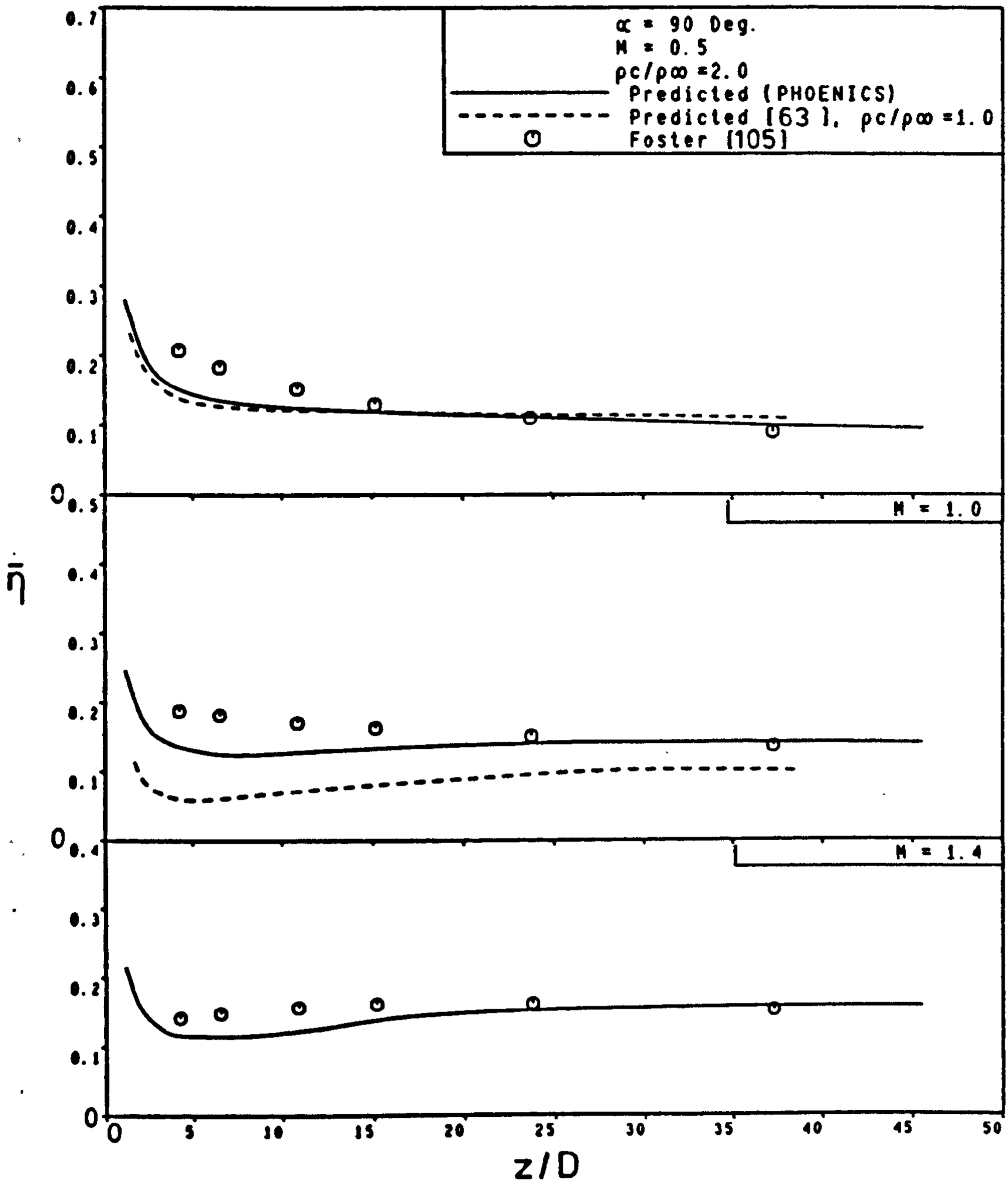

Fig. 9.14 Comparison between predicted and measured laterally averaged effectiveness following injection through a row of holes.

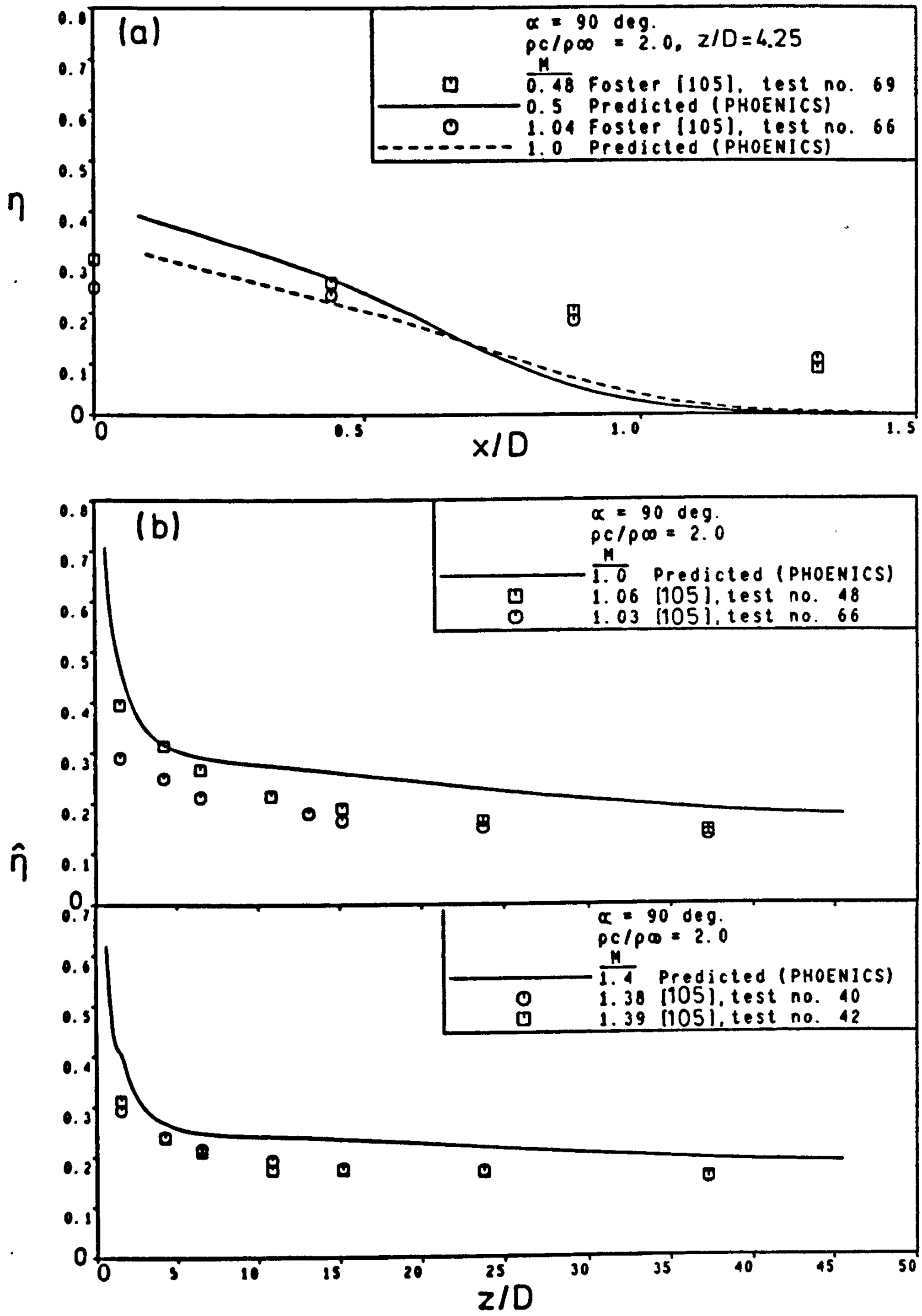

Fig. 9.15 Comparison between predicted and measured effectiveness following injection through a row of holes.

Mention should also be made that the computed heat transfer coefficient results were not checked for grid-dependence as time was not available. Further work (refining the hole cross-section or the domain) may still be required to obtain grid-independent solutions.

Moreover, one should keep in mind that all of the cases examined lay in the strong injection regime where strong jet-mainstream mixing took place behind a hole. Therefore, it can hardly be expected that a turbulence model as simple as the standard k-ε model will simulate accurately the complex mixing region after a hole.

The inadequacy of some of the predictions are believed to stem from the following reasons,

- The assumption that the eddy viscosity is isotropic in the three-dimensional reverse flow zone behind a hole,
- Overestimation of the generation of turbulent kinetic energy near the wall, and,
- Difficulty in simulating accurately the inlet conditions of kinetic energy of turbulence in absence of available measurements.

Further improvement in predictions, therefore, could be acquired if the turbulence model as well as the inlet conditions are modified to account for the points outlined above.

CHAPTER 10

CONCLUSIONS

Here, conclusions are drawn from the discussions of the results in the previous Chapters.

An experimental investigation of cooling film heat transfer coefficients for injection through a row of holes has been undertaken, with particular interest devoted to the influence of two film cooling parameters, the coolant-to-mainstream density ratio and mainstream acceleration. The shortage of experimental information with some degree of simulation of real engine environment as outlined in chapters 2 and 3 has led to carrying out the present systematic programme.

The successful use of foreign gas injection in the mass transfer technique employed for measuring the heat transfer coefficient has enabled the simulation of typical turbine blade density ratios without resorting to the unreliable method of heating the mainstream.

The results have indicated amongst other findings the inadequacies of directly applying some of the film cooling data measured at constant property conditions to turbine blade film cooling calculations at engine conditions. For this data to be effectively utilized, it must be properly scaled to engine practice.

The highly three-dimensional, highly turbulent nature and reverse flow regions exhibited in the film cooling process, has so far precluded the advanced computational methods from adequately predicting the heat transfer on film cooled surfaces. The ability of a general purpose computational fluid dynamics program to predict heat transfer associated with film cooling has been explored through comparison of the computed results with the

experimental data.

The current experimental and numerical work presented and discussed in the preceding chapters, has been aimed at providing designers of film cooled turbine components with information needed for better predictability of external heat transfer. In the following, the conclusions that have been reached are outlined.

10.1 INJECTION HYDRODYNAMIC EFFECTS

- The heat transfer coefficient is increased by injection, and increases with injection rate, for both 35° and 90° injection.

The 90° injection gives higher heat transfer coefficients in regions just downstream of the holes than 35° injection. For 90° holes at M=2 the increase in the local coefficient over the no-injection values exceeded 100%, while for 35° holes 65% increase was measured. The corresponding increase in the spanwise average coefficients was 75% and 36% for 90° and 35° injection respectively. Far downstream, the persistence of the structure of the 35° jets yields higher heat transfer coefficients than for the rapidly falling off structure of normal jets.

- Upstream of the holes, there was little influence on the heat transfer coefficient by 35° injection, while for normal injection an increase of up to 16% was observed for the highest blowing rate. The influence was noticed, however, for only 2 to 3 hole diameters upstream.

- Normal injection through a row of holes results in a higher heat transfer coefficient between the holes than that through a single hole. Mixing between neighbouring jets enhances the heat transfer.

- It has been shown that injection significantly increases the heat transfer coefficient, in particular at large blowing rates close to the injection site. This increase in the heat transfer coefficient may, in fact, be more than counterbalance the cooling effects of injection and cause a net increase in the heat load. It follows that injection at rates in excess of unity may not be favourable.

10.2 DENSITY RATIO

(i) 90° Injection

- The heat transfer coefficient following normal injection through a single hole or a row of holes is insensitive to jet to mainstream density ratio variation. Maximum difference in the heat transfer coefficient of 5% for 52% density ratio difference was found only at the high blowing rate of 2. The rapid interaction and dilution of the jets by the mainstream destroys their identity, so that the coupling between the injection and heat transfer coefficient is not that strong. This results in little difference in the enhanced coefficients with the variation of the mass and momentum flux ratios.

- The blowing rate, M, satisfactorily correlates heat transfer coefficient data under varying density ratio for normal injection. As a consequence, previous normal injection heat transfer studies at density ratios not representative of gas turbine conditions can be directly applied without correction provided only that blowing parameters are matched.

The normalised spanwise average heat transfer coefficient, $\bar{h}/h_o$, is well-correlated by,

$$\bar{h}/h_o = 1.0 + 0.555 \exp\{-0.14(x/D)M^{-0.5}\}$$

in the range,

$$0.5 \leq M \leq 1.5, \text{ and } 1.5 \leq x/D \leq 60 ,$$

and with ±5% uncertainty.

(ii) 35° Injection

- For 35° injection, the heat transfer coefficient at a fixed blowing parameter is strongly dependent on the density ratio, decreasing as the density ratio increases. The reductions in the heat transfer coefficient were found to be in the main within 10% for changes in the density ratio from 1 to 1.52, although they have reached 20% at some downstream locations for the highest blowing rate of 2.

The jet-mainstream mixing in inclined injection is of lesser extent than in normal injection, so that the jets are preserved longer. At a fixed blowing

rate, the higher momentum of the lighter gas injectant is reflected in greater mixing with the mainstream, and thus enhanced heat transfer.

Accordingly, previous heat transfer studies using inclined injection at density ratios close to unity are inadequate in their present form, and need scaling for application in gas turbine design. The relation suggested in this study may be used for this purpose.

- For the range of blowing rates studied, the coolant-to-mainstream velocity ratio is the key parameter in correlating data at differing density ratios. Plotting the normalised spanwise average heat transfer coefficient against $(x/D)(u_c/u_\infty)^{-4/3}$ collapses data for a range of velocity and density ratios. The recommended correlating curve is,

$$\bar{h}/h_o = 1.025 + 0.35 \exp\{-0.15(x/D)(u_c/u_\infty)^{-4/3}\}$$

in the range,

$$0.5 \le u_c/u_\infty \le 1.5, \text{ and } 1.5 \le x/D \le 60 ,$$

and with ±7% uncertainty.

- Most of the tests for 35° and 90° injection performed here, exhibited a similar characteristic in that gross separation from the surface has occurred in the wake of the holes (I>0.16). Consequently, the data falls in the strong injection regime and should have correlated well with the velocity ratio [32]. However, as reported above, the normal injection data were brought together better with M. This suggests that subdivision of the strong injection regime according to injection inclination is needed.

It is abundantly clear that the angle of injection is the essential feature in the observed difference in characteristics between the two geometries examined. As the injection angle is reduced from 90° to 35°, the gross structure of jet-mainstream mixing is changed, leading to more apparent effect of density ratio, and change of data key scaling parameter from M to u_c/u_∞. Furthermore, the film cooling heat transfer coefficients exhibit a considerably higher degree of sensitivity to the influence of blowing rates, momentum flux ratios, and even Reynolds number [22, & 23].

10.3 MAINSTREAM ACCELERATION

- Mainstream acceleration works by suppressing injection induced turbulence, and hence reducing the heat transfer coefficient.

The results obtained were for 35° injection only. They reveal that for both acceleration parameters of $1.9x10^{-6}$ and $5x10^{-6}$ examined, the heat transfer coefficient under the film was lowered as compared with that at zero pressure gradient condition. The spanwise average coefficients normalized by the corresponding zero acceleration values, $\bar{h}/(\bar{h})_o$, approximate to a linear character with the acceleration parameter, K. At any given blowing rate, the coefficients ratio decreased as K was increased. The effect of M on the heat transfer coefficients ratio was weak at the lower K value, and distinct at the higher K; an increase in M leading to a decrease in effect of acceleration on the coefficients ratio. Stronger blowing appeared to have resisted more the domination of the imposed pressure gradients.

The overall average reduction in the averaged coefficients for all M covered at unity density ratio was as follows,

at $K = 1.9x10^{-6}$, $\bar{h}$ was reduced by about 8%, and

at $K = 5.0x10^{-6}$, $\bar{h}$ was reduced by about 23.5% for $M<1.5$, and by 19% for $M\geq1.5$.

These results have the practical implication that data obtained at zero pressure gradient conditions can be corrected for favourable pressure gradients allowing predictions over more realistic conditions on turbine blades.

- The effect of strong mainstream acceleration ($K=5x10^{-6}$) on cooling film heat transfer coefficient in the presence of density ratio was similar to that at unity density ratio for $M<1.5$, where the influence of M was quite weak. A substantial overall reduction in $\bar{h}/(\bar{h})_o$ of about 27% was present for $M>0.5$.

- The effect of raising the density ratio by 52% at constant acceleration of $K=5x10^{-6}$ on the heat transfer coefficient was also similar to that at zero pressure gradient. The decrease in the coefficients reached 20% at some downstream positions for the large blowing rates.

- The heat transfer coefficient data gathered in the absence of density and pressure gradients for M>0.5 could be transformed into data at conditions more characteristic of gas turbines (ρ_j/ρ_∞=1.52 & K=5x10^{-6}) by using the following correction factors; close to a hole (x/D<5), the overall average reduction conversion factor is about 30%, further downstream, the factor is about 35%.

- Empirical evidence has pointed to the fact that the heat transfer coefficient data in the presence of acceleration and density ratio scales reasonably well with $(x/D)(u_j/u_\infty)^{-4/3}$, the data correlating parameter at zero acceleration. The laterally averaged heat transfer coefficient ratio data was scaled using the following correlation,

$$\bar{h}/h_o = [1.0 - 0.04(Kx10^6)][1.025 + 0.35 \exp\{-0.15(x/D)(u_j/u_\infty)^{-4/3}\}]$$

However, the scatter was large particularly for the data at the larger density ratio in the presence of acceleration.

10.4 NUMERICAL STUDIES USING PHOENICS

The heat transfer coefficient has been predicted using the general purpose computer code PHOENICS. Generalised wall functions were used in which the heat flux was calculated using the kinetic energy of turbulence as the characteristic velocity scale rather than the friction velocity. This way plausible predictions of wall heat flux at jet separation regions were obtained.

- For the cases of normal injection through a row of holes, the overall level of agreement of calculated heat transfer coefficient with experiment was quite satisfactory. At unity density ratio, the predicted $\bar{h}/h_o$ agree with measurements within 15% for large M. Best agreement though was achieved at M=0.5 probably because the jet-mainstream mixing was less intensive.

In the presence of density ratio (ρ_j/ρ_∞=1.46), the computed results of $\bar{h}/h_o$ were also reasonably predicted at distances greater than 5D, but lower predictions than measurements were obtained closer to the holes.

The lateral distribution of the heat transfer coefficient, however, was less well predicted; a substantial underestimation of turbulent mixing at centreline locations was evident.

- For the cases of injection through a row of 35° holes, the calculated and measured $\bar{h}/h_o$ agreed fairly well qualitatively, but quantitatively, the calculated $\bar{h}/h_o$ overestimated the measurements by as much as 24% close to a hole ($z/D<4$), and as much as 15% farther downstream. The lateral distribution of the calculated h/h_o was also higher than measurements, although the trends at low M were predicted correctly. Overprediction of the heat transfer coefficient is believed to have been caused by overestimation of generation of turbulent kinetic energy near the wall.

- The overall predicted level of laterally averaged effectiveness, $\bar{\eta}$, for both 90° and 35° holes was in fairly good agreement with experiment. The predictions were generally little lower than measurements, although maximum differences of 30% close to a hole were observed at some cases.

The predicted lateral distribution of effectiveness was found to be higher than measurements at centreline locations and considerably lower at mid-pitch positions for both 90° and 35° holes.

10.5 RECOMMENDATIONS FOR FURTHER WORK

As the ability of models for accurate prediction of external heat transfer of film cooled surfaces at conditions characteristic of engines has not been as yet well established, experimental results remain the foundation for design, and a great deal more is still needed.

The ease with which highly-detailed heat transfer data could be obtained using the swollen polymer technique, makes this method ideal for collection of further reliable data. Thus a data base representative to some degree of realistic engine conditions can be assembled.

The current work could be continued by investigating the heat transfer for different configurations encountered in blade cooling design, such as two rows of holes looking at the effect of spacing and interaction between the two rows

of holes. Shaped holes which offer better cooling effectiveness [47], and one and two rows of crosswise angled holes, or other geometries that could be investigated.

The effect of surface curvature on film cooling heat transfer coefficients could be studied using the present experimental technique, as could the effect of pressure gradients for this geometry. In addition, the effects of variation in Reynolds number could be examined. As the foregoing parameters are expected to exhibit some dependence on the density ratio, investigation of their interacted effects would be of considerable value.

The swollen polymer technique has further been developed for the measurement of film cooling effectiveness [77]. Measurements of both effectiveness and heat transfer coefficient under similar conditions enables accurate determination of heat loads under the influence of the various parameters that could be investigated.

Other work beyond the scope of the present apparatus includes the effects of Mach number, compressibility and rotation.

Future numerical work should incorporate one of the modified versions of the k-ε turbulence model (see reference [111]) in conjunction with the generalised wall functions in PHOENICS. However, grid-independent solutions must be obtained.

Generally, future numerical work should concentrate on developing more sophisticated turbulence models that represent more efficiently the three-dimensional mixing behaviour of a jet in crossflow.

It is hoped that, the preceding suggestions for research activity will, in conjunction with the results of the current work, help to establish design methods of greater accuracy that enhance the confidence in initial designs of film cooled components of gas turbines.

REFERENCES

[1] Sampl, S.R. and Shank, M.E., "State of the Art in Aircraft Gas Turbine Technology," Presented at the 1985 Beijing Inter. Gas Turbine Sympos:ium and Exposition, Beijing, People's Republic of China, September 1-7, 1985.

[2] Rudey, R.A. and Graham, R.W., "A Review of NASA Combustor and Turbine Heat Transfer Research," ASME paper 84-GT-113, 1984.

[3] Hartmann, M.J., "Aeronautical Propulsion - Present Status and Future Directions," ASME paper 84-GT-288, 1984.

[4] Armstrong, F.W., "Gas Turbine Evolution," Inst. of Mech. Eng., 1975.

[5] Moffat, R.J. and Kays, W.M., "The Turbulent Boundary Layer on a Porous Plate: Experimental Heat Transfer with Uniform Blowing and Suction," Int. J. of Heat and Mass Trans., Vol. 11, 1968, pp. 1547-1566.

[6] Moffat, R. J., "Turbine Blade Cooling,"Heat Transfer and Fluid Flow in Rotating Machinery," Edited by Yang, Hemisphere, 1987.

[7] Elovic, E. and Koffel, W.K., "Some Considerations in the Thermal Design or Turbine Airfoil Cooling systems," The 1979 Int. Joint Gas Turbine Congress & Exhibition, July 9-11, 1979.

[8] Stepka, F.S., "Uncertainties in Predicting Turbine Blade Metal Temperatures," ASME paper 80-HT-25, 1980.

[9] Goldstein, R. J., "Film Cooling," Advances in Heat Transfer, Vol. 7, 1971, pp. 321-379.

[10] Metzger, D. E., Carper, H. J. and Swank, L. R., "Heat Transfer with Film Cooling Near Nontangential Injection Slots," ASME J. of Eng. for Power, April 1968, pp. 157-163.

[11] Choe, H., Kays W. M. and Moffat R. J., "Turbulent Boundary Layer on a Full Coverage Film Cooled - an Experimental heat transfer Study with Normal Injection," NASA CR-2642, Jan. 1976.

[12] Forth, C. J. P., Loftus, P. J. and Jones, T. V., "The Effect of Density Ratio on the Film-Cooling of a Flat Plate," AGARD CP 390, Paper No. 10, 1985.

[13] Metzger, D. E., Takeuchi D. I. and Kuenstler O. A., "Effectiveness and Heat Transfer with Full Coverage Film Cooling," ASME J. of Eng. for Power, Vol. 95, 1973, pp. 180-184.

[14] Ville, J. P. and Richard, B. E., "The Measurement of Film Cooling Effectiveness on Turbine Components in Short Duration Wind Tunnels," AGARD CP 229, Paper 34, Feb. 1978.

[15] Metzger, D. E. and Fletcher, D. D., "Evaluation of Heat Transfer for Film Cooled Turbine Vanes," J. of Aircraft, Vol. 8, No. 10, 1971, pp. 33-38.

[16] Choe, H., Kays, W. M. and Moffat, R. J., "The Superposition Approach to Film Cooling," ASME Paper No. 74-WA/HT-27, New York, 1974.

[17] Hartnett, J. P., "Mass Transfer Cooling," Hand Book of Heat Transfer Applications, Edited by Rohsenow, Hartnett and Ganic',McGraw-Hill Book Co., 1985.

[18] Bergeles, G., Gosman, A.D. and Launder, B.E., "The Near-Field Character of a Jet Discharged Normal to a Main Stream," ASME, J. of Heat Transfer, 1976, pp. 373-376.

[19] Colladay, R. S. and Russell, L. M., "Streakline Flow Visualization of Discrete Hole Film Cooling for Gas Turbine Applications," ASME J. of Heat Transfer, May 1976, pp. 245-250.

[20] Ramsey, J. W. and Goldstein, R. J., "Interaction of a Heated Jet with a Deflecting Flow," ASME J. of Heat Transfer, Vol 93,1971, pp. 365-372.

[21] Hay, N., Lampard, D. and Saluja, C.L., "Effects of Cooling Films on the Heat Transfer Coefficient on a Flat Plate with Zero Mainstream pressure Gradient," ASME, Paper 84-GT-40, 1984.

[22] Eriksen, V. L. and Goldstein, R. J., "Heat Transfer and Film Cooling Following Injection Through Inclined Circular Holes," ASME J. of Heat Transfer, Vol. 96, May 1974, pp.239-245.

[23] Eriksen, V.L. and Goldstein, R.J., "Heat Transfer and Film Cooling Following Normal Injecton Through a Round Hole," ASME, J. of Engineering For Power, 1974, pp. 329-334.

[24] Liess, C., "Experimental investigation of Film Cooling with Injection from a Row of Holes for the Application to Gas Turbine Blades," ASME J. of Engineering for Power, Vol. 97, 1975, pp. 21-27.

[25] Goldstein, R.J. and Yoshida, T., "The Influence of a Laminar Boundary Layer and Laminar Injection on Film Cooling Performance," ASME, J. of Heat Transfer, Vol. 104, 1982, pp. 355-362.

[26] Hay, N., Lampard, D. and Saluja, C.L., "Effects of the Condition of the Approach Boundary Layer and of Mainstream Pressure Gradients on the Heat Transfer Coefficient on Film-Cooled Surfaces," ASME, J. of Eng. for Power,84-GT-47, 1984.

[27] Kruse, H., "Effects of Hole Geometry, Wall Curvature and Pressure Gradient on Film Cooling Downstream of a Single Row," AGARD-CP-390, Paper No. 8, 1985.

[28] Mayle, R.E. and Camarata, F.J., "Multihole Cooling Film Effectiveness and Heat Transfer," ASME, J. of Heat Transfer, 1975, pp. 534-538.

[29] Crawford, M.E., Kays, W.M. and Moffat, R.J., "Full-Coverage Film Cooling, Part 1: Comparison of Heat Transfer data for Three Injection Angles," ASME, J. of Eng. for Power, Vol. 102, 1980, pp. 1000-1005.

[30] Furuhama, K. and Moffat, R.J., "Turbulent Boundary Layer Heat Transfer on a Convex Wall With Discrete Hole Injection," ASME/JSME Thermal Eng. Joint Conf., Hawaii, 1983.

[31] Forth, C.J.P., "An Investigation of Scaling Parameters Governing Film-Cooling," PhD Thesis, University of Oxford, 1985.

[32] Forth, C. J. P. and Jones, T. V., "Scaling Parameters in Film-Cooling," 8th. Int. Heat Transfer Conference, 1986, pp. 1271-1276.

[33] Loftus, P.J. and Jones, T.V., "The Effect of Temperature Ratios on the Film Cooling Process," ASME, J. of Eng. for Power, Vol 105, 1983, pp. 615-620.

[34] Ligrani, P.M. and Camci, C., "Adiabatic Film Cooling Effectiveness From Heat Transfer Measurements in Compressible, Variable-Property Flow," ASME, J. of Heat Transfer, Vol.107, 1985, pp. 313-320.

[35] Jabbari, M.Y. and Goldstein, R.J., "Adiabatic Wall Temperature and Heat Transfer Downstream of Injection Through Two Rows of Holes," ASME, J. of Eng. for Power, Vol. 100, 1978, pp. 303-307.

[36] Teekaram, A.J.H., Forth, C.J.P. and Jones, T.V., "The Use of Foreign gas to Simulate the Effects of Density Ratios in Film-Cooling," ASME, 88-GT-37, 1988.

[37] Hartnett, J.P., Birkebak, R.C. and Eckert, E.R.G., "Velocity Distributions, Temperature Distributions, Effectiveness and Heat Transfer in Cooling of a Surface with a Pressure Gradient," Int. Development in Heat Transfer, Pt. IV, ASME, New York, 1961, pp. 682-689.

[38] Warren, J.M. and Metzger, D.E., "Heat Transfer with Film Cooling in the Presence of a Laminarizing Mainstream," ASME, 72-HT-11, 1972.

[39] Jabbari, M.Y. and Goldstein, R.J., "Effect of Mainstream Acceleration on Adiabatic Wall Temperature and Heat Transfer Downstream of Gas Injection," 6th. Int. H. T. Conf., Toronto, Canada, Aug. 7-11, 1978.

[40] Goldstein, R.J., Eckert, E.R.G., Eriksen, V.L. and Ramsey, J.W., "Film Cooling Following Injection Through Inclined Circular Tubes," NASA CR-72612, 1969.

[41] Pedersen, D. R., "Effect of Density Ratio on Film Cooling Effectiveness for Injection Through a Row of Holes and a Porous Slot," PhD Thesis, University of Minnesota, 1972.

[42] Brown, A. and Saluja, C.L, "Film Cooling from a single Hole and a Row of Holes of Variable Pitch to Diameter Ratio," Int. J. Heat Mass Transfer , Vol 22, 1979, pp. 525.

[43] Kadotani, K. and Goldstein, R.J., "Effect of Mainstream Variables on Jets Issuing from a Row of Inclined Round Holes," ASME J. of Eng. for Power, Vol. 101, 1979, pp. 298-304.

[44] Kadotani, K. and Goldstein, R.J., "On the Nature of Jets Entering a Turbulent Flow Part B-Film Cooling Performance," ASME, J. of ENg. for Power, Vol. 101, 1979, pp. 466-470.

[45] Goldstein, R.J., Eckert, E.R.G., Chiang, H.D. and Elovic, E., "Effect of Surface Roughness on Film Cooling Performance," ASME, 84-GT-41, 1984.

[46] Afejuku, W.O., Hay, N. and Lampard, D., "The Film Cooling Effectiveness of Double Rows of Holes," ASME, J. of Eng. for Power, Vol. 102, 1980, pp. 601.

[47] Goldstein, R. J., Eckert, E. R. G. and Burggraf, F., "Effects of Hole Geometry and Density on Three-Dimensional Film Cooling," Int. J. Heat Mass Transfer, Vol. 17, 1974, pp. 595-607.

[48] Ito, S., Goldstein, R. J. and Eckert, E. R. G., "Film Cooling of a Gas Turbine Blade," ASME J. of Engineering for Power, Vol. 100, 1978, pp. 476-481.

[49] Eriksen, V.L., Eckert, E.R.G. and Goldstein, R.J., "A Model for the Analysis of the Temperature Field Downstream of a Heated Jet Injected Into an Isothermal Crossflow at an Angle of 90 Degrees," NASA CR-72990, 1971.

[50] Stollery, J.L. and El-Ehwany, A.A.M., "A Note on the Use of a Boundary-Layer Model for Correlating Film-Cooling Data," Int. J. Heat Mass Transfer, Vol 8, 1965.

[51] Goldstein, R.J., Eckert, E.R.G. and Ramsey, J.M., "Film Cooling with Injection Through a Circular Hole," NASA CR-54604, 1968.

[52] Pedersen, D. R., Eckert, E. R. and Goldstein, R. J., "Film Cooling with Large Density Differences Between the Mainstream and the Secondary Fluid Measured by the Heat Mass Transfer Analogy," ASME J. of Heat Transfer, Vol. 99, 1977, pp. 620-627.

[53] Metzger, D.E., Biddle, J.R. and Warren, M., "Evaluation of Film Cooling Performance on Gas Turbine Surfaces," AGARD-CP-73-71, Paper 24, 1971.

[54] Foster, R. C. and Haji-Sheikh, A., "An Experimental Investigation of Boundary Layer and Heat Transfer in the Region of Separated Flow Downstream of Normal Injection Slots," ASME J. of Heat Transfer, May 1975, pp. 260-266.

[55] Fitt, A.D., Ockendon, J.R. and Jones, T.V., "Aerodynamics of Slot Film-Cooling; Theory and Experiment," J. Fluid Mechanics, Vol. 160, 1985.

[56] Narayan, K.Y. and Narashima, R., "Parametric Analysis of Turbulent Wall Jets," Aero, Quarterly, 1973.

[57] Patankar, S.V., Basu, D.K. and Alpay, S.A., "Prediction of the Three-Dimensional Velocity Field of a Deflected Turbulent Jet," ASME, J. of Fluids Engineering, Vol. 15, 1977, pp. 758-762.

[58] Bergeles, G., Gosman, A.D. and Launder, B.E., "The Prediction of Three-Dimensional Discrete-Hole Cooling Processes, Part 1: Laminar Flow," ASME, J. of Eng. for Power, 1976, pp. 379-386.

[59] Bergeles, G., Gosman, A.D. and Launder, B.E., "Double-Row Discrete-Hole Cooling: An Experimental and Numerical Study," ASME, J. of Eng. for Power, vol. 102, 1980, pp. 498-503.

[60] Bergeles, G., Gosman, A.D. and Launder, B.E., "The Predictio of Three-Dimensional Discrete-Hole Cooling Processes, Part 2: Turbulent Flow," ASME, J. of Heat Transfer, Vol. 103, 1981, pp.141-145.

[61] Crawford, M.E., Kays, W.M. and Moffat, R.J., "Full-Coverage Film Cooling, Part II: Heat Transfer Data and Numerical Simulation," ASME, J. of Eng. for Power, Vol. 102, 1980, pp. 1006-1012.

[62] Miller, K.L. and Crawford, M.E., "Numerical Simulation of Single, Double and Multiple Row Film Cooling Effectiveness and Heat Transfer," ASME 84-GT-112, 1984.

[63] Demuren, A.O., Rodi, W. and Schonung, B., "Systematic Study of Film Cooling with a Three-Dimensional Calculation Procedure," ASME, J. of Turbomachinery, Vol. 108, 1986, pp. 124-130.

[64] Schonung, B. and Rodi, W., "Prediction of Film Cooling by a Row of Holes with a Two-Dimensional Boundary-Layer Procedure," ASME, 87-GT-122, 1987.

[65] Lam, C.K.G. and Bremhorst, K.A., "Modified Form of the k-ε Model for Predicting Wall Turbulence," ASME, J. Fluids Eng., Vol. 103, 1981, pp. 456-460.

[66] Foster, N. W. and Lampard, D., "Effects of Density and Velocity Ratio on Discrete Hole Film Cooling," AIAA J., Vol. 13, No. 8, 1975, pp. 1112-1114.

[67] Button, B.L. and Mohamad, T.T., "Experimental Techniques to Determine the Convective Heat Transfer Coefficients for Flat and Curved Surfaces," High Temperature Technology, 1983, pp. 163-170.

[68] Hay, N., "Heat Transfer Measurements in Steady State Facilities," in VKI Lecture Series 'Measurement Techniques in Turbomachines', 1985.

[69] Mick, W.J. and Mayle, R.E., "Stagnation Film Cooling and Heat Transfer, Including Its Effect Within the Hole Pattern," ASME, J. of Turbomachinary, Vol. 110, 1988, pp. 66-72.

[70] Hippensteele, S.A., Russell, L.M. and Stepka, F.S., "Evaluation of a Method for Heat Transfer Measurements and Thermal Visualization Using a Composite of a Heat Element and Liquid Crystals," ASME, J. of Heat Transfer, Vol. 105, 1983, pp. 184-189.

[71] Goldstein, R. J. and Taylor, J. R., "Mass Transfer in the Neighborhood of Jets Entering a Crossflow," ASME J. of Heat Transfer, Vol. 104, 1982, pp. 715-721.

[72] Webster, W.P. and Yavuzkurt, S., "Measurements of Mass Transfer Coefficient and Effectiveness in the Recovery Region of a Film-Cooled Surface," ASME, 86-GT-134, 1986.

[73] Saluja, C. L., Lampard, D., Hay, N. and Burns, I., "The Determination of Heat Transfer Coefficients on Film Cooled Surfaces Using the Swollen Polymer Technique," 1st. U. K. National Heat Transfer Conference, Leeds, 1984.

[74] Goldstein, R.J., "Some Measurement Techniques in Heat Transfer," Sixth Int. Heat Transfer Conf., Toronto, Canada, Vol. 6, 1978, pp. 495-508.

[75] Launder, B.E. and York, J., "Discrete-Hole Cooling in the Presence of Free Stream Turbulence and strong Favourable Pressure Gradient," Int. J. Heat Mass Transfer, Vol. 17, 1974, pp. 1403-1409.

[76] Eckert, E.R.G. and Drake, R.M., "Analysis of Heat and Mass Transfer," MGraw-Hill Kogakusha Ltd., 1972.

[77] Hay, N., Lampard, D., Maali, R. and Burns, I, "Simultaneous Determination of Heat Transfer Coefficient and Adiabatic Wall Effectiveness on a Film Cooled Surface Using the Swollen Polymer Technique," 8th. Int. Heat Transfer Conf., San Francisco, 1986.

[78] Han, J.C., Chandra, P.R. and Lau, S.C., "Local Heat/Mass Transfer Distribution Around Sharp 180° Turn in a Smooth Square Channel," Heat Transfer and Fluid Flow in Rotating Machinery, Edited by Yang, Hemisphere, 1987.

[79] Eckert, E.R.G. and Goldstein, R.J., "Measurements in Heat Transfer," Hemisphere Publishing Corp., Wash., 1976.

[80] Macleod, N. and Todd, R. B., "The Experimental Determination of Wall Fluid Mass-Transfer Coefficients Using Plasticised Polymer Surface Coatings," Int. J. Heat Mass Transfer, Vol. 16, 1973, pp. 485-503.

[81] Kapur, D.N. and Macleod, N., "The Determination of Local Mass-Transfer Coefficients by Holographic Interferometry - I," Int. J. Heat Mass Transfer, Vol. 17, 1974, pp. 1151-1162.

[82] Ammari, H. D., "Internal Report," Dept. of Mech. Eng., University of Nottingham, July 1989.

[83] Kapur, D.N., "The Profilometric Determination of Mass Transfer Coefficients by Holographic Interferometry," PhD. Thesis, University of Edinburgh, 1973.

[84] Kapur, D. N. and Macleod, N., "Vapour Pressure Determination for Certain High-Boiling Liquids by Holography," Ind. Eng. Chem., Prod. Res. Dev., Vol. 15, No. 1, 1976, pp. 50-54.

[85] Ostrovsky, Yu.I., Butusov, M.M. and Ostrovskaya, G.V., "Interferometry by Holography," Springer Series in Optical Sciences, Vol. 20, Springer-Verlag, 1980.

[86] Hay, N., Lampard, D. and Saluja, C.L., "Application of the Swollen Polymer Technique to the Study of Heat Transfer on Film Cooled Surfaces," 7th International Heat Transfer Conference, Munich, Vol. 4, 1982, pp. 503-508.

[87] Ennos, A.E., "Measurement of In-Plane Surface Strain by Hologram Interferometry," J. Physics E., Vol. 1, 1968, pp. 731-734.

[88] Kapur, D.N. and Macleod, N., "The Estimation of Local Heat Transfer Coefficients for Two-Dimensional Surface Roughness Elements by Holographic Interferometry," Conf. The Eng. Uses of Holography, Strathclyde, U.K., 1975.

[89] Maali, R., "Film Cooling Project, Handover Report," Dept. of Mech. Eng., University of Nottingham, 1985.

[90] Masliyah, J.H. and Nguyen, T.T., "Holographic Determination of Mass Transfer Due to Impinging Square Jet," Canadian J. Chem. Eng., Vol. 54, 1976, pp. 299-304.

[91] Masliyah, J.H. and Nguyen, T.T., "Experimental Study of Mass Transfer Due to Impinging Rectangular Jet," Canadian J. Chem. Eng., Vol. 55, 1977, pp. 156-160.

[92] Masliyah, J.H. and Nguyen, T.T., "Mass Transfer Due to Impinging Slot Jet," Int. J. Heat Mass Transfer, Vol. 22, 1979, pp. 237-244.

[93] Paterson, W.R., Colledge, R.A., Macnab, J.I. and Joy, J.A., "Solid-Gas Mass Transfer Measurement by the Swollen Polymer Method: Proving of Swelling Agents," Int. J. Heat Mass Transfer, Vol. 30, No. 2, 1987, pp. 279-287.

[94] Bradshaw, P. and Pankhurst, "The Design of Law Speed Wind Tunnels," Progress in Aeronautical Sciences, Vol. 5, No. 1, 1964.

[95] Moretti, P.M. and Kays, W.M., "Heat Transfer to a Turbulent Boundary Layer with Varying Free-Stream Velocity and Varying Surface Temperature-An Experimental Study," Int. Heat Mass Transfer, Vol. 8, 1965, pp. 1187-1202.

[96] Bradshaw, P., "Turbulence," Topics in Applied Physics, Edited by P. Bradshaw, Vol. 12, Springer-Verlag, 1976.

[97] Patel, V.C. and Head, M.R., "Revision of Turbulent to Laminar Flow," J. of Fluid Mechanics, Vol. 34, Part 2, 1968, pp. 371.

[98] Kline, S. J. and McClintock, F. A., "Describing Uncertainties in Single Sample Experiments," Mechanical Engineering, 1953, pp. 3-8.

[99] Kays, W. M. and Crawford, M. E., "Convective Heat and Mass Transfer," McGraw-Hill, New York, 1980.

[100] Back, L.H., Cuffel, R.F. and Massier, P.F., "Laminarization of a Turbulent Boundary Layer in Nozzle Flow-Boundary Layer and Heat Transfer Measurements with Wall Cooling," ASME, J. of Heat Transfer, 1970, pp. 333-344.

[101] Bird, R.B., Stewart, W.E. and Lightfoot, E.N., "Transport Phenomena," Wiley, 1960.

[102] Brokaw, R.S., "Predicting Transport Properties of Dilute Gases," I & E C Process Design and Development, Vol. 8, No. 2, 1969, pp. 240-253.

[103] Pietrzyk, J.R., Bogard, D.G. and Crawford, M.E., "Effects of Density Ratio on the Hydrodynamics of Film Cooling," ASME Paper No. 89-GT-175, 1989.

[104] Eriksen, V. L., "Film Cooling Effectiveness and Heat Transfer with Injection Through Holes," NACA CR 72991, University of Minnesota.

[105] Foster, N.W., "Film Cooling of Gas Turbine Blades," PhD Thesis, University of Nottingham, 1976.

[106] Mick, W.J. and Mayle, R.E., "Stagnation Film Cooling and Heat Transfer, Including Its Effect Within the Hole Pattern," ASME J. of Turbomachinery, Vol. 110, 1988, pp. 66-72.

[107] Rosten, H.I. and Spalding, D.B., "The PHOENICS Beginner's Guide," CHAM TR/100, Document Revision 04, Software Version 1.4, 1987.

[108] Rosten, H.I. and Spalding, D.B., "The PHOENICS Reference Manual," CHAM TR/200, Document Revision 06, Software Version 1.4, 1987.

[109] Gunton, M.G., Rosten, H.I., Spalding, D.B. and Tatchel, D.G., "PHOENICS: An Instruction Manual," CHAM TR/75, 1983.

[110] Launder, B.E. and Spalding, D.B., "The Numerical Computation of Turbulent Flows," Computer Methods in Applied Mechanics and Engineering, Vol. 3, 1974, pp. 269-289.

[111] Nagano, Y. and Hishida, M., "Improved Form of the K-E Model for Wall Turbulent Shear Flows," ASME, J. of Fluids Engineering, Vol. 109, 1987, pp. 156-160.

[112] Jayatillika, C.L.V., "The Influence of Prandtl Number and Surface Roughness on the Resistance of the Laminar Sublayer to Momentum and Heat Transfer," Prog. in Heat and Mass Transfer, Vol. 1, Pergamon Press, 1969.

[113] Rosten, H.I. and Worrell, J.K., "Generalised Wall Functions for Turbulent Flow Including Wall Roughness," CHAM/PER/88/2, 1988.

[114] Rodi, W. and Srivatsa, S.K., "A Locally Elliptic Calculation Procedure for Three-Dimensional Flows and Its Application to a Jet in Cross Flow," Comp. Meth. Appl. Mech. Engg., Vol. 23, 1980, pp. 67-83.

[115] Thermodynamic Research Centre, "Selected Values of Properties of Hydrocarbons and Related Compounds," API Research Project 44, Texas A&M University, College Station, TX, Table 23-2-(1.101)-ka, 1974.

[116] Ammari, H.D., "Error Analysis of the Swollen Polymer Technique," Dept. of Mech. Eng., University of Nottingham, 1986.

[117] Reid, R.C., Prausnitz, J.M. and Sherwood, T.K., "The Properties of Gases and Liquids," McGraw-Hill, 1977.

[118] Hirschfelder, J.O.,Curtiss, C.F. and Bird, R.B., "Molecular Theory of Gases and Liquids," Wiley, 1954.

[119] Reid, C.R. and Sherwood, T.K., "The Properties of Gases and Liquids," McGraw-Hill, 1958.

APPENDIX A

CHOICE OF SUITABLE SWELLING AGENT

In order to choose a suitable swelling agent it is necessary for the agent to satisfy the following properties to provide long enough constant rate period,

i) high diffusivity within the polymer.

ii) relatively low vapour pressure, and,

iii) high swelling power.

The diffusivities of swelling agents in rubbers have a rough correspondence with their liquid viscosities [83]. The vapour pressure can be obtained from the literature. The swelling power is a function of the polymer-swelling agent system and is determined experimentally.

The equilibrium swelling of some silicone rubber (RTV615)-swelling agent systems was obtained experimentally by employing aluminium thin circular discs with a thin RTV615 rubber coating bonded to a 0.5mm recession in the discs. These were immersed in a bath of the swelling agent to be examined for a period of time until their swollen weight became constant indicating the completion of absorption of the swelling agent by the dry rubber. The difference between the weights of the dry and swollen rubber yielded the amount of swelling agent absorbed, from which the percentage of volume swelling was calculated. Plots of the percentage swelling of RTV615 by three organic liquids; diethyl adipate, butyl carbitol and anisaldehyde, are shown in Fig. A.1. The swelling liquids were chosen for their low vapour pressure and they were readily available at adequate purity. However, as observed in the figure their swelling power is rather small. Therefore attention was directed at swelling agents already examined by other workers which have higher swelling power.

In view of the work reported by [86 & 92], ethyl salicylate is the most widely used swelling agent in the swollen polymer method. Data on ethyl salicylate amongst other agents is given in [83 & 84]. More recently, Paterson

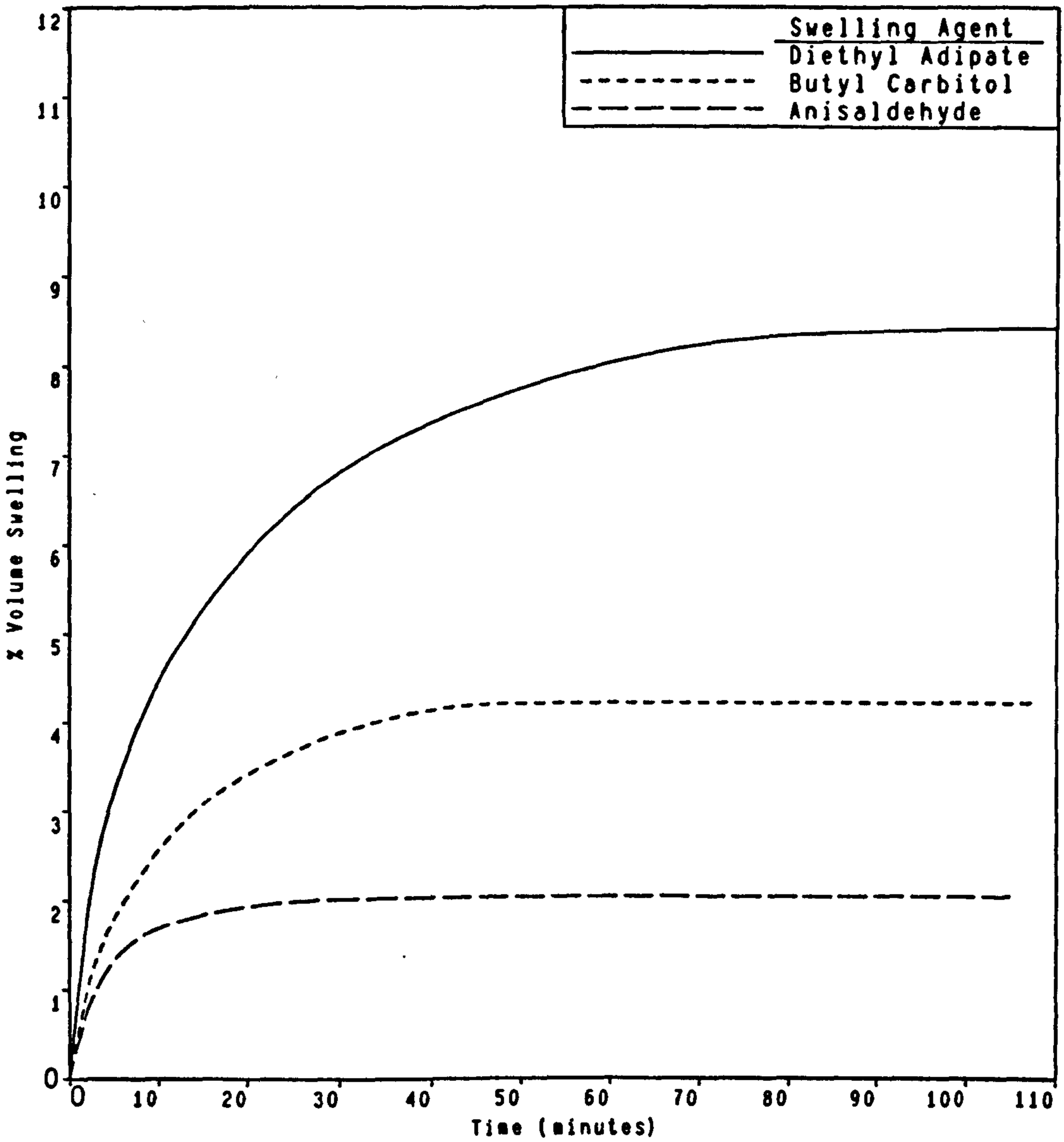

Fig. A.1 Volume swelling of silicone rubber RTV615 by swelling agents with time.

et al [93] have reported highly reliable data on ethyl salicylate and other organic compounds including tetradecane. Along with ethyl salicylate, comparison is made with isobutyl benzoate and tetradecane representing high, intermediate and relatively low vapour pressure organic substances respectively.

The equations in the theoretical analysis of [80], have been replaced by a simple iterative computer solution to obtain more readily the constant rate period for any specified polymer-swelling agent system. Figs. A.2 and A.3 display the constant rate period of ethyl salicylate system against the mass transfer coefficient. The figures show that the use of ethyl salicylate as a swelling agent for RTV615 rubber gives inconveniently short experimental times at high rates of transfer. Experiments, therefore, could only be operated at relatively low temperatures which was not possible for the existing experimental setup in the air flow laboratory as it stands, or, heavily exceeding the 5% tolerated vapour pressure change, thus, introducing uncertainty and loosing accuracy. Isobutyl benzoate gives longer run times as shown in Fig. A.4, but there again, it could not be used at the rather high blowing rates that cause high mass transfer close to the injection site without manipulating the operating temperature or relaxing the 5% vapour pressure change. By contrast, tetradecane (see Fig. A.4) gives comfortably large constant rate periods at high rates of mass transfer.

In order to compare the effectiveness and reliability of ethyl salicylate and tetradecane in practice, preliminary film cooling tests employing both chosen swelling agents were carried out at ambient temperatures. The conclusions were in favour of tetradecane in all aspects. Mass transfer results using ethyl salicylate were partly inconsistent, and the uncertainty associated with the identification of fringe order using the air-gauge was determined by submitting the swollen polymer coating to 66 air gauge measurements taken at a room temperature of 18°C. The mean fringe order error of which was +2.5 fringes and the standard deviation from the mean was 1.1 fringes. The mass transfer results using tetradecane were consistent, and the fringe order

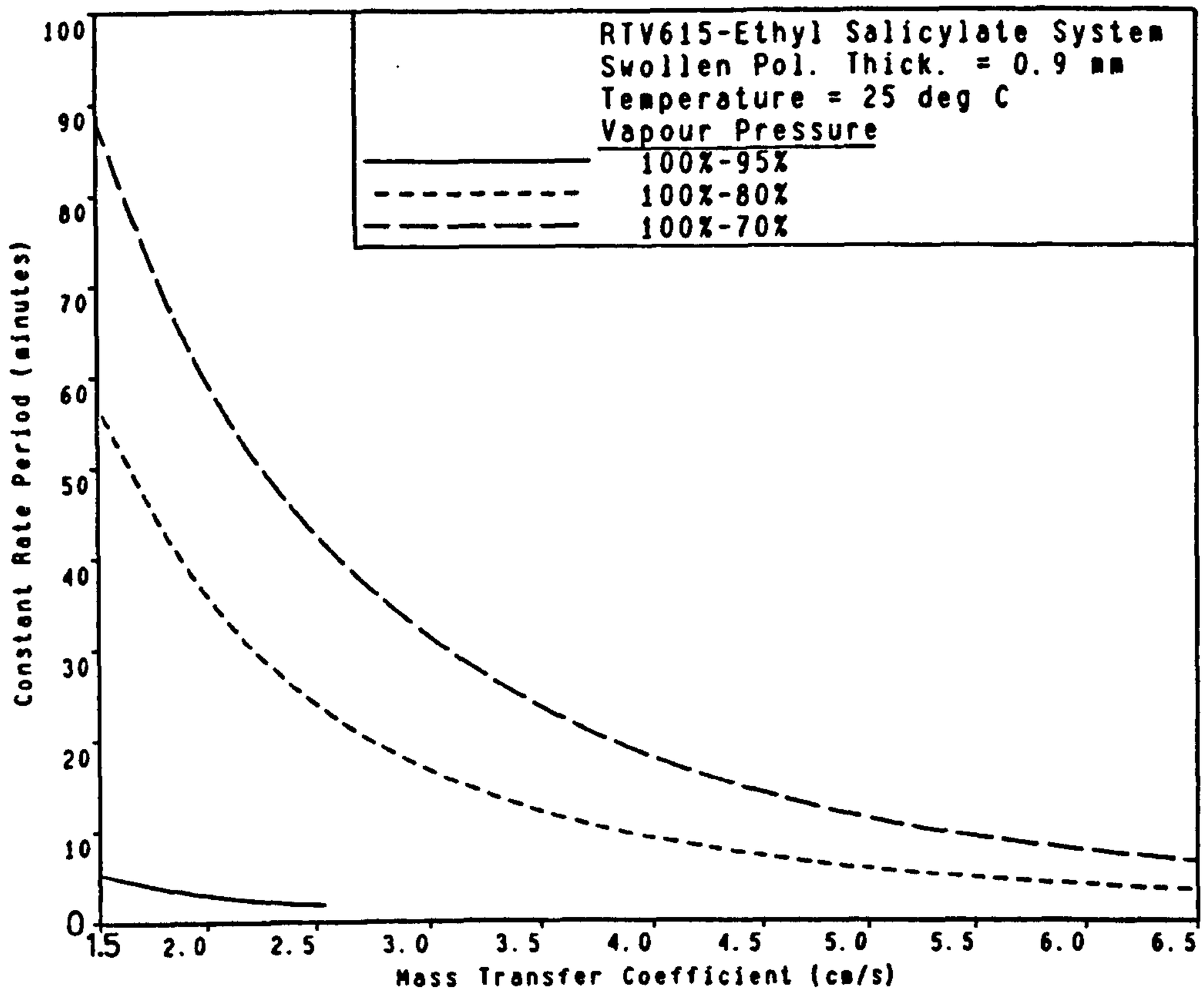

Fig. A.2 Effect of tolerated vapour pressure on predicted constant rate period.

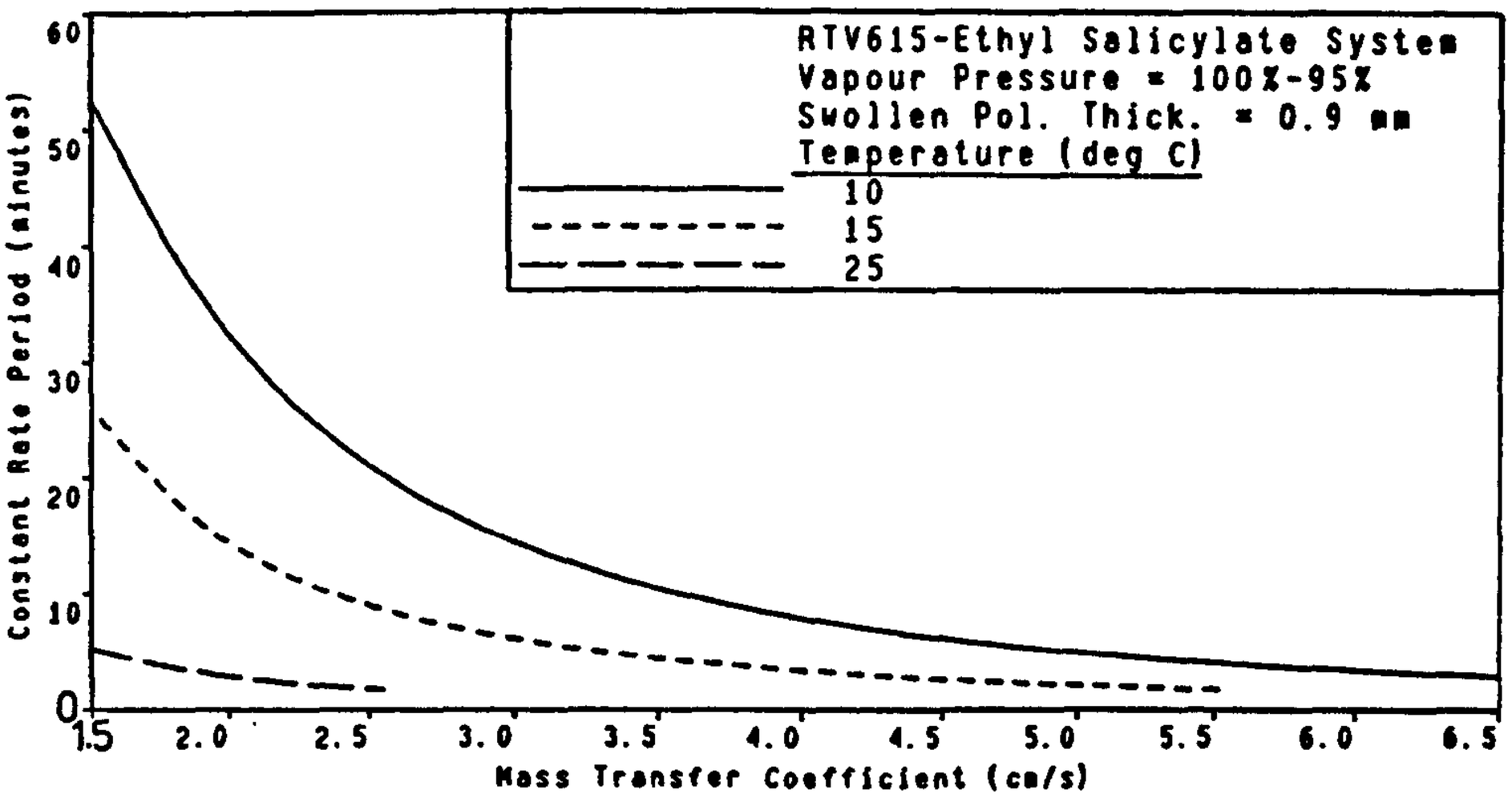

Fig. A.3 Effect of temperature on predicted constant rate period.

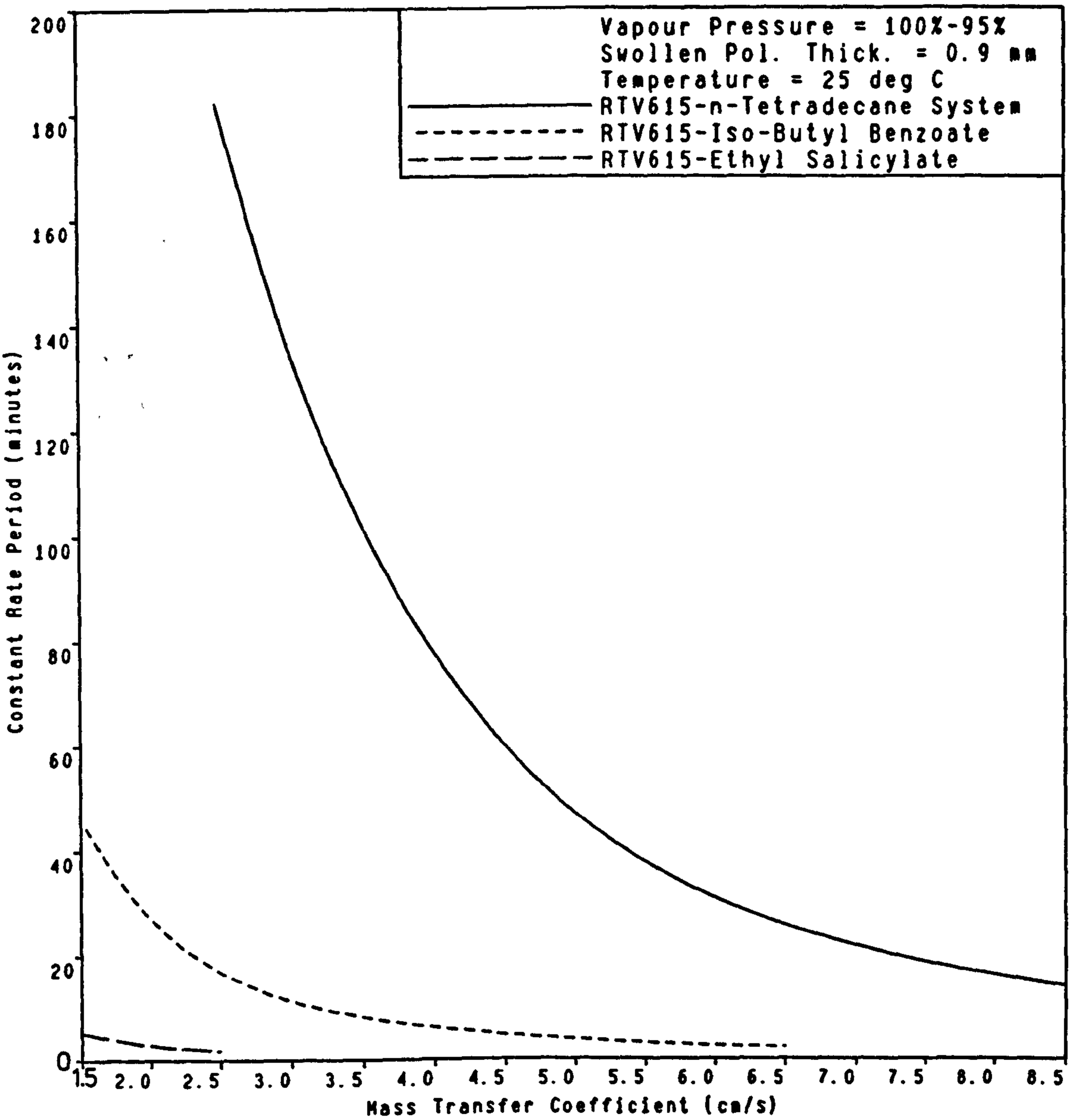

Fig. A.4 Comparison of predicted constant rate period for three different systems.

identification analysis resulted in a mean fringe order error of +1.4 fringes and a standard deviation of 0.6 fringes out of 58 measurements taken at a higher temperature, 26°C. Furthermore, tests investigating evaporation of the swelling agent by the air-gauge air supply impingement on the swollen coating were carried out. Air-gauge manometer pressure readings were taken against time and plotted in Fig. A.5. It is observed that the pressure-time curve is steeper for the ethyl salicylate case indicating faster evaporation had occurred due to its higher vapour pressure. Moreover, the curvature of the graphs partly caused by the continued increase in distance between the air-gauge probe and the coating surface due to evaporation, is more pronounced when ethyl salicylate was used as the swelling agent. The manometer pressure decreased almost linearly for the first 4 to 5 minutes for the coating swollen by tetradecane.

The swollen polymer method requires accurate vapour pressure data. The vapour pressure of ethyl salicylate recently measured at ambient temperatures by Paterson et al [93] is 25% lower than that measured by Kapur and Macleod [84]. Whereas tetradecane vapour pressure data at relatively low temperatures (17-56°C) established by Paterson et al [93] is only 5% greater than that reported in the literature by the Thermodynamic Research Centre [115].

Upon the analysis conducted above, it was concluded that n-tetradecane is the most appropriate swelling agent for the present work.

An idea of what the fringe order is likely to be when employing tetradecane in mass transfer experiments is shown in Fig. A.6. The figure displays estimates of fringe order corresponding to mass transfer rates in an assumed 15 minutes test duration at different temperatures. These estimates were deduced from the theoretically calculated recessions. It is interesting to note that the fringe order estimates at a mass transfer coefficient about 3.5cm/s were found to agree quite well with those measured experimentally in the course of this research, thus confirming the accuracy of the theoretical analysis.

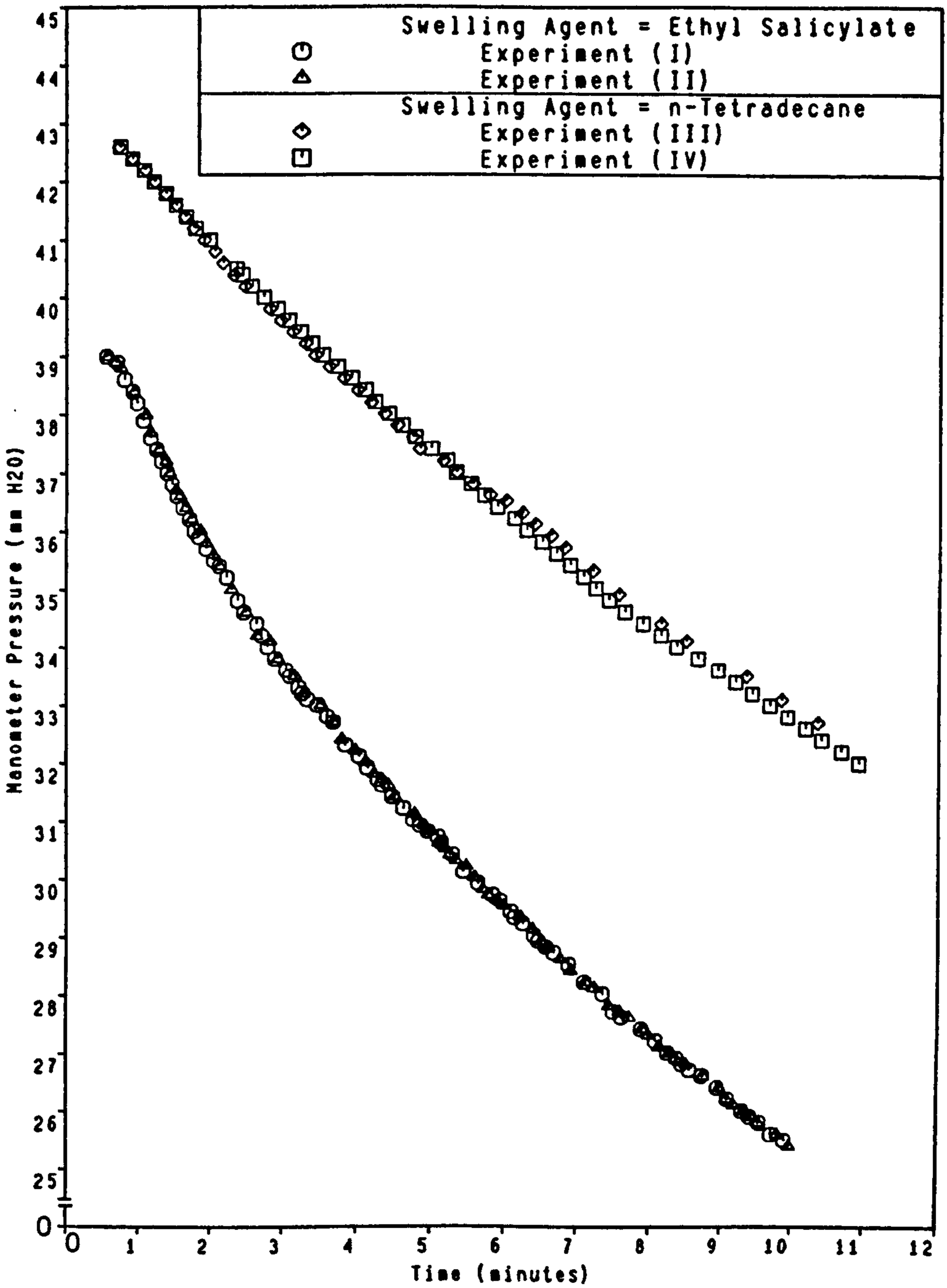

Fig. A.5 Variation of manometer pressure due to evaporation of swelling agent from the swollen polymer by the air-gauge supply with time.

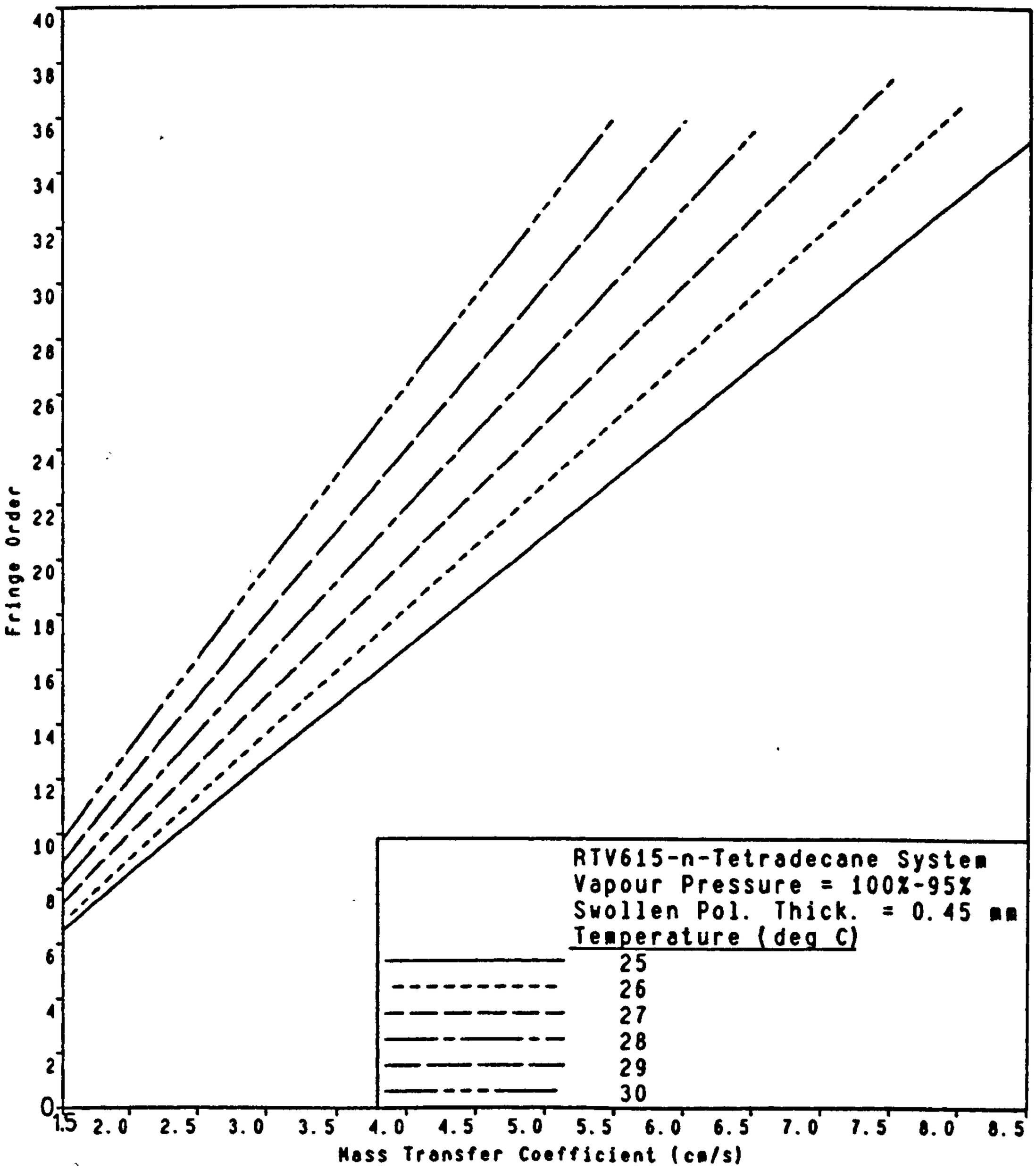

Fig. A.6 Predicted fringe order for experiments of 15 minutes duration.

APPENDIX B

CALIBRATION OF THE AIR-GAUGE

Calibration of the air-gauge was nessecary for the relation between the air-gauge back pressure and air-gauge probe-to-surface distance to be determined. Three experiments, as described by Kapur and Macleod [88], were therefore conducted.

The micrometer head of the air-gauge probe assembly had graduations of 0.0001" divisions. When the former was rotated the probe tip moved forwards or rearwards according to the exact value and direction of rotation, hence the probe could be finely adjusted in the horizontal plane normal to the test-plate surface.

Due to the effects of evaporation of the swelling agent on the displacement between the air-gauge probe and the swollen polymer surface at the point of measurement, the dummy plate was used instead. The back pressure readings measured on the water filled Betz manometer were taken corresponding to each 0.0002" displacement away from the surface. A plot of the manometer back pressure against the distance traversed by the micrometer is presented in Fig. B.1. It can be seen that there is a part of the graph for which the pressure-displacement relation is linear. This corresponds to a back pressure range between 30.0 and 44.0 mm H_2O and to a distance from the surface of 36.75 and 19.10 microns respectively. The steepest gradient for which the air-gauge pressure is most sensitive to the probe displacement happens to be at that linear range. Therefore, to improve accuracy, all recession measurements of the film cooling tests were taken inside the linear range.

From the slope of the linear range of the graph, an increase of the distance between the probe and the surface (or recession of a swollen polymer surface) corresponding to one mm back pressure drop is equal to 1.2995 microns, accordingly for a pressure drop P mm H_2O,

Recession = 1.2995 x P microns.

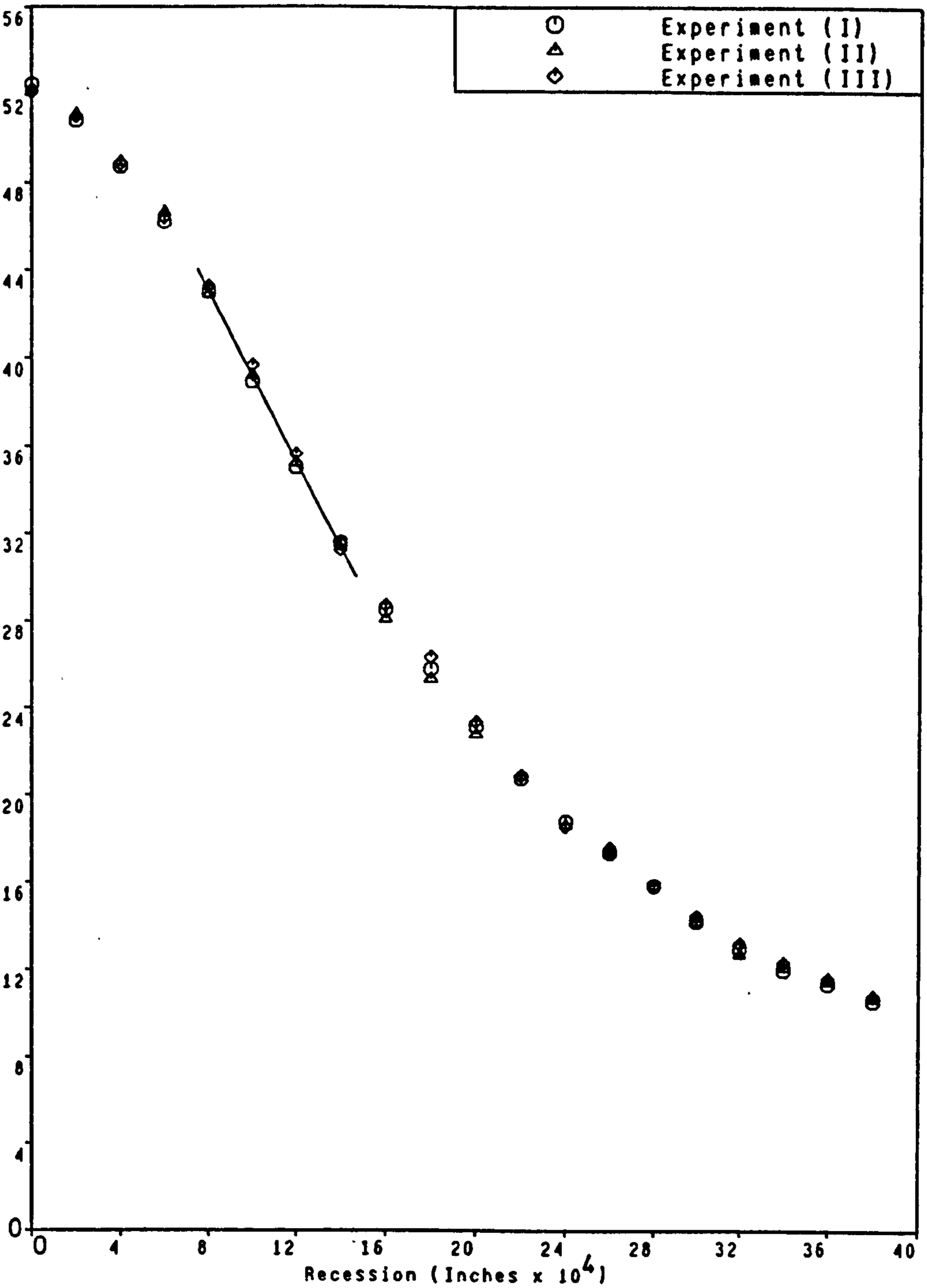

Fig. B.1 Calibration of the air-gauge.

APPENDIX C

EXPERIMENTAL DIFFICULTIES ENCOUNTERED

There were many experimental difficulties encountered using the existing experimental technique. An outline of the major problems that have been overcome in the preparation of the apparatus is as follows:

i) The proper choice of a swelling agent to provide a constant rate period long enough to minimise start-up and shut-down errors.

ii) Reduction of the errors associated with evaporation of swelling agent by impingement of the air-gauge air supply on the polymer surface at the point of measurement.

iii) The three-dimensionality of the mainstream over the test surface.

iv) The interferograms suffered from the appearance of spurious fringes which superimposed the fringes actually produced by the film cooling experiments. Full investigation of this problem is discussed elsewhere [116], however a brief description of the stages in identifying the source of this problem follows:

a- Careful replacement of the test plate on the kinematic mount for the double-exposure holograms produced no spurious fringes.

b- Clamping of the test plate to the floor of the tunnel test section by nuts and bolts produced spurious fringes. The effect was removed by the use of spring clamps with rubber pads.

c- Deflection of the test plate by the mainstream static pressure was thought to be the cause of the appearance of spurious fringes in tests conducted in a wind tunnel by Kapur [83]. The large aluminium test plate was replaced by a newly made stainless steel test plate of the same thickness but of smaller diameter, and, hence, much stiffer. However, the spurious fringes did not disappear so that hysteresis associated with deflection of the test plate by the static pressure was not the sole or dominant source of the appearance of false fringes.

d- Successful elimination of the spurious fringes was finally achieved when tests conducted with the difference in the temperature of the test plate between the two exposures did not exceed about 0.5°C. The temperature variation was therefore the major cause of producing false fringes. A constant temperature throughout the experimental apparatus during the course of an experiment was therefore essential for accurate determination of mass (heat) transfer coefficients. Uniform temperatures were accomplished by the provision of controlled electric heaters to the tunnel environmental chamber and to the newly built enclosure of the holographic table.

APPENDIX D

UNCERTAINTY ANALYSIS

The uncertainties on the absolute and ratios of local and laterally averaged heat transfer coefficients are evaluated according to the method of Kline and McClintock [98] as follows (full details are given in [82]):

(i) The heat transfer coefficient ratio with and without injection, h/h_o,is calculated using equation (6.11),

$$h/h_o = n/n_o$$

The uncertainty, $\delta(h/h_o)$, is estimated through the individual uncertainty associated with each factor as follows,

$$\delta\left[\frac{h}{h_o}\right] = \left[\left(\frac{\partial(n/n_o)}{\partial n}\,\delta n\right)^2 + \left(\frac{\partial(n/n_o)}{\partial n_o}\,\delta n_o\right)^2\right]^{1/2} \qquad \text{- - - (D.1)}$$

where, $\partial(n/n_o)/\partial n = 1/n_o$, and $\partial(n/n_o)/\partial n_o = -n/n_o^2$.

The estimated uncertainty on the measurement of the fringe order, δn ($=\delta n_o$), is taken from the standard deviation from the mean of 58 measurements as ±0.6 fringes.

Substituting in eq. (D.1), a heat transfer coefficient ratio uncertainty of ±4% is determined for near the injection field ($x/D<10$) where a fringe order value of 30 is assumed, while an uncertainty of ±5% is determined in the farfield ($x/D>10$) where n is around 17.

(ii) The lateral average heat transfer coefficient ratio, $\bar{h}/h_o$, is determined from equation (6.12),

$$\frac{\bar{h}}{h_o} = \frac{\bar{n}}{n_o} = \frac{1}{(s/D)/2}\int_0^{(s/D)/2}\frac{n(x/D,z/D)}{n(x/D)}\,d(z/D)$$

The uncertainty on the calculated averaged fringe order, $\delta\bar{n}$, based on a 95% confidence level is estimated as ±2.1 fringes in the nearfield and ±1.5 fringes in the farfield.

Following the procedure carried out in (i) above, uncertainties of ±7.9% and ±9.4% on the lateral average coefficients ratio, $\bar{h}/h_o$, in the nearfield and farfield respectively are determined.

(iii) The absolute mass transfer coefficient, h_m, is determined from equation (6.5),

$$h_m = \rho_{sc}\,\delta / C_w\,t$$

Hence,

$$\delta h_m = \left[\left(\frac{\partial h_m}{\partial \rho_{sc}}\delta\rho_{sc}\right)^2 + \left(\frac{\partial h_m}{\partial \delta}\delta\delta\right)^2 + \left(\frac{\partial h_m}{\partial C_w}\delta C_w\right)^2 + \left(\frac{\partial h_m}{\partial t}\delta t\right)^2\right]^{1/2} \text{- - (D.2)}$$

The uncertainties on the different measurements are estimated as follows,

(a) $\delta\rho_{sc} = \pm 0.0035$ g/cm³, estimated using equation (4.6), based on the uncertainty in the mass fraction of swelling agent in the swollen polymer of ±0.013 as given by [93].

(b) $\delta t = \pm 15$ seconds in a 12 minutes test time based on 98% confidence level.

(c) $\delta C_w = \pm 5.386\text{x}10^{-9}$ g/cm³, estimated using equation (4.5) and applying the method of [98], based on the uncertainties $\delta T = \pm 0.3$K and $\delta P_v = 5.076\text{x}10^{-4}$ mmHg estimated from eq. (6.6).

(d) $\delta\delta = \pm 0.231$ microns, estimated using first eq.(4.7) to determine $\delta\delta/1\text{fringe} = \pm 0.00362$ microns. The latter was based on the uncertainty in the volume fraction in the swollen polymer of ±0.0077 as given by [93] and using eq. (6.7). Then the method of [98] was applied to equation (6.8) where $\delta n = \pm 0.6$ fringe.

By substituting these values in equation (D.2), a mass transfer coefficient uncertainty of ±6.7% is determined.

(iv) The uncertainty on the laterally averaged heat transfer coefficient ratio in the presence of favourable pressure gradients is as determined in (ii) above so that,

$\delta(\bar{h}/h_o) = \delta(\bar{h}_{MF}/h_{oMF}) = \delta(\bar{h}_{SF}/h_{oSF}) = \pm 7.9\%$ in the nearfield and = ±9.4% in the farfield.

Therefore,

$\delta\bar{h}_{MF} = \pm 7.9\%\ (h_{oMF} \pm \delta h_{oMF}) = \pm 8.43\%\ h_{oMF}$ in the nearfield, and = ±10.03% h_{oMF} in the farfield. Similarly, for $\delta\bar{h}_{SF}$ and $\delta\bar{h}$.

The estimated uncertainties then are,

$\delta\bar{h}_{MF} = \pm 0.270$ cm/s
$\delta\bar{h}_{SF} = \pm 0.185$ cm/s in the nearfield
$\delta\bar{h} = \pm 0.295$ cm/s
and,
$\delta\bar{h}_{MF} = \pm 0.321$ cm/s
$\delta\bar{h}_{SF} = \pm 0.221$ cm/s in the farfield
$\delta\bar{h} = \pm 0.351$ cm/s

By applying the method of [98] and substituting these values in, $\frac{\bar{h}_{MF}}{\bar{h}}$ and $\frac{\bar{h}_{SF}}{\bar{h}}$ uncertainties on the laterally averaged heat transfer coefficients ratios, $\bar{h}_{MF}/\bar{h}$, and, $\bar{h}_{SF}/\bar{h}$, of ±9.4% and ±8.2% respectively in the nearfield, and ±13.4% and ±12.4% respectively in the farfield are determined.

APPENDIX E

CALCULATION OF DIFFUSION COEFFICIENTS AND SCHMIDT NUMBERS

(i) Calculation of Diffusion Coefficients

In the absence of experimental information, the best present method in estimating diffusion coefficients of nonpolar-nonpolar gases or polar-nonpolar gases, is the semi-empirical expression based on consideration of the kinetic theory of gases and the Lennard-Jones potential of intermolecular forces. This is (the expression can be found in several text books, see [117] for example),

$$D_{12}=0.0018583\ T^{3/2}\ [(M_1+M_2)\ /\ M_1\ M_2]^{1/2}\ /\ P\ \sigma_{12}\ C_D \qquad \text{- - - (E.1)}$$

where, D_{12} = diffusion coefficient, cm^2/s

T = temperature, K

M_1, M_2 = molecular weight of species 1 and 2

P = pressure, atm

σ_{12} = characteristic Lennard-Jones length force constant, A°, and

C_D = diffusion collision integral, dimensionless (= kT / ε_{12}), where k is Boltzmann's constant and ε_{12} is a characteristic Lennard-Jones energy force constant, erg.

In case there are no data on σ_{12} and ε_{12}, it is customary to use the following empirical relations [118],

$$\sigma_{12} = (\sigma_1 + \sigma_2) / 2 \qquad \text{- - - (E.2)}$$

$$\varepsilon_{12} = (\varepsilon_1\ \varepsilon_2)^{1/2} \qquad \text{- - - (E.3)}$$

The most reliable values of the force constants σ and ε are obtained by correlating experimental viscosity data [102]. However if the data are not available as is the case with n-tetradecane, estimates for nonpolar gases can possibly be obtained from other properties, such as the boiling point, T_b, and the molar volume at the boiling point, V_b, as cited by Brokaw [102],

$$\varepsilon / k = 1.18\ T_b \qquad \text{,(Svehla, 1962)} \qquad \text{- - - (E.4)}$$

$$V_b = \pi\ N\ \sigma^3 / 3\ \text{, yielding, } \sigma = 1.166\ V_b^{1/3} \qquad \text{,(from [118])} \qquad \text{- - (E.5)}$$

here N is Avogadro's number.

The molar volume at the boiling point V_b is estimated by either Schroeder's or Le Bas's method which are simply based on addition of atomic volume increments [119].

Other empirical relations are reported in many text books, such as those based on the critical point instead of the boiling point [101 & 119]. However, the diffusion coefficients of tetradecane diffusing in air, other gases and gas mixtures were calculated using the force constants relations cited by Brokaw [102] since better agreement was reached with the experimental data of Paterson et al [93].

(ii) Diffusion in Multicomponent Gas Mixtures

Steady state conditions prevailed in the film cooling experiments; the feed streams were of constant concentration at uniform temperature and pressure. Steady-state diffusion in multicomponent gas mixtures is described by this relation [117],

$$D_{1m} = 1 / \Sigma^{n}_{i=2} \, x_i / D_{1i} \qquad \text{- - - (E.6)}$$

where D_{1m}= diffusion coefficient of component 1 in the mixture of m species,

D_{1i}= binary diffusion coefficient of 1i system, and

x_i= mole fraction of component i.

This relation assumes, for practical calculations, that one gas only diffusing in a non diffusing gas mixture. Equation (E.6) was considered to apply to the processes under investigation based on the simplifying assumption that tetradecane only was diffusing in the other gases.

The correlations described above conclude the theoretical aspects of estimating the diffusion coefficients in binary and multicomponent gas mixtures.

(iii) Estimation of Viscosities of Gas Mixtures and Schmidt Numbers

Viscosities of the gas mixtures were needed in the estimation of Schmidt numbers. They were estimated following the procedure of Brokaw [102] who

used an approximate formula for the viscosity of gas mixtures derived by Sutherland (1895), which is based on simple mean-free path arguments. The expression is,

$$\mu_{mix} = \Sigma^{m}_{i=1}\ x_i\ \mu_i\ /(x_i + \Sigma^{m}_{j=1}\ O_{ij}\ x_j) \qquad \text{- - - (E.7)}$$

where μ_{mix} is the mixture viscosity while μ_i is the viscosity of component i; x_i and x_j are mole fractions designating the composition. Brokaw in a particular complete study of gas mixtures developed an accurate theoretical expression for O_{ij}, so that it can be obtained from,

$$O_{ij} = S_{ij}\ A_{ij}\ (\mu_i/\mu_j)^{1/2}$$

here S_{ij} can be taken as unity for mixtures of nonpolar gases. In a mixture of polar-nonpolar gases, however, the interactions are essentially of a nonpolar nature so that S_{ij} can also be assumed as unity [102]. A_{ij} is a lengthy function of molecular weight ratio (M_i/M_j) only, which is given in a scale in [102] and plotted against (M_i/M_j) in Reid et al [117].

The expression (E.7) have been tested extensively by comparison with experimental data on 280 mixtures involving 25 gas pairs [102]. For these mixtures the average error was 0.7%.

Other expressions for O_{ij} and correlations for the estimation of viscosities of gas mixtures at low pressures are reported in [117].

Once the viscosity and diffusion coefficient of tetradecane diffusing in the various gases and gas mixtures have been calculated, the Schmidt number was estimated using the established relation,

$$Sc = \mu_2 / \rho_2\ D_{12}$$

where the subscript 2 denotes the gas or gas mixture of which tetradecane is diffusing into.